FACULTY OF ENGINEERING AND ARCHITECTURE

Biomechanical Insights into Pulmonary Autografts and Aortic Dissections Using Fluid-Solid Interaction Simulations

Amith Balasubramanya

Doctoral dissertation submitted to obtain the academic degree of
Doctor of Biomedical Engineering

Supervisors

Prof. Patrick Segers, PhD* - Prof. Joris Degroote, PhD** - Prof. Nele Famaey, PhD*

* Department of Electronics and Information Systems
Faculty of Engineering and Architecture, Ghent University

** Department of Electromechanical, Systems and Metal Engineering
Faculty of Engineering and Architecture, Ghent University

December 2025

GHENT UNIVERSITY

ISBN 978-94-93464-90-2
NUR 954
Wettelijk depot: D/2025/10.500/150

Members of the Examination Board

Chair

Honorary Prof. Ronny Verhoeven, PhD, Ghent University

Other members entitled to vote

Prof. Tom De Mulder, PhD, Ghent University
Lauranne Maes, PhD, Ghent University
Selene Pirola, PhD, Technische Universiteit Delft, the Netherlands
Prof. Alberto Redaelli, PhD, Politecnico di Milano, Italy

Supervisors

Prof. Patrick Segers, PhD, Ghent University
Prof. Joris Degroote, PhD, Ghent University
Prof. Nele Famaey, PhD, Ghent University

Preface

One of the questions asked during an interview for my PhD position here was along the lines of "PhD is a lonely journey. Do you think you're up for the challenge". While instinctively saying yes, the question lingered in my mind when I arrived in Belgium. Being back to an academic setting after almost 3 years was definitely not easy and with the pandemic less than 6 months into my PhD, chaos can be the only way I could describe my first year. However, as I write this, I can confidently say I was surrounded by amazing people who made sure those lonely moments were few and far between.

First and foremost I would wholeheartedly thank my main supervisor **Prof. Patrick Segers** for his unending support and guidance. Patrick, you took a punt on an unknown guy after two skype meetings. Not quite sure what you saw in me at that time, but I am extremely grateful. I wasn't the easiest one to deal with, often frustrating you to no end, but you persisted till the end and hopefully, it was worth it. You always call spade a spade and I really appreciate your directness with me. I can safely say, you helped me grow not only as a researcher, but personally in many regards as well. Me being here, writing this would not have been possible without your guidance. Secondly, **Prof. Joris Degroote** whom I've often referred to other colleagues as the smartest person I've met and for good reason. I can safely say that I ended up learning something new every single meeting we've had and it was an honor to speak every year during your CFD course. It was something I deeply enjoyed. A lot of this work would not have been possible without you. Thank you!! And finally **Prof. Nele Famaey** with whom my interactions were limited, but always enjoyable. Something I always wanted to mention was how much I enjoyed your teaching. I started to appreciate tissue mechanics much more after your lectures online. **Saskia** for all the administrative help and my fellow linux nerd with a distinctive laugh, **Jurgen** for all the IT support. Thank you to **Prof.**

Charlotte Debbaut for all the teaching opportunities which I thoroughly enjoyed, **Dr.ir.Annette Caenen** for always being available for a brainstorming session, **Dr.ir.Henri Dolfen** for helping me traverse through the world of CoCoNuT and finally **Dr.ir.Lauranne Maes** for all the help while initially starting off the pulmonary autograft study. It was great having you as a jury member. Thank you to all my collaborators from Torino and Düsseldorf. My sincere thanks to the Chair and all members of the jury, especially with the suggestions to improve the final manuscript.

I arrived in Belgium all gung ho without even having a place to stay. Min bror **Ajie**, you gave me a place to stay when I arrived. Thanks for exploring the food scene in Brussels and Ghent together, cafes to work, checking in from time to time and getting me into watches ;). Can't believe it's been more than 10 years since we know each other. Here's to many more "happy vibes". A good indication of my friendship with **Federico** appeared as early as our second conversation — we talked so long I missed my tram stop. We shared a little over a year together during the lockdown which was more than enough to build an amazing friendship. That first year was bearable because of the citadel-park "runs", Easter celebrations with Natali and Daime, surprise birthday parties and occasional boxing lessons… You kept motivating me throughout these years and I'm glad we've kept in touch. **Carlos**, thanks for the champions league nights, the walks during the lockdown and numerous coffee house visits. Was my pleasure to cat sit and I'm always up for the job ;).I'm loooking forward to vlogs of those numerous bike trips of yours.

Sarah, I am glad I could change the initial impression you had of me to form probably the unlikeliest friendship. We are polar opposites, but somehow we got along great. Sharing Fluent woes and the occasional philosophical discussion during our long walks, conference travels, going to France instead of West Flanders ;). It was amazing sharing time in and out of the office with you. Thank you for always checking in and motivating me through the last hurdle. I'm happy to see you thriving in Stockholm. **Lise** for being not only an amazing colleague, but also an amazing collaborator. My first visit to West Flanders was extremely memorable (despite the detour) and I enjoyed dancing my heart out at your wedding. Oh and congratulations btw ;). I can safely say that when my fellow man of culture, **Simeon** arrived at the office a year later, he and I quickly became the antithesis of the otherwise calm and focused atmosphere. I enjoyed nerding out over kickboxing, MMA. Your vast knowledge of history and 'interesting' questions made lunchtime memorable.

I remember the first day **Tim** started his PhD and we went for lunch together. He's a pretty shy one I thought. Oh how wrong I was. Was a blast teaching Biomechanics and CBFM with you. Learnt quite a bit from those impressive presentation skills of yours. Although I don't recall much of the ever-laughing, enthusiastic version of **Saar** from when you were a student in MI2CM, I certainly saw much more of that during our CBFM teaching sessions. Was great fun teaching that together with you. Joli poli **Jolan**, I really enjoyed our lunchtime conversations and the occasional mini coffee breaks. I'll never forget that two hour long conversation we had when you made me eventually decipher about you and Saar. Was fantastic to discuss football and other topics Mr.Stoic himself **Matthias**. Thanks for the dinner invites with you and Eline. It was nice to see a fellow Would I lie to you fan in **Gert**. **Emma**, it was fun exploring the light festival with you. I hope the tea gods have been generous at your new job. **Elias**, will I expect you take over the mantle for the Top Three's in the future? **Nicole**, I see you and acknowledge you. The infectious energy you bring is always a delight. Learnt a wee bit more about Belgium after those years of conversations with you all. Thank you ;)

It was always amazing trying to find words in common between Farsi and Hindi with the ever growing Iranian presence at the 3 PM tea break, especially **Samaneh**, my occasional officemate **Mohammad** and **Hooman**. Thanks **Ghazal** for showing me the ropes while teaching MI2CM together. **Sina**, I want to see Sinalize become a household name and convinced it will ;). **Ashkan**, was always fun running into you all across Ghent. After 6 years of constantly inviting me, I'll try to make it to one of your classes (maybe).

Transition of **Melissa** from being a quiet intern to the life of the office, was a joy to behold. Was the beginning of an amazing friendship and I was overjoyed when you joined the lab for your PhD later. Not only were you fantastic company with impulsive boat trips, improv shows, concert trips and numerous dinners, but also those long grueling hours and weekends at the office. Truly thank you for always being a constant presence and checking in. Those walks with you and **Sarah** were always a highlight. My alleged spouse **Wouter**, honestly there's never a dull moment when we hang out. Those long discourses where I am more often than not the devil's advocate is something I'll always cherish. My cafe working spree started with you, so thank you for the fantastic company and being the occasional ear to my silly woes. You are forgiven for chopping off

those locks. And together with **Yousof**, we form a chaotic trifecta. I call **Yousof**, the current voice of the lab. You are not scared to voice your opinion even though many (sometimes even I) might disagree. It's refreshing!! I've always enjoyed quietly listening (occasionally butting in) to your conversations while you sat atop the counter at Block B. I've mentioned this, but I'm glad you finally started finding you feet in Ghent. You got this ;). Thank you for all the support. **Bhawna**, thanks for always checking in and the motivation towards the end of my PhD. Your persistence on speaking Hindi with me despite my terrible command over the language always amuses me. I hope to have a fluent conversation in Hindi with you someday. You're extremely upfront with me, which I always value and appreciate. Hope to see you in Ghent more often.

It's amazing to see people you've supervised grow into fellow colleagues. **Bea** - from long Teams calls during the CBFM course to longer conversations about your PhD and crazy birthday parties, its been a pleasure. Ms. 'It's way past my bedtime' **Ariana** - thanks for the dinner invites and lovely conversations; Mr. Politician **Jellis** - Make sure you lower those taxes eh and **Jessie**, easily one of the most organized people I know. Thanks for always checking in and those lovely walks. Make sure you take a few breaks every now and then. I'll do my best to check back ;). **Boris**, I'll always cherish that dance/headbang at the Gentse Feesten. I wish you all nothing but the best.

Can't forget about the lovely neighbors from Block B now can we? **Prof. Stefaan Vandenberghe**, you opened up greatly over time during our lunches and I always enjoyed stories of your travels. You were almost a cultural ambassador of Belgium for me, constantly telling me different places to visit. Thank you for everything. **Jens** and I started our PhD together. I'm not quite sure when we started to pick on each other, but I wouldn't change it for anything. Thanks for dragging me 'almost' home after the BBQ along with Ms. 'Sure to become a professor' **Florence**. **Mariele**, thanks for the fun conversations when I dropped by your office to meet you and sushi chef extraordinaire **Paulo**. I'm glad we have kept in touch after your PhD and it's always fun catching up when you visit Ghent. Here's to many more visits. **Maya**, we got much much closer during the latter stages of my PhD. Thanks for being a constant presence during the last few months. It was great that you could open up and I hope I was atleast half the help you were. Can't wait for the 19^{th} ;). **Rabia** and **Thibault**, I enjoyed the Gentse Fessten with you thanks for the conversations when I visit the CORE.

Giuseppe, **Parham**, **Paula**, **Tom** and the numerous newbies who might read this, thanks for bearing my presence at the RTP during the last few days. **Marta**, it was amazing traveling to ESB with you. I really enjoyed our conversations. **Robbe**, I'm glad you'll be able to continue part of this work. I am sure you'll do great. I wish you all the very best.

After four years living alone in a matchbox in the city center, I moved to Corbiestraat with **Giulia** and **Krists**. I wasn't around much at first, always tucked away in the lab, but slowly Krists and I ended up having fun conversations—from history and Baltic culture to rather personal ones over the occasional Pita/Fries run. I really enjoy your dark sense of humor. And over time I grew closer to **Giulia**, the glue of the house. Thanks for the walks, the conversations, and for letting me crash during the mouse invasion of July 2024. And a year later, after **Rūta** moved in with Krists, I found an amazing friend and a study buddy. Thanks for pushing me to begin running and proof reading my thesis with Giulia. I thoroughly enjoyed De Krook study sessions, Panos lunch breaks, walks with Krists and sitting outside the library with lovely conversations during rather uncertain times of my PhD. I'm sure you'll do great during the next few months. You'll make a great PhD student if you want to pursue one. **Eric**, thanks for the amazing banter, awesome conversations and I'm looking forward to your defense soon. Last but not least, another amazing friendship along with Rūta was **Kim**. You started off very quiet, but I'm super proud of your progress over the last year. Thanks for the amazing walks, conversations during rather dark times of my PhD, being an ever so constant presence helping with every little thing possible. I'm glad to have run into you and thank you for helping with the awesome cover design.

My thanks for all my friends in India - undergrad folks, L&T gang, **Pravir**, **Shetty**, **Kavya**, **Anil**, **Sadhvi**, **Zeishah** and everyone else who have kept in contact over the years. Another intern extraordinaire,**Unai**. It's a pity you're arriving a day later. **Jill**, for being a very dear friend the past year and surprising me with random kayak trips and dance lessons. **Evelien** for actually introducing me to De Krook. It was honor to be a protagonist in your short story. Special thanks to **Pranav** for actually instilling that scientific curiosity almost 16 years ago. Another special thanks goes to **Dr. Anirudh Rao** for being constantly supportive, instilling strict scientific rigor and helping during the final stages of my PhD.

Absolutely nothing would have been possible without the unwavering support of my family. My father **Balasubramanya**, the

ever so perfectionist, my mother **Tharamani**, the ever so pragmatic. That lovely contrast kept me in check. My father worrying about every little detail and making sure I do my tasks on time. My mother, knowing how lazy I can get pushing me the right way. Constantly curious about my research, checking in every single day, being there during the lowest of lows and always celebrating my victories. I hope this work makes both of you proud. I am so happy you would be able to see me defend in person. This would not have been possible without you both. My lovely grandmother **Smt.Padmavatamma** who's well into her 90's, but hasn't lost that enthusiasm. If you ever see a bright smile on my face, I'm probably on a video call with my parents and saying hi to her. My late grandfather **Sri Chandrashekariah**, who from what I remember, wanted me to be a doctor. Well, not the kind he wanted, but hopefully close :). How can I forget my ever annoying sister deary **Bhavana**. Yelling at me when I deserved it, but when things get tough, always being there. I know this will annoy you when you read it, so I'll emphasize, Thank you!! My even more annoying niece, **Siri**. You'll roll your eyes when you read this, but it really brightens my day when we banter over facetime calls, and my brother-in-law **Adarsha**, with whom I can talk about anything ranging from politics to cricket. But you're forthright and straightforward when necessary with me. Thank you!! I dedicate this work to all of you.

In Memorium - A few people couldn't see me finish this journey. They cannot read this, so I'll dedicate this work partly to them. My grandmother **Smt.Kaveramma** who's smile brought me immense joy when we spoke. Ajji, it's a pity I couldn't see you the last few years. We video called whenever Amma went to visit. You learnt how to be tech savvy well into your late 80's. I'm holding onto those voice messages dearly. You are deeply missed. **Sheel**, you had asked me about moving to Belgium potentially and that was probably one of our last conversations. You were taken too soon. You are missed. **Rakshith**, we hadn't been in contact for a while, but the news of your passing last year shook me. Those lovely school memories will always linger. You are missed. **Madhu**, the news of your death reached me the morning of my private defense. I took me a while to process this as a lot happened that day. But once the news sunk in, it was hard to digest. You are missed.

Go on, you've read this far. Turn a few pages and tell me what you think ;)

Table of contents

Preface i

Table of contents vii

Abbreviations and symbols xi

Summary xv

Samenvatting xxi

Introduction 1

I Background 9

1 Fundamentals of Aortic Structure, Hemodynamics and Pathologies 11
1.1 Aorta . . . 11
1.1.1 Tissue . . . 13
1.1.2 Lumen . . . 14
1.2 Pathologies of interest . . . 16
1.2.1 Pulmonary autograft to treat aortic valve disease (Ross procedure) . . . 16
1.2.2 Aortic dissection . . . 20

2 Numerical Approaches to Model Hemodynamics and Tissue Mechanics in the Aorta 27
2.1 Hemodynamic model . . . 27
2.1.1 Governing equations of fluid flow . . . 28
2.1.2 Closing the governing equation - Boundary and initial conditions . . . 30
2.2 Tissue model . . . 33
2.2.1 Governing equations for tissue mechanics . . . 33

2.2.2 Constitutive modeling 33
2.2.3 Initial and boundary conditions 36
2.3 Discretization and grid generation 38
2.4 Coupling hemodynamics and tissue models 39
2.4.1 Monolithic and Partitioned approaches 40
2.4.2 Algorithms to solve partioned FSI 41
2.4.2.1 Arbitrary Lagrangian Eulerian method 43
2.4.2.2 Chimera or Overset Grid Technique . 45
2.5 Hemodynamic parameters of interest 45
2.6 Structural parameters of interest 50

II Applications 53

3 Pulmonary Autografts 55
3.1 State-of-the-art 55
3.2 Methodology 59
3.2.1 Experiments, imaging data, geometry 59
3.2.2 Grid generation 59
3.2.3 Tissue and blood properties 61
3.2.4 Boundary conditions 61
3.2.5 Solver settings 62
3.2.6 WSS metrics 63
3.2.7 WSS metrics : FSI v CFD comparison 68
3.2.8 Intravascular flow metrics 69
3.3 Results 69
3.3.1 Model performance 69
3.3.2 Pulmonary autograft intravascular flow patterns 71
3.3.3 Wall shear stress and related metrics 75
3.4 Discussion 88
3.4.1 Autograft dilatation and canonical WSS metrics 88
3.4.2 Non-canonical metrics and hemodynamics . . . 89
3.4.3 Potential applications 92
3.4.4 Assumptions and limitations 94

4 Aortic Dissections 99
4.1 State-of-the-art 99
4.2 Methodology 105
4.2.1 Structural model 105
4.2.2 Fluid model 109
4.2.3 Coupled model 110
4.2.4 Hemodynamic parameters 111

4.3 Results 112
4.3.1 Pressure 112
4.3.2 Membrane displacement and area 115
4.3.3 Flow 118
4.4 Discussion 120

4A Wave Propagation in the Aortic Dissection Model 137
4A.1 Background and methodology 137
4A.2 Geometry, material properties and boundary conditions 139
4A.3 Results 141

III Discussion 147

5 Conclusions and outlook 149
5.1 Key results - Did we achieve our objective? 149
5.1.1 Pulmonary autograft 150
5.1.2 Aortic dissection 151
5.2 Assumptions and limitations 152
5.3 Future work and translation to clinic 155
5.3.1 Translation to the clinic - What is in our favor and what isn't 158

Appendices 161

A An Overset Meshing Approach for Aortic Dissection 163

B Linear Elastic Constitutive Model for Type-B Aortic Dissection 167

Bibliography 171

Abbreviations and symbols

The following list summarizes the most commonly used abbreviations and symbols in this dissertation.

Abbreviations

0D	Zero-dimensional
1D	One-dimensional
2D	Two-dimensional
3D	Three-dimensional
4D	Four-dimensional
ABM	Agent-based model
BCW	Backward compression wave
BEW	Backward expansion wave
CFD	Computational fluid dynamics
CoCoNuT	Coupling code for numerical tools
CSM	Computational structural mechanics
CT	Computed tomography
FCW	Forward compression wave
FEW	Forward expansion wave
FEM	Finite Element Method
FL	False lumen
FLEF	False lumen ejection fraction
FSI	Fluid–solid interaction
FSG	Fluid–solid growth and remodeling
FVM	Finite Volume Method
G&R	Growth and remodeling
GOH	Gasser–Ogden–Holzapfel
IMT	Intimal medial thickness
IQN-ILS	Interface quasi-Newton with approximation of the Jacobian's inverse from a least-squares model
LOA	Limits of agreement
LPM	Lumped parameter model

MRI	Magnetic resonance imaging
OSI	Oscillatory shear index
PA	Pulmonary autograft
PC-MRI	Phase-contrast magnetic resonance imaging
PEARS	Personalized external aortic root support
PET	Primary entry tear
PINN	Physics-informed neural networks
PWV	Pulse wave velocity
RBC	Red blood cells
RET	Re-entry tear
RRT	Relative residence time
SA	Luminal surface area
SI	Similarity index
SMC	Smooth muscle cells
TAWSS	Time-averaged wall shear stress
TBAD	Type-B aortic dissection
TEVAR	Thoracic endovascular aortic repair
TL	True lumen
TMP	Transmural pressure
TSVI	Topological shear variation index
WBC	White blood cells
WSA	Wave separation analysis
WSS	Wall shear stress

Symbols

α	Mean collagen fiber angle
α_w	Womersley number
$\bar{\bar{\epsilon}}$	Strain rate tensor
κ	Collagen fiber dispersion
$\bar{\bar{\sigma}}$	Cauchy stress tensor
τ	Wall shear stress
$\hat{\tau}$	Normalized wall shear stress
Ψ	(Total) strain energy density function
$d\pi_+$	Forward wave power
$d\pi_-$	Backward wave power
ρ_f	Density of fluid
ρ_s	Density of solid
A	Area
$\bar{\bar{C}}$	Right Cauchy–Green tensor
C	Arterial compliance

C_{10}	Elastin shear modulus
c	Wave speed
$\bar{\bar{F}}$	Deformation gradient tensor
f_b	Body force
$\mathcal{F}$	Flow solver
$\bar{\bar{G}}$	Deposition stretch tensor
$\bar{\bar{I}}$	Identity tensor
I_i	i^{th} invariant of right Cauchy–Green tensor
k	Coupling iteration
k_1	Collagen fiber stiffness
k_2	Collagen fiber stiffening
$\vec{n}$	Unit normal vector
P	Pressure
P_+	Forward pressure
P_-	Backward pressure
$\overline{P}$	Mean arterial pressure
Q	Flow rate
Q_+	Forward flow rate
Q_-	Backward flow rate
$\overline{Q}$	Mean flow rate
R_e	Reynolds number
$R_{e_{crit}}$	Critical Reynolds number
$\mathcal{R}$	Residual operator
$\mathcal{R}'$	Jacobian of the residual operator
$\widehat{\mathcal{R}'^{-1}}$	Inverse Jacobian approximation of the residual operator
$\mathcal{S}$	Structural solver
S_t	Strouhal number
T	Trianglular element
t	Time
$\mathcal{T}$	Time period of the cardiac cycle
$\overline{\mathrm{TMP}}$	Cycle-averaged transmural pressure
$\vec{u_s}$	Displacement of structure
V	Volume
V_F	Anterograde flow volume
V_R	Retrograde flow volume
$\vec{v_f}$	Velocity of fluid
$\vec{w}$	Grid velocity
x	x-coordinate
$\boldsymbol{x}$	Interface displacement input
$\tilde{\mathbf{x}}$	Interface displacement output
y	y-coordinate
$\boldsymbol{y}$	Interface traction input

$\tilde{\mathbf{y}}$	Interface traction output
z	z-coordinate
Z_c	Characteristic impedance
Z_{in}	Input impedance

Summary

Introduction

The aorta, which is the main artery in the body, has a remarkable ability to adapt with changing mechanical loads through growth and remodeling of the aortic wall. This occurs in an adaptive manner that helps to maintain homeostasis, whereby, for example, the stresses felt by cells are kept within certain limits. However, there are circumstances in which adaptation does not occur or is not possible. In surgical procedures, for example, such as pulmonary autograft (where part of the pulmonary artery is moved to replace part of the aorta), the adaptation can be maladaptive, leading to a weakening and severe expansion of the vessel wall. Another example is a condition such as aortic dissection, in which the weakened vessel wall is subject to prolonged growth. Biomechanical signals are essential stimuli for growth and remodeling, or lead to inappropriate tissue formation. Biomechanical signals can (sometimes) be measured using in vivo imaging and/or invasive pressure sensors and are often considered the gold standard. At the same time, some signals are not measurable (e.g., the stresses in the aortic wall) due to limited spatial resolution (e.g., when measuring parameters such as wall shear stress) or due to the invasive nature of pressure measurement.

With advances in computational methods and computing power, biomechanical in silico models offer a powerful alternative for determining biomechanical signals that stimulate vascular growth and remodeling (G&R). Commonly used in silico approaches study, either the structural behavior of the vessel wall using computational structural mechanics (CSM) or the dynamics of blood flow using computational fluid dynamics (CFD). While there is nothing wrong with these approaches for specific problems, these processes are interconnected: blood flow deforms the surrounding vessel wall, and the resulting deformation in turn affects blood flow. This problem is therefore best approached using fluid-solid interaction simulations (FSI), especially

for problems involving large deformations and tissue displacements. However, a disadvantage is that FSI techniques are computationally more expensive and (much) more complex to solve.

This thesis uses strongly coupled FSI models to investigate two cases in which arterial growth and remodeling are of vital importance: (i) a pulmonary autograft in the aortic position that is yet to be remodeled, immediately after surgery, and (ii) acute type-B aortic dissections (TBAD). The first two chapters provide an introduction to pulmonary autografts, aortic dissections and present the relevant numerical background for their investigation.

Study 1: Pulmonary Autografts (Ross procedure)

A commonly used treatment for aortic valve disease is replacement of the aortic valve with a mechanical prosthesis. This treatment is highly effective but has long-term side effects, such as lifelong anticoagulation therapy. An attractive alternative for younger patients is to use their own pulmonary valve as an autograft and place it in the aortic position, whereby the (less heavily stressed) pulmonary valve is then replaced by a replacement valve. When the pulmonary graft is placed in the aortic position, it is exposed to significantly higher pressures than in the pulmonary position, causing it to undergo a process of growth and remodeling, with a risk of maladaptation, resulting in dilatation or failure. In this thesis, computational models are built for a section of the pulmonary artery in three sheep models that have been placed in the aortic position (and in which the damaged valves are not taken into account). These computer models can then be used to supplement the in vivo experiments.

Wall shear stress (WSS) is one of the most important biomechanical stimuli of G&R. To investigate WSS in pulmonary autografts, a strongly coupled FSI framework is developed, in which an attempt was made to model physiological reality as accurately as possible. For example, arteries in vivo are not stress-free, but are subject to residual stresses, which can easily be observed when an artery is removed from the body: it will spring back. In this study, a pre-stress algorithm is applied to reconstruct the physiological stress state. The non-linear anisotropic nature of arterial tissue is also taken into account by implementing the Gasser-Ogden-Holzapfel material model, the parameters of which were previously determined using bi-axial tests. The structural model of the blood vessel is then linked (in a strong, implicit way) to a fluid model, using the in-house developed

open-source coupling tool CoCoNuT. The boundary conditions for the fluid model are animal-specific and were determined in vivo based on MRI measurements in sheep models. Although examining WSS data at individual points in time throughout the cardiac cycle is intuitive, FSI simulations generate large datasets. A valuable consideration that is widely used within the community is the evaluation of averages over the cardiac cycle. Traditional (canonical) metrics such as time-averaged WSS (TAWSS) and oscillatory shear index (OSI) are widely used, and variations in these metrics are associated with the onset and progression of vascular disease. In this study, these canonical measurements are compared with a recently proposed metric based on WSS divergences, which intuitively explains whether the WSS vector exerts a compressive or expansive effect on the endothelial tissue. The extent of this compressive/expansive effect can be estimated using the topological shear variation index (TSVI).

The results of the calculations were compared with flow velocities measured in vivo for validation purposes, and both models showed good agreement. This was not only for the FSI models, but also for models in which the vessel wall could not expand (i.e. CFD models). The displacement of the vessel wall is considerable, with significant volumetric changes of up to 20% during the cardiac cycle for all sheep models studied. Despite these large volumetric changes, canonical metrics such as TAWSS and OSI, obtained via CFD and FSI, remain strongly correlated. The instantaneous WSS divergence patterns also retain the qualitative similarities between the two techniques. Where the large deformations of the autograft do have a greater influence is in the calculation of TSVI, where a moderate correlation between the FSI and CFD simulations is observed. Finally, the extent to which the results of one technique spatially overlap with the results of the other technique (co-localization analysis) is quantified and calculated as a similarity index. This revealed moderate co-localization for zones of the vessel wall exposed to low TAWSS thresholds and for zones exposed to high OSI and TSVI thresholds.

In general, CFD-based simulations can be considered adequate for determining canonical metrics, for example in models that aim to predict arterial G&R based on these biomechanical stimuli. However, if non-canonical metrics such as TSVI are used as mechanical-biological stimuli in G&R simulations, an FSI approach is certainly justified.

Study 2: Aortic Dissection

Type B aortic dissections (TBAD) are characterized by a tear in the inner wall (the intimo-medial layer) of the aorta, allowing blood to flow from the true lumen (TL) to a parallel false lumen (FL). This false lumen is created by a split and delamination of the aortic wall over a certain length and is separated from the true lumen by a thin flexible membrane, also known as an intimal flap. In TBAD, the dissection is located in the descending part of the aorta.

Multiple branches typically extend from the true and/or false lumen to internal organs and structures, perfusing between 7 to 21% of the cardiac output. Despite their physiological importance, these branches are often overlooked, both in vivo and in the development of computational models of TBAD. An important reason for this is the difficulty to accurately visualize these smaller side branches through medical imaging. While previous studies have examined the long-term evolution of TBADs in relation to the presence of side branches, what has been less studied is the role that the presence of side branches plays on blood pressure in the false lumen, even though it is assumed that pressure in the false lumen has a strong positive correlation with the (undesirable) growth of the false lumen.

In this thesis, an FSI model of an aortic dissection was developed to study the hemodynamics (blood pressure and flow) in TBAD, and in particular the effect of the presence of side branches. To construct the model, a thick-walled cylinder is initially considered that mimics a healthy descending aorta. In the subsequent step, in order to create the dissection over a predetermined length, the segment to be dissected and the associated entry and re-entry tears are modeled as predefined slits, which are initially kept closed with connecting elements. When setting up the model, the pre-stresses present in the tissue are taken into account again, as well as the influence of surrounding tissues (such as the spine), which are modeled using linear springs. A diastolic blood pressure of 80 mm Hg is then applied throughout the cylinder, resulting in the tears and dissected membrane being formed. In this way, a model of acute dissection is created from this healthy configuration, with a quasi stress-free intimal flap. This is a situation that elegantly mimics the pathophysiological reality. To model the anisotropic nature of arterial tissue, the Gasser-Ogden-Holzapfel constitutive law is used, whereby the material parameters are determined on the basis of physiological values of the pulse wave velocity.

To arrive at an FSI model, the resulting tissue model is again strongly coupled with the fluid model. This thesis examines four

scenarios: (i) there is no side branch in the model; (ii) the model contains a single side branch in the false lumen; (iii) the model contains a single side branch in the false lumen, but the model does not contain a re-entry tear; and (iv) the model contains a single side branch that originates in the true lumen. The boundary conditions for the outflow are prescribed in such a way that the total vascular resistance remains the same in all scenarios, ensuring a consistent basis for comparison of the results.

All models result in large displacements of the intimal flap, especially near the tears, entirely in line with values reported in the clinical literature. The largest displacements are found for the model without a side branch (scenario 1). The simulations show that the intimal flap makes a "see-saw" like motion along the axis of the aorta, with large fluctuations during the systolic phase, which stabilize during the diastolic phase.

Where it was intuitively expected that perfusion via the side branch reduces pressure in the false lumen compared to a scenario without a side branch, the simulations consistently show higher systolic pressures for all cases with a side branch. These higher pressures are found in both the true and false lumina. Location of the side branch also plays an important role, with the presence of a side branch in the false lumen resulting in higher pressure than when the side branch originates in the true lumen. To further investigate this pressure increase, the input impedance just proximal to the dissections is also calculated. The model without a side branch showed a lower impedance modulus across the various harmonic components. From a lumped parameter perspective, this lower impedance indicates higher functional compliance in the dissected aorta without a side branch and/or lower inertia effects, probably as a result of altered TL-FL interactions. This changing impedance can also be explained by changes in the pattern of wave transmission and reflection in the model due to the presence of the moving intimal flap. Comparison of the results with those obtained in a dissection-free geometry shows that the presence of a dissection results in increased systolic pressure, possibly because the 'see-saw' motion of the intimal flap causes a backward pressure wave, thereby amplifying the systolic pressure.

These results suggest that side branches in TBAD not only influence the flow patterns in the true and false lumina, but also the overall hemodynamics, leading to increased pressures in the true and

false lumen (while maintaining fluid flow and total vascular resistance). These results should be viewed with caution and, given the idealized nature of the geometry studied, cannot simply be extrapolated to clinical reality.

Conclusion

The two studies presented in this thesis are independent applications of FSI and are biologically not related whatsoever. What both studies have in common is that they investigate the extent to which FSI simulations are necessary to determine biomechanical stimuli known to play a role in arterial growth and remodeling. The first study (pulmonary autograft) shows that the necessity of FSI is generally rather limited, although the displacements of the vessel wall do make a difference for the calculation of non-canonical metrics of wall shear stress. For the second study (type B aortic dissection), no direct comparison with CFD models is performed. This is not very meaningful given the large displacements and high mobility of the intimal flap and the resulting hemodynamics. In the final chapter, the obtained results are approached from a broader perspective, discussing the challenges of translating them into a clinical context.

Samenvatting

Inleiding

De aorta, de belangrijkste slagader in het lichaam, heeft een opmerkelijk vermogen om zich aan te passen aan veranderende mechanische belastingen door groei en hermodellering van de aortawand. Dat gebeurt op een adaptieve manier die helpt om de zogenaamde homeostase te handhaven, waarbij bvb. de spanningen gevoeld door cellen binnen bepaalde grenzen worden behouden. Er zijn echter omstandigheden mogelijk waarbij adaptatie niet gebeurt of niet mogelijk is. Bij chirurgische ingrepen zoals bijvoorbeeld bij een pulmonale autotransplantatie (waar een deel van de longslagader wordt verplaatst ter vervanging van een deel van de aorta), kan de aanpassing maladaptief zijn, wat kan leiden tot een verzwakte vaatwand en sterke uitzetting van de vaatwand. Een ander voorbeeld is een aandoening zoals een aortadissectie, waarbij de verzwakte vaatwand onderhevig is aan langdurige groei. Biomechanische signalen zijn essentiële stimuli van groei en hermodellering, of leiden tot onaangepast weefsel. Biomechanische signalen kunnen (soms) worden gemeten via in-vivo beeldvorming en/of invasieve druksensoren en worden vaak als gouden standaard beschouwd. Tegelijk zijn sommige signalen niet meetbaar (bvb. de spanningen in de aortawand) of worden metingen belemmerd door een beperkte ruimtelijke resolutie (bvb. bij het meten van parameters zoals wandschuifspanning) of het invasieve karakter van het meten van druk.

Met de vooruitgang op het gebied van computationele methoden en rekenkracht bieden biomechanische in-silico-modellen een krachtig alternatief voor het bepalen van biomechanische signalen die vasculaire groei en hermodellering (G&R) stimuleren. Veelgebruikte in-silico-benaderingen bestuderen ofwel het structurele gedrag van de vaatwand door middel van computationele structuurmechanica (CSM) ofwel de dynamica van de bloedstroming door middel van computationele vloeistofdynamica (CFD). Hoewel er niets mis is met

deze benaderingen voor specifieke problemen, zijn deze processen onderling verbonden: de bloedstroom vervormt de omliggende vaatwand en de daaruit voortvloeiende vervorming beïnvloedt dan weer de bloedstroom. Dit probleem kan dan ook best worden benaderd door middel van vloeistof-structuurinteractiesimulaties (FSI), vooral bij problemen waar grote vervormingen en weefselverplaatsingen optreden. Een nadeel echter, is dat FSI-technieken computationeel duurder zijn en (veel) complexer om op te lossen.

Deze thesis maakt gebruik van sterk gekoppelde FSI-modellen om twee casussen te onderzoeken waarbij arteriële groei en hermodellering letterlijk van levensbelang zijn: (i) een nog te hermodelleren pulmonale autotransplantaat in aortapositie, onmiddellijk na de operatie, en (ii) acute type-B aortadissecties (TBAD). In de eerste twee hoofdstukken wordt een introductie gegeven tot pulmonale autotransplantaten en aortadissecties en wordt de relevante numerieke achtergrond voor het onderzoek ervan gegeven.

Studie 1: Pulmonale autotransplantaten (Ross-procedure)

Een veelgebruikte behandeling voor aortaklepaandoeningen is vervanging van de aortaklep door een mechanische prothese. Deze behandeling is zeer effectief, maar heeft langdurige bijwerkingen, zoals levenslange antistollingstherapie. Een aantrekkelijk alternatief voor jongere patiënten is om de eigen pulmonale klep te gebruiken als autotransplantaat en deze in de aortapositie te plaatsen, waarbij de (minder sterk belaste) pulmonaalklep dan zelf wordt vervangen door een vervangende klep. Wanneer het pulmonale transplantaat in aortapositie wordt geplaatst, wordt deze blootgesteld aan aanzienlijke hogere drukken dan in de pulmonale positie, waardoor deze een proces van groei en hermodellering moet doormaken, met risico op maladaptatie met dilatatie of falen. In deze thesis bouwen we computationele modellen van een deel van de longslagader in 3 schapenmodellen die in de aortapositie zijn geplaatst (en waarbij we geen rekening houden met aangetaste kleppen). Deze computermodellen kunnen dan worden gebruikt als aanvulling op de in-vivo-experimenten.

De wandschuifspanning (WSS) is één van de belangrijkste biomechanische stimuli van G&R. Om WSS in pulmonale autotransplantaten te onderzoeken, is een sterk gekoppeld FSI-raamwerk ontwikkeld, waarbij we hebben getracht de fysiologische realiteit zo accuraat mogelijk te modelleren. Zo zijn slagaders in vivo niet spanningsvrij, maar staan ze onder een initiële spanning, die makkelijk

kan worden waargenomen wanneer een slagader uit het lichaam wordt gehaald: deze zal namelijk terugveren. In dit onderzoek werd een voorspanningsalgoritme toegepast om de fysiologische spanningsstatus te reconstrueren. Er wordt ook rekening gehouden met de niet-lineaire anisotrope aard van arterieel weefsel door implemenatie van het Gasser-Ogden-Holzapfel-materiaalmodel, waarvan de parameters eerder zijn bepaald met behulp van bi-axiale tests. Het structurele model van het bloedvat wordt dan gekoppeld (op een sterke, impliciete manier) aan een vloeistofmodel, waarbij gebruik werd gemaakt van het intern ontwikkelende koppelingstool CoCoNuT. De randvoorwaarden voor het vloeistofmodel zijn dier-specifiek en werden in vivo bepaald op basis van MRI-metingen in de schapenmodellen. Hoewel het onderzoeken van WSS-gegevens op individuele tijdstippen doorheen de hartcyclus intuïtief is, genereren FSI-simulaties grote datasets. Een waardevolle afweging die binnen de gemeenschap veel wordt gebruikt, is het evalueren van gemiddelden over de hartcyclus. Traditionele (canonieke) meetwaarden zoals tijdgemiddelde WSS en oscillatory shear index (OSI) worden op grote schaal toegepast en variaties in deze meetwaarden worden in verband gebracht met het ontstaan en de progressie van vaatziekten. In dit onderzoek worden deze canonieke meetwaarden vergeleken met een recent vooropgesteld metriek op basis van WSS-divergenties, die intuïtief verklaart of de WSS-vector een compressieve of expansieve werking uitoefent op het endotheel weefsel. De omvang van deze compressieve/expansieve werking kan worden begroot via de topologische schuifvariatie-index (TSVI).

De resultaten van de berekeningen werden, ter validatie, vergeleken met in vivo gemeten stroomsnelheden, en beide vertoonden een goede overeenstemming. Dit was het geval voor de FSI-modellen, maar ook voor modellen waarbij de vaatwand niet kon uitzetten (CFD-modellen). De verplaatsing van de vaatwand is nochtans aanzienlijk, met significante volumetrische veranderingen tot 20% gedurende de hartcyclus, en dit voor alle onderzochte schapenmodellen. Ondanks deze grote volumetrische veranderingen blijven canonieke meetwaarden zoals TAWSS en OSI, verkregen via CFD en FSI, sterk gecorreleerd. Ook de momentane WSS-divergentiepatronen behouden kwalitatief de overeenkomsten tussen de twee technieken. Waar de grote vervormingen van het autotransplantaat wel een grotere invloed hebben, is bij de berekening van TSVI, waar we een matige correlatie vonden tussen de FSI en CFD-oplossing. Tot slot hebben we ook gekwantificeerd in welke mate resultaten van de ene techniek ruimtelijk overlappen

met de resultaten van de andere techniek (co-lokalisatieanalyse) via het berekenen van een similariteitsindex. Deze bracht een matige co-lokalisatie aan het licht voor zones van de vaatwand blootgesteld aan lage TAWSS-drempelwaarden, en van de zones blootgesteld aan hoge OSI- en TSVI-drempelwaarden.

Over het algemeen kunnen op CFD gebaseerde simulaties als adequaat worden beschouwd voor de bepaling van canonieke metrieken, bijvoorbeeld in modellen die arteriële G&R willen voorspellen op basis van deze biomechanische stimuli. Als echter niet-canonieke metrieken zoals de TSVI worden gebruikt als mechanisch-biologische stimuli in G&R-simulaties, is een FSI-benadering zeker gerechtvaardigd.

Studie 2: Aortadissectie

Type-B aortadissecties (TBAD) worden gekenmerkt door een scheur in de binnenwand (de intimo-mediale laag) van de aorta waardoor bloed vanuit het echte lumen (True Lumen; TL), naar een parallel vals lumen (False lumen; FL), kan stromen. Dat vals lumen ontstaat door een splitsing en delaminatie van de aortawand over een bepaalde lengte, en wordt van het echte lumen gescheiden door een dun flexibel membraan, ook wel intimale flap genoemd. Bij TBAD bevindt de dissectie zich in het neergaande deel van de aorta (de aorta descendens).

Vanuit het echte en/of valse lumen vertrekken doorgaans meerdere vertakkingen naar inwendige organen en structuren, die 7 tot 21% van het hartminuutvolume afvoeren. Ondanks hun fysiologische belang worden deze vertakkingen vaak verwaarloosd, zowel in vivo als bij het opzetten van computermodellen van TBAD. Een belangrijke reden hiervoor is de moeilijkheid om deze vaak kleinere zijtakken nauwkeurig te visualiseren met medische beeldvorming. Er zijn nochtans eerder studies uitgevoerd die de lange-termijn evolutie van TBAD's hebben bestudeerd in relatie tot de aanwezigheid van zijtakken. Wat veel minder is bestudeerd, is welke rol de aanwezigheid van zijtakken heeft op de bloeddruk in het valse lumen, en dit terwijl er wordt aangenomen dat de bloeddruk in het valse lumen een sterke positieve correlatie heeft met de (ongewenste) groei van het valse lumen.

In deze thesis werd een FSI-model van een aortadissectie ontwikkeld om de hemodynamica (bloeddruk en bloedstroming) in TBAD te bestuderen, en in het bijzonder het effect van de

aanwezigheid van zijtakken. Om het model op te bouwen vertrekken we in eerste instantie van een dikwandige cilinder die een gezonde aorta (descendens) nabootst. Om in een verdere stap de dissectie te kunnen creëren over een vooraf bepaalde lengte, worden het te dissecteren segment en de bijbehorende opwaartse (entry-tear) en afwaartse scheur (re-entry tear) gemodelleerd als vooraf gedefinieerde spleten, die in eerste instantie dicht worden gehouden met connecterende elementen. Bij het opzetten van het model wordt opnieuw rekening gehouden met de aanwezige voorspanningen in het weefsel, alsook met de invloed van omliggende weefsels (zoals bijvoorbeeld de wervelkolom), die met behulp van lineaire veren wordt gemodelleerd. We leggen vervolgens een diastolische bloeddruk aan van 80 mm Hg in de hele cilinder, waarna we de connecties, die de speten dichthouden, verwijderen. Op die manier ontstaat vanuit deze gezonde configuratie een model van een acute dissectie, met een quasi spanningsvrije intimale flap. Dit is een situatie die de pathofysiologische realiteit op een elegante manier nabootst. Om de anisotrope aard van arterieel weefsel te modelleren gebruiken we opnieuw de constitutieve wet van Gasser-Ogden-Holzapfel, waarbij de materiaalparameters worden bepaald op basis van fysiologische waarden van de polsgolfsnelheid.

Om tot een FSI-model te komen wordt het resulterende weefselmodel opnieuw gekoppeld aan een vloeistofmodel. In deze thesis worden vier scenario's bestudeerd: (i) er is geen zijtak aanwezig in het model; (ii) het model bevat een enkele zijtak in het valse lumen; (iii) het model bevat een enkele zijtak in het valse lumen, maar het model bevat geen re-entry scheur en (iv) het model bevat een enkele zijtak die in het echte lumen ontstaat. De randvoorwaarden voor de uitstroom in de verschillende scenario‘s worden op een dermate manier voorgeschreven zodat de totale vasculaire weerstand in alle scenario's dezelfde blijft, waardoor een consistente basis voor vergelijking van de resultaten wordt gewaarborgd.

Alle modellen resulteren in grote verplaatsingen van de intimale flap in de buurt van de scheuren, geheel in lijn met waarden die in de klinische literatuur worden gerapporteerd. De grootste verplaatsingen worden gevonden voor het model zonder zijtak (scenario 1). De simulaties tonen aan dat de intimale flap een grote schommelende beweging maakt langs de as van de aorta, met grote schommelingen tijdens de systolische fase, die stabiliseren tijdens de diastolische fase.

Daar waar we intuïtief hadden verwacht dat perfusie via de zijtak de druk in het valse lumen zou verlagen in vergelijking met een

scenario zonder zijtak, laten de simulaties consequent hogere systolische drukken zien in alle gevallen met een zijtak. We vinden deze hogere drukken zowel in het echte als valse lumen terug. De locatie van de zijtak speelt ook een belangrijke rol, waarbij de aanwezigheid van een zijtak in het valse lumen een hogere druk oplevert dan wanneer de zijtak ontspringt in het echte lumen. Om deze drukverhoging verder te onderzoeken, wordt ook de ingangsimpedantie net proximaal van de dissecties berekend. Het model zonder zijtak vertoonde een lagere impedantiemodulus over de verschillende harmonische componenten. Vanuit een 'lumped parameter' perspectief wijst deze lagere impedantie op een hogere functionele compliantie in de gedissecteerde aorta zonder zijtak en/of lagere inertie-effecten, waarschijnlijk als gevolg van veranderde TL-FL-interacties. Deze veranderende impedantie kan ook worden verklaard door wijzigingen in het patroon van golftransmissie en reflectie in het model door de aanwezigheid van de bewegende intimale flap. Vergelijking van de resultaten met deze bekomen in een dissectievrije geometrie toont aan dat de aanwezigheid van een dissectie resulteert in een verhoogde systolische druk, mogelijks doordat de 'schommelbeweging' van de intimale flap een teruglopende drukgolf veroorzaakt, waardoor de systolische druk wordt versterkt.

Onze resultaten suggereren dat zijtakken in TBAD niet enkel de stromingspatronen in het echte en valse lumen beïnvloeden, maar ook de algehele hemodynamica en leiden tot verhoogde drukken in het echte en valse lumen (bij behoud van vloeistofdebiet en totale vasculaire weerstand). Deze resultaten dienen wel met het nodige voorbehoud te worden bekeken en kunnen, gezien het geïdealiseerde karakter van de bestudeerde geometrie, niet zomaar worden geëxtrapoleerd naar de klinische realiteit.

Conclusie

De twee studies die in dit proefschrift worden gepresenteerd, zijn op zichzelf staande toepassingen van FSI en zijn biologisch gezien niet met elkaar verbonden. Wat beide studies gemeen hebben is dat ze beide onderzoeken in welke mate FSI-simulaties een noodzaak zijn om biomechanische stimuli te bepalen waarvan bekend is dat ze een rol spelen in arteriële groei en hermodellering. De eerste studie (pulmonale autograft) toont aan dat de noodzaak van FSI algemeen eerder beperkt is, hoewel de verplaatsingen van de vaatwand wel degelijk een verschil uitmaken voor de berekening van niet-canonieke metrieken van de wandschuifspanning. Voor de tweede studie (type

B aorta-dissectie) is er geen directe vergelijking met CFD-modellen uitgevoerd. Deze is weinig zinvol gezien de zeer grote optredende verplaatsingen en grote mobiliteit van de intimale flap en de daaruit voortvloeiende hemodynamiek. In het laatste hoofdstuk worden de behaalde resultaten vanuit een breder perspectief benaderd, waarbij de uitdagingen om de behaalde resultaten te vertalen naar de klinische context worden besproken.

Introduction

'Movement is medicine' they say. While this adage is more representative to movement or physical activity in humans for overall health, it is hard not to extrapolate this metaphorically for the inner workings of the cardiovascular system. Flow of blood is fundamentally a mechanical process [1], with the rhythmic expansion and contraction of the heart and resulting pressure gradients aiding the movement of blood through the arteries. As the nutrient rich blood flows, it dynamically interacts with the arterial wall stimulating biochemical signals and triggering mechanical responses. Upon exposure to altered mechanical stimuli, arterial tissues have the remarkable ability to adapt to the changing mechanical environment by growing (change in mass, volume) and remodeling (change in microstructure) [2]. This adaptive capability of growth and remodeling (G&R) underlies the fundamental principle of homeostasis - the idea that arteries strive to maintain a preferred mechanical and biological state [1, 2]. When this homeostatic state is disrupted by changes in pressure or flow, the arteries will try to adapt or respond accordingly.

The mechanical stimuli and the forces that trigger growth can be studied with the fundamental laws of mechanics and fall under the purview of biomechanics while the study of the biological response to such forces that trigger growth and remodeling is called mechanobiology [2]. In conjunction, they are used to study long-term effects and parameters that trigger the responses for G&R. While physiological adaptive G&R is desirable and often necessary to maintain healthy cardiovascular function (think of the adaptation that the body undergoes from fetal life to adulthood), altered mechanical states due to surgical intervention or disease can lead to maladaptive growth and remodeling which lead to loss in the desired homeostatic environment [1]. A notable instance of maladaptive behavior post-surgery is the pulmonary autograft in the Ross procedure [3], where the explanted pulmonary valve is placed in a high pressure aortic position experiencing excessive dilation and potential structural failure due to its

original adaptation to a low pressure environment [4]. Similar to a healthy aorta, the diseased dissected aortic wall responds to elevated pressure [5, 6], stress and inflammation [7] by growth and remodeling (G&R) which can lead to progressive dilation and maladaptive behavior.

G&R is a long-term continuous process that unfolds over varying time-scales ranging from days to years and decades [8]. While it essentially takes place over an individual's lifetime, we are particularly interested in G&R phenomena that play over shorter periods, in response to rather dramatic events such as aortic surgery or aortic dissection. While understanding the arterial structure and function during and after the G&R phase is essential, identifying the biomechanical cues that trigger G&R, which have smaller time scales (in the order of seconds to hours) is as crucial. Certain aortic pathologies present with large displacements of aortic structures, likely leading to altered pressure and flow states. At the same time, it has been known that pressure build–up and wall stress [5, 6], and shear stress exerted on the aortic wall by blood [9] are among a few factors that contribute to long–term growth or remodeling in aortic pathologies. These factors, however, are not trivial to assess. In vivo (Latin for 'within the living') is often the gold–standard and one of the more common ways to determine mechanical factors such as pressure, flow and often involves animal models and imaging techniques. However, biomechanical stimuli such as wall stress are non–measurable, derived quantities from the pressure and flow field. Techniques such as 4D flow MRI do not have the resolution in time or space for accurate measurement of the flow field near the aortic wall, and may underestimate wall shear stress [10] questioning the reliability of the calculated parameter. Further, accurate measurement of pressure in complex geometries is challenging without invasive techniques [6]. Ethical concerns aside, these factors combined with the fact that imaging data might not always be available indicates in vivo techniques cannot always be used to calculate hemodynamic variables in such pathologies.

A viable alternative to these experimental techniques is the in silico (Latin for 'in silicon') technique where computer simulations are used to calculate parameters like pressure or wall (shear) stress. In silico methods have gained popularity with improvement in computer technology and while the terminology was spawned in the late 1980's, the techniques used in cardiovascular biomechanics gained popularity during the cold–war when computers were used to solve

complex mathematical problems [2]. In Biomechanics, the often used techniques are finite element (FE) and finite volume methods (FVM) with both being used to convert complex non–linear differential equations into systems of algebraic equations. Researchers often employ these techniques standalone to either gain insight into the behavior of blood, computing pressure and wall shear stress and other fluid properties using computational fluid dynamics (CFD) ; or investigate stresses acting on the arterial wall and resultant tissue mechanics using computational structural mechanics (CSM). While standalone CFD and CSM studies might give preliminary insight into hemodynamic parameters of interest, the dynamic interaction between blood and tissue in the arterial wall is more accurately captured using Fluid-Solid interaction (FSI). One other advantage an in silico model possesses is the ability to parameterize the geometry, material properties, boundary conditions using idealized or patient–inspired models allowing for a more systematic investigation of factors that may influence disease progression.

Goal of the thesis

Keeping the above introduction in mind, the broader goal of the thesis is to employ fluid–solid interaction simulations to gain insight into biomechanical cues playing a role in the mechanobiologically driven growth and remodelling process in specific aortic pathologies. We take two pathologies into consideration which are not related to each other, but both present large displacements of arterial structures and susceptible to long-term maladaptive G&R.
The broader goal of the thesis is answered by identifying two specific objectives which are each defined based on a pathology of interest.

Objective 1: Develop a strongly coupled fluid-solid interaction model to gain insight into hemodynamics of a yet to remodel pulmonary autograft

The developed FSI framework supports ongoing in vivo research in a large animal model at KU Leuven in understanding the mechanobiology of pulmonary autograft remodeling in the context of the Ross procedure (see further). The framework is showcased using accurate material properties and state-of-the-art boundary conditions in three ovine models. With the developed framework, we aim to comprehensively compare wall shear stress metrics (which are difficult to calculate in vivo due to poor imaging resolution) that

have been identified to influence long term G&R.

Objective 2: Develop a strongly coupled fluid-solid interaction model to assess pressure and flow dynamics in the false lumen of an acute type–B aortic dissection, with a particular focus on the effect of the presence of a sidebranch.

Aortic dissections are complications where pressure information, particularly inside the false lumen, is challenging to obtain non-invasively [6]. With advancement in computational resources, in silico techniques have been used more commonly to obtain pressure estimation in aortic dissection, but most studies tend to neglect side branches emanating from the false lumen due to constraints in imaging modalities [11], resort to CFD and discard the motion of the dissected membrane, or develop models with stiff and rather immobile membranes, which cannot represent an acute aortic dissection.

We aim to compute pressure and other flow metrics which have been known to influence dissection growth. These hemodynamic parameters are computed with and without the presence of side-branches emanating from the true and false lumen.

Outline

The dissertation is divided into three parts:
(I) **Background**, where as the name suggests, a brief medical/biological and mathematical background is provided along with state-of-the-art on modeling the aortic pathologies of interest. This is done so in two chapters, with chapter 1 providing background into the anatomy and (patho)physiology, which includes a brief description of the aorta, blood flowing through the aorta and surrounding tissue constituents. A brief introduction on pulmonary autografts and aortic dissections are provided with information how long term growth and remodeling occurs in these scenarios. Chapter 2 delves into a more detailed mathematical background on the equations used to solve flow and structural mechanics, the appropriate boundary conditions and relevant hemodynamic metrics such as wall shear stress. A brief description on coupling flow and tissue mechanics is also provided. At the end of each section, information on where these described concepts are relevant in the subsequent Chapters are mentioned.

(II) **Applications** The background information is applied to the problems of interest with Chapter 3 focusing on a yet to remodel pulmonary autograft mostly covering Objective 1. Chapter 4 focuses on an idealized acute Type-B aortic dissection. Chapter 4A is an extension of the dissection study with a focus on wave seperation analysis with comparisons performed for a dissection free geometry. These chapters along with the Appendices together cover Objective 2.

(III) **Conclusion and outlook** Chapter 5 discusses if the research objectives were met and what were the final observations and conclusions. Limitations and potential future work to aid a possible translation to a clinical setting are also discussed.

Throughout the PhD journey, additional research was performed which were not published as journal contributions, but are still significant to report. This work is reported in two appendices.
Appendix A discusses an alternative approach to model grid motion for idealized dissections namely the Chimera technique as an alternative to the technique used in Chapter 4. This Chapter is added to the appendix as even though it encompasses the objective of gaining insight into dissections, an FSI approach is not utilized. Further, this chapter aims to provide the reader on lessons learnt in order to obtain Objective 2. Chapter B is similar and though FSI is used on idealized dissections, a much more simplified constitutive model is used to describe tissue behavior. Lessons from Appendix A, B helped us to understand the challenges while modeling dissections and further aided in finalizing the approach used in Chapters 4 and 4A.
This research was undertaken within the BioMMedA (Biophysical Models for Medical Applications) research unit at the Institute of Biomedical Engineering and Technology (IbiTech-BioMMeda) at Ghent university, in a collaboration with the Fluid mechanics team at the Department of Electromechanical, Systems and Metal Engineering, Ghent University and the Soft Tissue Biomechanics group at the Division of Biomechanics, KU Leuven.

First Author Peer-Reviewed Articles

Balasubramanya, A., Maes, L., Rega, F., Mazzi, V., Morbiducci, U., Famaey, N., Degroote, J., Segers, P. (2024). Hemodynamics and wall shear metrics in a pulmonary autograft: comparing a fluid-structure interaction and computational fluid dynamics approach. *Computers in Biology and Medicine*, 176. https://doi.org/10.1016/j.compbiomed.2024.108604

Balasubramanya, A., Gheysen, L., Wagenhauser, M. ,Famaey, N., Degroote, J., Segers, P. (2025). Hemodynamics in aortic dissections: A fluid-solid interaction study in an idealized dissection model with a false lumen side branch. *Journal of Biomechanics*. https://doi.org/10.1016/j.jbiomech.2025.112771

Conference Contributions

Balasubramanya, A., Degroote, J., Gheysen, L., Famaey, N., & Segers, P. (2020). CFD study of type-B aortic dissections with flap motion: proof of concept of overset meshing. *Presented at the 19th National Day on Biomedical Engineering, Brussels as an online presentation.*

Balasubramanya, A., Vastmans, J., Maes, L., Peirlinck, M., Claus, P., Rega, F., Segers, P. (2022). Fluid-structure interaction simulation of simplified Ross procedure for assessment of in-vivo wall-shear stress dynamics. *Presented at the 17th International Symposium on Biomechanics in Vascular Biology and Cardiovascular Disease, Rotterdam, the Netherlands as a poster.*

Balasubramanya, A., Vastmans, J., Maes, L., Peirlinck, M., Claus, P., Rega, F., Segers, P. (2022). Fluid-structure interaction of simplified Ross procedure as a stepping stone to a fluid-solid-growth framework of arterial tissues. *Presented at the 9th World Congress of Biomechanics, Taipei, Taiwan as a poster.*

Balasubramanya, A., Gheysen, L., Famaey, N., Degroote, J., & Segers, P. (2023). Fluid-structure interaction simulations in an idealized model of the dissected aorta: relation between false lumen pressure and outflow via side branches. *Presented at the 2023 Summer Biomechanics, Bioengineering and Biotransport Conference (SB3C 2023), Vail, CO, USA as a poster.*

Balasubramanya, A., Gheysen, L., Wagenhäuser, Markus, Famaey, N., Degroote, J., Segers, P. (2025). Hemodynamics in acute Type-B aortic dissection: FSI study in an idealized dissection with a false lumen side branch. *Presented at 2025 European Society of Biomechanics (ESB 2025) Conference, Zurich, Switzerland as a podium presentation.*

Balasubramanya, A., Gheysen, L., Wagenhäuser, Markus, Famaey, N., Degroote, J., **Segers, P**. (2025). Impact of false lumen side branch on aortic pressure in Type-B Aortic Dissections: Insights from a fluid-solid interaction study in an idealized model *Presented at* 10^{th} *International Biofluid Mechanics and Mechanobiology Symposium (IBMS 10), Irvine, CA, USA as a podium presentation.*

I

Background

Chapters

1 Fundamentals of Aortic Structure, Hemodynamics and Pathologies **11**

2 Numerical Approaches to Model Hemodynamics and Tissue Mechanics in the Aorta **27**

Chapter 1

Fundamentals of Aortic Structure, Hemodynamics and Pathologies

This chapter provides some background knowledge on the structure and function of the aorta along with the composition of tissues and the blood. With this background information, the pathologies of interest are introduced, and a brief explanation of the causes and how these pathologies grow, and remodel are also mentioned.

1.1 Aorta

Aorta is the largest artery in the human body with a diameter of about 2–3 cm [12] originating from the left ventricle and channeling downwards towards the abdomen transporting oxygen-rich blood throughout the body over the systemic circulation. The aorta is a critical component of the cardiovascular system with especially the thoracic aorta being a highly elastic/compliant structure that allows it to withstand and accommodate the pressure of blood pumped by the heart [12, 13]. Anatomically, the aorta consists of three main segments namely the ascending aorta, aortic arch and the descending aorta which consists of the thoracic and abdominal aorta as shown in Figure 1.1.

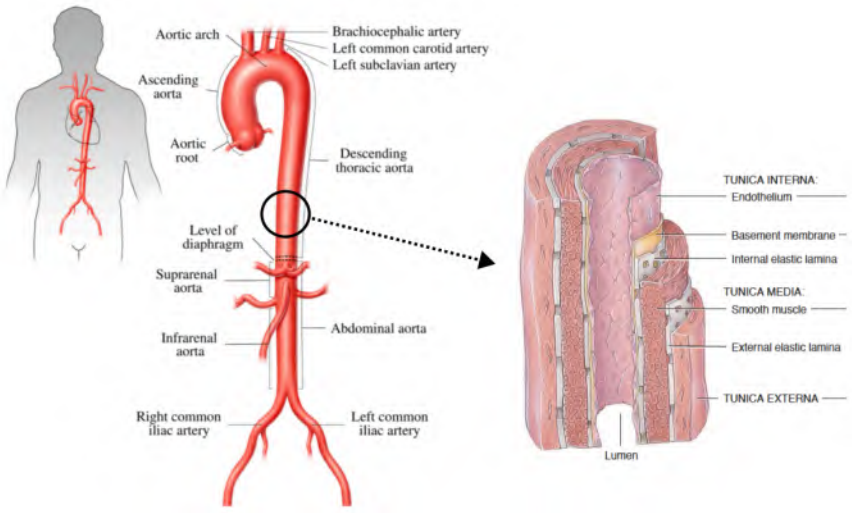

Figure 1.1: The figure to the left shows different sections of the aorta, and figure to the right shows a cross-section of the aorta highlighting the constituents of the tissue. Image adapted from [14] and [12]

.

The ascending aorta is about 5cm long and emerges from the left ventricle. At the origin or root of the ascending aorta, three distinct dilations exist called aortic sinuses, two of which give rise to the right and left coronary artery which are responsible for providing blood to the entire heart muscle. The ascending aorta ends at the level of the sternal angle after which the aorta arches [12]. The aortic arch is a continuation of the ascending aorta and is about 4 cm long containing the subclavian and carotid arteries which supply blood to the arms and to the head, respectively. After the fourth and fifth thoracic vertebrae (T4, T5), the aortic arch ends after which the descending aorta begins [12].

The descending thoracic aorta extends until the level of the diaphragm which is the twelfth vertebrae (T12) and is approximately 20cm long. Along its course, the descending aorta branches into numerous small arteries and visceral branches like the intercostal and lumbar arteries [12].

The abdominal aorta is a continuation of the thoracic aorta extending from the diaphragm to the L4 vertebra, where it splits into the right and left common iliac arteries called the iliac bifurcation. Similar to the thoracic aorta, many visceral branches arise from the surface of the abdominal aorta like the celiac trunk, the renal arteries and the superior and inferior mesenteric arteries [12].

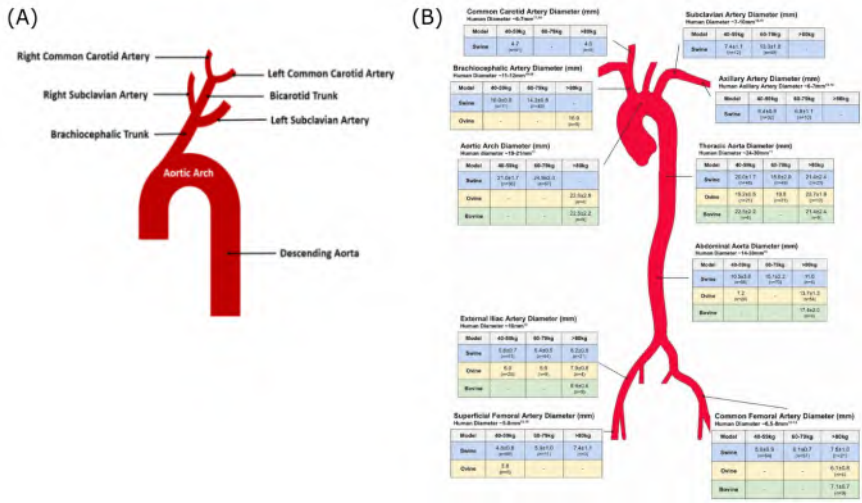

Figure 1.2: Panel (A) illustrates the aortic configuration of an idealized ovine aorta, adapted from *. Panel (B) illustrates the differences between a human aorta and large animal models including the ovine aorta, adapted from Georges et al. [15].

Comparative anatomical data illustrate that the sheep aorta differs from the human aorta in both geometry and branching architecture especially in the ascending aortic section as illustrated in Figure 1.2 (A), with a single large brachiocephalic trunk giving rise to both carotid arteries and the right subclavian artery, in contrast to the three-branch human pattern. Measurements across large animal models consistently show that ovine arterial diameters are smaller throughout the thoracic and abdominal aorta, as well as in major supra-aortic branches, when compared with human reference values [15] as observed in Figure 1.2 (B). These reductions in diameter are accompanied by thinner walls consistent with observations reported in large-animal vascular assessment studies [15].

1.1.1 Tissue

Figure 1.1 not only highlights the aortic structure axially, but also how the aortic tissue surrounding blood is layered. As seen in the figure, the arterial tissue mainly consists of three layers or tunica. The layer of tissue in direct vicinity of blood as it flows across the lumen is called the tunica interna or intima. The intima consists of a single layer of endothelial cells which are flat and elongated along the direction of blood flow. Long thought to be passive, the endothelial cells

*Source: https://www.imm-recherche.com/week20210119/

are activated as blood imparts a tangential force and the resultant stress is commonly referred to as wall shear stress (WSS) [16], which triggers intracellular signaling upon WSS which provides a stimulus for production of multiple biomolecules that affect smooth muscle cells (SMC) [14]. The intima is the thinnest of the layers and barely contributes to the aortic thickness [12]. The intima is separated from the next layer, the tunica media [12] by a thin sheet of elastic tissue called the internal elastic lamina. The medial layer contributes up to 80% of the total aortic thickness [17] and is mainly compromised of large amount of elastic fibers surrounded by SMC's and collagen fibers. The extent of SMC contraction is helpful in mechanoregulation [12]. The elastic fibers mainly consist of elastin which gives the wall the ability to expand and contract while collagen bundles help maintain tensile strength in the aortic wall [14]. Importantly, the composition of the aortic media changes along its length with the proximal thoracic aorta is rich in elastin and elastic lamellae, whereas toward the distal regions, the elastin-to-collagen ratios decrease [18], resulting in a progressively stiffer, more muscular wall with fewer lamellar units. The combined thickness of the intima and the media called Intimal-Medial thickness (IMT) is a very important biomarker for ageing and atherosclerosis [19] The final layer, separated from the media through an external elastic membrane is called tunica externa or adventitia, which makes up the remaining aortic wall thickness. The adventitia contains tiny blood vessels called vasa vasorum which ensures blood and oxygen supply to the tissue [12]. The adventitia is collagen dominant and these wavy collagen fibers tend to straighten at higher pressure preventing over-distension at supra-physiological loads [20].

1.1.2 Lumen

Blood is a liquid connective tissue comprising a fluid extracellular matrix called plasma and various formed elements such as cells and their fragments [12]. Approximately 55% of blood is plasma and 45% are formed elements. Out of the 45%, close to 99% of the formed elements contain red blood cells (RBC), with remaining 1% containing white blood cells (WBC) and platelets [21]. The proportion of RBCs relative to the total blood volume is called Hematocrit [12, 21]. In section 1.1.1, we briefly mentioned about WSS which shall henceforth be referred to as τ. If blood flows at a velocity (v), rate of change in velocity when one fluid layer passes the other is called strain-rate ($\dot{\gamma}$). A fluid is called Newtonian when it obeys the Newton's law of viscosity i.e. there is a linear relationship between shear-stress and

shear-rate and given by the formula:

$$\tau = \mu \frac{dv}{dy}$$

Here, μ denotes the dynamic viscosity, defined as the force required to overcome intermolecular friction [22]; v is the fluid velocity in the direction of flow; and y is the coordinate measured normal to the direction of flow, representing the distance from the wall. At room temperature, the dynamic viscosity of blood with a normal haematocrit of approximately 45% is about 0.0035 Pa·s [21]. Blood is a non-Newtonian fluid which is shear-thinning in nature i.e. at low shear rates, the red blood cells clump together or aggregate called Rouleaux, which increases the viscosity. At higher shear-rates ($>$ 200 s^{-1}), the viscosity tends to be constant, highlighting a Newtonian like behavior as shown in Figure 1.3. In order to model the non-Newtonian effects of blood, various viscosity models of blood have been postulated, where the viscosity is a function of hematocrit and shear-rate. A comprehensive overview of models can be found in a review by Yilmaz et al. [23].

To account for such shear-dependent behavior, various constitutive models have been proposed in which blood viscosity is expressed as a function of both shear rate and haematocrit [23]. The non-Newtonian nature of blood becomes more pronounced in smaller vessels, where the Fåhræus–Lindqvist effect [21, 24] occurs. This effect arises from the migration of red blood cells toward the vessel center, forming a plasma rich cell-free layer near the wall. The presence of this low-viscosity layer reduces the apparent viscosity of blood as vessel diameter decreases. In contrast, in large arteries where shear rates are high and the cell-free layer is relatively thin, blood behaves nearly as a Newtonian fluid, leading most *in silico* studies to adopt this simplification [25].

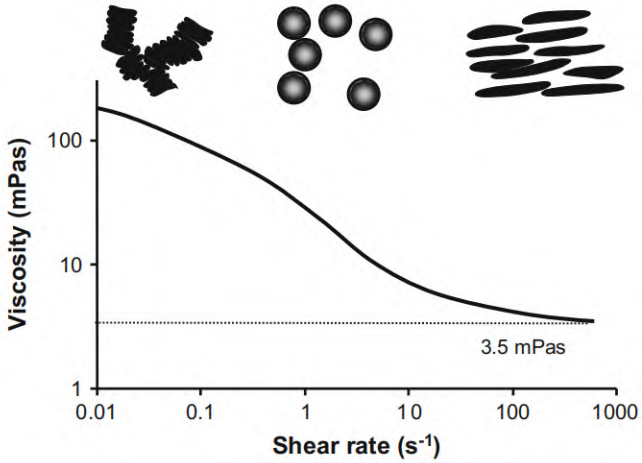

Figure 1.3: Viscosity (μ) as a function of shear-rate ($\dot{\gamma}$). Viscosity tends to be decrease at higher shear rates highlighting the shear thinning nature of blood, with it eventually becoming constant. Image adapted from Hoskins et al. [21]

Another less featured, but important assumption is considering blood as a single phase fluid (i.e. uniform distribution of cellular components) in-silico. A more realistic assumption would to model blood as a mixture of plasma, RBC and WBC i.e. a multiphase fluid. Literature suggests that bulk parameters such as velocity and pressure were only marginally changed with the multi-phase assumption [26], but changes in WSS were observed [26–28].
Throughout the course of this thesis, blood is assumed as a single phase fluid under a Newtonian assumption.

1.2 Pathologies of interest

1.2.1 Pulmonary autograft to treat aortic valve disease (Ross procedure)

With improvements in surgical procedures over the past century, different techniques exist for replacing diseased organs or tissues [29]. A graft is a section of live cells,tissue or organs removed surgically and transplanted to another [30]. Grafts are classified by the relationship between a donor and the recipient. An autograft refers to excision of tissue from one's own body from one location to the other [31]. The advantage of an autograft is a similar genetic makeup and lower risk of rejection [30] as the transplanted tissue ideally integrates or remodels to its new environment [32]. The main disadvantage is potential donor-site maladaptation and morbidity [30]. An allograft/homograft

refers to excision from a donor of the same species (human to human for instance) [31]. Since the transfer is from one human to another, the risk of rejection and infection are quite high [30]. Finally, a xenograft refers to excision of tissues/organs from two different species (eg: animal to human) [30]. Xenografts are advantageous in terms of availability and ease of implantation, yet they run the risk of rejection [30] and experimental models show severe calcification in xenograft walls [33].

Aortic valve disease is characterized by failure of the aortic valve to effectively ensure unidirectional ventricular outflow [34]. Common causes of aortic valve disease are calcific degeneration in the cusps often leading to stenosis [35] or abnormalities in the aortic root leading to regurgitation [36]. Treatment options to replace the failed valves range from a mechanical valve to a bioprosthetic one (porcine or bovine) [37]. Mechanical valves, while highly durable, require life-long anticoagulation medication which might be detrimental in young children [37]. Though bioprosthetic valves avoid long-term anticoagulation therapy, they are prone to structural degeneration [37]. An alternative surgical procedure suggested by Sir Donald Ross in 1967 involves replacing a diseased aortic valve with a patient's own pulmonary valve in the aortic root position [3]. In place of the pulmonary valve, the right ventricular outflow tract is reconstructed with a cryopreserved pulmonary valve from a cadaver [38] (see Figure 1.4). This procedure is surgically complex but very suitable for young patients particularly due to the absence of anti-coagulation therapy, improved hemodynamic performance, and the possibility of remodeling making the Ross procedure an attractive procedure for valve replacement [32].

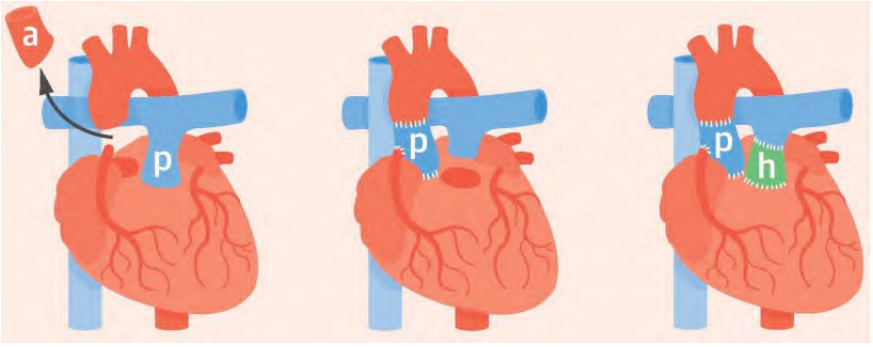

Figure 1.4: Schematic figure showing the Ross procedure where 'a' refers to the diseased aortic valve, 'p' refers to the pulmonary valve and 'h' refers to a homograft that replaces the pulmonary valve and redirects flow at the right ventricular outflow tract. Image adapted from [38]

While having its merits, the pulmonary autograft experiences a significant change in environment after the Ross procedure due to altered hemodynamic conditions. At rest, aortic pressure is typically about 120/80 mmHg, whereas pulmonary artery pressure is about 25/10 mmHg (mean systemic ∼90 mmHg vs mean pulmonary ∼15 mmHg), i.e., roughly a five- to six-fold increase in load . This jump in pressure often causes a small immediate diameter increase [4].

It has been previously alluded to in the Introductory chapter that upon exposure to unnatural loading, tissues have the tendency to grow and remodel in an attempt to maintain homeostatic conditions. The pulmonary autograft is definitely such an example where exposure to systemic pressure leads to changes both in short-term and long-term. This was observed by Rabkin-Akinawa et al. [39] who observed that within a few weeks to several years after implantation, pulmonary autografts developed intimal thickening, resulting in leaflets three times thicker than the native pulmonary valve and a similar thickness to the aortic valve. Explanted pulmonary autografts on average six years after surgery similarly showed intimal thickening, loss and fragmentation of elastic lamellae in the media and pronounced fibrosis of the adventitia [40]. These structural changes suggest that the early adaptive remodeling seen in the autograft wall can, over time, evolve toward a more maladaptive pattern. Building on these observations, Yacoub et al. [41] examined long-term explanted autografts and showed that all layers of the pulmonary autograft namely the leaflets, media, and adventitia undergo varying degrees of remodeling, which were largely adaptive in nature. They described the formation of a thin neointima on leaflets, an increased number of lamellar units within the media comparable to the native aortic root, and an expansion of the vasa vasorum in the outer media and adventitia, indicating adaptation of the autograft under systemic load. In contrast, Mookhoek et al. [42] analyzed explanted pulmonary autografts after long-term exposure to systemic pressure and found that, despite marked wall thickening, the autograft remained substantially more compliant than the native aortic root, indicating that although structural growth and matrix remodeling occur, mechanical adaptation of the pulmonary autograft remains incomplete even after more than a decade in systemic circulation.

Experimental animal models offer insight into the initial adaptive mechanisms of pulmonary autografts [4]. The biomechanical responses of the pulmonary autograft over time have been studied experimentally in porcine models where the authors state that

while the pulmonary autograft revascularizes, the reason for dimensional increase is a combination of acute dilation due to excessive pressure post-surgery in conjunction with long-term growth [40, 43, 44]. To prevent such excessive dilation, Personalized External Aortic Root Support (PEARS) technique is used which involves applying a custom-made external mesh sleeve around the aortic root to prevent dilation. Building on this concept and to reduce complications during surgery, Vanderveken and colleagues introduced a simplified Ross interposition model in which a short segment of pulmonary artery is sewn into the descending aorta so that pulmonary tissue experiences systemic pressures [45]. The authors explored reinforcing the pulmonary autograft to study how mechanical support influences vessel wall behavior. In this setting, unreinforced segments dilate over time, while macroporous mesh reinforcement limits diameter growth but is associated with lower compliance and smooth-muscle atrophy/thinning within the supported wall [45]. Follow-up work in the same ovine model confirmed load-dependent remodeling and reported shifts toward higher circumferential stiffness relative to native pulmonary artery, consistent with matrix reorganization with increased stiffness six-months post-surgery [46, 47]. Further details about pulmonary autografts in animal models can be found in a detailed review by Van Hoof et al. [4].

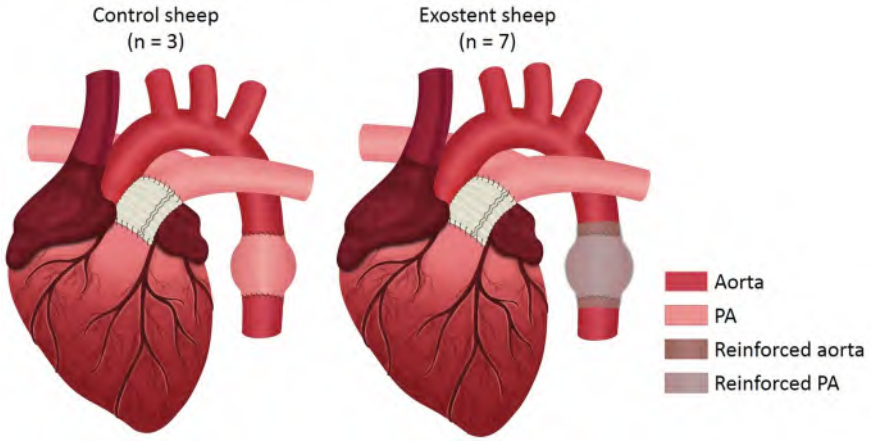

Figure 1.5: Schematic figure showing a simplified Ross procedure employed by Vandervaken et al. [45]

The ovine aorta exhibits classical arterial behavior i.e. it shows a nonlinear, strain-stiffening response with a circumferential stiffness dominance and regional variation along its length. Experimental data

demonstrate that stiffness increases progressively from proximal to distal aorta, correlating with a rise in collagen content and reduction in elastin [48]. Developmental studies link low-strain elasticity to elastin, and high-strain elasticity to collagen-associated structural components [49]. Moreover, biaxial and pressurization tests confirm the ovine thoracic aorta behaves anisotropically under multiaxial loading [50].

Similarly, the ovine pulmonary artery (PA) displays nonlinear and anisotropic mechanical behavior. Studies within the same sheep species show region dependent differences in PA wall mechanics and collagen recruitment during growth [51]. In comparison with pediatric human PA tissue, the ovine PA is thicker, more compliant, and less anisotropic, with a more gradual stress–strain progression under physiological loads [52].
During the course of this thesis, we will work with a simplified version of the pulmonary autograft proposed by the soft tissue research group at KU Leuven [4, 45, 46] where the pulmonary artery is placed in aortic position and mechanics of the valve are not taken into consideration. This illustration is shown in Figure 1.5.

1.2.2 Aortic dissection

Aortic dissections are characterized by delamination of the aortic wall, i.e. the intimal and a part of the medial layer. In the presence of one or more tears, this delamination allows blood to flow along its normal pathway via the true lumen (TL) as well as along an alternative channel called the false lumen (FL) separated by a thin dissected membrane called intimal flap (IF) [53] as shown in Figure 1.6.

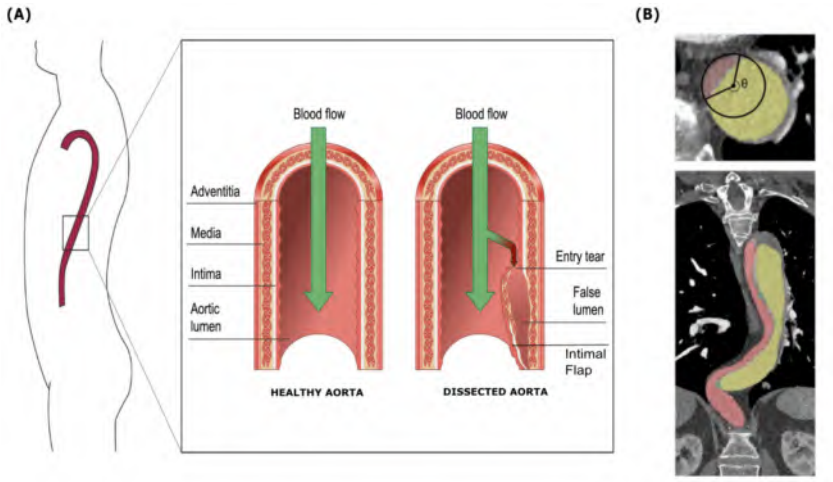

Figure 1.6: Panel (A) shows the occurence of dissection in the descending aortic section. Image adapted from [54]. Panel (B) shows a CT scan with the axial (upper panel) and coronal (lower panel) slice of an aortic dissection. The true lumen is highlighted in light pink and the false lumen in yellow. Image adapted from [55].

Aortic dissections are categorized based on occurrence of the intimal tear initiation and extent upto which the dissection propagates [14]. Two main classifications exist, shown in Figure 1.7. The oldest is the DeBakey type [56] with Type I initiating at the ascending aortic arch and propagating till the abdominal aorta. Initiation and propagation are restricted to the ascending aort for Type II. Finally, Type III initiates distal to the left subclavian artery and is further classified as (a) and (b) based on the extent of propagation of the dissection. The Stanford system [57] simplifies the DeBakey system with Type A dissections involving the ascending aorta and Type B aortic dissections (TBAD) excluding the ascending aorta and occuring distal to the left subclavian artery. Dissections can be fast moving and are temporally categorized within the first 14 days of occurrence as the acute phase where the highest rate of mortality is observed. Within weeks 2 to 6, the dissection is said to be sub-acute and transitioning into sub-acute after eventually within a month or so, becoming chronic [58].
In this work, acute Type B aortic dissections are studied.

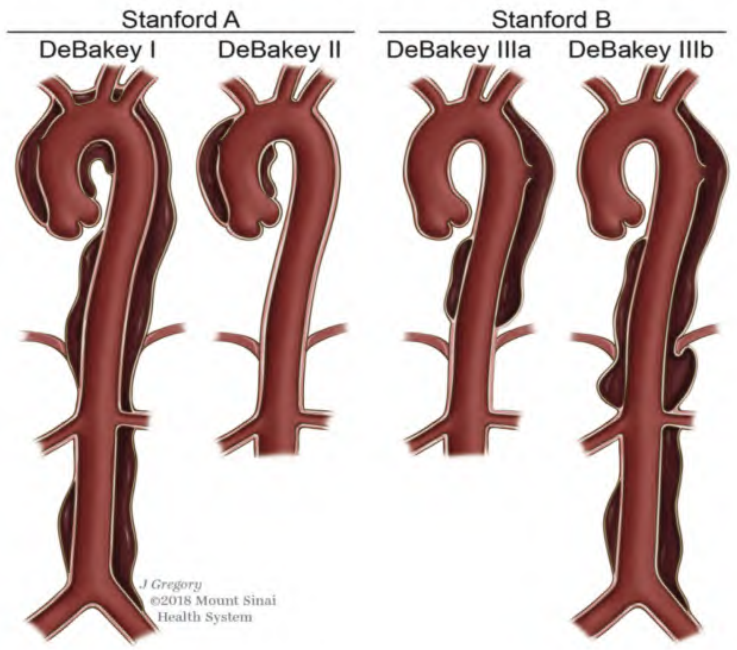

Figure 1.7: Classification of dissection type based on location. Image adapted from Tadros et al. [59].

Propogation and Causes: The occurrence and propagation of aortic dissections can be divided into six stages described in a review by Pepe et al. [54] based on the paper by Tsai et al. [60] which is the prevailing clinical consensus. They are as follows:

- **Stage 1** The patient has tissue abnormalities or increased radial and circumferential wall stress. Though the exact cause remains unclear (see later). Symptoms include sharp chest pain [61].
- **Stage 2** Tear in the intimo-medial layer leads to the formation of a small false lumen.
- **Stage 3** Longitudinal propagation of the false lumen downstream. No thrombosis is formed yet, but a disturbed blood flow pasterns exist.
- **Stage 4** The false lumen reaches its final shape, with one or more re-entry tears being formed. The false lumen is fully pressurized by this stage.

- **Stage 5 (maybe)** A thrombosis accumulates from the distal side of the false lumen occluding the re-entry tears. According to Peterss et al. [58], partially patent FL occurs in 42% within the first 14 days or acute phase in their cohort.
- **Stage 6 (maybe)** Complete thrombus is formed in the false lumen. The blood pressure within the false lumen is very low and non pulsatile. A completely thrombosed FL rarely occurs in the acute phase with Peterss et al. [58] observing $< 10\%$ of their cohort in 3 years.

It must be noted that surgical intervention (see later) might already be performed by Stage 4 if the symptoms are severe, leading to Stages 5 and 6 only optionally occurring. While this explains the propagation of TBADs, the exact mechanism underlying their initiation remains unclear. Factors such as elevated mean and systolic pressures [62] and wall anisotropy, particularly in the radial direction [63], have been associated with the formation of intimal tears. In addition to wall microstructure and mechanical stresses, vascular geometry also appears to play a role. Trachet et al. [64] demonstrated that, in the Angiotensin II-infused ApoE$^{-/-}$ mouse model, medial tears frequently develop near side-branch openings where local wall stress and flow disturbances are highest. The authors observed that ruptures of small side branches, such as the celiac and mesenteric arteries, often occur together with the formation of medial tears and intramural hematomas. These lesions then propagate along the outer curvature of the suprarenal aorta, eventually forming the false lumens characteristic of dissection. The study further showed that the length of these hematomas was closely related to the number of ruptured side branches, suggesting that the geometry along with stress concentration around branch points play an important role in tear initiation and propagation.

While transitioning from acute to the chronic phase, aortic dissections undergo growth and remodeling. In-vivo studies indicate a rapid diameter change in the acute phase, with stabilization in the sub-acute phase and a plateau in diameter change around 88 days post-dissection [58]. Patency of the FL plays an important role in growth with an in-vivo study by Sueyoshi et al. [65] indicating that a group of patients with consistent blood flow to the false lumen had an increased growth rate (3.3 mm/year) compared to those without (1.4 mm/year). Mean aortic dilatation rates were 9.31 mm/year in the acute phase, 1.30 mm/year in the sub-acute phase, and 0.32 mm/year

in the chronic phase [14]. Morphological features such as size, location and number of tears, diameter and extension of the false lumen have been identified as influencing aortic dilation and growth rate [66]. Hemodynamically, pressure build up in the false lumen also referred to as false lumen pressurization [5, 6] is linked to aortic growth. Multiple metrics have been defined in literature with the recently defined false lumen ejection fraction (FLEF) which is the ratio of retrograde flow during diastole to the anterograde flow during systole having a strong positive correlation with aortic growth [5, 6]. It is not just the aortic wall which changes, but also the elastin dominant intimal flap which is thin and highly mobile during the acute phase transforms to a thicker, less mobile one during the chronic phase [58]. In-vivo images also show that the flap loses its curvature and straightens over time [58, 67].

Wall dilation is not the only noticeable feature as the dissection transitions. Microstructral changes in the flap and false lumen wall have been observed. Severe elastin damage and medial fibrosis appeared within two weeks of dissection onset and progressed over time, affecting over 90% of patients within the first year. This medial fibrosis correlates with the intimal flap stiffening over time [58]. Ex-vivo samples also indicated reduced elastin and increased collagen content in the medial wall as the dissection becomes chronic indicative of remodeling [68]. These abundant experimental data indicating G&R have also been backed up in-silico by Gheysen et al. [7] with the dissected membrane microstructure indicating collagen increase and elastin degradation.

A common prognostic classification of acute TBAD's are either complicated or uncomplicated. Although only about 30% of TBAD cases are initially categorized as complicated [69], these cases are particularly challenging to manage due to their severity. Complicated dissections are typically associated with persistent hypertension, evidence of malperfusion, uncontrolled chest or abdominal pain and in severe instances, aortic rupture [14, 69]. Such situations necessitate urgent surgical or endovascular intervention. Open surgical repair may be elected in selected patients if no suitable landing zone is found, but thoracic endovascular aortic repair (TEVAR) has become the preferred treatment approach in current day practice. The principle behind TEVAR is to deploy a stent graft that seals the proximal intimal entry tear, thereby redirecting blood flow into the true lumen and promoting false lumen thrombosis and aortic remodeling. In contrast, uncomplicated dissections are typically managed conservatively through aggressive medical therapy aimed at controlling

blood pressure [14]. Intervention in uncomplicated dissections are generally reserved for patients who develop complications or demonstrate high-risk features predictive of disease progression (see Figure 1.8).

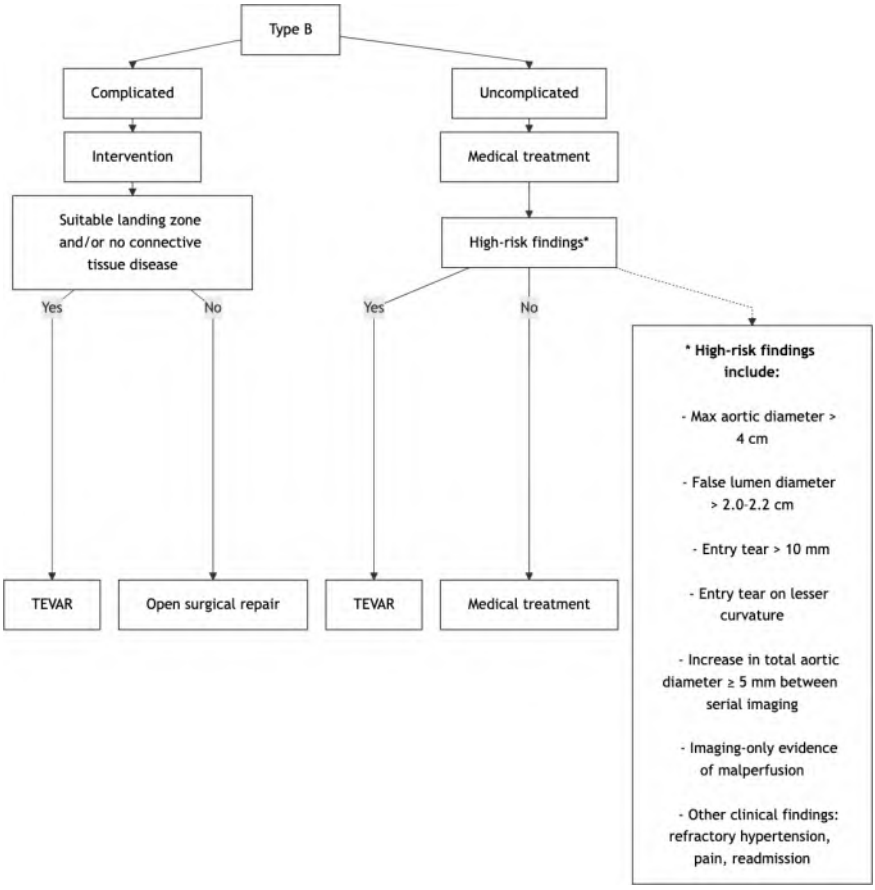

Figure 1.8: Treatment strategies for Type-B aortic dissections according to the American Health Association guidelines [70] summarized. Image adapted from [14].

Chapter 2

Numerical Approaches to Model Hemodynamics and Tissue Mechanics in the Aorta

While the last chapter dealt with introducing the problems of interest, this chapter provides fundamentals on the numerical techniques used to study blood flow, surrounding tissue mechanics, and their coupling to gain specific insights into these problems. This chapter is not meant to be an exhaustive guide, but rather a small primer to cover the concepts to be used in the following chapters. Vectors are referred to as ($\vec{\bullet}$) and tensors are referred to as ($\bar{\bar{\bullet}}$). *All equations are defined in the cartesian co-ordinate system. All formulations are described under the continuum assumption, which is considered valid for both blood and tissue at the scales of interest.*

2.1 Hemodynamic model

The flow of blood can be modeled within a broad framework of computational fluid dynamics (CFD) where numerical techniques are used to solve the equations that govern fluid flow motion. While CFD has a long history in engineering applications [71], the use in hemodynamics has been significantly growing over the past few years [72]. The derivations presented here follow standard continuum mechanics and CFD references such as Versteeg and Malalasekera [71] and

Ferziger and Perić [73].
During the course of this thesis, hemodynamics are studied using the commercial finite volume solver (see later) Ansys Fluent (Ansys Inc, PA, USA). Note that Ansys Fluent is a general purpose CFD solver used to solve a broad variety of problems. Specialized solvers exist for solving hemodynamics such as SimVascular [74] and CRIMSON [75]. The choice of solver is user and problem dependent but the governing equations are still based on conservation principles. However, the choice of discretization such as finite element versus finite volume (see later for both) may vary.

2.1.1 Governing equations of fluid flow

The starting point is the **Reynolds Transport Theorem** (RTT), which bridges a Lagrangian (or system) description and an Eulerian (or control volume) description. A system denotes a fixed collection of fluid particles followed in time, whereas a control volume (CV) is a region in space through which fluid can enter and leave which can either be fixed, moving or deforming [76]. In the present derivation, the *Eulerian framework* (see later) is used for a fixed, non-deforming control volume. Equations for a deforming control volume can be found in Section 2.4.2.1. RTT for a fixed control volume reads as follows:

$$\frac{dB}{dt} = \frac{\partial}{\partial t} \iiint_V \rho_f b \, dV + \iint_A \rho_f b \, (\vec{v_f} \cdot \vec{n}) \, dA \tag{2.1}$$

where $b = B/m$ is the intensive property per unit mass, ρ_f the fluid density, $\vec{v_f}$ the velocity field of the fluid, $\vec{n}$ the outward surface normal, dV the volume element, and dA the surface element.

Applying Gauss divergence theorem to transform the surface flux into a volume integral gives:

$$\iint_A (\vec{v_f} \cdot \vec{n}) \, dA = \iiint_V \nabla \cdot \vec{v_f} \, dV. \tag{2.2}$$

Conservation of mass

The principle of conservation of mass states that mass can neither be created nor destroyed i.e. the rate of change of mass within a control volume must equal the net influx of mass across its boundary. Applying this principle to Equation 2.1 with $B = m$ (so that $b = 1$), we obtain:

$$\frac{\partial}{\partial t} \iiint_V \rho_f \, dV + \iint_A \rho_f \, (\vec{v_f} \cdot \vec{n}) \, dA = 0. \tag{2.3}$$

The right-hand side is equal to zero since mass accumulation inside the control volume is balanced by inflow or outflow through the surface. This equation must hold true for any arbitrary control volume. By applying Gauss divergence theorem, we obtain

$$\frac{\partial \rho_f}{\partial t} + \nabla \cdot (\rho_f \, \vec{v_f}) = 0, \tag{2.4}$$

which is the general form of the *continuity equation*. Blood is an incompressible fluid with constant density ($\rho_f = \text{const}$), so Equation (2.4) reduces to

$$\nabla \cdot \vec{v_f} = 0. \tag{2.5}$$

Conservation of momentum

The conservation of linear momentum is a direct consequence of Newton's second law, which states that the rate of change of momentum of a system is equal to the sum of external forces acting on it. Applying this to Equation 2.1 for a fixed control volume, we identify $B = \int_{\text{sys}} \vec{v_f} \, dm$ as the linear momentum of the system, so that $b = \vec{v_f}$.

$$\frac{\partial}{\partial t} \iiint_V \rho_f \vec{v_f} \, dV + \iint_A \rho_f \vec{v_f} (\vec{v_f} \cdot \vec{n}) \, dA = \iint_A \bar{\bar{\sigma}} \, \vec{n} \, dA + \iiint_V \rho_f \vec{f_b} \, dV, \tag{2.6}$$

where the right-hand side represents the total external force acting on the control volume, with $\iint_A \bar{\bar{\sigma}} \, \vec{n} \, dA$ corresponding to the *surface forces* (given by the Cauchy stress tensor) and $\iiint_V \rho_f \vec{f_b} \, dV$ to the *body forces* (e.g. gravity).

Applying the divergence theorem to the surface traction term in (2.6) and noting that the result must hold for any arbitrary control volume, the local momentum balance yields

$$\rho_f \left(\frac{\partial \vec{v_f}}{\partial t} + \vec{v_f} \cdot \nabla \vec{v_f} \right) = \nabla \cdot \bar{\bar{\sigma}} + \rho_f \vec{f_b}. \tag{2.7}$$

Equation (2.7) is the general form of the *Cauchy momentum equation*. It has been alluded to in Chapter 1 that blood will be assumed as a Newtonian fluid in this dissertation. For a Newtonian fluid, the constitutive law reads as follows:

$$\bar{\bar{\sigma}} = -p \, \bar{\bar{I}} + 2\mu \, \bar{\bar{\varepsilon}}_f, \tag{2.8}$$

where p is the pressure, $\bar{\bar{I}}$ the unit tensor, μ the constant dynamic viscosity and $\bar{\bar{\varepsilon}}_f$ the strain-rate-tensor defined as

$$\bar{\bar{\varepsilon}}_f = \tfrac{1}{2} \left[\nabla \vec{v_f} + (\nabla \vec{v_f})^T \right]. \tag{2.9}$$

Substituting the Newtonian constitutive law (2.8)–(2.9) into the Cauchy momentum equation (2.7) gives the Navier-Stokes equation

$$\frac{\partial}{\partial t}\left(\rho_f \vec{v_f}\right) + \nabla \cdot \left(\rho_f \vec{v_f}\, \vec{v_f}\right) = -\nabla p + \mu \nabla^2 \vec{v_f} + \rho_f \vec{f_b}. \tag{2.10}$$

This represents the conservative form of the momentum equation. The conservation of energy can also be derived in a similar manner, but we will not be using this during the course of this thesis as the temperature can be assumed constant.

2.1.2 Closing the governing equation - Boundary and initial conditions

The governing equations of fluid motion describe the conservation of mass and momentum, but do not yield a unique solution by themselves. As equations 2.4 and 2.10 are partial differential equations which evolve spatially (x, y, z) and temporally (t), boundary conditions must be specified on the boundary of the domain and for unsteady problems, initial conditions at t=0 [71, 73].

In cardiovascular mechanics, initial and boundary conditions have a direct physiological interpretation. Inflow boundary conditions define how blood enters a vessel segment (the aorta in this work) and are prescribed as velocity/flow profiles obtained from measurements (if available), or from literature as idealized waveforms [77, 78]. These flow profiles correspond to Dirichlet conditions (prescribed flow). Depending on the data source, different inflow shapes can be prescribed, ranging from flat or parabolic distributions to Womersley-type pulsatile profiles, as described in Figure 2.1 (A). When patient-specific imaging data are available, 3D flow fields can be reconstructed from 4D flow MRI data and imposed at the inlet for each time point in the cardiac cycle, as shown for two representative cases in Figure 2.1 (B) [78].

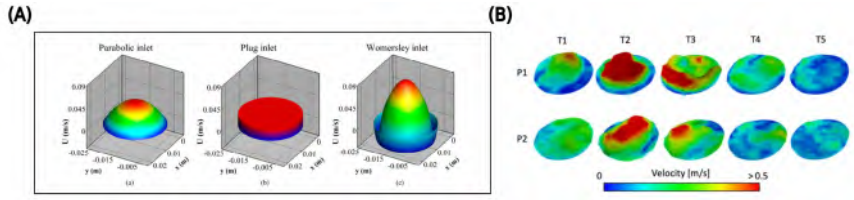

Figure 2.1: Image (A) represents a parabolic, plug and Womersley type profile imposed at the inlet adapted from [79] and (B) represents a 3D inflow profile at different time-points in the cardiac cycle imposed from 4D flow MRI for two patients adapted from [78].

Similarly, outflow boundary conditions describe how blood leaves the vessel segment. The simplest approach is to impose outlet pressure waveforms directly, corresponding to a Neumann condition. More advanced approaches utilize lumped parameter models (LPM) such as the Windkessel formulation, which accurately represent the downstream vasculature in terms of electrical analogues such as resistors and capacitors [80]. In these models, outlet pressure is computed dynamically from flow and the lumped parameters using ordinary differential equations and imposed as a time-varying pressure profile at the outlet [81].

At the vessel wall, rigid-wall simulations most often employ the no-slip Dirichlet condition. In fluid–structure interaction (FSI) models, however, the wall is deformable and coupling conditions are enforced that ensure continuity of velocity (kinematic condition) and balance of tractions (dynamic condition) across the interface [82] (see section 2.4). Finally, initial conditions define the velocity field at the beginning of a simulation. A common approach is to run a steady-state solution and use the converged fields as the initial state for the unsteady case [83].
In this thesis, a flat inflow profile both derived from literature and from MRI data are used at the inlet and LPM's are used at the outlet. Fluid flow simulations are initialized from a previous steady-state solution.

Lumped parameter models

Lumped parameter models are a mathematical representation of any complex system (artery in our case) where the spatial terms are ignored and only the temporal variation of parameters is considered (hence also called 0D models). LPM's are a great example of reduced order modeling and utilize ordinary differential equations to resolve parameters, hence making it computationally faster than solving a system in 3D. An example of LPM in the cardiovascular system is the Windkessel (WK) model, where hydraulic equivalents of electrical circuits are used to find a relationship between pressure and flow in a large arteries (see Figure 2.2). LPM's can either be used as a standalone analysis for the arterial system or be used as boundary condition at the outlets, and the commonly used WK models are highlighted in Figure 2.2. In CFD calculations, the most commonly used model is the three-element WK models (R,C and Z_c) (see Figure

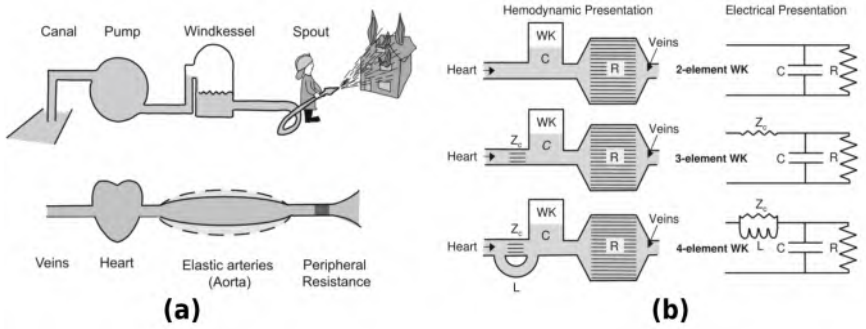

Figure 2.2: Panel (a) highlights the concept of the Windkessel effect while (b) highlights the different type of WK models with their respective hydraulic and electrical analogues. Image adapted from [80]

2.2) and is mathematically given by *

$$\frac{dP(t)}{dt} = \frac{Z_c + R}{RC}Q(t) + Z_c\frac{dQ(t)}{dt} - \frac{P(t)}{RC} \tag{2.11}$$

where,

$$R = \frac{\overline{P}}{\overline{Q}}, \quad C = \frac{dV}{dP}, \quad Z_c = \frac{\rho_f c}{A} \tag{2.12}$$

R is the arterial resistance or opposition to flow given by the ratio between $\overline{P}$, the mean arterial pressure in Pa and $\overline{Q}$, the mean flow in m^3s^{-1}. C is the total arterial compliance given by the ratio of dV, the change in volume of blood in m^3 to a corresponding change in pressure dP. Z_c or the characteristic impedance is dimensionally similar to resistance and is the ratio of pressure and flow in the absence of any wave reflections [84]. Z_c can also be calculated as the ratio between the density of the fluid ρ_f, the local wave-speed c and cross-sectional area A. As seen in Figure 2.2, for a 3 element WK model, the total resistance should yield $(R + Z_c)$. So modeling the characteristic impedance as resistor gives rise to errors in lower frequency ranges of the input impedance [80]. However, these errors are small as impedance is typically 5 to 7% of the proximal resistance [80]. Therefore, in CFD calculations, the characteristic impedance is modeled as a resistor. Additional information on Windkessel models and calculating the relevant parameters can be found in a detailed review by Segers et al. [84] and Westerhof et al. [80].
In this thesis The 3-element WK model is implemented explicitly i.e.

*Detailed derivation 3-element WK models can be seen here: https://leifh.folk.ntnu.no/teaching/tkt4150/._main026.html#fig:WKp

the pressure value at the outlet is updated using the flow rate at the end of each time-step in the finite volume solver Fluent (Ansys Inc, PA, USA) using customized user-defined functions (UDF).

2.2 Tissue model

While fluid dynamics in the cardiovascular system is commonly investigated using computational fluid dynamics (CFD), the structural response of the arterial wall is addressed within the framework of computational solid mechanics (CSM), often solved using a finite element method (see later), though some exceptions exist [85, 86]. In contrast to blood, which is modeled as a continuum occupying a fixed control volume using an Eulerian description, the vessel wall is a deformable solid whose material points are tracked throughout the cardiac cycle using a Lagrangian description (see later). Most equations and notations used in this section are from the standard textbook by Holzapfel [87].

2.2.1 Governing equations for tissue mechanics

The balance of momentum in the solid domain is expressed as

$$\rho_s \frac{D^2 \vec{u_s}}{Dt^2} = \nabla \cdot \bar{\bar{\sigma}} + \vec{b}, \tag{2.13}$$

where ρ_s is the solid density, $\vec{u}_s$ is the displacement vector, $\bar{\bar{\sigma}}$ is the Cauchy stress tensor, and $\vec{b}$ represents body forces (e.g., gravity).

In contrast to fluids, where equation 2.1 is required to convert system quantities into control-volume form, the Lagrangian description used for solids inherently follows each material point (see later). As a result, the acceleration term on the left-hand side represents a material derivative. The stress tensor plays a role analogous to that in fluids, but its constitutive definition depends on the material model adopted for the tissue. In this thesis, arterial wall mechanics are solved using the commercial finite element package Abaqus (Dassault Systèmes, Providence, RI, USA).

2.2.2 Constitutive modeling

Cardiovascular tissues such as the aortic wall are structurally complex and heterogeneous comprising multiple constituents including smooth muscle cells, elastin, and collagen fibers as described in Chapter 1. These microstructural components give rise to nonlinear, anisotropic,

and time-dependent material behavior [20, 88, 89], which must be accounted for in constitutive modeling. Depending on the scale and application, simplified linear-elastic descriptions may be sufficient, but more detailed hyperelastic or viscoelastic models are often required to capture the physiological mechanics of the wall [90].

To formulate constitutive models for soft tissues, the relation between the reference ($\vec{X}$) and deformed configurations ($\vec{x}$) must first be established. Let $\vec{X}$ denote the position vector of a material point in the undeformed (reference) configuration, and $\vec{x}$ the corresponding position vector in the deformed (current) configuration [87].

The displacement vector $\vec{u}_s$ is then defined as the difference between the current and reference positions,

$$\vec{u}_s(\vec{X}, t) = \vec{x}(\vec{X}, t) - \vec{X}. \tag{2.14}$$

The local deformation is characterized by the deformation gradient tensor

$$\bar{\bar{F}} = \frac{\partial \vec{x}}{\partial \vec{X}} \tag{2.15}$$

which maps an infinitesimal material line element from the reference to the deformed configuration,

$$d\vec{x} = \bar{\bar{F}}\, d\vec{X}. \tag{2.16}$$

Different stress measures are used depending on whether forces and areas are defined in the reference or the deformed configuration:

- The **Cauchy stress tensor** $\bar{\sigma}$, which acts in the current (deformed) configuration and represents the true force per unit deformed area.
- The **first Piola–Kirchhoff stress tensor** $\bar{\bar{P}}$, which relates forces in the current configuration to areas in the reference configuration. This tensor is generally not symmetric.
- The **second Piola–Kirchhoff stress tensor** $\bar{\bar{S}}$, which is symmetric and fully expressed in the reference configuration.

These stress measures are related through the deformation gradient tensor $\bar{\bar{F}}$ and the Jacobian of deformation $J = \det\left(\bar{\bar{F}}\right)$. The

transformation between reference and current configurations are performed using a *push-forward* and *pull-back* operations [87] and are as follows:

$$\bar{\bar{\sigma}} = \frac{1}{J}\,\bar{\bar{F}}\,\bar{\bar{S}}\,\bar{\bar{F}}^{T}, \tag{2.17}$$

which maps the second Piola–Kirchhoff stress into the current configuration (push-forward), and

$$\bar{\bar{S}} = J\,\bar{\bar{F}}^{-1}\,\bar{\bar{\sigma}}\,\bar{\bar{F}}^{-T}, \tag{2.18}$$

which maps the Cauchy stress back to the reference configuration (pull-back).

These relations ensure that stresses can be consistently represented in either configuration depending on the chosen constitutive framework. Hyperelastic formulations, including the Gasser–Ogden–Holzapfel model introduced next, are typically expressed in the reference configuration using the strain invariants of the right Cauchy–Green tensor $\bar{\bar{C}}$.

Gasser–Ogden–Holzapfel model

The arterial wall is modeled as a fiber–reinforced hyperelastic material described by the Gasser–Ogden–Holzapfel (GOH) formulation [88]. The strain–energy density function Ψ is additively decomposed into isotropic (elastin–dominated) and anisotropic (collagen–fiber) contributions as

$$\Psi = C_{10}(I_1 - 3) + \frac{k_1}{2k_2}\left(\sum_{i=4,6} \exp\big(k_2[\,\kappa I_1 + (1-3\kappa)I_i - 1\,]^2\big) - 1\right) \tag{2.19}$$

where C_{10} represents the stiffness of the isotropic matrix, k_1 represents the collagen fiber stiffness, k_2 the stiffening parameter, κ defines the degree of fiber dispersion. The invariants I_1, I_4, and I_6 are first, fourth and sixth invariants of the right Cauchy–Green deformation tensor $\bar{\bar{C}} = \bar{\bar{F}}^{\mathrm{T}}\bar{\bar{F}}$ with I_4, and I_6 depending on the mean collagen fiber angle α which is defined with respect to the circumferential direction.

The Cauchy stress tensor described in the previous section is then expressed as:

$$\bar{\bar{\sigma}} = \frac{\partial \Psi}{\partial \bar{\bar{F}}}\,\bar{\bar{F}}^{\mathrm{T}} - p\,\bar{\bar{I}}, \tag{2.20}$$

where p acts as a Lagrange multiplier representing the hydrostatic pressure that enforces the incompressibility constraint.
In this thesis, hybrid elements were employed in the finite element solver Abaqus (Dassault Systèmes, RI, USA), wherein the pressure field p acts as a Lagrange multiplier that enforces the incompressibility constraint $J = \det \bar{F} = 1$. Consequently, no volumetric penalty or compressibility parameter (D) was included.
Parameters of the GOH model are often estimated from in vitro experiments and fitting the model to test data obtained from uniaxial and biaxial tests [91]. To complement these measurements and enable an *in-vivo* characterization, Gheysen et al. [92] proposed estimating material parameters using pulse wave velocity (PWV).
In Chapter 3, GOH parameters previously estimated from mechanical testing is used and in Chapters 4 and 4A, parameters estimated from physiological PWV is used.

2.2.3 Initial and boundary conditions

Similar to Section 2.1.2, initial and boundary conditions must be defined to describe the state of the structural system. Boundary conditions are applied at the vessel inlets and outlets typically containing axial and allowing radial and circumferential movement [87, 93]. Additional support from surrounding tissues and spine are prescribed to resist excessive displacement while still allowing outward expansion [94]. At the fluid–structure interface, coupling conditions enforce continuity of displacements and balance of tractions (see later) between the fluid and solid domains [82]. Initial conditions define the stress state of the vessel wall. Unlike fluids, when arteries are excised, they are not stress-free when unloaded. Arteries shrink axially and open circumferentially reflecting the presence of residual stress [95]. Neglecting them and assuming the initial configuration to be zero-pressure, stress-free can affect the results as shown in Figure 2.3 [93]. Multiple inverse techniques have been defined in literature to obtain the zero

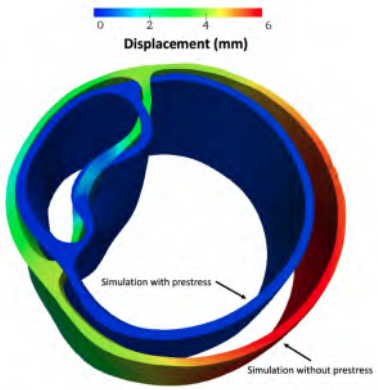

Figure 2.3: Comparison of displacements with and without prestress in aortic dissections shown by Baumler et al. [93].

pressure state [96–98]. In this work, a deposition-stretch algorithm proposed by Famaey et al. [99] is used to obtain the residual stresses. A brief overview is provided below

Deposition stretch algorithm

In this algorithm, the in-vivo geometry is taken as the reference state, and each constituent i is assigned a deposition stretch tensor $\bar{\bar{G}}^i$ that maps the unknown unloaded configuration to the observed in-vivo state [55, 99]. Collagen is generally modeled with a constant deposition stretch g^c along the fiber direction, consistent with experimental observations of mature arteries [100]. Elastin, however, is evaluated locally and requires an iterative procedure. In the first step, the diastolic pressure is applied to the vessel wall and this pressurization produces a deformation gradient $\bar{\bar{F}}_1$, which in reality should not occur if the in-vivo state is in equilibrium. The deformation is therefore interpreted as missing deposition stretch and the elastin stretch tensor is updated to $\bar{\bar{G}}^e = \bar{\bar{F}}_1$.

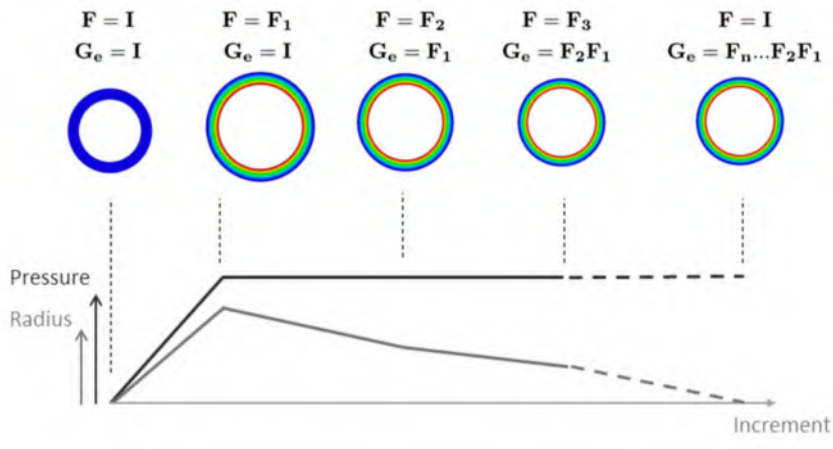

Figure 2.4: Schematic representation of deposition stretch algorithm described by Famaey et al. [99]

In the subsequent iterations, $\bar{\bar{G}}^e$ is updated with the resulting deformation gradient causing the vessel wall to recoil. After n iterations when $\bar{\bar{F}}_n$ is negligible, elastin deposition stretch tensor is given by

$$\bar{\bar{G}}^e = \bar{\bar{F}}_n \cdots \bar{\bar{F}}_2 \bar{\bar{F}}_1.$$

The process is terminated when the average nodal displacement is less than a fixed fraction of the wall thickness (e.g. 1%) [99]. The

resulting deposition stretch tensor incorporates the in-vivo loading, the axial stretches, and the residual stresses. Thus, although the final configuration and deposition stretch tensor are explicitly determined, the stresses are obtained implicitly, yielding a prestressed geometry. This algorithm will henceforth be referred to as the prestressing algorithm. Details regarding implementing this in the finite element solver Abaqus can be found in [101].
In this thesis, a finite element approach is adopted to obtain the in vivo configuration [101, 102] for Study 1. In Study 2, the implementation is done in a healthy thick walled cylinder in Matlab (Mathworks Inc, USA). The resulting deposition stretches are then applied in the FE framework, and the diastolic pressure is applied as an additional load to obtain the in vivo configuration [55].

2.3 Discretization and grid generation

To solve the governing equations of fluid and solid mechanics described in Sections 2.1 and 2.2, the computational domain must first be represented on a numerical grid, after which the equations are discretized into algebraic form. Grids may be structured or unstructured in nature with the latter primarily being used in cardiovascular geometries, though exceptions with structured grids exist [103]. General-purpose meshing tools such as Ansys ICEM (Ansys Inc., PA, USA) can generate such grids, while cardiovascular solvers like SimVascular [74] and CRIMSON [75] include built-in mesh generation platforms tailored to vascular models. Once a computational grid is available, the governing equations are converted to algebraic form [71]. This process, known as discretization, can be carried out using different numerical frameworks. Two broad frameworks used during this work are the finite element (FE) and finite volume (FV) methods.

The finite volume method discretizes the governing equations by integrating them over control volumes and evaluating fluxes across their faces [73]. For each control volume one algebraic equation for the unknown field variables exists ensuring the conservation laws are satisfied both locally and globally. Strict conservation property and robustness have established FVM as the dominant approach in CFD [71, 73].

The finite element method, on the other hand, is based on a weak formulation of the governing equations [104]. An approximate solution is presented within each element using shape functions, and the element contributions are assembled into a global system of equations. FEM is particularly well suited for problems involving complex

geometries [104], heterogeneous material properties [87], and structural deformation, and has therefore become the standard in CSM [105].
Prof. Brian Spalding, often credited as a founder of the finite volume method (FVM), famously remarked:

> 'Now however I recognize the FVM/FEM dichotomy as being comparable with those between Protestant and Catholic, or Sunni and Shia. That is to say that it promotes needless conflict; and expense; and loss of opportunity.'
>
> Brian Spalding

His words highlight the artificial divide that has grown between the finite volume and finite element communities. In practice, both are powerful discretization approaches with overlapping capabilities, and the choice is often guided more by convention and software availability than strict limitations. FEM-based fluid solvers such as SimVascular and CRIMSON are widely used in cardiovascular modeling, and finite volume packages like OpenFOAM also include solid mechanics modules.
For time-dependent problems, spatial discretization must be complemented by temporal discretization. Depending on the application, either explicit or implicit time integration schemes are used to advance the solution through successive time steps [71, 73].
In this thesis, a pragmatic approach is followed: FVM is used for the fluid equations to exploit its conservative flux formulation, while FEM is employed for the solid equations to leverage its strengths in structural analysis.

2.4 Coupling hemodynamics and tissue models

Arteries are compliant by nature, meaning that the flow of blood induces deformation on the surrounding structural domain Ω_s, while the resulting displacement, in turn, modifies the fluid domain Ω_f. Inherently, this is a fluid–structure interaction (FSI) problem. To capture this two–way interaction, the open source coupling tool CoCoNuT[†], developed in the Fluid Mechanics Team of Ghent University is employed.

[†]https://pyfsi.github.io/coconut/

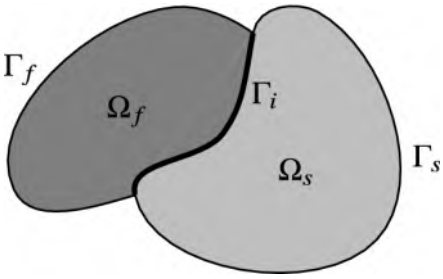

Figure 2.5: Schematic representation of the fluid domain Ω_f, the structural domain Ω_s, and their common interface Γ_i [106].

Comprehensive description of FSI and coupling algorithms are described in reviews by Degroote [82] and Delaissé et al. [106]. Only a brief overview on relevant theory to understand the subsequent chapters is provided here. As illustrated in Fig. 2.5, the fluid domain Ω_f with boundary Γ_f and the structural domain Ω_s with boundary Γ_s are coupled through their common interface Γ_i. The governing equations in Ω_f are detailed in Section 2.1, and those in Ω_s in Section 2.2. In addition to their respective boundary conditions on Γ_f and Γ_s, any FSI formulation must also enforce equilibrium along Γ_i. For a no-slip interface, two coupling conditions arise.

First, the kinematic condition requires continuity of velocity across the interface,

$$\vec{v_f} = \frac{\partial \vec{u_s}}{\partial t} \quad \text{on } \Gamma_i, \tag{2.21}$$

where $\vec{v_f}$ is the fluid velocity in Ω_f and $\vec{u_s}$ the structural displacement in Ω_s. This condition also implies equality of accelerations at the interface.
Second, the dynamic condition enforces traction equilibrium,

$$\bar{\bar{\sigma}}_f \cdot \vec{n_f} + \bar{\bar{\sigma}}_s \cdot \vec{n_s} = \vec{0} \quad \text{on } \Gamma_i, \tag{2.22}$$

where $\bar{\bar{\sigma}}_f$ and $\bar{\bar{\sigma}}_s$ denote the Cauchy stress tensors in the fluid and solid domains, respectively, and $\vec{n_{f,s}}$ are the corresponding outward unit normals from the domain $\Omega_{f,s}$[82].

2.4.1 Monolithic and Partitioned approaches

Numerical treatment of FSI problems follows two broad strategies namely monolithic and partitoned approaches [82]. In a monolithic approach, equations (2.10) of the fluid and (2.13) of the solid, together with interface conditions are assembled into a single system and solved simultaneously, for instance using a Newton–Raphson approach [82]. Upon convergence of the solver, the interface equilibrium conditions are inherently satisfied. Since the equations are solved together, no coupling iterations between solutions of fluid and structural equations are necessary [82].

On the other hand, equations of fluid and structure can be solved separately or in a partitioned manner. Here, boundary conditions are applied at the interface and multiple iterations within a time-step called coupling iterations are performed till appropriate convergence is obtained. The modular nature of partitioned methods makes them attractive, since existing state-of-the-art solvers for fluid and structural mechanics can be combined with relatively little modification, albeit at a higher computational cost [82].
From a cardiovascular perspective, the fluid equations compute the tractions exerted by blood on the vessel wall. If the resulting wall displacement is not communicated back to the flow solver, the simulation is referred to as one-way coupled FSI, which is computationally cheaper. When the wall deformation is instead transferred back to the fluid solver, the interaction is referred to as two-way coupled FSI. In this case, the fluid mesh must be updated and additional coupling iterations are required to achieve consistency.
Partitioned strategies can further be classified into weak and strong coupling. In weak coupling (also called explicit coupling), the fluid and structural solvers are advanced only once per time step without coupling iterations. The equilibrium conditions are not strictly enforced. Explicit coupling tends to suffer from added-mass effect for incompressible flows which is quite prevalent in cardiovascular problems, especially since blood and the surrounding tissues have similar densities [107]. Strong coupling on the other hand enforces interface conditions through iterative exchanges between solvers until convergence is reached at each time step.
Throughout the course of this thesis, we will be working on partitioned, strongly coupled methods to solve the FSI problems.

2.4.2 Algorithms to solve partioned FSI

Strongly coupled partitioned FSI problems can be solved using either fixed-point iterations such as Gauss-=Seidel or quasi-Newton approaches. Fixed-point schemes such as Gauss–Seidel are straightforward but often suffer from stability issues due to the added-mass effect. Quasi-Newton approaches help address these difficulties by accelerating convergence and improving robustness [82, 108].
A schematic representation of Gauss-Seidel and IQN-ILS (Interface quasi-Newton with inverse Jacobian from a Least Square model) can be found in Figure 2.6. In CoCoNuT , the IQN-ILS algorithm is one of the quasi-Newton methods supported. Upon solving the fluid flow problem in solver $\mathcal{F}$, a traction $\tilde{\mathbf{y}}$ is obtained for an input displacement $\mathbf{x}$ represented symbolically as: $\mathcal{F}(\mathbf{x}) = \tilde{\mathbf{y}}$. This can be similarly

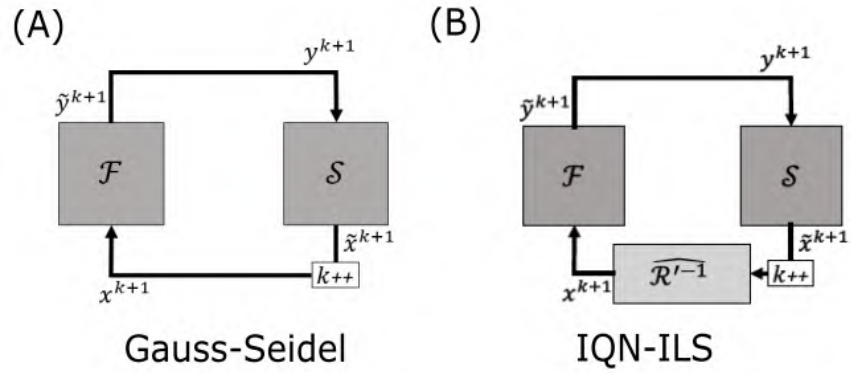

Figure 2.6: Panel (A) shows the symbolic representation of the Gauss–Seidel approach and (B) the IQN-ILS coupling algorithm. Image adapted from [109].

replicated for the structure as: $\mathcal{S}(\mathbf{y}) = \tilde{\mathbf{x}}$.
For the Gauss-Seidel approach, the resultant output from one solver is directly passed onto the other [109] and after each iteration k, a residual $\mathbf{r^k} = \tilde{\mathbf{x}} - \mathbf{x^k}$ is calculated until the desired convergence is reached.

For the IQN-ILS, it can be observed from Figure 2.6 (B) that the output from the structural solver is not directly passed on to the fluid solver. A residual operator $\mathcal{R}(\mathbf{x}^k)$ is defined returning the residual $\mathbf{r}^k$ as a function of $\mathbf{x}^k$ with the ultimate goal of finding $\mathbf{x}$ for which $\mathcal{R}(\mathbf{x}) = \mathbf{0}$. In this approach, the Jacobian of the equation is used to get an estimate of $\mathbf{x^{k+1}}$ [110]

$$\mathcal{R}'(\mathbf{x}^k)\left(\mathbf{x}^{k+1} - \mathbf{x}^k\right) = -\,\mathbf{r}^k,$$

where $\mathcal{R}'(\mathbf{x}^k)$ denotes the Jacobian of the residual operator.

In our work, both the flow $\mathcal{F}$ and structural solver $\mathcal{S}$ are black boxes which means the Jacobian $\mathcal{R}'(\mathbf{x}^k)$ cannot be computed directly. Hence, quasi-Newton methods are used to approximate the Jacobian resulting in

$$\widetilde{\mathcal{R}}'(\mathbf{x}^k)\left(\mathbf{x}^{k+1} - \mathbf{x}^k\right) = -\,\mathbf{r}^k,$$

where $\widetilde{\mathcal{R}}'(\mathbf{x}^k)$ is an approximate Jacobian. Instead of solving the system of linear equations with the Jacobian in each iteration [109], $\mathbf{x^{k+1}}$ can be written as:

$$\mathbf{x}^{k+1} = \mathbf{x}^k - \widehat{\mathcal{R}'^{-1}}(\mathbf{x}^k)\,\mathbf{r}^k,$$

where $\widehat{\mathcal{R}'^{-1}}(\mathbf{x}^k)$ denotes the approximated inverse Jacobian used in the IQN-ILS algorithm. Detailed description of these can be found in the papers by Degroote [82], Delaissé [106] and the thesis of Delaissé [110].

2.4.2.1 Arbitrary Lagrangian Eulerian method

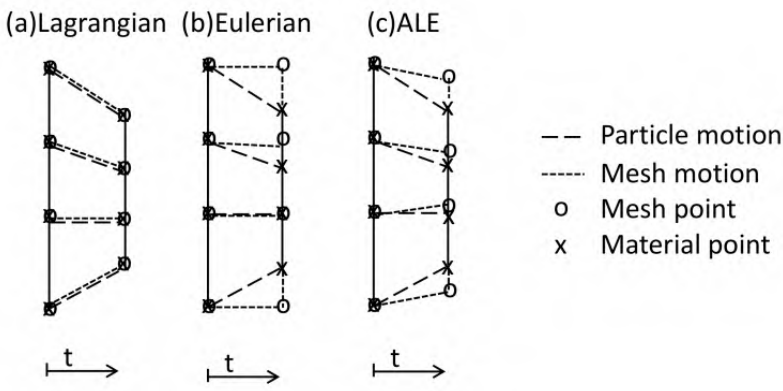

Figure 2.7: Figure highlighting the three descriptions used in this thesis. Panel (a) describes the Lagrangian approach, (b) the Eulerian and (c) the Arbitrary Lagrangian-Eulerian formulation. Image adapted from Donnea [111]

The three descriptions shown in Fig. 2.7 provide different frames of reference for representing motion in continua. To mathematically formulate the Arbitrary Lagrangian–Eulerian (ALE) framework, it is necessary to generalize the conservation equations, originally defined for a fixed control volume, to one that can move or deform in time. The integral forms of the continuity and momentum equations for a fixed control volume are given by Equations 2.3 and 2.6, and their extension to a deformable control volume reads as follows:

$$\frac{\partial}{\partial t}\iiint_V \rho_f \, dV + \iint_A \rho_f \, (\vec{v_f} - \vec{w}) \cdot \vec{n} \, dA = 0 \tag{2.23}$$

$$\frac{\partial}{\partial t}\iiint_V \rho_f \vec{v_f} \, dV + \iint_A \rho_f \left[(\vec{v_f} - \vec{w}) \cdot \vec{n}\right] \vec{v_f} \, dA = \iint_A \bar{\bar{\sigma}}_f \cdot \vec{n} \, dA + \iiint_V \vec{f_b} \, dV \tag{2.24}$$

The Geometric Conservation Law (GCL) [112] ensures that the temporal change of the control volume is consistent with the grid velocity, expressed as

$$\frac{\partial}{\partial t}\iiint_V dV = \iint_A \vec{w} \cdot \vec{n} \, dA. \tag{2.25}$$

Substituting Equation 2.25 to Equation 2.23, we get the conservation of mass previously expressed in Equation 2.4. Here, $\vec{w}$ denotes the velocity of the computational mesh, which may coincide with the fluid velocity (Lagrangian), completely vanish for fixed grids (Eulerian), or take an arbitrary value (ALE). It is important to note that the mesh velocity $\vec{w}$ is prescribed at the fluid–structure interface, where it coincides with the structural velocity.
The three descriptions can be summarized as follows:

- **Lagrangian:** the computational mesh moves with the material, i.e. $\vec{w} = \vec{v_f}$. Convective fluxes vanish because the control volume follows the material particles. This approach is used to solve equations described in section 2.2.
- **Eulerian:** the computational mesh is fixed in space, i.e. $\vec{w} = \vec{0}$. Material flows through the stationary control volume and this is the standard approach used to solve standalone CFD problems described in Equation 2.1.
- **Arbitrary Lagrangian–Eulerian (ALE):** the computational mesh moves with an arbitrary velocity $\vec{w}$, which may differ from both the material velocity and zero.

Defining $\vec{w}$ at the interface completes the mathematical picture, but in practice, one must also decide how the interior mesh follows this motion. Common techniques that exist are the spring based smoothing approach where the computational mesh is described as a network of linear interconnected springs which link the nodes. The undeformed mesh represents the equilibrium configuration of the spring system. When a boundary node is displaced, the connected springs exert forces proportional to the imposed displacement, and the resulting equilibrium determines the new positions of the interior nodes [82]. An alternative approach is to distribute boundary displacements into the interior nodes by solving a diffusion equation. The diffusion coefficient can be defined in different ways depending on the desired mesh behavior. A common choice is to scale it with the distance from the wall, which helps preserve mesh quality close to deforming boundaries. Instead, it can also be based on the cell volume where larger elements absorb a greater portion of the deformation than smaller ones [82].
The strongly coupled FSI problems tackled in Chapters 3, 4 are solved using the ALE formulation.

2.4.2.2 Chimera or Overset Grid Technique

The Arbitrary Lagrangian–Eulerian (ALE) method described in the previous section is not without limitations. In particular, while dealing with large structural motions or highly deformable domains, mesh distortion can become severe. Rather than having a single fluid grid which deforms along with the structure like ALE, the fluid domain in the Chimera method relies on one or more overlapping component (overset) grids. These component grids are embedded on a fixed background Cartesian grid. Cells which are not part of the fluid domain and ones that are overlapped with the structure are eliminated in a process called hole cutting shown schematically in Figure 2.8.

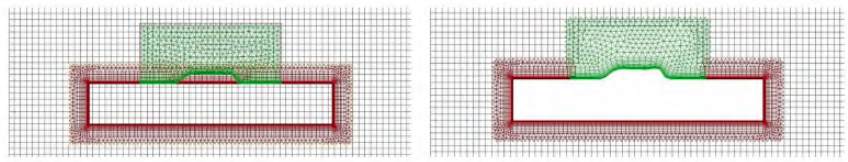

Figure 2.8: Schematic showing how overlapping boundaries with the same boundary conditions behave during hole cutting. Image adapted from Ansys User manual [113].

The eliminated cells are called dead cells [113]. Once the cells are eliminated donor cells in the background grid interpolate with the receptor cells in the component grid and vice-versa. Cells where the flow equations are solved are called solve cells [113] and an ALE approach is used to deform the fluid mesh. This approach is particularly useful in a biomedical context for valvular mechanics where multiple component meshes can be defined [114–116]. In a nutshell, the Chimera technique can be thought of as a mixture of the ALE technique and fixed grid methods like immersed boundary. Since the component grid(s) is attached to the structure, mesh quality is preserved even under very large displacement [82]. This makes it particularly useful in calculating hemodynamic parameters at the wall like wall shear stresses. *An overset approach is used to calculate the large deformation of the intimal flap as a proof of concept using prescribed boundary movement in Appendix A.*

2.5 Hemodynamic parameters of interest

Upon solving the strongly coupled FSI problem for our pathologies of interest based on techniques described in section 2.4, relevant parameters need to be investigated especially to gain insights into the

problem at hand. The traction vector at the interface, calculated based on Cauchy stress tensor in Eq.2.8, decomposes into a normal component (dominated by pressure) and tangential component, which is wall shear stress (WSS) as observed in Figure 2.9.

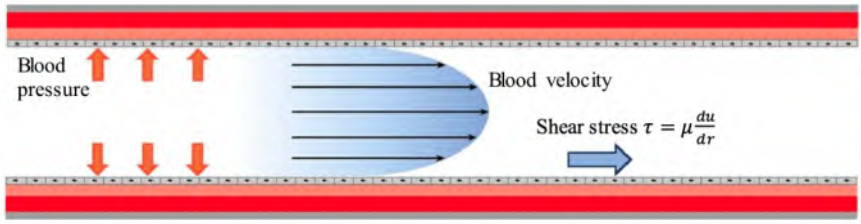

Figure 2.9: Schematic representing dominant flow based stresses acting on the vessel wall. Image adapted from [117]

WSS is a widely used parameter to assess vascular diseases and to stratify risk [16, 118]. Regions of low WSS have been linked to atherosclerosis and the formation of an intraluminal thrombus [16, 119]. High WSS has been linked to endothelial injury and lesion initiation or rupture, for instance in cerebral aneurysms [120–122].

Since the problems being solved are 3D FSI in nature, computing instantaneous WSS for each time-point is cumbersome. While many studies report WSS at certain time-points in the cardiac cycle, calculating cycle-averaged metrics provides a practical alternative to instantaneous values. Multiple cycle-averaged wall shear stress metrics have been defined in literature [123–126]. Detailed comparison of these metrics for certain pathologies [127] and comprehensive reviews detailing their link to vascular biology [128] exist. Out of the many metrics, during this dissertation the canonical and the oldest defined ones namely time-averaged WSS (TAWSS) and oscillatory shear index (OSI) [129] are compared with the non canonical WSS divergence based metric [130] namely toplogical shear variation index (TSVI) [131]. The phrase topology is borrowed from dynamical-systems theory and was first introduced in a fluid-mechanical context by Tobak and Peake [132], who analysed the organisation of surface streamlines, specifically critical points such as sources and sinks where the skin-friction vector field vanishes. A brief description of these metrics along with their vascular significance is provided in Table 2.1.

Canonical metrics like TAWSS and OSI are widely used as a metric in most in-silico studies. TSVI on the other-hand is relatively new [131] and deserves some attention. This metric is based on the

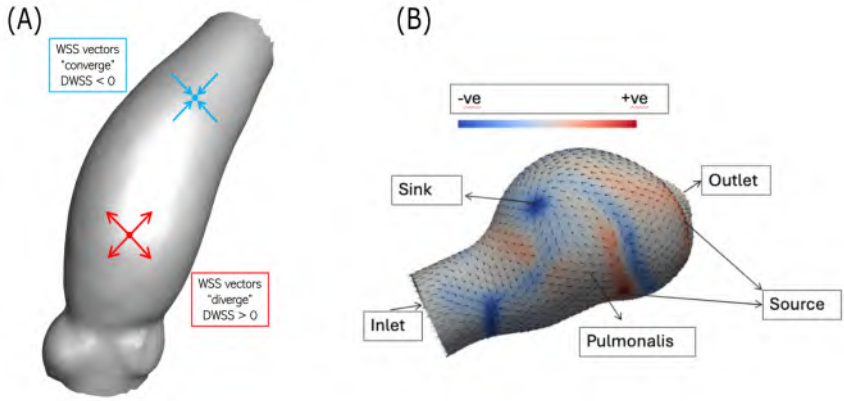

Figure 2.10: Panel (A) shows a schematic on how the WSS vectors point when the divergence of WSS is positive and negative. Panel (B) shows the vectors pointing for a pulmonary autograft simulated in Chapter 3. Panel (A) adapted from [133].

divergence of WSS and an intuitive example along with the application can be found in Figure 2.10. The divergence of WSS yields a scalar value and a positive value indicates an expansion-like action and a negative a contraction-like action applied on the endothelium. Low and oscillatory WSS is shown to have a link with intimal-medial thickening [134] and vascular remodeling [135] underlining its significance in vascular pathophysiology. Variations in WSS occur both spatially and temporally within a geometric structure due to changes in velocity across it. Recent research has highlighted connections between spatial heterogeneity in hemodynamics and related metrics with vascular growth [136] further highlighting the importance of WSS in vascular growth for all configurations. Canonical metrics like TAWSS and OSI are single variables often computed across the entire cardiac cycle which can be helpful in determining global WSS behavior. A recent review by Mutlu et al. [128] suggested that disturbed hemodynamics often associated with low TAWSS and high OSI are hallmarks of rupture (which is the worst case scenario for G&R) in aneurysmal geometries. Mousavi et al. proposed relative residence time (RRT) which is a function of TAWSS and OSI as a driver for localized elastin loss in ascending thoracic aneurysms using a one-way coupled fluid-solid growth model and observed that RRT calculated using CFD analysis played an important role in disease progression and remodeling [137]. More recently, divergence of WSS (DIV_W) along with related metrics quantifying the contraction and expansion action applied on the endothelium by shear forces [130, 138]

have gained traction to understand the association between hemodynamics and disease progression. TSVI was found to predict temporal variation of wall thickness/plaque progression in longitudinal follow-up of porcine [139] as well as human coronary arteries [140], and intima-media thickness in human carotid arteries after a long-term follow-up [141] which are hallmarks of G&R.

In order to calculate TSVI, the normalized WSS vector field is used as shown in Figure 2.11. This allows the identification of expansion and contraction independent of local magnitude variations in WSS vector fields [130]. TSVI is calculated as the standard deviation of the normalized WSS divergence over an entire cardiac cycle [142]. Intuitively, it gives a measure of the variation in expansion and contraction action on the endothelium [131, 142]. *In this thesis, an Eulerian based description of WSS skeletons can be found [130]. This theory is extended to large displacements.*

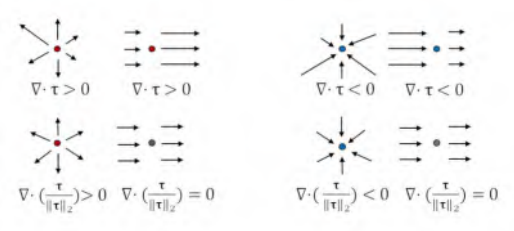

Figure 2.11: Schematic representing the difference when WSS vector is used and normalized WSS vector is used to calculate the divergence. Image adapted from [130].

Table 2.1: Overview of wall shear stress (WSS) metrics used in this dissertation

Metric	Formula/Definition	Description	G&R Significance
Time-Averaged Wall Shear Stress (TAWSS)	$\mathrm{TAWSS} = \frac{1}{T}\int_0^T \|\vec{\tau}(t)\|\, dt$	Mean WSS magnitude over a cardiac cycle [129]	Low TAWSS associates with intimal thickening [134] and aneurysmal expansion (longitudinal) [143].
Oscillatory Shear Index (OSI)	$\mathrm{OSI} = \frac{1}{2}\left(1 - \frac{\left\|\int_0^T \vec{\tau}(t)\, dt\right\|}{\int_0^T \|\vec{\tau}(t)\|\, dt}\right)$	Degree of directional change in WSS (0–0.5) [129]	High OSI (disturbed flow) correlated with increased vessel wall thickness [144] .
Topological Shear Variation Index (TSVI)	$\mathrm{TSVI} = \left\{\frac{1}{T}\int_0^T \left[\nabla\cdot\hat{\vec{\tau}}(t) - \overline{\nabla\cdot\hat{\vec{\tau}}}\right]^2 dt\right\}^{1/2}$, $\hat{\vec{\tau}}(t) = \frac{\vec{\tau}(t)}{\|\vec{\tau}(t)\|}$	RMS variation of divergence of normalized WSS field [131]	High TSVI co-localizes with wall thickening in longitudinal coronary data [131].

2.6 Structural parameters of interest

In the previous section, hemodynamic parameters of interest which are known in literature to drive vascular G&R are highlighted. However, most computational studies that model vascular G&R consider structural parameters of interest. While it is beyond the scope of this thesis, a quick overview is warranted.

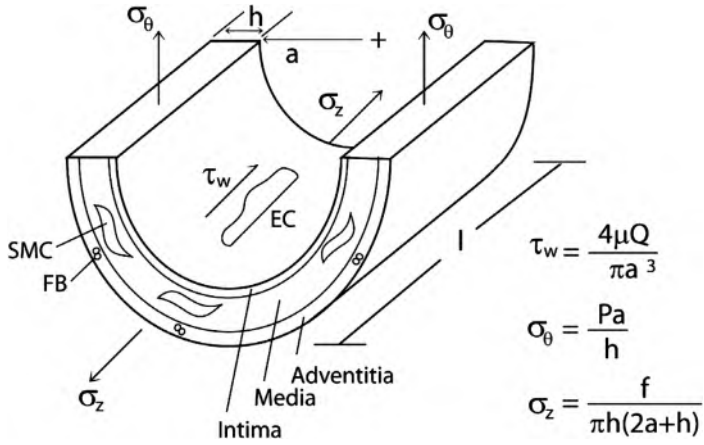

Figure 2.12: Schematic sketch showing the geometric parameters namely radius a, thickness h and length l of an artery with the three layers previously described in section 1.1.1 which consist of endothelial cells, smooth muscle cells and fibroblast along with the associated stresses acting on the wall namely wall shear stress τ_w, circumferential stress σ_θ and axial stress σ_z. Image adapted from [145].

As illustrated in Figure 2.12, vascular tissues are subjected to circumferential stress (σ_θ), axial stress (σ_z), and WSS (τ_w), which act on endothelial cells (EC), smooth muscle cells (SMC), and fibroblasts (FB) across the intima, media, and adventitia. The role of WSS has already been illustrated in the previous section. The structural stresses or wall stresses are central to the constrained mixture theory introduced by Humphrey and Rajagopal [89] and extended to a finite element method by Valentin et al. [146], in which the vessel wall is modeled as a composite of evolving constituents with collagen, elastin, and smooth muscle, each with its own preferred mechanical state. In these models, wall stress is decomposed into constituent-level stresses, so that each fiber family (e.g. collagen) responds to its own deposition stretch, preferred orientation, and temporal evolution. For example, Maes et al. [147] modeled pulmonary autograft remodeling under aortic pressures using a homogenized constrained

mixture framework, computing collagen fiber stretches and stresses to drive mechano and inflammation-mediated mass turnover. Similarly, Gheysen et al. [7] modeled an idealized dissected aorta with a mechanical framework in which collagen fiber stress is a key mechanical driver in stress mediated G&R, complemented by imposed inflammation patterns. Structural loading also shapes the vessel's microstructure, as shown by the layer-specific fiber distribution model of Vander Linden et al. [148], which examines how collagen orientation arises under homeostatic stresses rather than time-dependent G&R. Their comparison of stress- and stretch-based alignment rules demonstrated that constituent-level stress best reproduces observed fiber architecture, underscoring that these same structural parameters not only drive remodeling but also establish the baseline microstructure that governs subsequent mechanical responses. Most studies that use computational models to study G&R are formulated under static pressure states (e.g., representative diastolic/mean/systolic pressures) rather than fully time-resolved pulsatile stresses. In contrast, Vervenne et al. [149] explicitly integrated diastolic, mean, and systolic pressures to represent pulsatile circumferential stress, demonstrating that pulsatile stresses rather than a single mean value could predict available experimental results in pulmonary autografts. Together, these works indicate that vascular remodeling is governed not just by bulk mechanical cues such as pressure or mean wall stress, but by constituent-specific mechanical environments; particularly fiber stress and stretch and their interaction with inflammatory signaling, pointing toward more physiologically grounded G&R models.

II

Applications

Chapters

3 Pulmonary Autografts **55**

4 Aortic Dissections **99**

4A Wave Propagation in the Aortic Dissection Model **137**

CHAPTER 3

Pulmonary Autografts

*This chapter aims to answer **Objective 1** and discusses how insights into hemodynamics can be obtained for a yet to remodel autograft using fluid-solid interaction. We have provided a brief overview on pulmonary autografts in Chapter 1, the relevant numerical techniques used are discussed in Chapter 2. The chapter is based on research published in the paper* *

3.1 State-of-the-art

Vascular tissue subject to altered mechanical loading conditions tends to adapt by growth and remodeling to restore its homeostatic condition [1]. The pulmonary autograft is a prime example of such tissue where diseased or injured aortic tissue is replaced by pulmonary tissue in the aortic position in young patients [147]. When placed in systemic position, the autograft is exposed to a seven-fold increase in pressure which renders the tissue prone to growth, remodeling, and maladaptive behavior [99]. Overview on animal models used is described in section 1.2.1.

Growth is associated with volumetric change, while remodeling, often in conjunction with growth, describes changes in microstructure,

*Balasubramanya A et al. (2024). 'Hemodynamics and wall shear metrics in a pulmonary autograft – comparing a fluid-structure interaction and computational fluid dynamics approach.' *Computers in Biology and Medicine*, 176. https://doi.org/10.1016/j.compbiomed.2024.108604.

with concomitant changes in wall stiffness, and global changes such as wall thickening [150]. Various computational models like the kinematic growth [151] and constrained mixture model [89, 152] have been developed to study growth and remodeling (G&R) in arterial tissues. Implementation of G&R in cardiovascular applications can be found in detailed reviews by Humphrey and Maes et al. [153, 154]. To study long term G&R in pulmonary autografts, a non-linear finite element (FE) model was developed by Famaey et al. [99], and different G&R algorithms were compared by Vastmans et al. [102] in ovine models to determine causes of dilation and long-term outcomes post-surgery [99, 102]. Maes et al. further postulated that inflammation also plays an important role in autograft dilation and accurately predicted adventitial thickening albeit in a thin-walled cylinder model [147]. Despite accurately modeling non-linear tissue behavior, reporting wall stresses in the pulmonary autograft immediately after surgery [155] and after long-term intervention [156], the underlying assumptions in computational models for the pulmonary autograft include uniform distribution of pressure at the autograft surface while not accounting for the effects of blood flow acting on the autograft via the frictional force acting at the blood-endothelium interface, quantifiable in terms of wall shear stress (WSS).
Limited temporal and spatial resolution of medical imaging hampers measurement of WSS, which is usually inferred through CFD modeling. This modeling technique often introduces the idealization of assuming vessels as rigid walls. In reality, the vasculature is not rigid and the interaction between the vessel wall and the flowing blood is a complex two-way coupled multi-physics problem which can be modeled using a fluid-structure interaction (FSI) approach. While G&R has been widely studied for pulmonary autografts as discussed in the previous section, no known CFD or FSI studies exist for the pulmonary autograft, making this the first of its kind to qualitatively and quantitatively study the pulmonary autograft.

Clinical Rationale

Keeping in mind that placing the pulmonary tissue in aortic position entails exposing a highly distensible autograft to systemic hemodynamic conditions, we conjecture that an FSI simulation provides more accurate analysis of near wall hemodynamics, to be subsequently used in conjunction with G&R. The aim of our work is to develop a strongly coupled, two-way FSI model for a pulmonary autograft immediately after surgery in multiple ovine models with variable autograft size. This model is comprehensively compared against a CFD

model, with the ultimate goal of gaining insight into long-term remodeling through the development of a coupled fluid-solid growth model. Our approach involves a qualitative and quantitative examination of canonical and non-canonical WSS metrics for both CFD and FSI models. We aim to assess whether the additional computational cost associated with FSI justifies its application. Our study also provides preliminary insights into the hemodynamics of pulmonary autografts, where very large deformations occur, with a closer look at the near-wall hemodynamics as depicted by the topological skeleton analysis of the WSS in terms of its divergence, whose underlying theory is expected to be challenged by the presence of very large deformations [130].

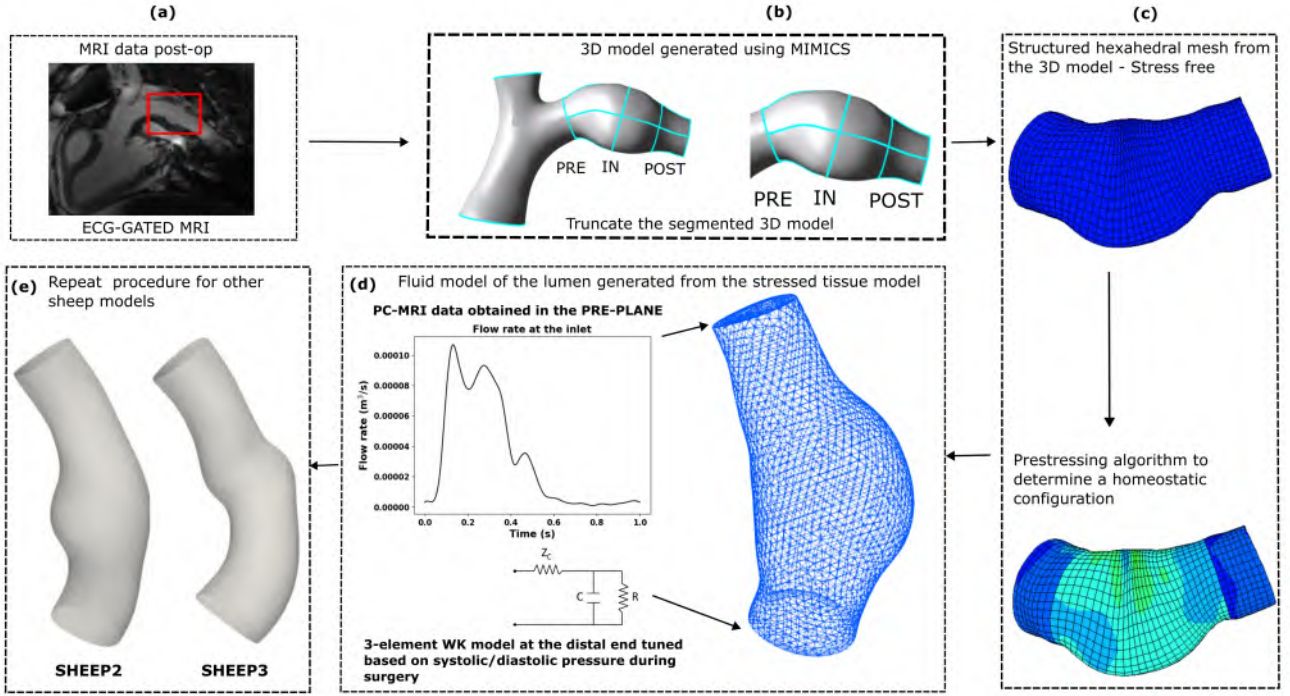

Figure 3.1: Panel (a) shows the ECG-Gated 4 days post-operation; (b) shows the planes at which flow measurements are taken along with a reconstructed 3D model; (c) shows a structured hexahedral mesh from the 3D model (initially stress-free) and subsequently the stressed configuration is determined using a prestressing algorithm; (d) Fluid mesh generated from the stressed configuration followed by appropriate boundary conditions, namely: Smoothed inlet flow profile measured using PC-MRI at the PRE plane and 3-element windkessel model at the POST plane to mimic pressure measurement during surgery; (e) Other sheep configurations determined using a similar approach.

3.2 Methodology

3.2.1 Experiments, imaging data, geometry

The work utilizes previously acquired data [47], with a pulmonary graft placed in the thoracic aortic position in eight sheep. The study was approved by the Animal Ethics Committee of KU Leuven (P135/2016). Post-operative follow-up included ECG-gated MRI scans post-surgery as shown in Fig 3.1 (a), out of which 3 representative datasets were selected for this computational study, here labeled Sheep 1 (1-day post-surgery), 2 and 3 (4 days post-surgery). Geometries were reconstructed using the image processing software Mimics (Materialize, Leuven, Belgium) [102]. Flow data was obtained using 2D Phase contrast MRI (PC-MRI) for Sheep 1 at 3 planes located proximal (PRE), inside (IN) and distal (POST) of the autograft Fig 3.1(b) for 36 phases to characterize the cardiac cycle, with spatial resolution of $1.25 \times 1.25 \times 3.7$ mm^3, encoding velocity $V_{\text{enc}} = 150$ cm/s, echo time $T_{\text{e}} = 4.28$ ms, repetition time $T_{\text{R}} = 27.72$ ms and flip angle $\alpha = 20°$. Aortic pressure measurements were obtained only during surgery, with systolic/diastolic pressure of 61/32 mmHg for Sheep 1 [47]. The datasets were selected such that the autograft size varies markedly in diameter/width ratio (D/L), as shown in Figure 3.2. Additionally, it is noteworthy that the (D/L) and the distal length (L_{d}) increases from Sheep 1 to Sheep 3, while the proximal length (L_{p}) is notably small for Sheep 1 but comparable for Sheep 2 and 3. Due to artifacts and missing data for Sheep 2 and 3, flow (proximal) and pressure (distal) data from Sheep 1 was used for calculations in Sheep models 2 and 3 as well. Sheep models also vary in terms of material properties, as illustrated in Table 3.1.

3.2.2 Grid generation

From the reconstructed geometries of the arterial wall, a structured hybrid hexahedral mesh [102] was generated using the in-house meshing tool PyFormex* [103] with 2 layers of solid elements in the radial direction as shown in Fig 3.1 (c). Once a structured mesh was generated for all sheep geometries, the homeostatic condition at diastolic pressure was determined. To obtain a stressed configuration, the prestressing algorithm developed in-house by Famaey et al. [99] and described in section 2.2.3 was applied using user-subroutines in Abaqus (Dassault Systems, USA). Initially, a diastolic pressure measured during surgery (32 mmHg) [47] was applied to the vessel wall's

*https://www.nongnu.org/pyformex/

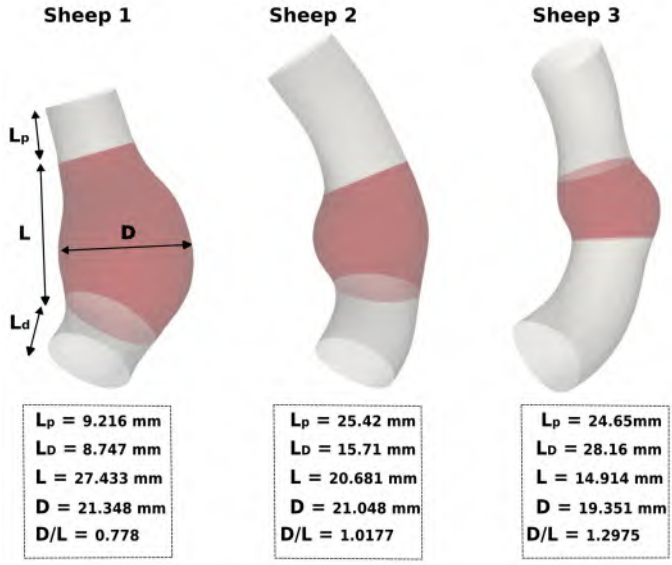

Figure 3.2: Morphology of the fluid models extracted from the structural model after homeostatic condition was reached. (D/L) ratio increases from Sheep 1 to 3.

inner surface leading to dilation. Subsequently, a deposition stretch tensor for elastin and collagen was applied at each integration point leading to stiffening and contracting back to the reference configuration. In case the reference configuration was not obtained yet, the remaining deformation gradient was multiplied with the existing deposition stretch tensor. This process was repeated iteratively until the in-vivo configuration was obtained [99]. Once the in-vivo configuration was obtained, the fluid domain was filled with tetrahedral cells while prismatic cells were strategically employed at the boundary to effectively capture the near-wall hemodynamics as shown in Fig 3.1 (d). The meshing tool ICEM CFD (Ansys Inc, USA) was employed to generate $487,590$ tetrahedral cells for Sheep 1, $565,931$ for Sheep 2, and $683,121$ for Sheep 3 with five prismatic cell layers adjacent to the wall for each geometry. The number of cells were determined using a mesh sensitivity analysis for Sheep 1, where time-averaged metrics along the cardiac cycle were calculated for 4 different grid sizes (shown in Table S1 and Fig S1) in the supplementary section S1 highlighting the behavior of time-averaged metrics with varying spatial resolution). Percentual variations were calculated with respect to the mesh with finest resolution. Median along with 90^{th} and 10^{th} percentile of WSS metrics were computed to ensure there were no outliers. Adopting Mesh 3, less than 5% and 7.25%

variations were observed for TAWSS and TSVI, respectively, with respect to the finest mesh (Fig S1). Based on mesh sensitivity analysis, the Mesh 3 was adopted to ensure a trade-off between accuracy and computational cost. Similar cell size as the selected mesh for Sheep 1 was used to generate the meshes in the other sheep models. Details regarding cell count are provided in Table S2 in the supplementary section S1. We also ensured that the number of triangles on the fluid wall was sufficiently high compared to the number of structural elements to guarantee an accurate fluid-solid interface representation and load/displacement interpolation.

3.2.3 Tissue and blood properties

A non-linear hyperelastic Gasser-Ogden-Holzapfel (GOH) constitutive model [88] described in section 2.2.2 was used to describe the material properties of the tissue in which the artery is modeled as a single layer (media and adventitia together). Planar biaxial tests were performed to obtain stress-stretch curves [47] which were used to determine the GOH parameters [102] detailed in Table 3.1 The

Table 3.1: Material parameters based on the experiments as reported by Vanderveken et al. [47] and obtained by Vastmans et al. [102].

Location	**Sheep**	C_{10} **(MPa)**	k_1 **(MPa)**	k_2 **(-)**	κ **(-)**	α **(rad)**	**Thickness (mm)**
Autograft	1	0.0027	0.0058	12.9093	0.2154	0.0056	1.45
	2	0.0029	0.0026	1.8988	0.1606	0.5854	2.80
	3	0.0026	0.0062	7.7760	0.2438	0.0126	1.80
Proximal Aorta	1	0.0098	0.0037	0.0001	0	0.0002	2.19
	2	0.0073	0.0391	0.0261	0.2084	0.4009	1.93
	3	0.0066	0.0114	1.6236	0	0.6161	1.66
Distal Aorta	1	0.0092	0.0030	0.0001	0	0.0003	2.29
	2	0.0073	0.0391	0.0261	0.2084	0.4009	1.93
	3	0.0066	0.0114	1.6236	0	0.6161	1.66

density of arterial tissue was set to be $1200\,\mathrm{kg\,m^{-3}}$ [157, 158] and the density of the pulmonary tissue was set at the same value. Blood was modeled as a Newtonian fluid with a density of $1051\,\mathrm{kg\,m^{-3}}$ and sheep specific dynamic viscosity of $0.00512\,\mathrm{kg\,m^{-1}\,s^{-1}}$ [159].

3.2.4 Boundary conditions

A Dirichlet type time-varying mass flow rate was prescribed in terms of flat velocity profile at the inflow section in the fluid solver. Mass flow rate was determined based on available volumetric flow data from PC-MRI measurements as described in Section 3.2.1 at the

PRE plane and smoothed as shown in Fig 3.1. To emulate downstream pressure, a 3-element windkessel model was prescribed at the distal outlet. Windkessel parameters were calculated such that aortic pressures 61/32 mmHg were retrieved when imposing flow data at the inflow section. The prescribed 3-element windkessel model parameters are $R = 1.8666 \times 10^8$ [kg · m^4 · s^{-1}], $C = 4.2 \times 10^{-9}$ [kg^{-1} · m^4 · s^2], and $Z = 8.7998 \times 10^6$ [kg · m^4 · s^{-1}]. (exhaustive details regarding the steps undertaken to determine these parameters are explained in Section S2). In the structural model, nodes at the proximal and distal end of the aorta were fixed except for movement in the radial direction. External tissue support was disregarded for our simulation as no parameters were available for an ovine geometry. To ensure equilibrium at the no-slip fluid-structure interface, a kinematic condition (equality of velocity) and a dynamic condition (equality of traction) were satisfied.

3.2.5 Solver settings

Blood flow simulations were performed using computational fluid dynamics (CFD) in Ansys Fluent 2021R2 (Ansys Inc, PA, USA) where the set of governing fluid equations for an incompressible fluid were discretized using a finite volume approach with a laminar flow assumption. The governing equations of fluid motion (see Section 2.1.1) were solved in a segregated manner, with pressure and velocity coupled using the PISO algorithm [160]. The convective and pressure terms were spatially discretized using the second-order upwind scheme and second-order standard scheme, respectively, with gradients of solution variables determined using the green-Gauss node approach. As for time integration, the implicit backward Euler method with a time-step of 0.004 seconds was adopted for all sheep models. A threshold for the absolute value of the scaled residuals of the governing fluid equations is chosen to be 10^{-5} to determine convergence of the fluid equations.

Governing equation for tissue (see Section 2.2.1) were discretized using the finite element solver Abaqus Standard 2022 (Simulia, Dassault Systems, USA) in a Lagrangian framework. A first-order accurate unsteady implicit analysis was performed utilizing the same time-step as the fluid solver. User subroutine UMAT was used to describe the material properties of the tissue layers [102] and UTRACLOAD and DLOAD subroutines to apply the non-uniform pressure and traction distributions obtained from the fluid solver in each time step.

A strongly coupled two-way partitioned FSI simulation was performed with communication between the two black box solvers (Fluent and Abaqus) using the in-house coupling tool CoCoNuT [†] [108]. First, the Navier-Stokes equations were solved and based on the obtained stresses at the boundary, the structural problem is solved implicitly. The flow equations on a moving grid were discretized using the Arbitrary Lagrangian-Eulerian method [161]. The interface position was altered based on the displacement obtained through the structural solver and was passed onto an IQN-ILS algorithm [106] (see Section 2.4.2), giving an updated position of the interface displacement and position used by the flow-solver. Multiple iterations within each time step were performed to ensure equilibrium at the interface. A maximum of 20 iterations with a threshold of 10^{-6} for the L2-norm of the residual of interface displacement or 10^{-3} for the ratio of the norm of the last and of the first coupling iteration were used as convergence criterion. Interior fluid nodes were moved based on a spring analogy with a specified spring stiffness when the FSI interface was moved.

Simulations were performed on a 128 core AMD Epyc 7H12 2.6 GHz processor with each cardiac cycle taking approximately 0.5 and 4 hours for CFD and FSI respectively. To ensure independence from transitory effects, results after the fourth cardiac cycle were considered after which there was insignificant peak amplitude variation of pressure downstream.
Theoretical details regarding the coupling model can be found in section 2.4.

3.2.6 WSS metrics

Next to basic metrics such as flow velocity and pressure, WSS metrics on the vessel wall were computed in the fluid solver for fixed and moving grids. To allow for this comparison, the number of triangles on each surface is kept the same at each time step by ensuring no remeshing on the fluid-structure interface or the surrounding fluid regions. Time-averaged wall shear stress ($TAWSS$) and Oscillatory shear index (OSI)[129], Divergence of WSS (DIV_W) [130, 131] and Topological shear variation index (TSVI) [139] were evaluated. Mathematical representation of WSS metrics are provided in Section 2.5. It is important to note that the original theory proposed for WSS divergence was for fixed grids [130]. While this is acceptable for CFD calculations, when the mesh deforms, the equations change. It

[†] https://pyfsi.github.io/coconut/

is important to note that the derivation below is only valid with the primary assumption that the normal component for velocity is insignificant compared to the tangential component similar to the original hypothesis of Mazzi et al.[130, 138].
On the luminal wall , at a generic point p inside a triangular element with vertices i, j, k at time t, the normalized wall shear stress (WSS) components are obtained by interpolating the vertex values in a Cartesian reference frame with barycentric piecewise linear basis functions as shown in Figure 3.3. Here, the notation $(\hat{\tau})$ indicates that the WSS vector has been normalized by its magnitude, i.e., $\hat{\tau} = \tau/\|\tau\|$. The normalized WSS components read

$$\begin{aligned}
\hat{\tau}_x(p,t) &= \frac{\tau_{x,i}(t)}{\|\tau_i(t)\|}B_i(p,t) + \frac{\tau_{x,j}(t)}{\|\tau_j(t)\|}B_j(p,t) + \frac{\tau_{x,k}(t)}{\|\tau_k(t)\|}B_k(p,t),\\
\hat{\tau}_y(p,t) &= \frac{\tau_{y,i}(t)}{\|\tau_i(t)\|}B_i(p,t) + \frac{\tau_{y,j}(t)}{\|\tau_j(t)\|}B_j(p,t) + \frac{\tau_{y,k}(t)}{\|\tau_k(t)\|}B_k(p,t),\\
\hat{\tau}_z(p,t) &= \frac{\tau_{z,i}(t)}{\|\tau_i(t)\|}B_i(p,t) + \frac{\tau_{z,j}(t)}{\|\tau_j(t)\|}B_j(p,t) + \frac{\tau_{z,k}(t)}{\|\tau_k(t)\|}B_k(p,t).
\end{aligned} \tag{3.1}$$

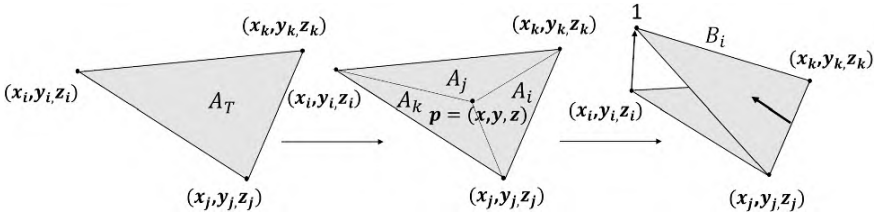

Figure 3.3: Schematic showing the piecewise linear basis functions. Image adapted from Mazzi et al. [130]

The basis functions read:

$$B_i(p,t) = \frac{A_i(p,t)}{A_T(t)}, \quad B_j(p,t) = \frac{A_j(p,t)}{A_T(t)}, \quad B_k(p,t) = \frac{A_k(p,t)}{A_T(t)}, \tag{3.2}$$

where $A_T(t)$ is the area of the triangle at time t and $A_i(p,t), A_j(p,t), A_k(p,t)$ are the subtriangle areas formed by p and the vertices opposite to i, j, k, respectively. Taking the spatial gradient of (3.1), the nodal values are constant with respect to p

and differentiation acts only on the basis functions:

$$\begin{aligned}
\nabla\hat{\tau}_x(p,t) &= \frac{\tau_{x,i}(t)}{\|\tau_i(t)\|}\nabla B_i(p,t) + \frac{\tau_{x,j}(t)}{\|\tau_j(t)\|}\nabla B_j(p,t) + \frac{\tau_{x,k}(t)}{\|\tau_k(t)\|}\nabla B_k(p,t),\\
\nabla\hat{\tau}_y(p,t) &= \frac{\tau_{y,i}(t)}{\|\tau_i(t)\|}\nabla B_i(p,t) + \frac{\tau_{y,j}(t)}{\|\tau_j(t)\|}\nabla B_j(p,t) + \frac{\tau_{y,k}(t)}{\|\tau_k(t)\|}\nabla B_k(p,t),\\
\nabla\hat{\tau}_z(p,t) &= \frac{\tau_{z,i}(t)}{\|\tau_i(t)\|}\nabla B_i(p,t) + \frac{\tau_{z,j}(t)}{\|\tau_j(t)\|}\nabla B_j(p,t) + \frac{\tau_{z,k}(t)}{\|\tau_k(t)\|}\nabla B_k(p,t).
\end{aligned} \tag{3.3}$$

The gradients of the basis function are defined as follows:

$$\begin{aligned}
\nabla B_i(p,t) &= \frac{\vec{n}_T(t)\times\vec{e}_{jk}(t)}{2A_T(t)},\\
\nabla B_j(p,t) &= \frac{\vec{n}_T(t)\times\vec{e}_{ki}(t)}{2A_T(t)},\\
\nabla B_k(p,t) &= \frac{\vec{n}_T(t)\times\vec{e}_{ij}(t)}{2A_T(t)}
\end{aligned} \tag{3.4}$$

Here:

- $\vec{n}_T$ represents a unit normal vector to the mesh triangle face T.
- $\vec{e}_{ij}$, $\vec{e}_{jk}$, and $\vec{e}_{ki}$ represent opposite edges of the triangle with vertices i, j, and k respectively.
- A_T represents the area of the mesh triangle at each instant in the cardiac cycle.

Combining (3.3), (3.4) and integrating over a cardiac cycle yields the cycle-averaged WSS divergence:

$$\frac{1}{\mathcal{T}}\int_0^{\mathcal{T}} \nabla\cdot\hat{\tau}(p,t)\,dt = \frac{1}{\mathcal{T}}\int_0^{\mathcal{T}} \left[\,\nabla\hat{\tau}_x(p,t)\cdot\hat{x}+\nabla\hat{\tau}_y(p,t)\cdot\hat{y}+\nabla\hat{\tau}_z(p,t)\cdot\hat{z}\,\right] dt. \tag{3.5}$$

Similar to Mazzi et al. [130], the cycle-averaged divergence of the normalized WSS vector field, calculated within each triangular face $T_{i,j,k}$, is assigned to the corresponding mesh vertices by averaging over all adjacent faces. For a given vertex ζ, the value of cycle-averaged divergence of the normalized WSS vector is obtained as

$$(\nabla\cdot\hat{\tau})_\zeta = \frac{\sum_{T_{i,j,k}\sim\zeta}\left(\frac{1}{\mathcal{T}}\int_0^{\mathcal{T}}\nabla\cdot\hat{\tau}(p,t)\,dt\right)_{T_{i,j,k}\sim\zeta}}{\#T_{i,j,k}}, \tag{3.6}$$

where $T_{i,j,k} \sim \zeta$ denotes the set of triangular faces sharing the vertex ζ, and $\#T_{i,j,k}$ is the number of such faces. So, once a converged FSI solution is obtained, WSS at the cell center (centroid) can be exported to any visualization tool (Paraview (Kitware Inc,USA) in our case). Here, WSS divergence at any instance and the cycle-averaged value can be calculated at the vertices based on Equation 3.6. Differences between the present approach used and the original formulation is shown in the table below.

Table 3.2: Comparison between the approach used in this thesis and the original Eulerian formulation for WSS skeletons [130].

Aspect	Present approach (moving wall)	Original formulation
Interpolation	Piecewise-linear with time-dependent basis: $\vec{\tau}(p,t) = \sum_{i\in\{i,j,k\}} \vec{\tau}_i(t)\, B_i(p,t)$.	Piecewise-linear with static basis: $\vec{\tau}(p,t) = \sum_{i\in\{i,j,k\}} \vec{\tau}_i(t)\, B_i(p)$.
Basis functions	$B_i(p,t) = A_i(p,t)/A_T(t)$; A_i and A_T vary with t.	$B_i(p) = A_i(p)/A_T$; time-invariant.
Gradient of basis	$\nabla B_i(p,t) = [\,\vec{n}_T(t) \times \vec{e}_{\mathrm{opp},i}(t)\,]/(2A_T(t))$.	$\nabla B_i(p) = [\,\vec{n}_T \times \vec{e}_{\mathrm{opp},i}\,]/(2A_T)$.
Instantaneous divergence	$\nabla\cdot\vec{\tau}(p,t)$ evaluated on the current surface $T(t)$.	$\nabla\cdot\vec{\tau}(p,t)$ evaluated on fixed T.
Divergence	Cycle-averaged divergence of normalized WSS: $\frac{1}{\mathcal{T}}\int_0^{\mathcal{T}} \nabla\cdot\big(\vec{\tau}(p,t)/\|\vec{\tau}(p,t)\|\big)\, dt$.	Divergence of normalized cycle-averaged WSS: $\nabla\cdot\big(\int_0^{\mathcal{T}} \vec{\tau}\, dt \;/\; \|\int_0^{\mathcal{T}} \vec{\tau}\, dt\|\big)$.
TSVI	$\Big\{\frac{1}{\mathcal{T}}\int_0^{\mathcal{T}} \big[\nabla\cdot\big(\vec{\tau}(p,t)/\|\vec{\tau}(p,t)\|\big) - \overline{\nabla\cdot(\vec{\tau}/\|\vec{\tau}\|)}\big]^2\, dt\Big\}^{1/2}$, computed on deforming surfaces $T(t)$ and reported on a representative configuration T.	Same TSVI definition but computed on fixed geometry T using instantaneous normalized WSS fields [142].

Note. By the triangle inequality, $\big\|\int_0^{\mathcal{T}} \vec{\tau}\, dt\big\| \le \int_0^{\mathcal{T}} \|\vec{\tau}\|\, dt$, the magnitude of the time-integrated WSS vector is always smaller than the integrated magnitudes when flow direction varies. Consequently, the divergence of the normalized cycle-averaged WSS vector field, $\nabla\cdot\big(\int_0^{\mathcal{T}} \vec{\tau}\, dt \;/\; \|\int_0^{\mathcal{T}} \vec{\tau}\, dt\|\big)$, is not equivalent to the cycle-averaged divergence of the normalized WSS field, $\frac{1}{\mathcal{T}}\int_0^{\mathcal{T}} \nabla\cdot\big(\vec{\tau}/\|\vec{\tau}\|\big)\, dt$ [127].

3.2.7 WSS metrics : FSI v CFD comparison

A point-by-point analysis was implemented where each nodal point from ϕ_{CFD} is compared with that of ϕ_{FSI} where ϕ represents the obtained WSS metric at each node of triangle surface mesh. To achieve this, results from the last cardiac cycle of the FSI geometry were mapped onto the reference CFD surface mesh. We also split the geometry into proximal, aneurysmal and distal segments, where the WSS metrics were compared at each nodal point. For each sheep model CFD *vs.* FSI pairs were compared in terms of correlation coefficient (r) testing if significant linear relationships emerge with results said to be statistically significant if $p < 0.05$.

The co-localization of surface areas (SAs) of CFD and FSI-based WSS metrics exposed to low or high values was evaluated in terms of the Sorensen-Dice coefficient or similarity index [162] which is given by the formula

$$SI = \frac{2\left|SA_i \cap SA_j\right|}{|SA_i| + \left|SA_j\right|} \tag{3.7}$$

- i refers to the set of WSS metrics obtained from FSI :

$$i = \{\mathrm{TAWSS}_{FSI}, \mathrm{OSI}_{FSI}, \mathrm{TSVI}_{FSI}\}.$$

- j refers to the set of corresponding WSS quantities obtained from CFD:

$$j = \{\mathrm{TAWSS}_{CFD}, \mathrm{OSI}_{CFD}, \mathrm{TSVI}_{CFD}\}.$$

Where, SA is the luminal surface area exposed to WSS quantities for below (for TAWSS) or above (for OSI and TSVI) a given threshold value. Values for SI range from 0 to 1, where 0 represents no spatial overlap and 1 represents complete spatial overlap between the WSS metrics where thresholds of FSI values are chosen to determine SA. The rationale for choosing specific thresholds stems from the study of Mazzi et al. [139] who posit that regions below 20^{th} percentile of TAWSS and regions above 80^{th} percentile of TSVI significantly co-localize with regions of increased wall thickness in carotid arteries. Therefore, for TAWSS, co-localization of TAWSS between FSI and CFD are determined based on surface areas exposed to regions below 10 percentile decrements. For instance, once the TAWSS is obtained for both FSI and CFD and they are mapped onto the same surface mesh as previously mentioned, regions below the 90^{th} percentile of

TAWSS for both models are compared based on surface area and the SI is computed based on Equation 3.7. This process is repeated for 80^{th} percentile and subsequently for 10 percentile decrements with emphasis on regions below the 20^{th} percentile as mentioned by Mazzi et al. [139]. Similarly, for OSI and TSVI, co-localization between FSI and CFD are determined based on surface areas exposed to regions above 10 percentile increments with emphasis on regions exposed to greater than 80th percentile.

3.2.8 Intravascular flow metrics

Primary and secondary vortices were identified using the Q-criterion [163] given by the equation:

$$Q = \frac{1}{2}\left(|\Omega|^2 - |S|^2\right) \tag{3.8}$$

where S is the (symmetric) strain rate tensor, expressed as

$$S_{ij} = \frac{1}{2}\left(\frac{\partial v_i}{\partial x_j} + \frac{\partial v_j}{\partial x_i}\right) \tag{3.9}$$

and Ω is the vorticity or anti-symmetric tensor, expressed as

$$\Omega_{ij} = \frac{1}{2}\left(\frac{\partial v_i}{\partial x_j} - \frac{\partial v_j}{\partial x_i}\right) \tag{3.10}$$

with v_i representing the i-th component of the fluid velocity vector.

3.3 Results

3.3.1 Model performance

PC-MRI flow rate waveform measured inside the autograft immediately after surgery is compared with the last cardiac cycle of the FSI and CFD simulations for Sheep 1 (Figure 3.4). From the comparison it emerges that there is an excellent agreement between measured and simulated flow rate waveforms, with a percentage variation of 3.78% for FSI and 7.23% for CFD in comparison with PC-MRI at peak flow. This indicates a slight overprediction of the systolic flow rate by CFD in comparison to FSI, which is to be expected due to the absence of volume buffering in CFD.

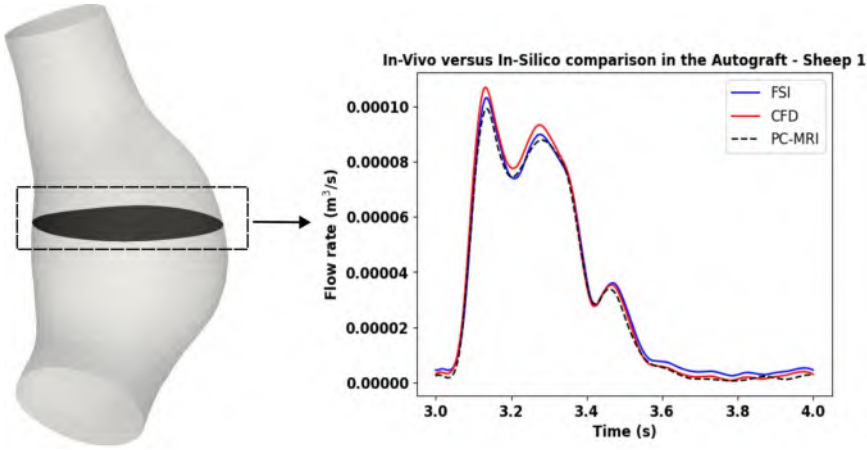

Figure 3.4: Validating our simulations by comparing FSI and CFD for Sheep 1 with PC-MRI data measured inside the pulmonary section.

Looking at the autograft volumetric variations along the cardiac cycle, the results highlight that a Windkessel-like function is exerted in the yet to remodel autografts, with diastolic-to-systolic volume changes of 21.83%, 16.25% and 17.72% for Sheep 1, 2 and 3, respectively as seen in Fig 3.5.

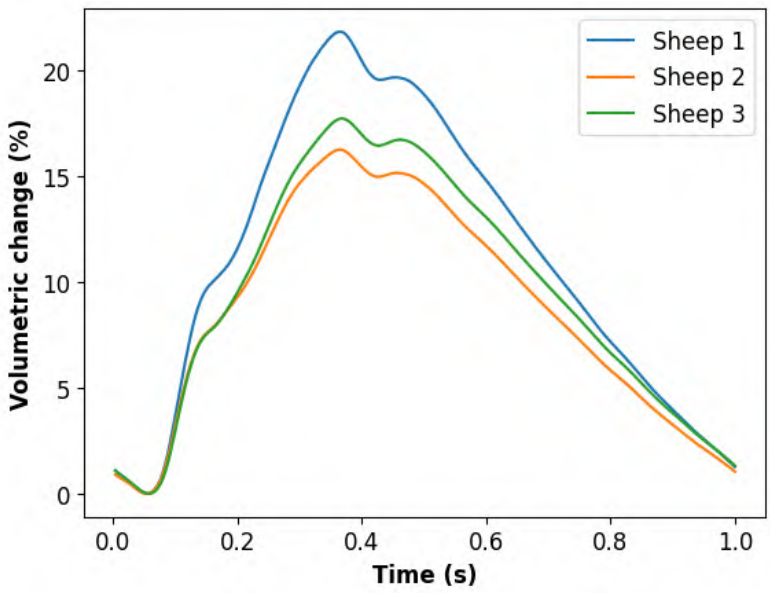

Figure 3.5: Percentual volumetric change across all sheep models throughout the cardiac cycle.

3.3.2 Pulmonary autograft intravascular flow patterns

Hemodynamics in the ovine models is analysed at three instants in our cardiac cycle, namely at peak flow (T1), peak pressure (T2) and during diastole (T3). To do that, the FSI and CFD velocity magnitude contour plots at three distinct cross-sections (proximal, mid and distal) of the autograft are compared. At peak flow T1, no discernible differences emerge between FSI and CFD simulations, in terms of velocity magnitude, as further confirmed from instantaneous streamlines visualizations (Fig 3.6) for Sheep 1 and (Fig 3.7), (Fig 3.8) for Sheep 2 and Sheep 3, respectively). Peak wall motion occurs at T2, where marginally larger recirculation regions characterize the FSI models compared to the corresponding CFD ones, with Dean-like secondary flows in the distal cross-section for Sheep 1 and 2, while for Sheep 3, a large single vortex secondary flow configuration dominates T2. The natural curvature in Sheep 2 and 3 and alignment of the posterior wall towards flow leads to these recirculation regions caused by adverse pressure gradients in the radial direction.

Overall, some changes in flow structures can be observed between paired FSI and CFD models with wall motion having some effect during the diastolic phase. During the diastolic phase, FSI models present a flow separation which is not observed in the rigid wall models and can be ascribed to the anterior wall motion. Iso-surfaces of Q-criterion of vorticity extracted for Q = 100 (being used as a threshold for both modelling approaches), highlight the presence of a primary hairpin-shaped vortex in Sheep 1 (Fig 3.6) and Sheep 2 (Fig 3.7)in the models at T1, with the unsteady shear layer still rolling up in Sheep 3 model (Fig 3.8). Around T2, the vortex impinges on the autograft wall into smaller streamwise and spanwise vortex puffs and slugs which persist at T3 (in particular for Sheep 1 (Fig 3.6)). Spanwise structures are more prevalent in CFD models while in FSI models, streamwise structures prevail.

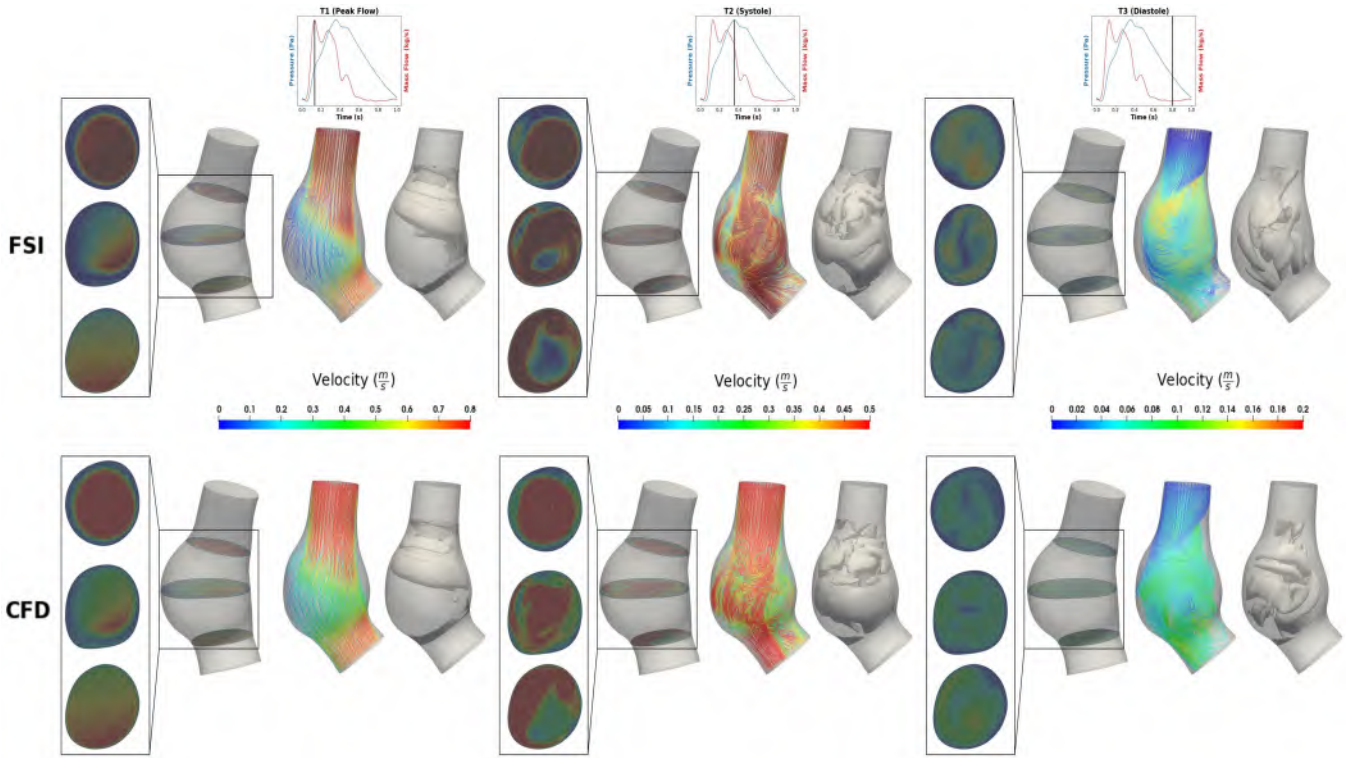

Figure 3.6: Hemodynamical comparison of Sheep 1 at 3 instants (T1, T2 and T3) during the 4^{th} cardiac cycle. The first figure for each time-point shows contour plots of velocity at 3 planes in the autograft with an enhanced version of the contour plots of velocity. The middle figure at each time-point shows velocity streamlines while the third figure at each time-point shows iso-surfaces of Q-criterion of vorticity for Q=100 s^{-1} captured only in the autograft.

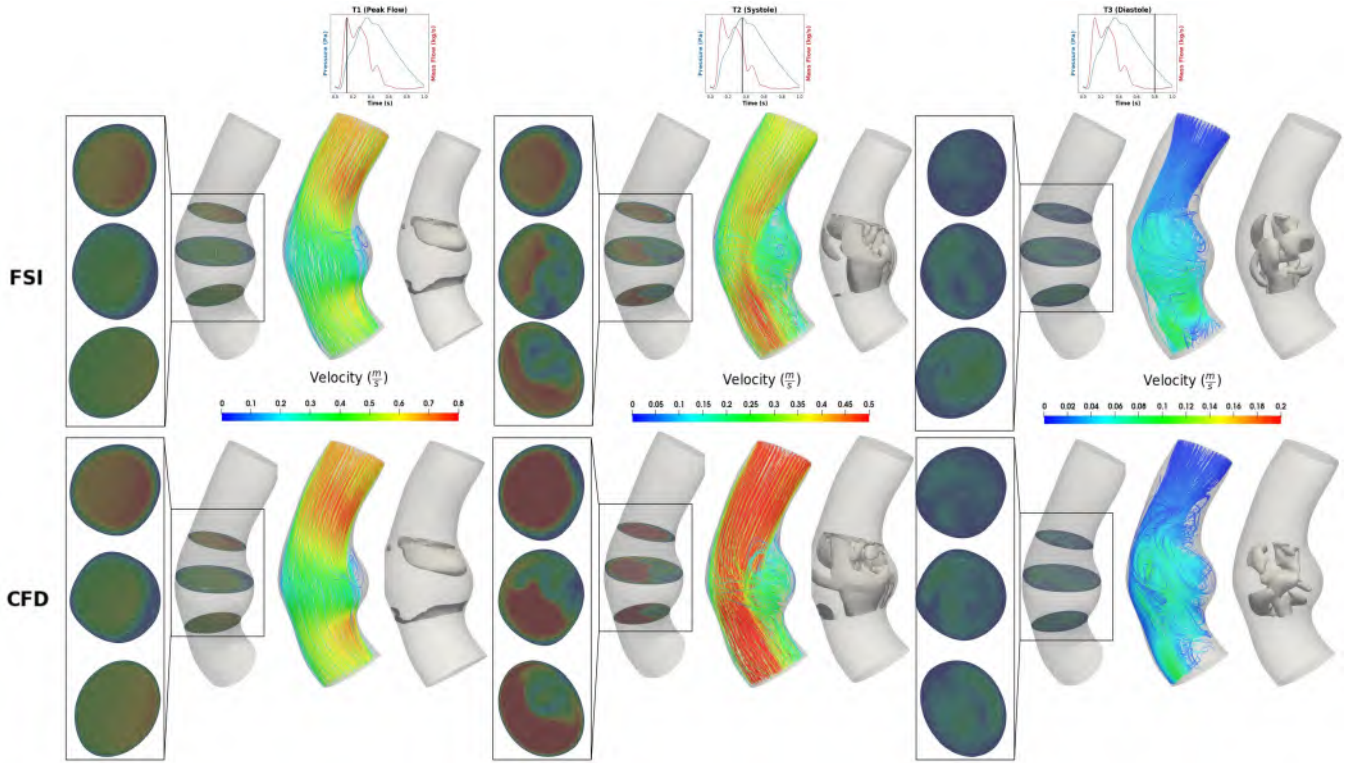

Figure 3.7: Hemodynamical comparison of Sheep 2 at 3 instants (T1, T2 and T3) during the 4^{th} cardiac cycle. The first figure for each time-point shows contour plots of velocity at 3 planes in the autograft with an enhanced version of the contour plots of velocity. The middle figure at each time-point shows velocity streamlines while the third figure at each time-point shows iso-surfaces of Q-criterion of vorticity for Q=100 s^{-1} captured only in the autograft.

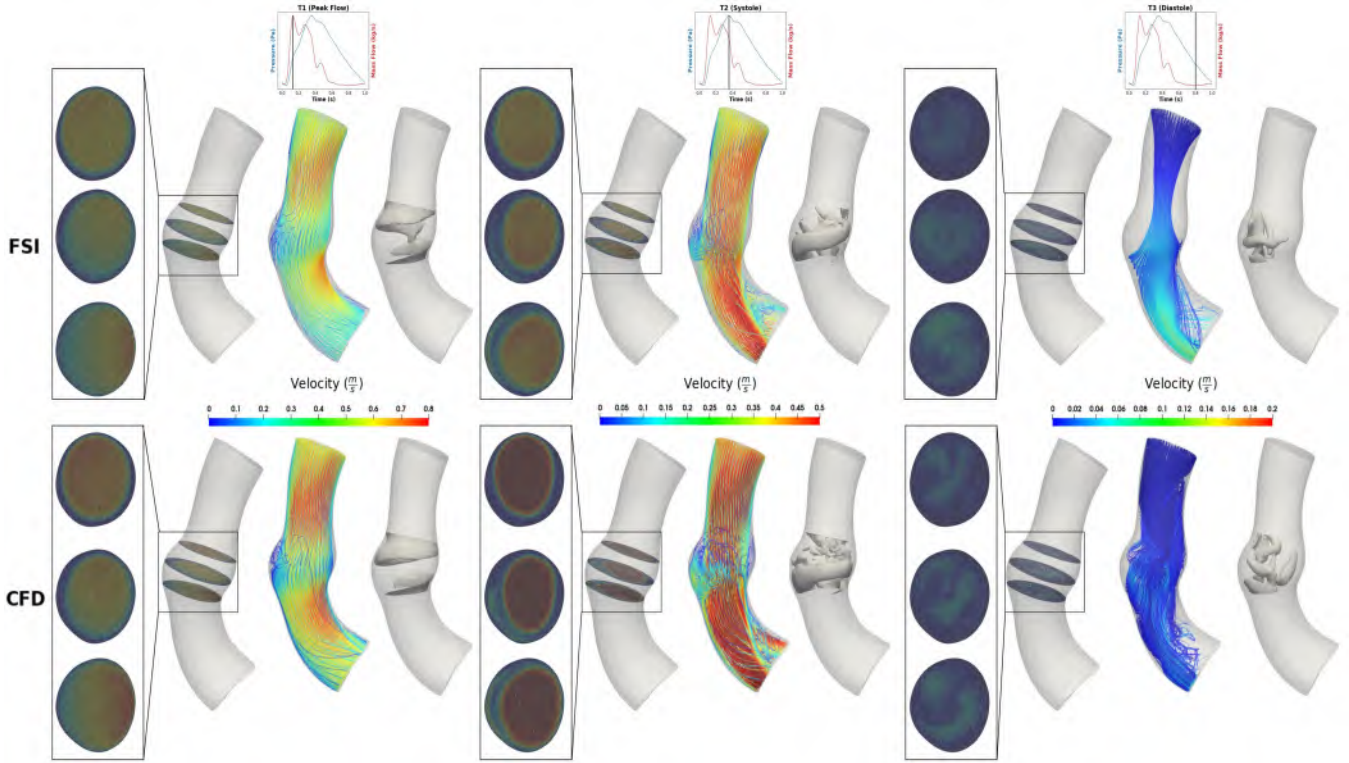

Figure 3.8: Hemodynamical comparison of Sheep 3 at 3 instants (T1, T2 and T3) during the 4^{th} cardiac cycle. The first figure for each time-point shows contour plots of velocity at 3 planes in the autograft with an enhanced version of the contour plots of velocity. The middle figure at each time-point shows velocity streamlines while the third figure at each time-point shows iso-surfaces of Q-criterion of vorticity for Q=100 s^{-1} captured only in the autograft.

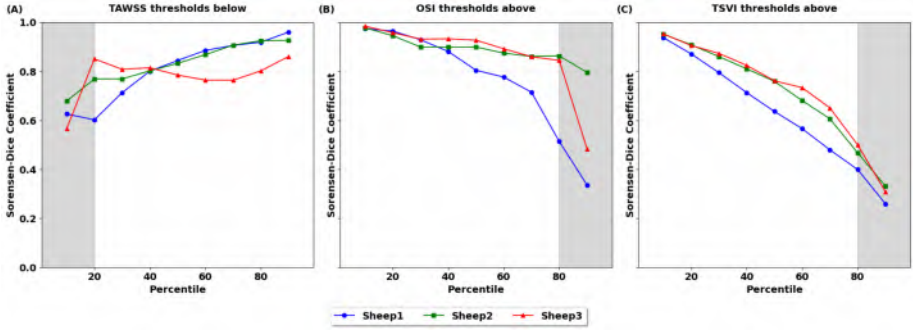

Figure 3.9: SI or Sorensen-Dice coefficient for all WSS metrics with 10 percentile increments of FSI threshold. Thresholds below 10 percentile increments are chosen for (A) TAWSS, while thresholds above 10 percentile increments are chosen for (B) OSI and (C) TSVI. The thresholds of interest are shaded in grey.

3.3.3 Wall shear stress and related metrics

TAWSS

TAWSS maximum values decrease with increase in (D/L) ratio, with $\max\{\text{TAWSS}_{FSI}, \text{TAWSS}_{CFD}\}$ comparable in Sheep 2, while $\max\{\text{TAWSS}_{\text{CFD}}\} > \max\{\text{TAWSS}_{\text{FSI}}\}$in sheep 1 and 3, as observed visually in Fig 3.10 (A,B). Increased values of TAWSS for each sheep are localized towards the inlet and in regions distal to the autograft, where vortices impinge the luminal wall. Extent of co-localization between $\text{TAWSS}_{\text{FSI}}$ and $\text{TAWSS}_{\text{CFD}}$ is evaluated based on SI as observed in 3.9 (A). Regions exposed to low TAWSS which are indicative of potential vascular remodelling [128, 134] indicates moderate to strong co-localization. An instance of this can be observed in Fig. 3.10 (D) where SAs exposed to TAWSS_{20} (below the 20^{th} percentile of the FSI threshold) are in the proximal neck of the autograft, with the highest co-localization of TAWSS_{20} observed for Sheep 2 and 3 (>0.75), while moderate co-localization is observed for Sheep 1 (>0.60). SAs exposed to progressively increased thresholds of WSS indicate marked improvement in spatial overlap for all sheep models, as observed in Fig 3.9 (A).

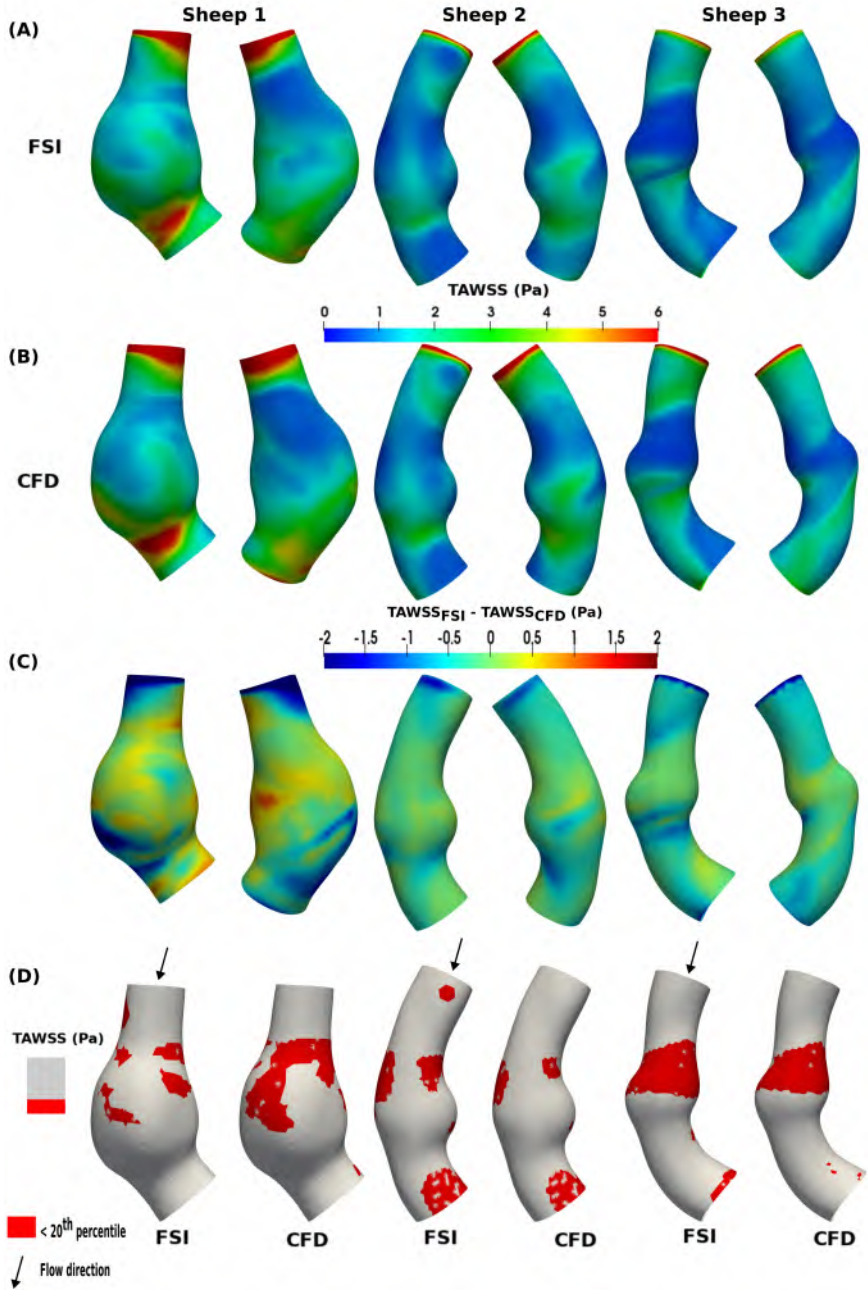

Figure 3.10: Panels (A) and (B) compare TAWSS (Pa) between FSI and CFD qualitatively for 3 ovine models. Panel (C) shows a qualitative difference map of TAWSS between FSI and CFD while panel (D) indicates SAs exposed to values below 20th percentile of TAWSS using FSI values threshold.

The violin plots in Figure 3.11 further confirm the reduction in TAWSS peak with increased (D/L) ratio. A similar behaviour is also observed for TAWSS median values. The correlation coefficient for TAWSS shows a very strong relationship ($r > 0.90$, $p < 0.01$) in all three sheep models observed in Fig 3.11 (B), suggesting that a very strong linear relationship exists between $\mathrm{TAWSS_{FSI}}$ and $\mathrm{TAWSS_{CFD}}$ values at paired nodal points. Focusing only on the autograft portion of the models, the r value (Fig. 3.16 (A)) remains almost unchanged for Sheep 2 and 3 ($r > 0.88$, $p < 0.01$), with the r value following the same trend as the systole/diastole volumetric changes presented previously in Fig 3.5. To further highlight the differences between the modeling techniques and observe values outside the LOA, data are also presented as Bland-Altman plots (Fig 3.11 (C)). Values outside the LOA exist mainly for high TAWSS in all sheep models and are focused mainly at the inlet and distal to the autograft, which is also visually observable in the qualitative difference maps Fig 3.10 (C). A negative bias can be observed for all sheep models, with significant variations occurring below the lower LOA, which might indicate over-prediction from CFD modeling.

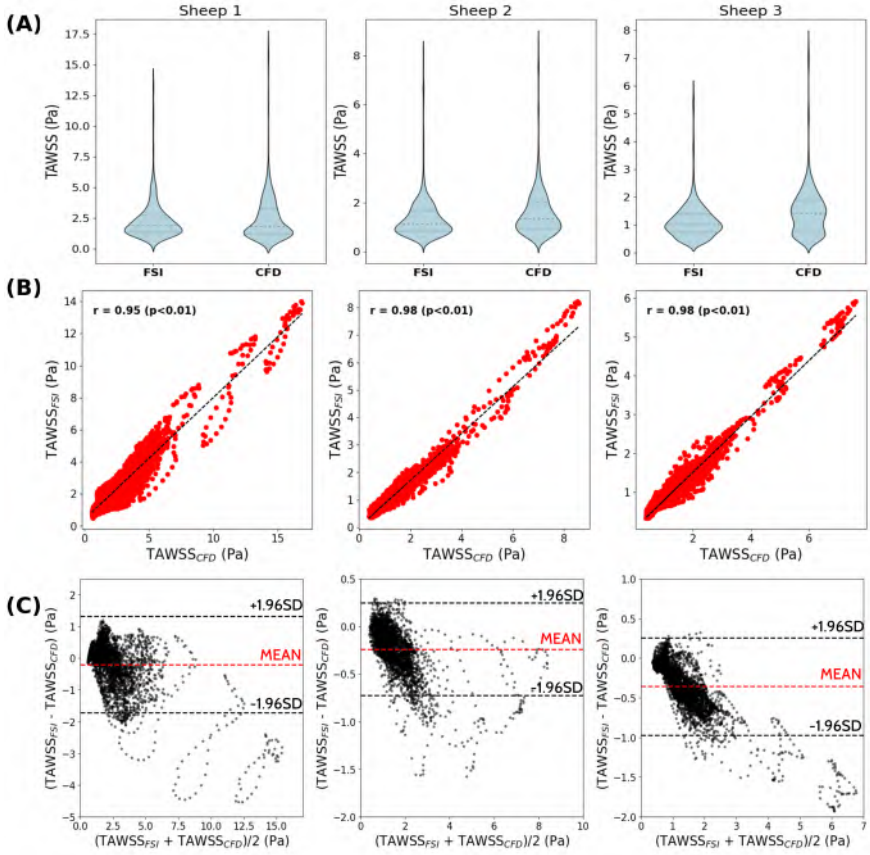

Figure 3.11: Quantitative comparison of TAWSS between FSI and CFD for our 3 ovine models. Results of the 4th cardiac cycle are analysed. Panel (A) compares the violin plots of TAWSS between FSI and CFD for our ovine models with the median and the inter-quartile range. (B) show correlation for each sheep respectively along with the correlation coefficient. (C) represents the Bland-Altmann plot.

OSI

SI luminal surface distribution, displayed in Fig 3.12 (A,B) for all sheep models indicate that high OSI_{FSI} and OSI_{CFD} are located on the autograft surface and on the anterior portion of the distal aorta. Extent of co-localization between OSI_{CFD} and OSI_{FSI}, as assessed using SI (refer Fig 3.9 (B)), demonstrates strong spatial alignment among SAs at low OSI thresholds across all sheep models. When examining SAs exposed to high OSI, indicative of flow reversal, Sheep 2 exhibits notable co-localization between OSI_{CFD} and OSI_{FSI}, while Sheep 1 displays the weakest co-location. This distinction is visually evident in Fig 3.12 (D) where SAs exposed to OSI_{80} (thresholds above the 80th percentile) demonstrate excellent co-localization for Sheep 2 and 3, but only moderate co-localization for Sheep 1. Although Sheep 2 maintains this level of alignment, there is a significant decrease observed for Sheep 3 at OSI_{90} (as shown in Fig 3.9 (B)), underscoring the influence of substantial volumetric changes on flow reversal.

Median values of OSI for each sheep present similar behaviour as TAWSS, with values decreasing with increase in (D/L) ratio for both FSI and CFD as observed in Fig 3.13 (A). Paired FSI and CFD nodal OSI value analysis reveals (Fig 3.13 (B)) that they are linearly correlated ($r = 0.83$, $p < 0.01$ for Sheep 1; $r > 0.9$, $p < 0.01$ for Sheep 2 and Sheep 3). Focusing on the autograft luminal surface only 3.16 (B), the linear relationship between paired OSI_{FSI} and OSI_{CFD} nodal values is still significant ($r = 0.73$, $p < 0.01$ for Sheep 1; $r = 0.83$, $p < 0.01$ and Sheep 2; $r = 0.92$, $p < 0.01$ for Sheep 3) but in general slightly weaker than considering the whole model, suggesting that the large distensibility/volumetric changes modify those near-wall hemodynamic features such as flow reversal that are quantified by OSI. Unlike TAWSS, the Bland-Altmann plot in Fig 3.13 (C) shows negligible bias and values existing outside the LOA can also be visually observed in Fig 3.12 (C).

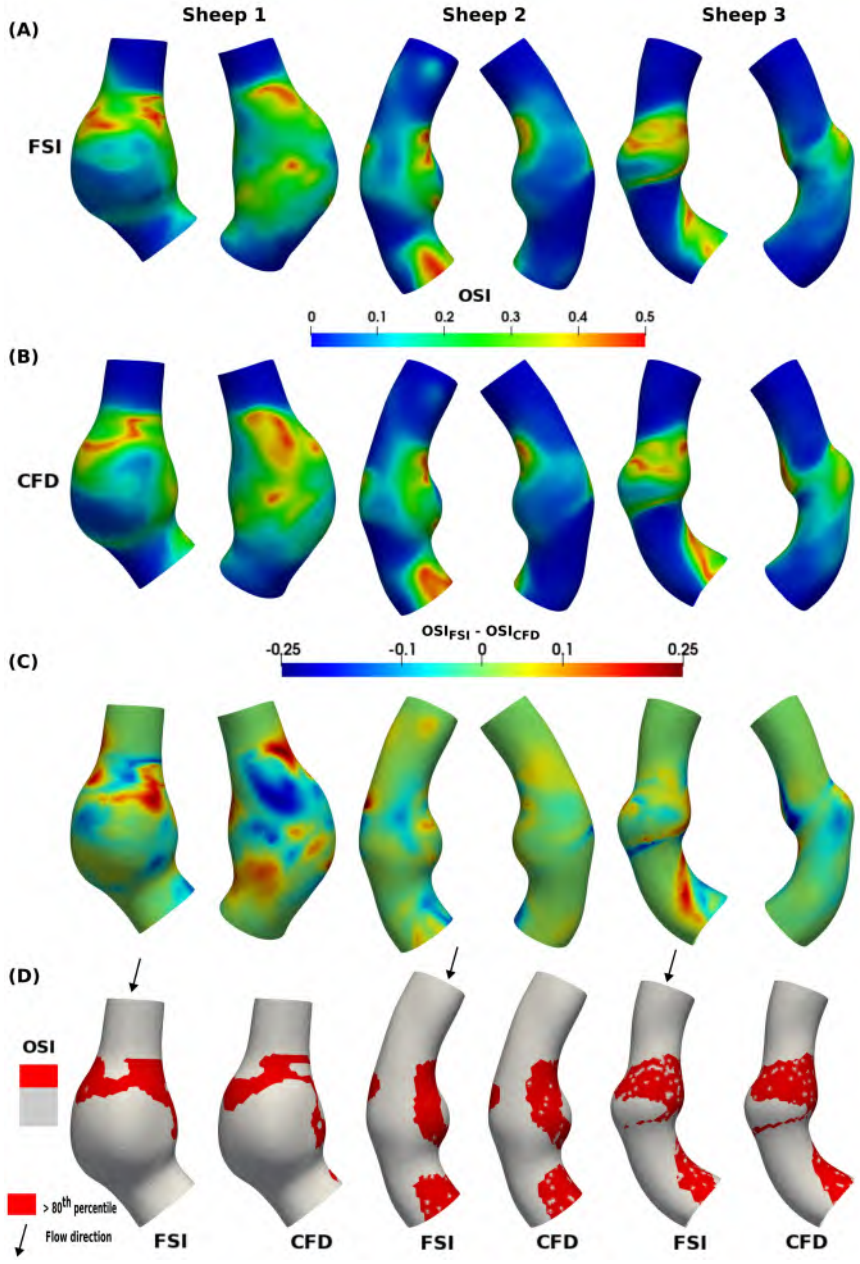

Figure 3.12: Panels (A) and (B) compare OSI between FSI and CFD qualitatively for 3 ovine models. Panel (C) shows a qualitative difference map of TAWSS between FSI and CFD while panel (D) indicates SAs exposed to values below 20^{th} percentile of OSI using FSI values threshold.

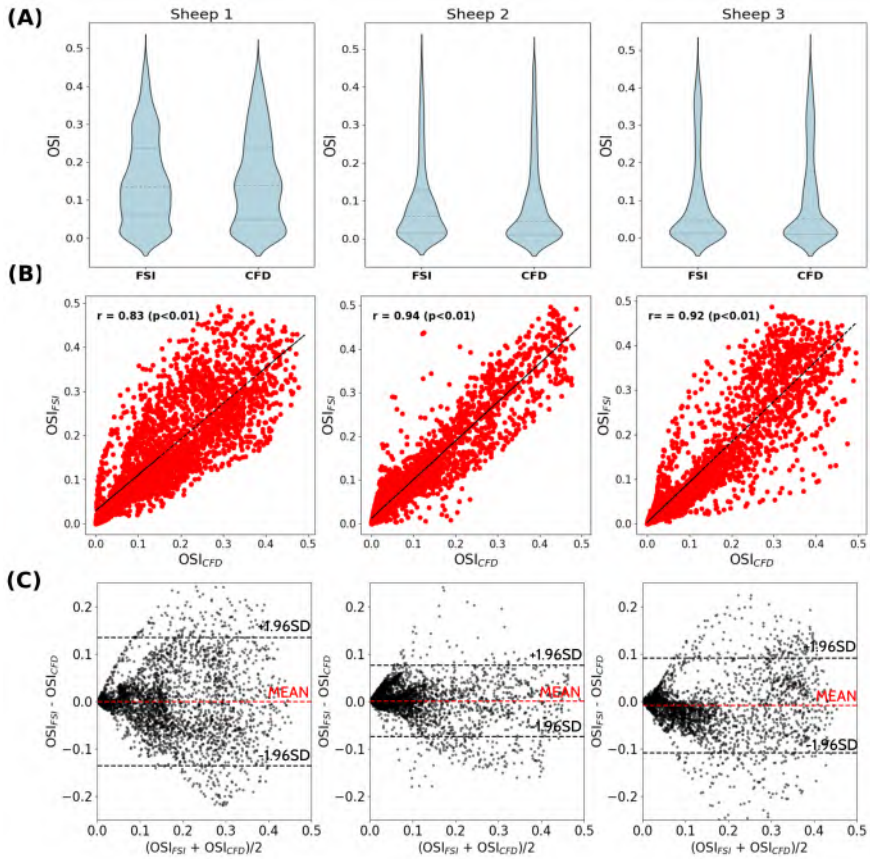

Figure 3.13: Quantitative comparison of TAWSS between FSI and CFD for our 3 ovine models. Results of the 4th cardiac cycle are analysed. Panel (A) compares the violin plots of OSI between FSI and CFD for our ovine models with the median and the inter-quartile range. (B) show correlation for each sheep respectively along with the correlation coefficient. (C) represents the Bland-Altmann plot.

TSVI

Upon visual inspection, the paired comparison between TSVI_{FSI} and TSVI_{CFD} maps suggests a remarkable influence of the autograft large displacements on this WSS topological skeleton feature (Fig 3.14(A,B)). Similar to TAWSS, $\max\{\text{TSVI}_{\text{CFD}}\} > \max\{\text{TSVI}_{\text{FSI}}\}$ for sheep 1 and 3, with $\max\{\text{TSVI}_{\text{CFD}}\} \sim \max\{\text{TSVI}_{\text{FSI}}\}$ for Sheep 2, as evidenced by the violin plots in Fig 3.15(A). Similarly, $\text{Median}(\text{TSVI}_{\text{FSI}}) \sim \text{Median}(\text{TSVI}_{\text{CFD}})$ for sheep 1 and 2, with the median TSVI values decreasing with an increased (D/L) ratio. The extent of co-localization between TSVI_{CFD} and TSVI_{FSI}, as

calculated using SI (see Fig 3.9(C)), demonstrates a consistent decrease in co-localization for SAs exposed to increasing thresholds of TSVI for all sheep models. There is a noticeable lack of spatial overlap observed for sheep exposed to higher TSVI thresholds, such as $TSVI_{80}$, as visually depicted in Fig 3.14(D). This suggests that even for relatively minor volumetric changes (as seen in Sheep 2), there remains a lack of spatial alignment between $TSVI_{CFD}$ and $TSVI_{FSI}$ for SAs exposed to high TSVI thresholds.
Finally, a significant but moderately paired TSVI nodal FSI *vs.* CFD values linear relationship emerged ($r < 0.7$, $p < 0.01$) observed in Fig 3.15(B) with the 'r' value decreasing with increased volumetric change, showing similar trends to TAWSS and OSI, which is further highlighted by observing just the autograft portion 3.16(C). Similar to OSI, the Bland-Altmann plot in Fig 3.15(C) shows negligible bias for sheep 1 and 2, with a negative bias for Sheep 3. Values existing at either ends of the LOA can be visually observed in Fig 3.14(C). Overall, the Sheep 1 model exhibited the weakest linear relationships for TAWSS, OSI, and TSVI, while Sheep 2 exhibited the strongest.

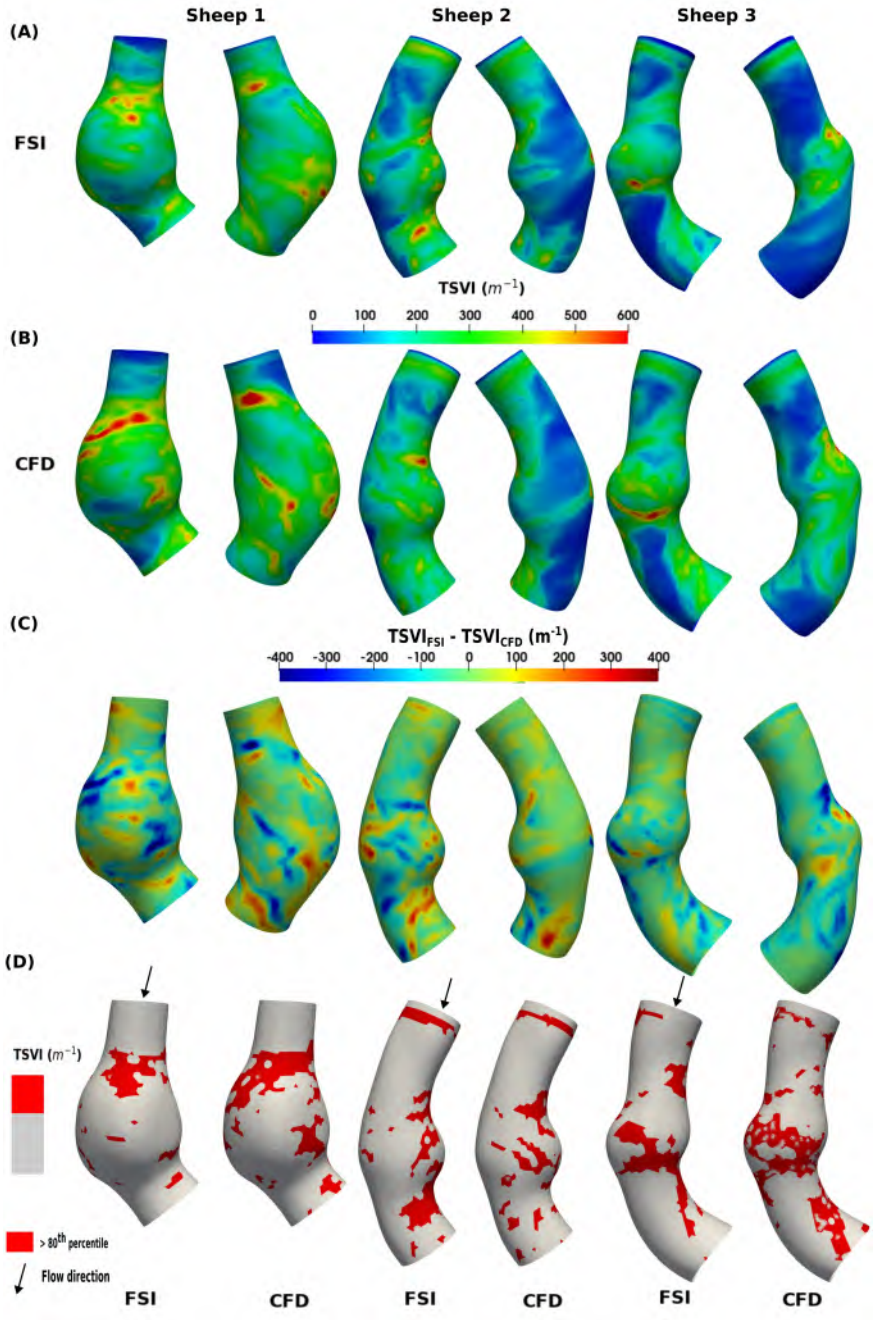

Figure 3.14: Panels (A) and (B) compare OSI between FSI and CFD qualitatively for 3 ovine models. Panel (C) shows a qualitative difference map of TSVI between FSI and CFD while panel (D) indicates SAs exposed to values below 20^{th} percentile of TSVI using FSI values threshold.

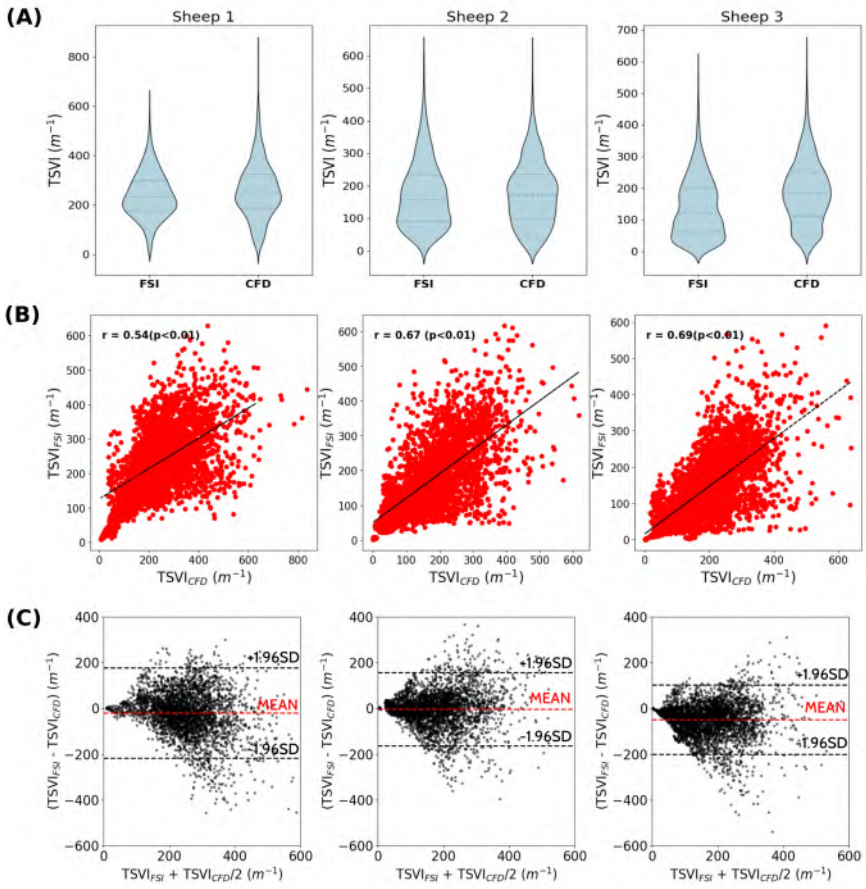

Figure 3.15: Quantitative comparison of TSVI between FSI and CFD for our 3 ovine models. Results of the 4th cardiac cycle are analysed. Panel (A) compares the violin plots of OSI between FSI and CFD for our ovine models with the median and the inter-quartile range. (B) show correlation for each sheep respectively along with the correlation coefficient. (C) represents the Bland-Altmann plot.

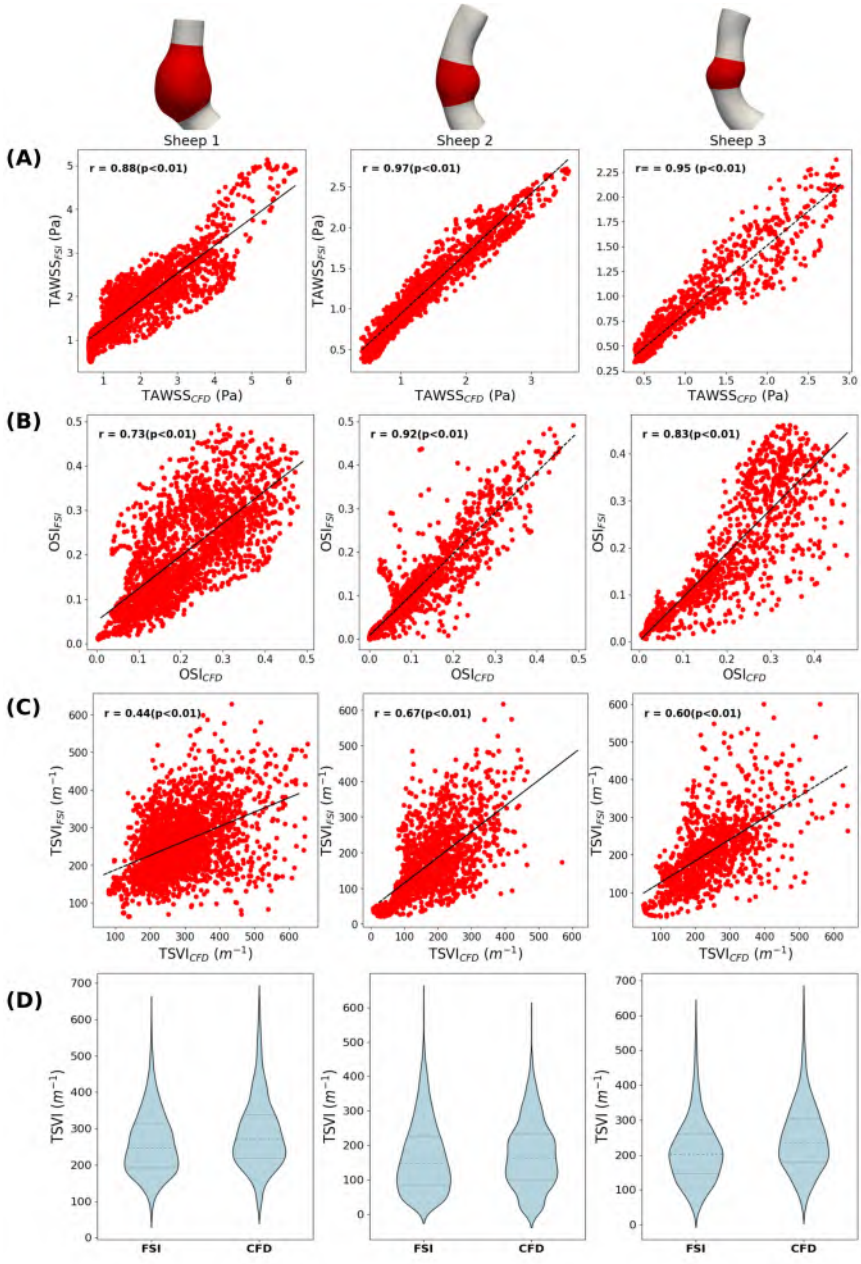

Figure 3.16: Correlation coefficient calculated for all our sheep models (A) TAWSS, (B) OSI, (C) TSVI specifically in the autograft potion and (D) represents violin plots of TSVI ($p < 0.01$)

WSS Divergence

Instantaneous normalized WSS divergence contours are compared for all sheep at the same 3 instants (as described in Section) throughout the 4^{th} cardiac cycle Fig 3.17- Sheep 1, Fig 3.18 - Sheep 2, Fig 3.19- Sheep 3. For ease of comparison, all FSI results are projected onto a CFD surface mesh. While similar WSS expansion and contraction patterns can be observed up to peak systole in FSI *vs.* CFD simulations of each sheep model, when large wall dilation occurs and temporal acceleration exceeds the spatial acceleration, different FSI *vs.* CFD normalized WSS divergence patterns characterize [130] the autograft surface in the three sheep models, with differences extending to the distal aorta in Sheep 2 and Sheep 3 models. Such differences in the FSI *vs.* CFD instantaneous WSS topological skeletons features reflect a varying intravascular hemodynamics, as highlighted by the animation in Movie M1[†].

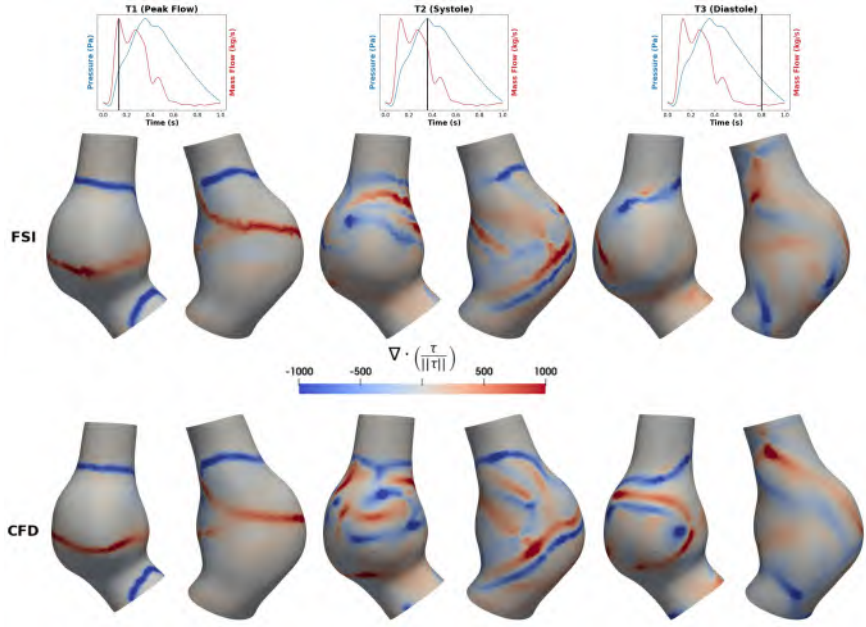

Figure 3.17: Qualitative comparison between FSI and CFD for normalized divergence at 3 time-points during the 4th cardiac cycle for Sheep 1.

[†]Movie M1 can be found in the supplemental section of [164]

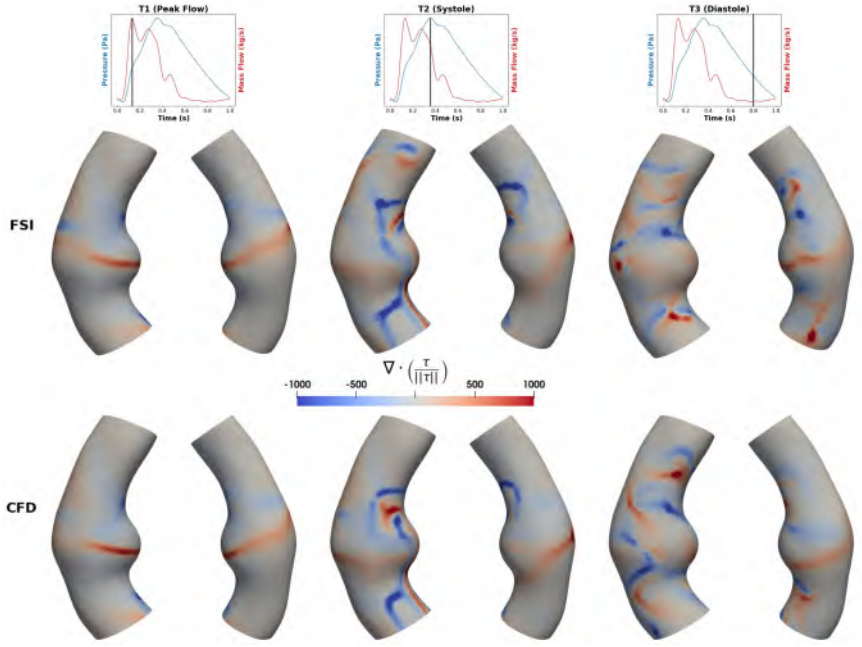

Figure 3.18: Qualitative comparison between FSI and CFD for normalized divergence at 3 time-points during the 4th cardiac cycle for Sheep 2.

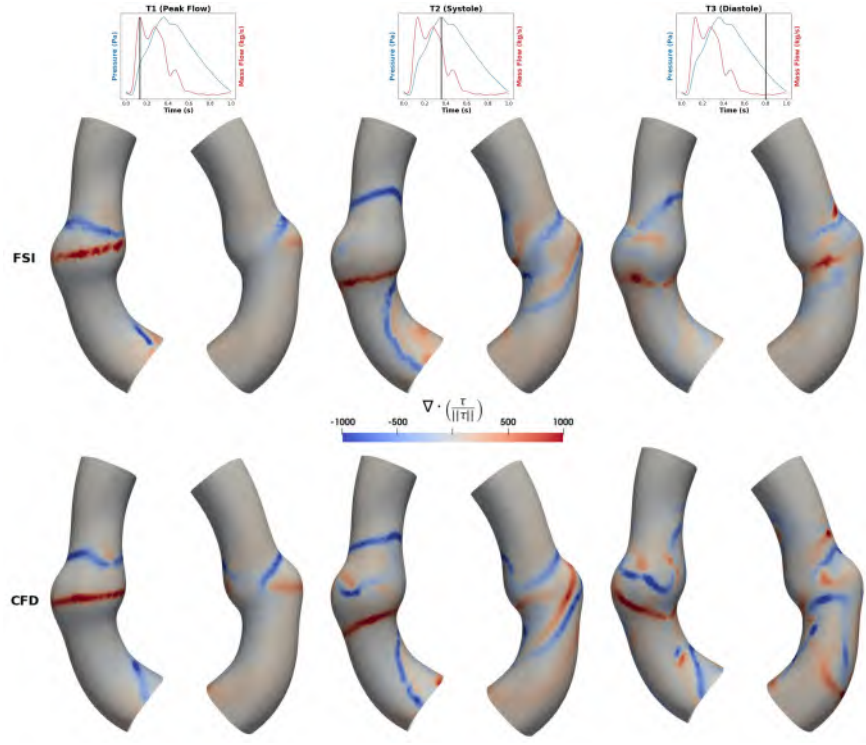

Figure 3.19: Qualitative comparison between FSI and CFD for normalized divergence at 3 time-points during the 4th cardiac cycle for Sheep 3.

3.4 Discussion

3.4.1 Autograft dilatation and canonical WSS metrics

While no known studies have investigated autograft hemodynamics specifically, the systemic pressure after surgery leads to an aneurysm-like geometry in the autograft, particularly the asymmetric-fusiform type [165]. Mendez et al. [166] compared CFD and FSI simulations in ascending aortic aneurysms in terms of peak WSS and observed a good agreement in stiffer and less compliant arteries. Several studies used FSI, CFD or a combination of both [165, 167–169] to qualitatively measure and quantify instantaneous WSS and canonical time-averaged metrics for growth and other biomechanical markers of disease for fusiform like aneurysm types. However, to the best of our knowledge none of the studies quantitatively or statistically has compared FSI and CFD simulations in terms of WSS-based metrics.

In this study, we aim at bridging a still existing gap of knowledge and obtain indications about the modeling techniques to be utilized when pulmonary autografts are implanted. We do so by firstly validating our simulations with in-vivo measured data immediately after surgery, where flow waveforms for Sheep 1 model acquired on an autograft cross-section predicted similar results for FSI and CFD simulations. At peak systole the flow waveforms were expectedly marginally lower in the FSI simulations compared to CFD simulations, a consequence of the volume buffering capacity [170]. Volumetric change/displacement in Sheep 2 model was the lowest, a result attributable to an autograft thickness being twice as large compared the other two sheep models (the other parameters in the material model being comparable).

It is yet unclear how the autograft dilatation affects WSS. While Kumar et al. suggested a non-linear increase/decrease in TAWSS and OSI with changes in maximal diameter [171], Philip et al. observed that increased maximal diameter leads to a decreased TAWSS for straight idealized aneurysmal models [168] and Salmasi et al. [172] posit that angulation in the proximal section has a linear relationship with TAWSS in ascending aortic aneurysms.

Although only based on 3 cases, our results hint that peak and median TAWSS may be more dependent on (D/L) ratio, while ‘r’ value quantifying the relationship between FSI and CFD, more on the volumetric change throughout the cardiac cycle. The strongest relationship between FSI and CFD can be found for Sheep 2 which is in line with work performed by Mendez et al. [166] where they

observed excellent relationship between 2-way FSI and CFD for instantaneous WSS in aneurysms with reduced diameter changes over a cardiac cycle. Overprediction of TAWSS by CFD particularly for higher values as evidenced in the Bland-Altmann plot and qualitative difference maps is in line with literature in murine aortas [170]. Strong correlation between FSI and CFD for TAWSS is in line with previous works [127, 173, 174] where ($r > 0.90$) albeit not in aneurysm geometries.

The spatial distribution of TAWSS and OSI values on the luminal surface of the three sheep models indicated high TAWSS distal to the autograft, low TAWSS on the dome and high OSI on the proximal neck and anterior side of the autograft (in Figures 3.10(D) and 3.12 (D) respectively), are in accordance with imaging work presented previously [175]. High OSI is representative of flow reversal/WSS multidirectionality [176] which is also indicative of flow disturbances. The directions of WSS vector can be observed in Movie M1 and vortex initiation at the proximal neck and recirculation zones anterior in the autograft characterized by high OSI values can be observed in 3.6. Relationships for OSI between FSI and CFD simulations follow trends similar to TAWSS, where larger volume change of the autograft lead to a weakened correlation. Sheep 2 model presents the strongest relationship between FSI and CFD OSI data, again due to the lowest distention as dictated by the highest autograft thickness, with Sheep 3 and Sheep 1 models exhibiting progressively weaker relationships with increased autograft distension capability. Overall strong relationship for all the three sheep models ($r > 0.8$, $p < 0.01$) is in line with previous FSI *vs.* CFD comparison studies [127].

3.4.2 Non-canonical metrics and hemodynamics

Several indicators of flow disturbances have been suggested in recent years to better link flow disturbances to vascular pathophysiology, also in aneurysmal arteries [177]. Among them, the analysis of the WSS topological skeleton is gaining momentum [130, 141, 178]. In particular TSVI quantifies the extent of the variability of the WSS expansion/contraction action that the endothelium faces along the cardiac cycle. Comparable median values are provided by FSI and CFD 3.15 (a) and 3.16 (D) over the simulated geometries, but a less robust linear relation than for TAWSS and OSI emerged between $TSVI_{FSI}$ *vs.* $TSVI_{CFD}$ ($r < 0.7$, $p < 0.01$) (Figure 3.15). The relationship seems to worsen with increased autograft distension capability. These results are in line with work published by Carpenter et al. [127] where relationship between $TSVI_{FSI}$ and $TSVI_{CFD}$ varied

markedly based on degree of stenosis and lesion length for a stenosed right coronary artery. However, the results are in stark contrast to ones published by Calò et al. [174], where an excellent relationship ($r > 0.89$) was observed between moving and rigid walls in the ascending aorta albeit without FSI, but rather a prescribed moving boundary method. To better understand why the agreement between FSI and CFD in terms of TSVI is less strong than TAWSS and OSI, we looked at normalized WSS divergence patterns since TSVI calculation is based on the normalized WSS divergence (see also Movie M1 showing how near wall hemodynamical features and normalized WSS divergence collocate).

Autograft hemodynamics has salient features previously observed in literature with a hairpin like vortex structure formed in each sheep. As flow enters the autograft, the sudden change in geometry causes the unstable shear layer to roll up and form these hairpin-like structures similar to the ones observed by Biasetti et al. [119]. The hairpin vortex impinges the wall towards the distal end of the autograft and breaks into smaller vortices both in streamwise and spanwise directions seen during diastole for all sheep. While there are no major differences in flow features due to wall motion when the temporal acceleration axially dominates the convective acceleration towards the radial direction, some changes can be observed during the diastolic phase when convective acceleration dominates. In a nutshell, flow features between FSI and CFD vary more towards the diastolic phase of the cardiac cycle.

The altered hemodynamics could explain why instantaneous normalized WSS divergence varies between FSI and CFD towards the diastolic phase, as observed in 3.17 despite similar extent of contraction/extension applied on the endothelium (Median ($TSVI_{FSI}$) ~ Median ($TSVI_{CFD}$)), the spatial location of the regions exposed to contraction/expansion varies due to distensibility in the wall and varying hemodynamics close to the proximity of the wall. This altered hemodynamics could explain the moderate relationship between $TSVI_{FSI}$ and $TSVI_{CFD}$.

An important feature to note is that the originally proposed Eulerian description was for rigid wall geometries [130]. Here, the normal component of near wall velocity is considered negligible in comparison to the tangential component. However, it must be noted that the autograft configuration is the most extreme case of extending this theory to moving walls, as for such large displacements, the normal component of near-wall velocity may not be non-negligible.

And as discussed, previous study by Calo et al. [174] show excellent relationship between rigid and moving wall geometries for small displacements. Hence, it is only for larger displacements that non-canonical relationship between the modeling technique worsens due altered hemodynamics near-wall, which in-turn alter the WSS divergence. Further mathematical investigation might be warranted to determine the impact of transient normal components, and also quantify up to what displacements a strong relationship exists for moving and rigid walls.

While the adopted Eulerian approach is effective for identifying fixed points i.e points where the WSS vector locally vanishes, it is inherently limited in its ability to resolve the associated stable and unstable manifolds. These manifolds represent the contraction and expansion directions of the WSS field and typically emanate from fixed points, often extending toward or connecting with other fixed points to form the WSS topological skeleton [131]. However an Eulerian approach can provide approximations of these manifolds [130]. A more suitable strategy for extracting these manifolds is the Lagrangian methodology proposed by Arzani et al. [138, 177], which reconstructs the manifolds through particle-trajectory integration. However, this approach entails substantially greater computational and implementation effort, including trajectory integration, temporal interpolation, and additional post-processing.

Above, we have documented the most prominent differences between FSI and CFD for the investigated metrics. Though we cannot draw strong conclusions due to the small sample size, we observe that vessels where large distensions occur lead to a less satisfactory agreement between FSI and CFD simulations in terms of WSS-based quantities, whereas peak and median values are dependent more on autograft morphology (i.e. (D/L) ratio). Whether or not these differences are important enough to embed FSI in an arterial G&R context is not straightforward to assess. While TAWSS exhibited excellent agreement for all sheep, a less strong but still significant agreement emerged for TSVI irrespective of large volumetric changes. The attention to TSVI is dictated by its already demonstrated physiological significance, with association between high TSVI and wall thickening in coronary [139] and carotid arteries [141], a hallmark of G&R. Keeping in mind our long-term goal of studying G&R of the autograft post-surgery over time, TSVI seems to be an effective biomechanical marker to link mechanical changes over time with near wall disturbed hemodynamics motivating to

a fluid-driven G&R approach. This coupled with the fact that poor spatial overlap exists between $TSVI_{CFD}$ and $TSVI_{FSI}$ for higher thresholds, indicate an FSI based fluid-structure-growth approach may be warranted if TSVI would be used as a driver for G&R in PAs, despite increased computational cost. While strong correlation might indicate CFD based approach can be warranted for canonical metrics based G&R as evidenced by Mousavi et al. [137], moderate spatial overlap for very low TAWSS and high OSI for large volumetric changes indicate that an FSI approach overall should be considered in the context of a fluid-structure-growth framework. Further, altered near-wall hemodynamics who's spatial distribution is also an indicator of growth [136] is better captured using an FSI approach.

3.4.3 Potential applications

The discussion has qualitatively and quantitatively examined the behavior of WSS metrics and altered hemodynamics on PA, but the potential applications of said findings need to be elucidated. This work fits within the context of developing a generic (multi-scale) arterial fluid-structure-growth framework to assist cardiac and vascular surgeons in assessing and anticipating the acute and long term impact of (non-)surgical interventions. This may especially be pertinent in young patients, where a solid understanding of arterial G&R may avoid re-interventions or solutions with a lifelong negative impact on the cardiovascular structures.

It has been previously emphasized that the spatial distribution of hemodynamic metrics correlates with growth [136] and computational studies have also noted that thickness distribution during growth and remodeling (G&R) is spatially heterogeneous [137, 179]. Our observations from Figures 3.10, 3.12 and 3.14 illustrate a spatially heterogeneous distribution of WSS metrics. It is suggested that setting thresholds for WSS metrics could potentially identify regions of thickening in future fluid-driven G&R simulations. This proposition is also supported by findings that associate high TSVI with wall thickening in coronary arteries and carotid arteries in computational and experimental studies. Though the rationale for choosing these metrics stems from them being effective biomarkers for G&R in aneurysm based configurations, it is important to acknowledge that aortic aneurysms are often stiffer. Therefore, effectiveness of the defined metrics and their correlation can only be conjectured for highly distensible autograft and would need validation through in-vivo data.

What would a potential FSG framework look like?

Vastmans et al. [102] compared two established G&R formulations (kinematic growth and the constrained-mixture model) to evaluate remodeling behaviour of the pulmonary autograft. While highly informative, their study was driven purely from a solid-mechanics perspective and did not account for fluid-derived stimuli. A natural extension is to incorporate the WSS-based metrics evaluated in this chapter and formulate a fluid–solid–growth (FSG) framework, in spirit similar to the small on large approach proposed by Figueroa et al. [8]. Such a framework could proceed as follows:

1. **Determine the homeostatic reference configuration.** Before any fluid simulation is performed, a homeostatic reference state is constructed using the prestressing algorithm employed in our study. This homeostatic configuration then serves as the reference geometry to the subsequent CFD or FSI simulations.

2. **Perform an FSI or CFD simulation under pulsatile loading.** Using the homeostatic reference configuration as the starting point, an FSI simulation is run to obtain physiologic flow fields and wall mechanics. This yields the WSS-based hemodynamic metrics (e.g. TAWSS, OSI, TSVI) as well as the associated structural response. If the fluid and solid meshes are non-conformal, WSS values must be interpolated to the integration points of the solid mesh. In the in-house tool CoCoNuT [108], suitable mappers are available for this purpose.

3. **Update constituent turnover using a WSS-driven G&R law.** Building on the general turnover structure of Vastmans et al., but introducing a WSS dependent stimulus following Rotsaert et al. [180], the collagen density may be updated according to

$$\rho_{\text{coll}}^{n+1} = \begin{cases} -\,k_{\phi,\text{coll}} \dfrac{\phi - \phi_{\text{hom}}}{\phi_{\text{hom}}}\, \rho_{\text{coll}}^{n}, & \phi = \text{TAWSS}, \\ +\,k_{\phi,\text{coll}} \dfrac{\phi - \phi_{\text{hom}}}{\phi_{\text{hom}}}\, \rho_{\text{coll}}^{n}, & \phi \in \{\text{OSI, TSVI}\}, \end{cases} \tag{3.11}$$

   where ρ_{coll} denotes the relative collagen density, n the current G&R time step, and $k_{\phi,\text{coll}}$ a rate constant determining sensitivity to the WSS metric ϕ. The signs reflect established correlations: regions of low TAWSS promote collagen production [181]

and in turn, wall thickening, whereas elevated OSI and TSVI correspond to disturbed flow and are associated with wall thickening [139].

4. **Comparison and validation.** A first assessment is to compare the collagen turnover predicted by the proposed FSG model with that obtained using the purely solid-mechanical framework of Vastmans et al. [102]. If wall-thickness measurements are available, regions of predicted collagen accumulation can be compared against areas exposed to low TAWSS or elevated OSI/TSVI.

3.4.4 Assumptions and limitations

A few assumptions and limitations hamper our study. Firstly, the pressure measurements were taken during surgery when the sheep were anesthetized. This leads to a lower systolic and diastolic pressure used to tune outlet windkessel boundary condition. This could imply that under healthy conditions higher pressures could lead to larger dilation in the autograft, which in turn could impact the hemodynamics and ultimately, WSS metrics. Due to artifacts in the data immediately after surgery in Sheep 2 and 3, flow data from Sheep 1 was used for both Sheep 2 and 3. Due to the computationally intensive simulation time for partitioned FSI simulations [106], we are limited to coarser grids for the structural model. Given that we intend to calculate WSS skeletons, we focused on a finer fluid mesh taking enough care to ensure that the mapping of the interface is accurate despite the coarse structural mesh. A first-order backward Euler scheme was used for temporal discretization. Such schemes may introduce numerical damping, potentially reducing the amplitude of systolic peaks. Since a time-step convergence analysis was not carried out, the extent of such damping remains unknown. Blood is modeled as a Newtonian fluid which stems from lack of sheep viscosity data to fit non-Newtonian models and the fact that non-Newtonian assumptions have insignificant effect on TAWSS as observed in ascending aortic aneurysms [182]. The statistical analysis employed in this work allowed us to quantify the impact of accounting for wall motion on computed WSS metrics. What remains unanswered, however, is the significance of these observed differences in light of many other sources of variability and uncertainty induced by biology and physiology (difference in anatomy, impact of breathing, exercise, motion etc.) and choices relating to boundary conditions, varied material properties, solver settings and so on.

Pertinent follow-up research is to conduct an uncertainty quantification analysis to assess the robustness and reliability of our results, accounting for the aforementioned factors and their potential impact on the overall conclusions that can be drawn from the study. Although PC-MRI data are available, a flat inlet profile is still applied. Prior work shows that realistic 3D inflow profiles can substantially change predicted hemodynamics. Pirola et al. [183] reported pronounced differences in WSS related metrics in the ascending aortic sections when secondary flow were omitted, but these effects were less pronounced in the descending aorta. Armour et al. [78] found that flat profiles particularly affect regions of low WSS, supporting the need to compare against a PC-MRI-derived inlet profile.

In conclusion, the here presented study presents the first of its kind FSI simulation in the pulmonary autograft for 3 different ovine models while also extending the Eulerian approach for WSS skeletons to a moving wall model. The study also comprehensively (qualitative and quantitatively) compared rigid wall and distensible wall model for canonical and non-canonical WSS metrics. The findings aim to further establish WSS topological skeletons as an important metric in vascular biology and mechanobiology. The finding also aims to be a pilot study and steppingstone for a strongly coupled fluid-solid growth framework using WSS metrics as a driving factor to observe remodeling of the pulmonalis 6 months after surgery and compare the results with a structural modeling simulation previously performed [102].

Additional information - Ross procedure

Supplementary S1: Mesh Sensitivity

	Fluid Elements	Boundary layers	Wall triangles
Mesh1	102,114	3	2018
Mesh2	241,425	4	3709
Mesh3	487,590	5	6414
Mesh4	1,119,112	6	10085

Table S1: Summary of mesh details for different configurations

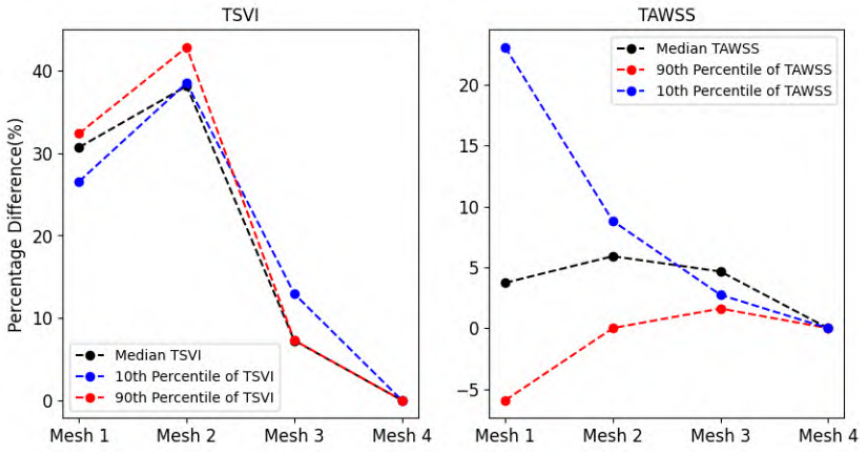

Figure S1: Panel to the left shows how median, 10^{th} and 90^{th} percentile of TSVI varies w.r.t mesh 4 which is the finest. Similarly, panel to the right shows the same for TAWSS.

	Fluid Elements	Boundary triangles	Structural elements
Sheep 1	487,590	6414	3312
Sheep 2	565,931	6747	3024
Sheep 3	683,121	7630	2880

Table S2: Summary of mesh details for different configurations

Supplementary S2: Calculating WK parameters

The following steps are used to calculate the WK parameters.

Step 1: Firstly, the initial guess of parameters is based on Equation 2.12, where the total resistance (R_{tot}) is calculated as:

$$R_{\text{tot}} = R + Z_c = \frac{\overline{P}}{\overline{Q}},$$

where $\overline{P}$ is obtained from ear pressure measurement during surgery, which was 41 mmHg. The flow rate ($\overline{Q}$) is calculated using the available PC-MRI data. Characteristic impedance (Z) is often 5 to 7%

of the peripheral resistance [80]. Aortic compliance (C) is calculated as:

$$C = \frac{dV}{dP},$$

where $dP = P_{\text{sys}} - P_{\text{dia}}$, which was 62/31 mmHg, and $dV = \int_0^{\mathcal{T}} Q(t)\,dt$, which is calculated by the area under the curve of the flow profile, where T is the time corresponding to the systolic peak.

Step 2: Pressure downstream is calculated using Equation 2.11. This ODE is discretized using the first-order backward Euler method to obtain pressure at the next time-advance. Once the initial guess of these parameters is performed, they are plugged into user-defined functions (UDF) of the Finite Volume solver FLUENT (Ansys Inc, PA, USA).

Step 3: These initial guesses are used in our rigid wall simulations as a pressure outlet boundary condition. After periodicity is achieved (4 cardiac cycles), the obtained pressure and flow waveform are exported for analysis. A minimization algorithm like the one proposed by Alimohammadi et al. [184] is utilized:

$$M = \sqrt{(P_{\text{sys}} - 62)^2 + (P_{\text{dia}} - 31)^2}.$$

Mismatch in pressure is tuned for a maximal value of 62 mmHg and a minimum value of 31 mmHg using the Nelder-Mead optimization, which leads to our final WK parameters. CFD and FSI simulations use a first-order backward Euler method to discretize the ODE, obtaining pressure at the subsequent time-advance, which is implemented using a user-defined function (UDF).

CHAPTER 4

Aortic Dissections

*This chapter aims to answer **Objective 2** and discusses how insights into hemodynamics of Type-B aortic dissections can be obtained using fluid-solid interaction. We have provided a brief overview on morphology, treatment strategy of Type-B aortic dissections in Chapter 1, section 1.2.2; the relevant numerical techniques used are discussed in Chapter 2. The chapter is based on* *

4.1 State-of-the-art

Type B aortic dissection (TBAD) is characterized by delamination of the descending thoracic aortic wall, i.e. the intimal and a part of the medial layer. In the presence of one or more tears, this delamination allows blood to flow along its normal pathway via the true lumen (TL) as well as along an alternative channel called the false lumen (FL) separated by a thin dissected membrane called intimal flap (IF). In the initial 14-day acute phase of dissection [58], the elastin-dominant flap remains highly mobile, yielding displacements up to 10 mm [185], resulting in complex, disturbed flow in the FL. During this period, the FL may be fully patent or partially/completely thrombosed [58],

*Balasubramanya.et.al (2025). Hemodynamics in aortic dissections: A fluid-solid interaction study in an idealized dissection model with a false lumen side branch. *Journal of Biomechanics*, 188, 112771. https://doi.org/10.1016/J.JBIOMECH.2025.112771.

with partial patency often indicative of maladaptive growth [60]. A critical but sometimes overlooked factor is the role of major (celiac, mesenteric, renal) and minor (intercostal, lumbar) branches emanating from the FL; as [186, 187] observed, an increased number of side branches (SBs) from the FL promotes complete patency. These SBs receive a substantial portion of cardiac output (anywhere between 7 to 21 %) [11]. Consequently, post-operative interventions for complicated TBAD like TEVAR, which typically involve occlusion of the primary entry tear (PET), can lead to ischemic complications due to reduced perfusion to these branches [188, 189].

Existing in-vivo studies characterize long-term evolution of acute dissections in the presence of SBs [189, 190], but assessing FL hemodynamic metrics such as pressure remains difficult without invasive catheterization [6]. Further, these SBs are small compared to imaging resolution. In such situations, computational models specifically, fluid-structure interaction (FSI) simulations, not only provide insight into FL hemodynamics, but can also provide information on the stresses acting on the vessel wall, hence having potential to be an effective rupture risk prediction tool [172]. Although advanced FSI simulations address acute Type-B dissection dynamics (see Table 4.1 for an overview of the boundary conditions, material characterization and presence of SB's), studies omit the influence of SBs from the FL. Ryzhakov et al.[191] observe sub 1 mm flap displacement when the intimal flap was modeled as a linear elastic material with a Young's modulus of 2 kPa in an idealized geometry. Meanwhile, using an isotropic hyperelastic material to characterize tissue behavior led to sub 3 mm flap displacements in some scenarios by Keramati et al. [192] in a simialr idealized setting. While some studies [93, 193] simulate SBs using FSI, none directly compare cases with and without them. Notably, Chong et al.[194, 195] observed a maximal displacement of 4.5 mm in the range of 5.5 ± 2.6 mm observed in vivo by Yang et al. [185] by using a 3-element windkessel model to describe downstream vasculature. None of the idealized models incorporate pre-stressing or the effect of surrounding tissue. To the best of our knowledge, the first patient specific effort for FSI was from Alimohammadi et al. [196] who incorporated realistic in and outflow boundary conditions, but report a sub 1 mm flap displacement. More recent contributions however have leaned towards physiological reality, with the work of Baumler et al. [93] being the most notable. In this study, the authors utilized a patient specific geometry with realistic inflow, outflow boundary conditions and incorporated residual stresses along with external tissue support. Comparisons were also made for geometries

without pre-stressing and tissue support to highlight the significance. Further, comparisons with different flap stiffness were also reported, and for a flap stiffness of 20 kPa, reported a displacement of 13.4 mm. This model was further extended [197, 198] to incorporate an anisotropic hyperelastic constitutive model (the Holzapfel–Gasser–Ogden formulation (HGO)). Maximum displacements of 3.5 mm was observed which though in line with the range described by Yang et al [185], was lower than 8.7 mm observed in vivo using 4D flow MRI by their group [93, 197]. Only two papers compare hemodynamic metrics in configurations with and without SBs [11, 199], both assuming a rigid wall assumption, hence a stationary flap. Notably, any flap motion, regardless of magnitude, impacts FL pressure and hemodynamics [194, 197].

The rationale for this study stems from an imaging study performed by Logghe et al. [187], where it was observed that the presence of minor side-branches played an important role in determining FL patency. The authors theorized that persistent flow through the major and minor side-branches emanating from the FL affect the patency, with the number of side-branches having a strong corelation with FL patency. This is illustrated in Figure 4.1. While the role of SB long term is observed [186, 187], pressure dynamics in the FL with and without the presence of SB's is unknown.

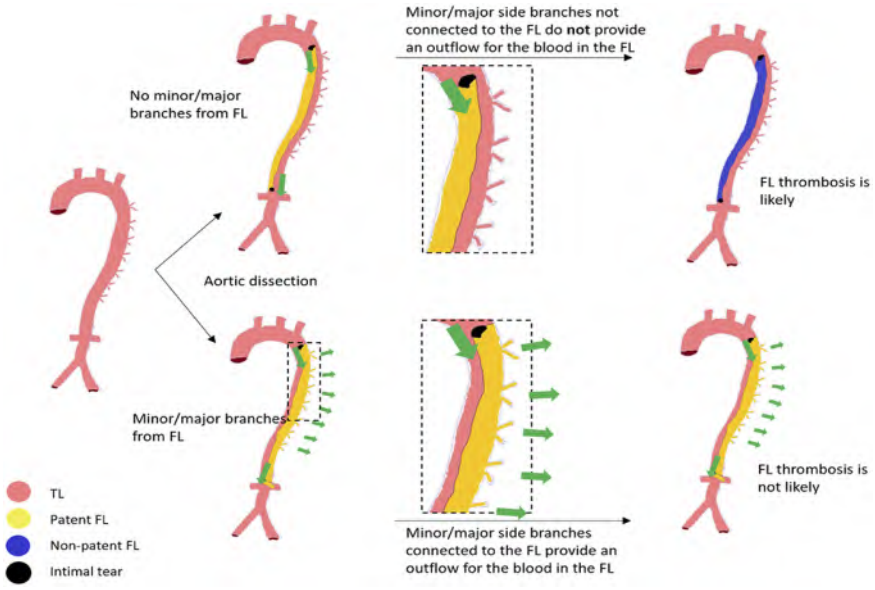

Figure 4.1: Rationale for including side branches as highlighted by Logghe et al.[187] who posit that the presence of major and minor side branches emanating from the FL leads to persistent outflow of blood leading to a higher likelihood of FL patency. Image adapted from [187]

Problem statement

The aim of this study is to develop a strongly coupled FSI model of an acute Type-B aortic dissection to examine the impact of a single SB from true and false lumen, along with the role of a re-entry tear (RET) on key hemodynamic metrics such as FL pressure build-up, cross-luminal pressure difference, and FL inflow/outflow through the primary tear- all critical factors in long term FL growth [6]. To the best of our knowledge, this is the first use of strongly coupled FSI simulations to compare hemodynamics with and without SBs in TBAD.

Table 4.1: A non-exhaustive list of most relevant studies on Type-B aortic dissections incorporating FSI with increasing complexity in material parameters, boundary conditions.

Reference	**Patient specific**	**SBs in FL**	**Inflow profile**	**Constitutive model**	**Residual stresses?**	**External tissue support?**
Chen et al. [200]	No	No	Based on experimental setup	Linear elastic-Isotropic	No	No
Ryzhakov et al. [191]	No	No	Based on experimental setup-Parabolic	Hyperelastic-Isotropic	No	No
Keramati et al. [192, 201]	No	No	Idealized	Hyperelastic–Isotropic	No	No
Chong et al. [194, 195]	No	Yes (but only for tethering)	Literature	Linear elastic-Isotropic	No	No
Kim et al. [193]	No	Yes, but no comparison without SBs.	Steady inflow	Hyperelastic-Isotropic	No	No
Lee et al. [202]	No	No	Steady inflow	Hyperelastic-Isotropic(Comparing Ogden 3^{rd} order and Neo-Hookean)	No	No

Continued on next page

Table 4.1: A non-exhaustive list of most relevant studies on Type-B aortic dissections incorporating FSI with increasing complexity in material parameters, boundary conditions. (Continued)

Deplano Guivier-Curien [203]; Khannous et al. [204]	Yes	No	Literature	Linear elastic-Isotropic	No	No
Qiao et al.[205]	Yes	No	Literature	Linear elastic-Isotropic	No	No
Alimohammadi et al. [196]	Yes	No	Patient-specific	Hyperelastic-Isotropic	No	No
Bäumler et al.[93]	Yes	Yes, but no comparison without SBs.	Patient-specific	Hyperelastic-Isotropic	Yes	Yes
Zimmermann et al. [206]	Yes	No	Patient-specific	Hyperelastic-Isotropic	Yes	Yes
Schussnig et al. [197]	Yes	No	Patient-specific	Comparing different material models. First study with Hyperelastic-Anisotropic HGOmodel	Yes	Yes

4.2 Methodology

4.2.1 Structural model

The geometrically idealized dissected model was generated similar to the approach adopted by Gheysen et al. [92] wherein, a long thick-walled cylindrical tube of $L_{tot} = 240mm$ depicting the descending aorta was initially considered stress free. The dissected membrane, primary entry tear (PET) and RET were modeled as predefined slits as observed in Figure 4.2(a). The opposing slit surfaces were meshed as separate (unconnected) element sets, with non-penetration contact constraints applied throughout the initialization procedure in the finite element solver Abaqus (Dassault Systèmes, France). The geometry consists of 72000 structured hybrid hexahedral elements divided into 6 mesh layers (4 medial and 2 adventitial) in the axial direction. The tissue of the arterial and dissected wall was modeled as a Gasser-Ogden-Holzapfel (GOH) material [88] (see section 2.2.2), the parameters of which were determined based on physiological values of pulse-wave velocity (PWV) [92] and are detailed in Table 4.2. A PWV of 7.233 m/s was chosen to mimic the stiffness corresponding to the median age of dissection patients [207, 208]. To compute the dissected configuration, deposition stretches were first calculated for the healthy cylindrical wall in Matlab (MathWorks Inc., USA) using the prestressing algorithm described in section 2.2.3 with a default elastin and collagen prestretch of 1.1, following the approach of Gheysen et al. [92]. These deposition stretches were then applied to the dissected wall model together with a uniform diastolic pressure of 80 mmHg and the in-vivo diastolic configuration was obtained iteratively. Since the mesh consists of unconnected elements at the tears and between the true and false lumen, the dissected membrane is free to deform during this prestressing step, allowing residual stresses in the flap to be released and resulting in a realistic quasi stress-free configuration. Starting from this prestressed diastolic state, the four configurations used in this study were generated: a case without side branch (NSB, Figure 4.2a); a side branch originating in the false lumen (SB_FL); a false-lumen side branch with only the proximal entry tear present (SB_FL_1T); and a side branch originating in the true lumen (SB_TL, Figure 4.2d).

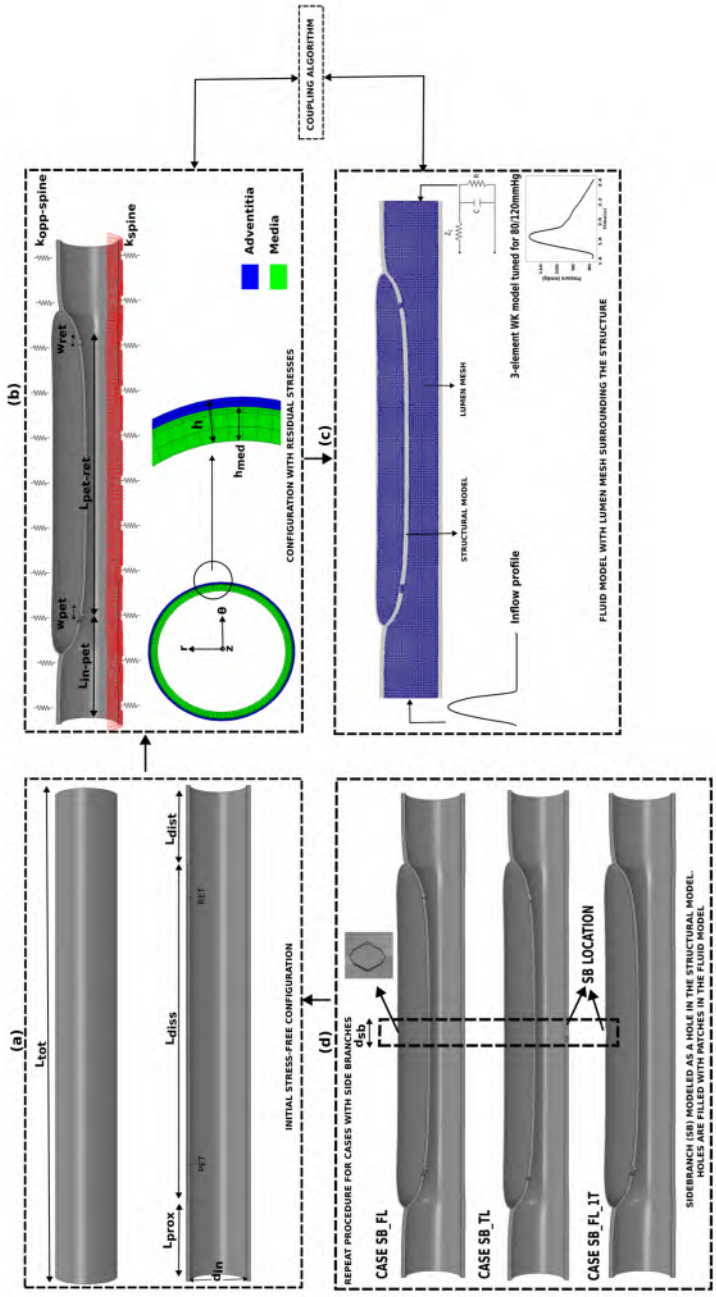

Figure 4.2: Overall methodology adopted to generate the initial configuration with the boundary conditions used. All symbols used in panels (a)-(c) are described in Table 4.3.

Table 4.2: Material parameters for PWV=7.333 m/s at diastolic pressure based on Gheysen et al. [92]

	Location	C_{10} (MPa)	k_1 (MPa)	k_2 (-)	κ (-)	α (rad)
Media	Intimal Flap	0.02000	0.014142	20.350076	0	0
	Aorta	0.02000	0.014142	20.350076	0	0
Adventitia	Aorta	0.0068	0.016546	20.350076	0.1666	1.5708

Table 4.3: Dimensions and parameters used for all cases along with the references from which they are obtained. The description can be visually observed in Fig 4.2.

Symbol	Description	Dimension	Reference(s)
d_{in}	Aortic diameter	27.3 mm	[209, 210]
h	Aortic thickness	1.85 mm	[209, 210]
h_{med}	Medial thickness	0.775.h	[92, 209]
h_{adv}	Adventitial thickness	$h - h_{med}$	[92, 209]
t_{diss}	Dissection thickness	$0.826.h_{med}$	[92, 209]
L_{tot}	Total length	240 mm	-
L_{prox}	Proximal aortic length	40 mm	-
L_{dist}	Distal aortic length	40 mm	-
L_{diss}	Dissection length	160 mm	[211]
L_{in-pet}	Distance from inlet to primary entry tear	55 mm	[211]
$L_{pet-ret}$	Distance between the tears	130 mm	[211]
w_{pet}	Primary entry tear width	21.34 mm	[92]
w_{ret}	Re-entry tear width	14.90 mm	[92]

Continued on next page

Table 4.3: Dimensions and parameters used for all cases along with the references from which they are obtained. The description can be visually observed in Fig 4.2. (Continued)

L_{in-sb}	Distance from inlet to side branch	120 mm	-
d_{sb}	Side branch diameter	≈5 mm	-
k_{spine}	Stiffness of spine	10^7 Pa/m	[94]
$k_{opp-spine}$	Stiffness around the vicinity of spine	10^4 Pa/m	[94]

Other than enabling visceral perfusion, SBs serve as tethers to prevent unrealistic motion[93]. The SB ostium was simplified as an opening for blood evacuation from the FL (see Figure 4.2 (d)), while surrounding tissues and the spine were modeled as viscoelastic supports using Robin boundary conditions. Stiffness values (k) were based on Moireau et al. [94], with higher values in parts of the aortic wall to represent spinal support (Figure 4.2, Table 4.3). Proximal, distal, and side branch nodes in the structural model were constrained to allow only radial movement. The surrounding tissue behavior is modeled using a viscoelastic Robin boundary condition given by the equation:

$$\bar{\bar{\sigma}} \cdot \bar{n} = -k\bar{u_s} - c\frac{d\bar{u_s}}{dt} - p_0\bar{n} \tag{4.1}$$

where k and c represent the viscoelastic response of the surrounding tissue, modeled using springs and dashpots, respectively, and p_0 is the intra-thoracic pressure modeling transient breathing effects [94].

Following the approach of Bäumler et al. [93], the transient components c and p_0 are neglected, considering only the spring stiffness k. Additionally, the lower part of the aortic wall is assigned a higher spring stiffness to account for its proximity to the spine [94], as illustrated in Figure 4.2. External tissue is prescribed as an elastic foundation in the finite element solver Abaqus (Dassault Systemes, RI, USA).
Theoretical details regarding the tissue model can be found in section 2.2.

4.2.2 Fluid model

Once the structural model was generated, the volume inside the lumen was filled with 1079545, 1079773, 1078378 and 1080308 tetrahedral cells for Cases NSB (Figure 4.2 (c)), SB_FL, SB_TL and SB_FL_1T respectively. These mesh configurations were determined based on a comprehensive grid sensitivity analysis performed for Case NSB (Supplementary S1), ensuring that the resolution was sufficient to capture the essential flow dynamics without excessive computational costs.

To analyze hemodynamics, blood flow simulations were performed using computational fluid dynamics (CFD) in Ansys Fluent 2021R2 (Ansys Inc., PA, USA). The governing equations of fluid motion were those of an incompressible Newtonian fluid, discretized using a finite volume approach. Given the peak Reynolds number of 3,791, which remained below the critical turbulence threshold of 4,802 (see section S3), a laminar flow assumption was adopted. The fluid governing equations were solved in a segregated manner within an Arbitrary Lagrangian-Eulerian (ALE) framework discussed in Chapter 2.

The coupling between pressure and velocity fields was handled using the PISO (Pressure Implicit with Splitting of Operators) algorithm [160], ensuring robust and stable convergence of the fluid equations. Spatial discretization of convective terms was performed using a second-order upwind scheme, while the pressure terms were approximated using a second-order standard scheme. Gradients of solution variables were computed using the Green-Gauss node-based approach to enhance accuracy, particularly in regions with high velocity gradients. Temporal integration was performed using an implicit backward Euler method with a fixed time step of 0.0032 seconds, giving 250 time-steps per cardiac cycle. Convergence of the fluid equations was determined by monitoring the scaled residuals, with a threshold of 10^{-5} for all governing equations.

At the inlet, a physiologically realistic mass flow rate was prescribed using a piecewise sinusoidal function [192]:

$$Q(t) = \begin{cases} A \cdot \sin\left(\frac{10\pi t}{3}\right) ; & 0 < t \leq 0.3 \\ \approx 0 \qquad ; & 0.3 < t \leq 0.8 \end{cases} \tag{4.2}$$

where A = 16.099 l/min, resulting in a mean flow of 3.87 l/min distal to the ascending aortic arch [212], which is proximal to the site of dissection initiation.

To mimic downstream vascular impedance, a three-element Windkessel (WK) model was implemented at the outlet. Parameters for the WK model were first determined in a rigid-wall simulation setup for Case NSB (Supplementary section S2), ensuring that the resulting pressures matched physiological systolic/diastolic values of 120/80 mmHg. These parameters were then employed in the FSI simulations, following the methodology described by Balasubramanya et al. [164]. Maintaining total resistance and compliance, the WK parameters for Cases with SB were adjusted to achieve a physiologically relevant 93/7 flow split between the downstream vasculature and the side branches (SB) (see Supplementary section S2). Final obtained WK parameters used in the simulation are detailed in the Table below:

Table 4.4: Windkessel parameters for all cases used in the simulation

Case	Location	R$\left(\frac{\text{Pa·s}}{\text{m}^3}\right)$	C$\left(\frac{\text{m}^3}{\text{Pa}}\right)$	Z $\left(\frac{\text{Pa·s}}{\text{m}^3}\right)$
No SB	Downstream	1.9335×10^8	8.5411×10^{-9}	9.4767×10^6
With SB	Downstream	2.02827×10^8	7.9432×10^{-9}	1.5266×10^7
	SB	2.6947×10^9	5.9788×10^{-10}	2.0283×10^8

To prevent unphysical numerical artifacts at SB locations, the fluid model treated these regions as patches, effectively sealing the openings created in the structural model. This ensured proper enforcement of boundary conditions while maintaining computational stability in the simulations. These enhancements provided a robust and physiologically relevant framework for investigating hemodynamics under varying conditions across the three cases.
Theorectical details regarding the flow model can be found in section 2.1.

4.2.3 Coupled model

A partitioned, strongly coupled, two-way FSI simulation was performed using the in-house tool CoCoNuT [106]. The structural and fluid model were temporally discretized with a time-step of 0.0032 seconds. Convergence was achieved when the L_2 norm of the displacement residual was below 10^{-3} m, with an average of 4 coupling

iterations per time-step required for convergence as described in more detail in Balasubramanya et al. [164] and Chapter 3.

Coupled simulations were performed on an AMD EPYC 7552 "Rome" processor with 96 and 16 cores necessary for fluid and structural model respectively. Each cardiac cycle required around 24 hours computing time with a periodic solution from the 3$^{\text{rd}}$ cardiac cycle being utilized for post-processing. Periodicity was set to be achieved when insignificant variation of the systolic peak ($< 1\%$) was achieved between two cardiac cycles.
Theorectical details regarding coupling models can be found in section 2.4.

4.2.4 Hemodynamic parameters

A number of hemodynamic parameters were evaluated along the length of the model at 11 equidistant planes ($\mathrm{P}_1 - \mathrm{P}_{10}$) spaced 20 mm apart, starting from the inlet (see Figure S2). Key results are presented at three representative planes: distal to PET (P_3), mid-dissection/at the SB (P_6), and proximal to RET (P_9).

Transmural Pressure (TMP)

Transmural pressure (TMP) was defined as the instantaneous pressure difference between the true lumen (TL) and false lumen (FL), expressed as:

$$\mathrm{TMP}(s,t) = P_{\mathrm{TL}}(s,t) - P_{\mathrm{FL}}(s,t) \tag{4.3}$$

where $P_{\mathrm{TL}}(s,t)$ and $P_{\mathrm{FL}}(s,t)$ are the area-averaged instantaneous pressures in the TL and FL, respectively, at a given location s and time t.

The cycle-averaged transmural pressure is given by:

$$\overline{\mathrm{TMP}}(s) = \frac{1}{\mathcal{T}} \int_0^{\mathcal{T}} \left[P_{\mathrm{TL}}(s,t) - P_{\mathrm{FL}}(s,t) \right] dt = \overline{P_{\mathrm{TL}}}(s) - \overline{P_{\mathrm{FL}}}(s) \tag{4.4}$$

where $\overline{P_{\mathrm{TL}}}(s)$ and $\overline{P_{\mathrm{FL}}}(s)$ are the time-averaged pressures in the TL and FL, respectively, at a location s.

False Lumen Ejection Fraction (FLEF)

False lumen ejection fraction (FLEF) is defined as the ratio of the retrograde flow volume (V_R) exiting the FL during the diastolic phase to the anterograde flow volume (V_F) entering the FL during the systolic phase at PET [5].

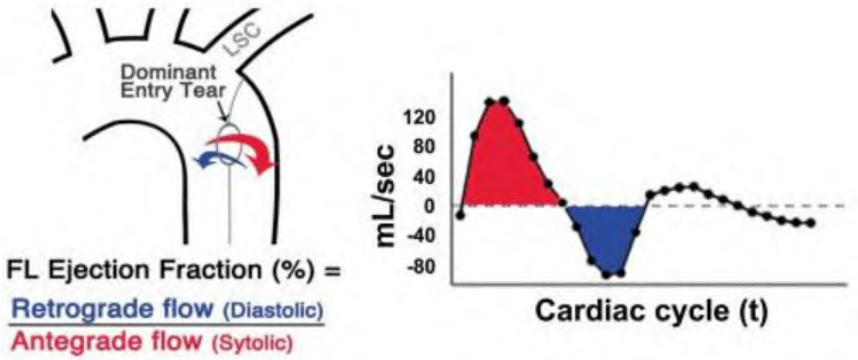

Figure 4.3: False lumen ejection fraction as defined by Burris et al. [5]. Image adapted from [5]

Mathematically, FLEF is given by:

$$\text{FLEF}(\%) = \frac{V_R}{V_F} \tag{4.5}$$

4.3 Results

4.3.1 Pressure

Compared to the case without a SB, cases with a SB show a consistent systolic pressure increase. The magnitude of pressure increase depends on the location of SB, with cases where SB is located in the FL showing higher magnitude ($\approx$ 6 mmHg) compared to cases where SB is in the TL ($\approx$ 3 mmHg) across all planes (Figure 4.4 , supplemental Figure S2). During diastole, blood pressure is slightly lower for cases with a SB, with mean differences limited to 1 mmHg. Waveform analysis reveals a dampened dicrotic notch in the TL from P1 to P11, while in the FL, the notch amplifies from P3 to P9. Volume-averaged pressure differences also show a systolic increase in cases with a SB, with TL pressure consistently exceeding FL pressure by a small margin (Figure 4.5(B), (C)). As shown in Figure 4.5(A), cycle-averaged transmural pressure ($\overline{\text{TMP}}$) remains below 1 mmHg, but positive across all planes, with ($\overline{\text{TMP}} \approx 0$) being observed at P8 for Case NSB called the first balance position [213]. Cases where SB is present in the FL show consistently higher ($\overline{\text{TMP}}$) compared to cases with SB in TL as observed in Figure 4.5 (a).

Figure 4.4: Area-averaged pressure at planes along the longitudinal direction of the dissection during the third cardiac cycle.

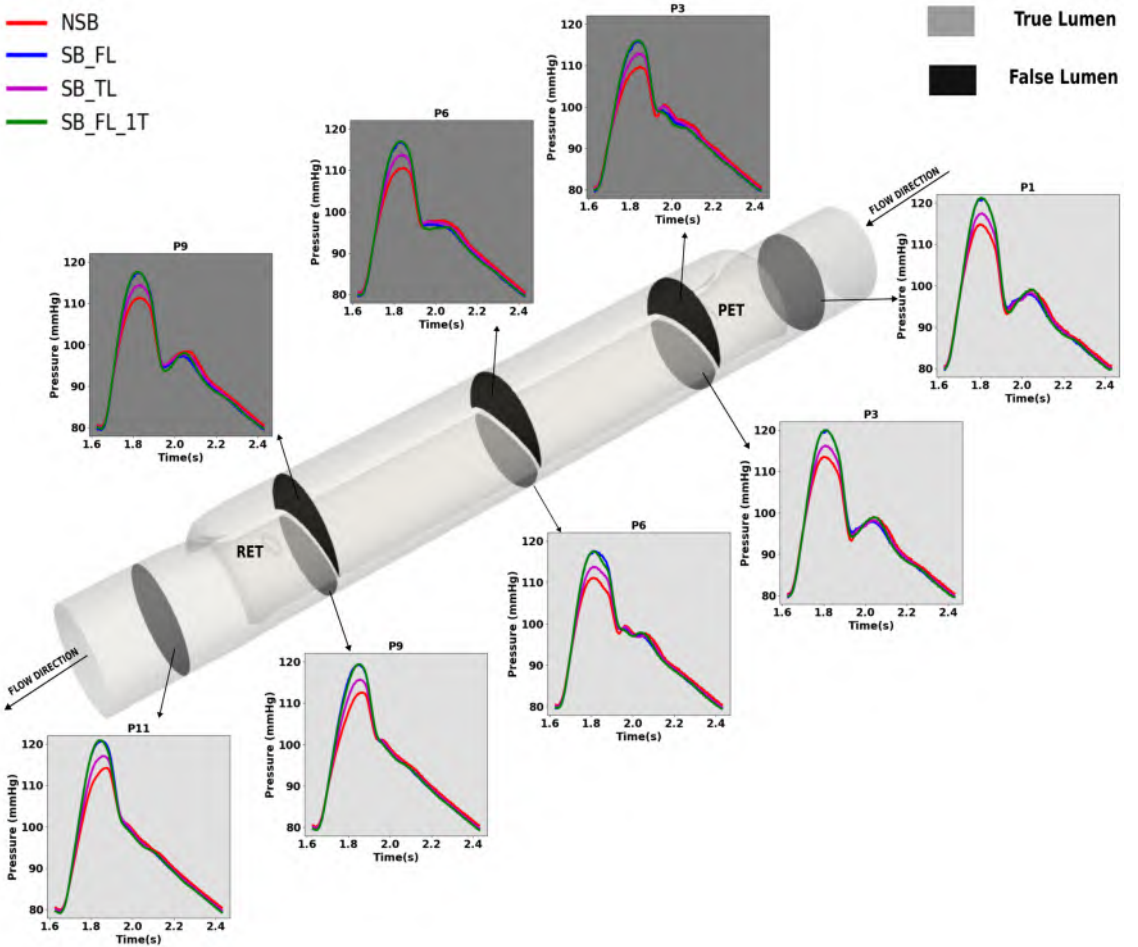

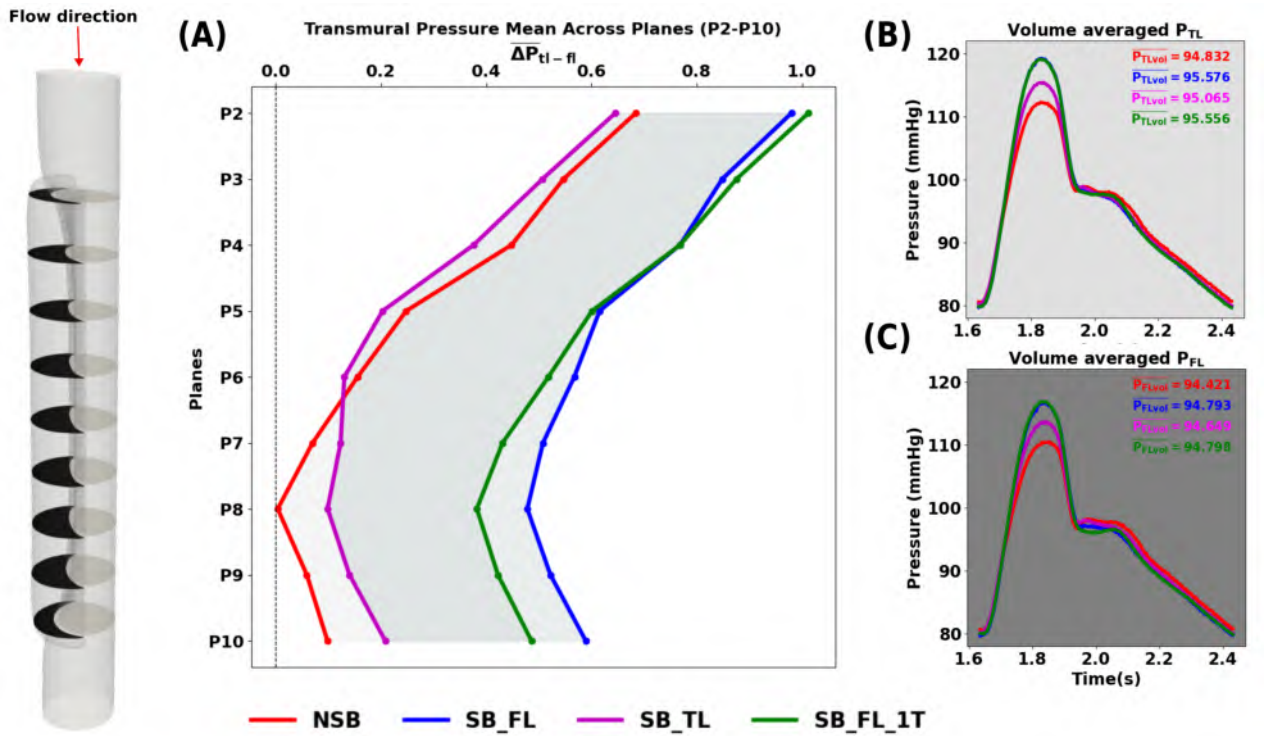

Figure 4.5: Panel (A) showcases cycle-averaged transmural pressure at each plane. Panels (B) and (C) showcase the volume-averaged pressure at the true and false lumen throughout the cardiac cycle.

Instantaneous transmural pressure (TMP) across the flap is similar for all cases, with TMP > 0 until P6, after which a sign change occurs during systolic phase for all cases (Figure 4.6, supplemental Figure S3). Range of TMP reaches up to 10mm Hg for all cases near regions close to the tear at (P2, P3) and (P9,P10). Presence of SB in either true or false lumen has similar effect on TMP as shown in (Figure 4.6, supplemental Figure S3). Case NSB has the highest range of TMP until P6 after which, Case SB_FL_1T has the highest range. Case SB_FL consistently shows the lowest TMP range (Figure 4.6(D)).

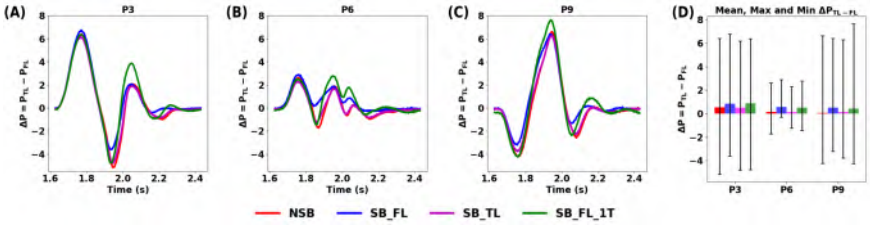

Figure 4.6: Panels (A)-(C) show instantaneous TMP variations during the last cardiac cycle at planes P3, P6 and P9. Panel (D) shows the cycle averaged pressures as a bar graph, with a whisker plot highlighting the range of values at the planes for each case.

4.3.2 Membrane displacement and area

Membrane displacements were recorded at nodes nearest to the planes on the flap (red dots in Figure 4.7) at three instants (T1 = Peak flow, T2 = Start of diastole/Inflection, T3 = Diastolic phase). Positive values indicate outward motion (i.e. TL area increase). The highest net displacement for all cases occurs at P3 (> 5.5 mm) between instants T1 and T2, with Cases NSB and SB_TL showing the largest displacement (8 mm and 7.5mm respectively at P3). Case SB_FL shows the lowest displacement across planes (Figure 4.7). A "see-saw" motion is observed in all cases (Movie M2(a)-(c))†, with positive displacement at systole up to P6, after which flap direction changes (Figure S4), similar to TMP behavior for all cases.

Temporal area changes follow a similar pattern to displacement with a positive area change for TL upto P6 and vice-versa for the FL as shown in Figure Figure 4.8. During diastole, backflow through the entry-tear causes increased TL area in Case SB_FL_1T due to the absence of an exit-tear, reducing FL area locally and increasing distal displacement despite the presence of a SB in the FL.

†Movie M2 (a)-(c) can be found in the supplemental section of Balasubramanya et al. [214]

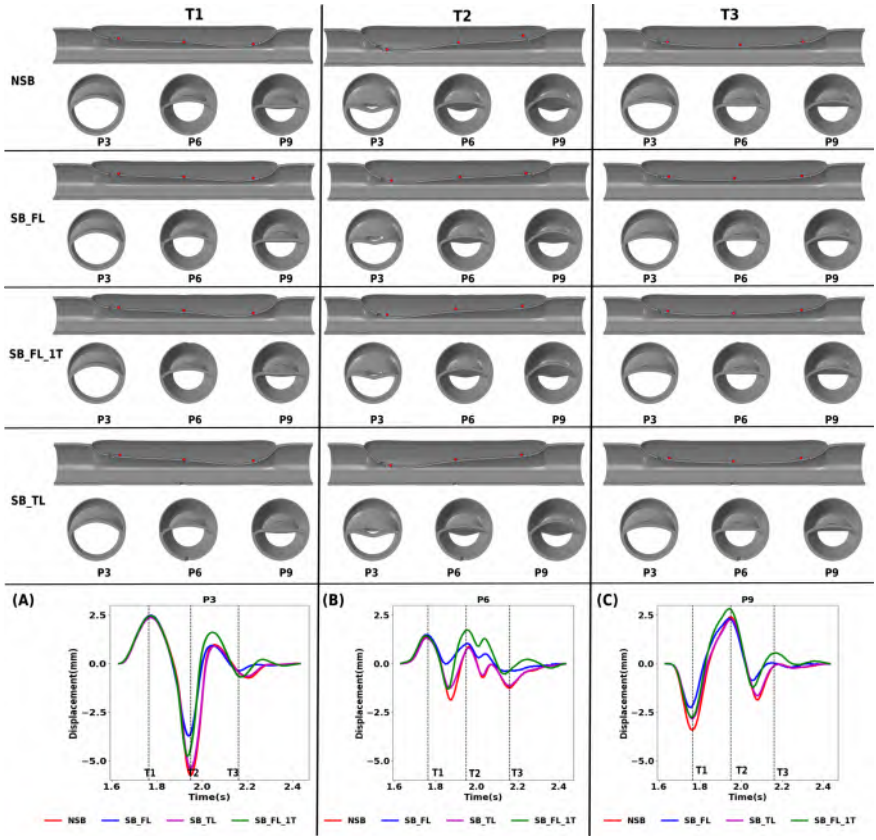

Figure 4.7: Longitudinal and circumferential cross-section of displacement at three unique instants for all cases. Lowest panel (A)–(C) indicates variation of displacement with time at a node point nearest to the planes of interest (P3 to P9) respectively.

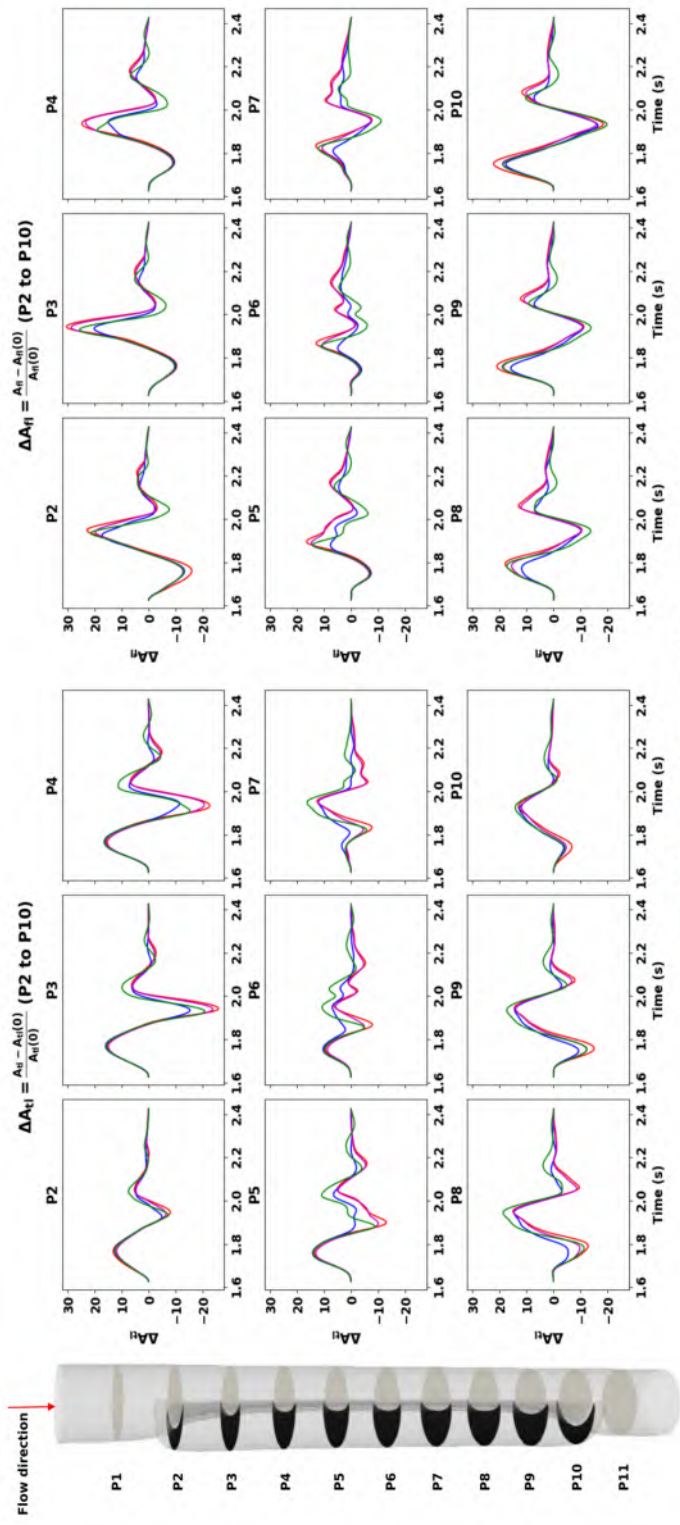

Figure 4.8: Percentual area changes for true and false lumen across all planes of interest.

4.3.3 Flow

Surface line integral convolution (LIC) plots at the same three instants as in the previous section are shown for all cases in Figure 4.9. Inflow is at its peak at T1, with an entry jet flowing through the entry-tear leading to a pair of counter-rotating vortices near the proximal tear for all cases. A simultaneous exit jet exists at the re-entry tear. Conversely at T2, an entry jet can be seen at the re-entry tear when it exists with a simultaneous exit jet at the proximal tear. After the see-saw motion, some residual effects persist as observed in T3 where a secondary entry and exit jet can be seen for all cases. The intensity of this jet is lower for SB_FL due to constant perfusion through the side-branches and non-existent for SB_FL_1T due to lack of re-entry tear. Disturbed flow can be observed for all cases post T3, with flow stasis observed for Case SB_FL_1T downstream to the FL due to lack of re-entry tear. All these effects can be seen in (Movies M3((a)-(c))[‡],

Peak systolic inflow via the entry tear at T1 is very similar for all cases, as is the simultaneous outflow via the re-entry tear. Without an evacuation route for the blood via the SB in the FL, cases NSB and SB_TL displays the highest change in FL volume and subsequently the lowest change in TL volume. Case SB_FL displays the lowest changes in FL volume, but the highest changes in TL volume (Figure 4.10 (E, F)). The location of SB plays an important role in FLEF, with lowered values for cases with SB in the FL (58.5% for SB_FL, 62.1% for SB_FL_1T) compared to cases without (77.5% for NSB,78.1% for SB_TL) as displayed in Figure 4.10(D).

[‡]Movie M3 (a)-(c) can be found in the supplemental section of Balasubramanya et al. [214]

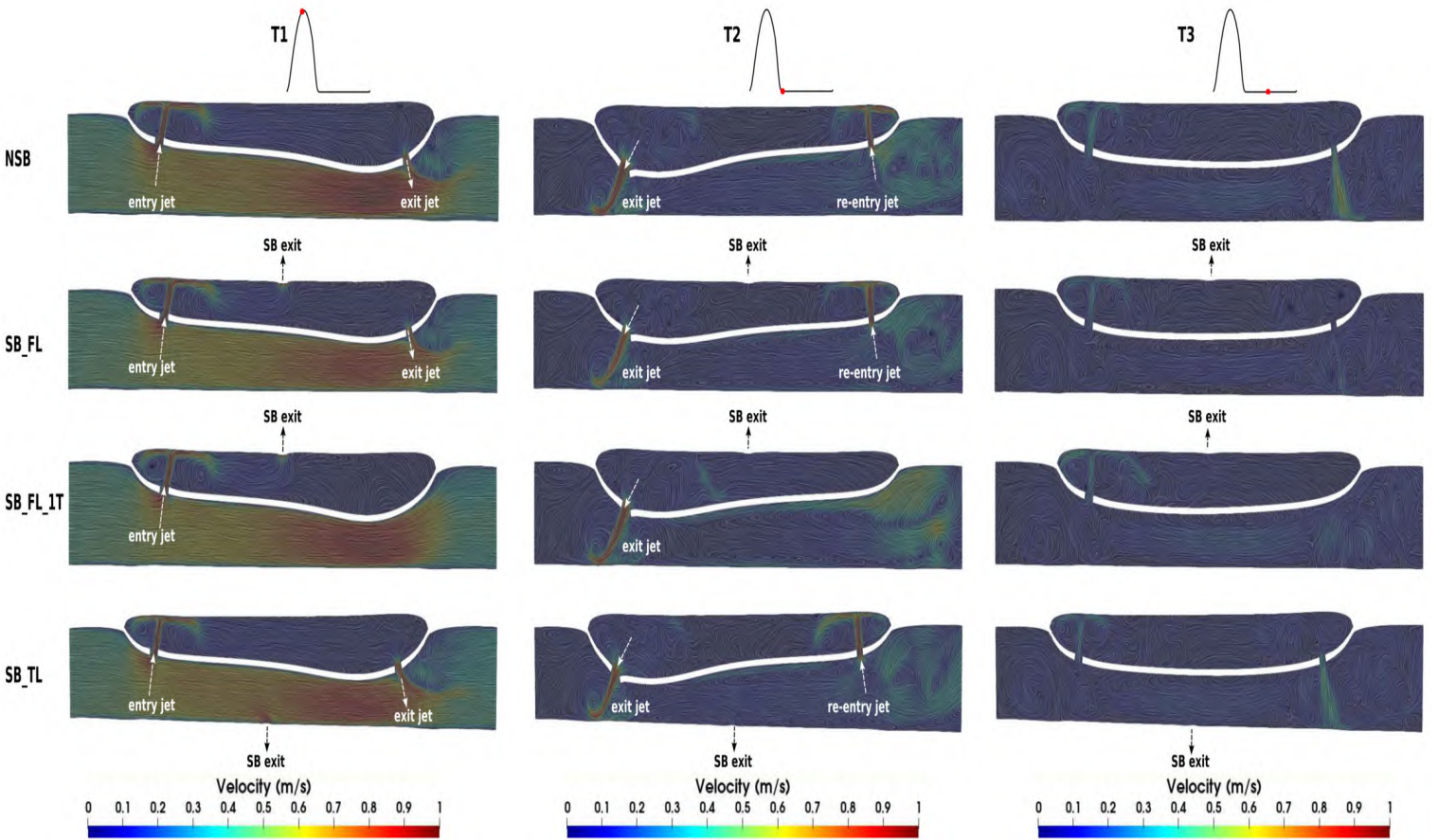

Figure 4.9: Vector plots of velocity sliced longitudinally along the centerline at 2 instants in time for all cases

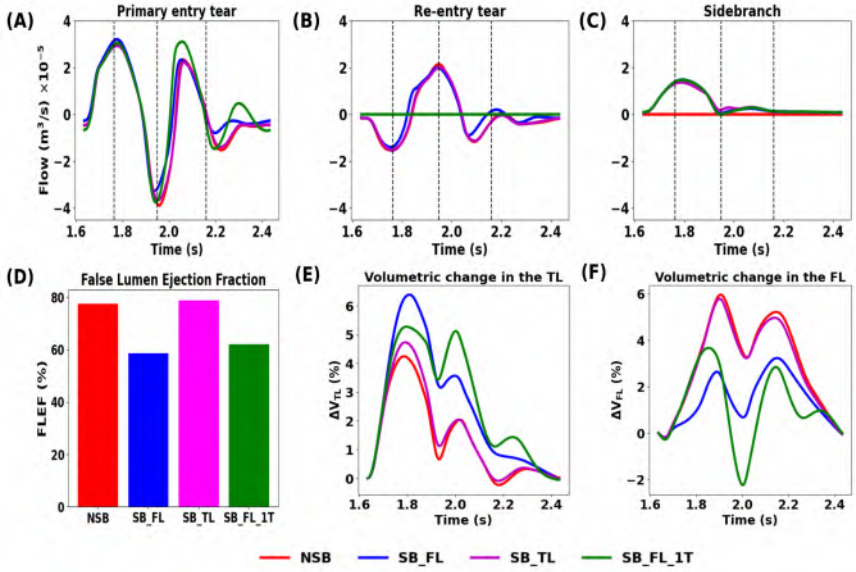

Figure 4.10: Upper panels (A)-(C) show flow rate through the primary entry tear, re-entry tear and side branch respectively. Panel (D) shows the false lumen ejection fraction for all cases. Panels (E) and (F) show the relative volumetric change of the true and false lumen with respect to their initial configuration.

4.4 Discussion

False lumen (FL) pressurization has been shown to correlate with aortic growth due to stresses being applied on the weakened aortic wall [6]. Further, perfusion through side branches (SBs) is also an established predictor of FL growth [189, 190] and patency [187]. Less understood however, is how the presence of SBs emanating from the FL or TL affects pressure dynamics and related metrics. Here, we present the first instance of a strongly coupled fluid-structure interaction (FSI) model both with and without a SB and exit tear to analyze hemodynamics in an idealized setup with advanced boundary conditions. Interesting though non-trivial observations emerge. Since distal windkessel compliance and aortic. As speculated in Logghe et al. [187], we expected the presence of a SB to reduce FL pressure by providing an additional evacuation route for blood from the FL. Surprisingly, simulations with a SB showed higher systolic pressures in both TL and FL (Figure 4.4). However, marginally lower diastolic pressures compensated for this, resulting in mean pressure differences between cases of less than 1 mmHg (Figure 4.5(A)), consistent with our aim to maintain total vascular resistance across scenarios. Cases where the SB was in the FL showed higher systolic pressure amplitude ($\approx$ 6mmHg more than Case NSB) compared to a SB

emanating from the TL (≈3 mmHg more than Case NSB). Since the inflow into the model is constant, the higher systolic pressure should arise from differences in impedance. To investigate overall behavior of the model, we computed the input impedance from pressure and flow at plane P1 (Figure 4.11).

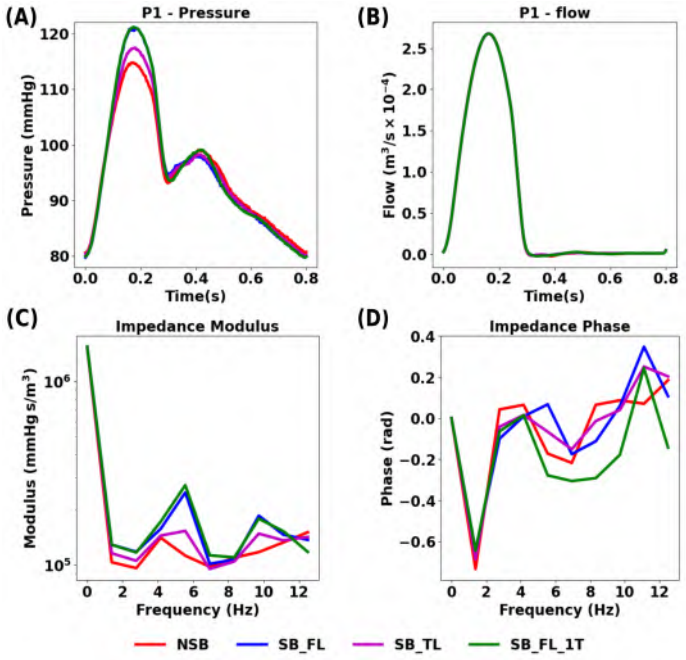

Figure 4.11: Panels (A), (B) show pressure and flow at plane P1. Panels (C) and (D) show modulus and phase of the input impedance calculated at P1

As intended, total resistance was equal across all cases (same impedance modulus at 0 Hz). However, for pulsatile components, Case NSB showed lower impedance modulus across harmonics, indicating higher functional compliance in the dissected aorta without a SB. Since the distal windkessel compliance and aortic material wall parameters were unchanged (supplemental Tables 4.2, 4.4), this increased compliance likely results from altered TL-FL interactions. The input impedance (Z_{in}) differs from the characteristic impedance in the fact that wave reflections are accounted for. It is given by the formula:

$$Z_{in} = \frac{fft(P)}{fft(Q)}$$

Material parameters impact luminal pressures; for instance, stiffer flaps affect TL/FL pressure differences as evidenced by Baumler et

al. [93] who observed 4.5 mmHg proximal systolic TMP decrease as flap stiffness dropped from 800 kPa to 20 kPa. Comparing Case NSB with FSI studies in Table 4.1, our anisotropic model yielded 6 mmHg proximal systolic TMP, compared to the TMP >10 mmHg obtained by [93, 206] for an isotropic model at 800 kPa and 1.2 MPa respectively in a patient-specific setting. Further downstream, instantaneous FL pressures exceeded TL pressures in systole with a similar TMP range (-4/+6 mmHg) as Bäumler et al. [93]. $\overline{\text{TMP}}$ was positive throughout the dissection in our cases, unlike patient-specific distensible [93] and rigid-wall studies [11, 213], where $\overline{\text{TMP}}$ turns negative distally (less than -1 mmHg). The point where shifts sign (i.e.) is called the first balance position [213], with a more distal position indicative of TL remodeling and occurred closest to P8 in Case NSB ($\approx$ 0 mmHg), with no observable position noticed for cases with a SB. We found to be slightly higher (0.2-0.6 mmHg) in presence of the SB in the FL, contrary to Stokes et al. [11], where 18% TL/FL perfusion through side-branches reduced . We speculate that observed differences relate to the much higher FL flow, and especially to the rigid wall setting used in Stokes et al. [11]. Location of SB plays a role as presence of SB in TL has no implications on $\overline{\text{TMP}}$ values, as they are similar to Case NSB until P6 (location of SB) after which $\overline{\text{TMP}}$ increases marginally for Case SB_TL(Figure 4.5(A)). Intuitively, an increased $\overline{\text{TMP}}$ would indicate increased mean TL pressure and reduction in mean FL pressure. This makes sense with the presence of a SB in the FL but is non-trivial to identify in our case due to increased magnitude of both TL and FL pressures as discussed previously.

In acute dissection, the yet to remodel elastin-dominant intimal flap has been known to show significant motion in-vivo (2.5–10 mm) [185] and in-vitro (14.3 mm) [215]. Comparing Case NSB to other FSI studies simulating dissection without SB, only a handful of studies [93, 194, 197] reported flap motion in the in-vivo range. Chong et al. [194] utilized 6.4 MPa as flap stiffness and observed 2.7 mm motion excluding residual stresses in a flap twice as long (319 mm), thinner (0.8mm) in an idealized setup without anisotropy, residual stresses and tissue-support. Bäumler et al. [93] observed that neglecting external tissue-support and residual stresses changes luminal cross-sectional area between 14-27%, highlighting the importance of accurate boundary condition choice. In the same study, the authors observed that reducing the flap stiffness from 800 kPa to 20kPa increased flap motion by 12 mm. In the same patient-specific setup as Bäumler et al. [93], sub-4 mm flap motion was observed considering

anisotropy by Schussnig et al. [197], highlighting the role of not just boundary conditions, but also material modeling choice. Our simulations showed "see-saw" motion (Movies M2(a-c)) similar to Chong et al. [194], with maximal range at the proximal, distal ends and stability mid-plane (P6). Our tubular, straight flap model may favor "see-saw" motion, while in reality the downstream aorta's taper and tortuosity dampen TL/FL changes in cross-section [93]. Beyond material choice, modeling methodology also affects flap mobility wherein our method, using stress-free delamination from an intact artery, shows max displacement at P3 (8 mm), consistent with in-vivo data [185, 198]. Comparatively reduced flap motion is observed for cases with SB in the FL despite similar volume influx during systole through the entry tear, but the presence of a SB reduced perfusion via the tears leading to reduced retrograde flow. This explains the decreased inward flap motion observed at P3 in the presence of a SB.

In the clinical setting, magnetic resonance imaging and 4D flow measurements provide insights into dissection hemodynamics and provide metrics such as FLEF and (relative) pressure differences derived from the flow field [6]. FLEF, proposed as an indicator of FL pressurization [5] has been shown to have a positive correlation with aortic growth [6]. Reduced FLEF suggests lower retrograde diastolic flow compared to systolic anterograde flow, indicative of a more stable hemodynamic environment with lower FL pressures. Marlevi et al. [6] also computed instantaneous relative pressure difference between the inlet and a downstream plane in the FL from the 4D MRI flow field. A strong to moderate negative correlation between maximum relative pressure and aortic growth was observed and it was suggested that aortic dissection characterized by elevated FLEF and lower relative pressure may reflect increased FL pressure [6]. Applied to our simulated cases, we found that the presence of a SB in the FL significantly lowered FLEF (from 78% to 60%), but this was not associated with lower FL pressure. Although the transmural pressure difference between TL and FL somewhat increased with a SB emanating from the FL (Figure 4.5(A)), the absolute pressure levels actually increased in systole. The presence of a SB was found to have marginal effects on relative pressure differences (see Figure 4.12) with highest relative pressure for all cases observed in P3 for the FL and P9 for TL.

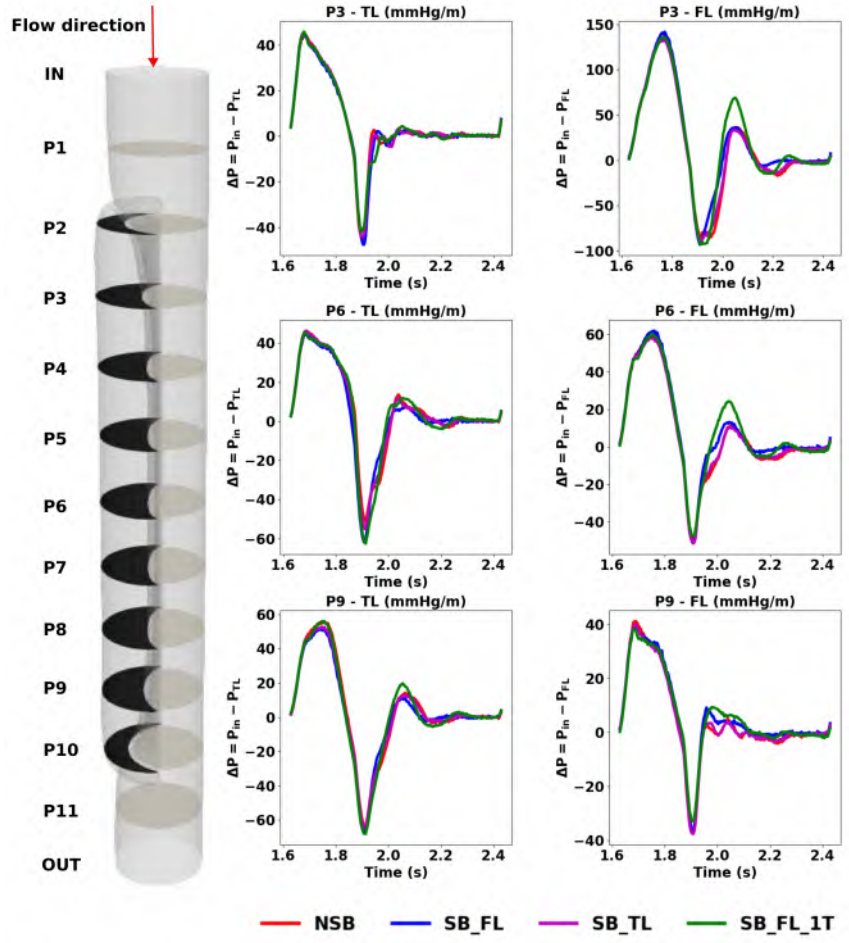

Figure 4.12: Relative pressure computed as difference between Inlet pressure (in) and pressure measured at a plane for both TL and FL per unit length at planes of interest.

A lack of re-entry tear (RET) in acute dissections can result from impaired outflow in a partially patent FL [58, 60]) or as a distal morphological feature [211]. An in-vitro study by Tsai et al. [216] where the distal tear is covered revealed an increased diastolic pressure compared to a case with both tears present. Insignificant diastolic pressure variations (pressure increase 0.15 mmHg) were observed when the re-entry tear was removed SB_FL_1T compared to SB_FL.

Computational models always come with choices for the boundary conditions [78, 217]. We used a fixed inlet mass flow and 3-element Windkessel models at the outlets to regulate pressure and distribute flow over the SB and distal aorta. We opted to keep total vascular

resistance constant for all simulations, which meant that the aortic outlet resistance was different for cases with and without a SB. We also needed to set a characteristic impedance (Z) at each outlet. For example, Stokes et al. [11] selected Z as 5.6% of the total resistance, while Bäumler et al. [93] used 9%. Our choice of 7% aligns with Westerhof et al. [80] who postulated that 'Z' is 5-7% of total resistance in mammals. Changing the value of Z affects the local wave reflection, frequency response and effective buffering achieved by windkessel compliance [218]. Sensitivity to these parameter choices has not been analyzed, as it falls beyond the current study's scope.

Despite incorporating advanced, physiologically relevant boundary conditions (e.g., windkessel outlets, residual tissue stresses, external tissue supports or anisotropic hyperelastic aortic tissue), the aortic dissection model has an idealized, straight geometry. Although the SB size is modeled after branches that could potentially arise from the FL [219], the chosen value does not correspond to any specific artery. Individual variations in location and size exist, so a generic SB size was selected for simplicity, without anatomical accuracy. Our objective was to compare the dynamics with and without a SB emanating from the FL, without focusing on any particular artery. Our current approach also assumes a fixed flow from the heart, which implies that any change in downstream impedance must translate into changes in pressure. In reality, due to dynamic heart-arterial interactions, concomitant changes in pressure and flow may be expected and the upstream boundary condition could incorporate a time-varying elastance model [220]. Future work should aim for more anatomically realistic patient-inspired or patient-specific models, with appropriately tuned boundary conditions, and a much more extended study on the impact of anatomical variations in aortic dissection length and geometry, variations in size, number and location of tears, number of side branches, mechanical properties of the dissected membrane, etc. Furthermore, validation using MRI-compatible 3D printed models of the current and more complex set-ups for in-vitro investigation is warranted. It must be noted that potential fenestration developed while generating SB in the FL (see Movies M2 (b, c) in the supplemental section of [214]) is not taken into consideration. A simulation with this fenestration must be taken into consideration as a future work.

What would a potential FSG framework look like?

Similar to Chapter 3, we postulate what a potential fluid-solid growth framework would look like. As dissections transition from

acute to chronic, they undergo G&R [7]. A constrained mixture approach to simulate this procedure was incorporated in a sliced section of a dissected membrane by Gheysen et al. [7] during a 90-day period. Though non-trivial, a natural first step is to extend this to the entire geometry rather than a slice.

1. **Extend the solid G&R model to the full dissection geometry.** A homeostatic configuration can be obtained using the methodology introduced earlier (Figure 4.2 in Section 4.2), after which the full intimal flap and outer wall can be assigned initial constituent distributions and homeostatic stress states.

2. **Perform a fluid–structure interaction (FSI) simulation under pulsatile loading.** This provides time-resolved wall mechanics (bulk stresses, deformation) and flow fields within the true and false lumen. Importantly, the FSI simulation naturally resolves *false-lumen pressure build-up*, a known driver of chronic dissection behavior, and transmits this pressure elevation into the resulting wall stresses. In contrast to Chapter 3, no stand-alone CFD step is required because the FSI simulation already resolves the hemodynamics.

3. **Extract mechanical stimuli and construct constituent-level stress measures.** The constrained-mixture G&R laws used by Gheysen et al. [7] rely on constituent stresses (e.g. collagen σ_{coll}), not directly on bulk wall stresses. Therefore, bulk stresses from FSI which is already influenced by pulsatile loading and pressure build-up must be projected onto the preferred collagen directions to obtain constituent-level stresses at each G&R time step. The collagen production term can then be updated following the stress-mediated G&R law of Gheysen et al. [7]:

$$k_{\sigma,\text{coll}} \left(\frac{\sigma^n_{\text{coll}} - \sigma_{\text{coll,h}}}{\sigma_{\text{coll,h}}} \right) \rho^n_{\text{coll}}, \tag{4.6}$$

where n denotes the current G&R time step, $k_{\sigma,\text{coll}}$ is a gain factor, and σ^n_{coll} is the collagen fiber stress obtained from the FSI-derived deformation and orientation field. Relative to the quasi-static loading in Gheysen et al., σ_{coll} here evolves under pulsatile, pressure-dependent FSI loading, providing a more physiologically representative mechanical stimulus for remodeling.

4. **Incorporate additional fluid-driven signals and thrombus growth.** A natural extension is to include WSS-related quantities and other hemodynamic parameters identified in Chapter 3 that may influence chronic dissection progression and thrombus formation [195, 221, 222]. The formation of a thrombus not only affects the mechanical state of the tissue but also alters the local hemodynamics within the false lumen. These can be added as supplementary biochemical or mechanotransduction terms in the G&R law.

Additional information - Aortic Dissection

Supplementary S1: Mesh sensitivity

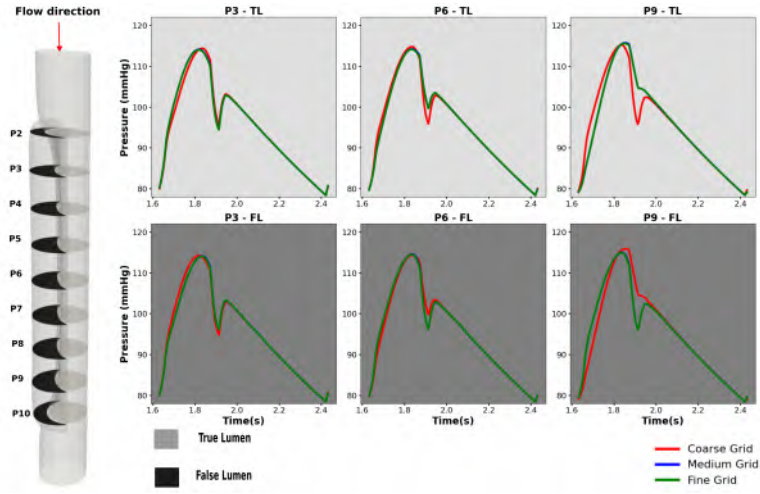

Figure S1: Absolute pressure at P3, P6, and P9 for coarse, medium, and fine grids.

A grid sensitivity study is performed to ensure negligible variation of parameters upon grid refinement. A coarse grid of 392809, medium grid of 1079545 and fine grid of 2464169 tetrahedral cells respectively were chosen in a rigid wall setting. We study temporal variation of absolute pressure at planes P3, P6 and P9 shown in Figure S1.
The grid convergence index (GCI) is the measure of how far away the computed solution is from the asymptotic numerical value [223].providing an error band on the grid. Each grid is refined with a refinement factor (r) which is calculated by first computing the cell size 'h':

$$r = \frac{h_{coarse}}{h_{medium}} \sim \frac{h_{medium}}{h_{fine}}$$

$$h_i = \left(\frac{1}{N_i} \sum V \right)^{\frac{1}{3}}$$

Where i= {Coarse, Medium, Fine}. Since the total volume throughout the domain does not change as it is a rigid-wall simulation, the refinement ratio is calculated as:

$$r = \left(\frac{N_{medium}}{N_{coarse}} \right)^{\frac{1}{3}} \sim \left(\frac{N_{fine}}{N_{medium}} \right)^{\frac{1}{3}}$$

'N' represents the number of cells for each mesh resolution. We obtained refinement ratios of 1.31 moving from coarse grid to medium grid, and 1.4 moving from medium to fine grid. We compute the average of it to gather the refinement ratio.

$r = \left(\frac{r_{medium,coarse} + r_{fine,medium}}{2} \right)$ GCI is calculated as:

$$GCI_{fine,medium} = 1.25 \left| E_{fine,medium} \right|, \quad GCI_{medium,coarse} = 1.25 \left| E_{medium,coarse} \right|$$

Where 1.25 is a factor of safety [223]. $E_{fine,medium}$ is the relative discretization error for the fine grid solution after refining from a medium grid, and $E_{medium,coarse}$ is the relative discretization error for the medium grid solution after refining from a coarse grid which are calculated as:

$$E_{fine,medium} = \frac{\left(\frac{\left| \phi_{medium} - \phi_{fine} \right|}{\phi_{fine}} \right)}{r^p - 1}$$

$$E_{medium,coarse} = \frac{\left(\frac{\left| \phi_{coarse} - \phi_{medium} \right|}{\phi_{medium}} \right)}{r^p - 1}$$

Where the numerator gives relative error between the solutions for each grid resolution. ϕ represents the value of interest for each spatial resolution. For instance, in our case ϕ is the area-averaged absolute pressure for each grid resolution at our planes of interest. Order of convergence 'p' is calculated as:

$$p = \frac{\ln \left(\frac{\left| \phi_{coarse} - \phi_{medium} \right|}{\left| \phi_{medium} - \phi_{fine} \right|} \right)}{\ln(r)}$$

Finally, the asymptotic convergence range (ACR) is calculated as:

$$ACR = r^p \frac{GCI_{medium,coarse}}{GCI_{fine,medium}}$$

If ACR ≈ 1, then refining the grid will not improve the precision of our quantity.

Grid convergence index (GCI) and asymptotic convergence range (ACR) for area-averaged absolute pressure values in true lumen (TL) and false lumen (FL) at three planes of interest

Planes	Pressure value computed		$GCI_{fine,medium}$	$GCI_{medium,coarse}$	ACR
P3	TL	min	7.11e-07	9.85e-06	1.000007
		mean	3.5e-05	0.0003	1.0002
		max	0.00026	0.001	1.0006
	FL	min	9.19e-07	6.74e-06	1.0000004
		mean	2.78e-06	9.06e-05	1.00007
		max	0.00391	0.0047	1.0006
P6	TL	min	1.10e-06	1.33e-05	1.000009
		mean	0.00015	0.00035	1.00016
		max	0.00011	0.00009	1.0006
	FL	min	2.5e-06	9.5e-06	0.99999
		mean	0.0012	0.0011	1.00005
		max	0.00038	0.0013	1.0007
P9	TL	min	7.52e-06	4.08e-05	1.0002
		mean	8.2e-06	8.27e-05	1.00006
		max	0.0004	0.0019	1.0011
	FL	min	1.59e-07	7.67e-06	0.99999
		mean	3.89e-05	0.0001	1.00007
		max	9.86e-05	0.001	1.0007

We observe that the GCI values for both grid refinements are very small ($< 1\%$) which is very desirable and ACR$\approx$1 for all grids. While this suggests a coarse grid might be desirable for minimal, mean and maximum values, instantaneous variations are not captured in this approach. Hence, we plot temporal variations of pressure at our planes of interest in Figure S2 below. We observe from Figure S1 that a coarse grid fails to capture the dicrotic notch effectively at P9 for both TL and FL. Insignificant variation is observed between medium

and coarse grid for instantaneous pressures. Therefore, considering GCI calculations and instantaneous pressures, we can safely say that a medium grid is sufficient to capture our quantity of interest.

Supplementary S2: Tuning WK models

Parameters from Case NSB were calculated based on [164]. A brief overview of the method is as follows:
No side branch calculation:

Total resistance (R_{tot}) is calculated as:

$$R_{\text{tot}} = R + Z = \frac{\overline{P}}{\overline{Q}},$$

where $\bar{P}$ is calculated using the expression:

$$\overline{P} = P_{\text{dia}} + \frac{1}{3}\left(P_{\text{sys}} - P_{\text{dia}}\right),$$

where $P_{\text{dia}} = 80$ mmHg and $P_{\text{sys}} = 120$ mmHg. $\overline{Q}$ is computed based on the inflow profile used in Equation 4.2.

Once R_{tot} is calculated, the characteristic impedance (Z), which we model as a resistor, is 5 to 7% of the peripheral resistance [80], and we choose $Z = 0.07R_{\text{tot}}$. Using a first-order backward Euler method to discretize the ODE, we obtain pressure at the subsequent time-advance, which is implemented using a user-defined function (UDF) in Ansys Fluent (Ansys Inc, USA), similar to [164].

Total compliance (C_{tot}) is calculated as:

$$C_{\text{tot}} = \frac{dV}{dP},$$

where $dP = P_{\text{sys}} - P_{\text{dia}}$ or the pulse pressure and dV is calculated as $dV = \int_0^{\mathcal{T}} Q(t)\,dt$:

$$dV = \int_0^{\mathcal{T}} Q(t)\,dt$$

where T is the time corresponding to the systolic peak, i.e., the area under the curve of the inflow profile.

The R, C, and Z values for Case 1 are the R and Z calculated using R_{tot} and $C = C_{\text{tot}}$.

Calculation for cases with sidebranch: Keeping the total resistance R_{tot} the same as Case 1, parameters for Cases 2 and 3 are calculated by the following expression:

$$R_{\text{tot},i} = \frac{R_{\text{tot}}}{q_i},$$

where $i \in \{\text{Downstream, Side branch}\}$.

Percentual flow splits were chosen based on Stokes et al.[11], who posit that 7 to 21% of cardiac output is perfused through major and minor side branches (SBs). We chose the lower threshold of 7% through the SB, leaving 93% of flow downstream.

q_i is calculated as:

$$q_i = \frac{\overline{Q_i}}{\overline{Q}},$$

where $\overline{Q}_{\text{downstream}} = 0.93\,\overline{Q}$ and $\overline{Q}_{\text{sidebranch}} = 0.07\,\overline{Q}$. Hence, $q_{\text{downstream}} = 0.93$ and $q_{\text{sidebranch}} = 0.07$. Here, '$q$' represents the desired flow splits.

Similarly, compliance for Cases 2 and 3 is calculated using the expression:

$$C_{\text{tot},i} = C_i \cdot q_i.$$

Substituting these equations, we get the values obtained in Table 4.4.

Supplementary S3: Flow regime

To determine the flow regime in the aorta, a critical Reynolds number (R_e^{crit}) is defined as a power-law function between the Womersley and Strouhal numbers [224], expressed as:

$$Re_{\text{critical}} = 169\,{\alpha_w}^{0.83}\,St^{-0.27}, \tag{4.7}$$

where α_w is the Womersley number and St is the Strouhal number. If $Re_{\max} < Re_{\text{critical}}$, the flow can be considered subcritical [126].

Womersley number (α_w) is a dimensionless parameter that represents the ratio of transient inertial forces to viscous forces in a pulsatile flow [225]. It is defined as:

$$\alpha_w = 0.5D\sqrt{\frac{2\pi f\rho}{\mu}}, \tag{4.8}$$

where D is the vessel diameter, f is the heart rate frequency, ρ is the fluid density, and μ is the dynamic viscosity. Using $D = 0.0273$ m, $f = 1.25$ Hz, $\rho = 1060$ kg/m^3, and $\mu = 0.0035$ Pa·s, gives $\alpha_w = 21.0$.

Strouhal number (S_t) is a dimensionless parameter describing the ratio of unsteady inertial effects to convective inertial effects in pulsatile flow, and can also be related to the non-dimensional stroke volume. It is defined as:

$$S_t = \frac{fL}{v_p - v_m}, \tag{4.9}$$

where L is the characteristic length (taken as the vessel diameter) and v_p and v_m are the peak and mean velocities, respectively [226]. For the present configuration, $S_t = 0.048$, which is typical for large arteries [226].

For Case NSB, the computed parameters yield $Re_{\text{critical}} = 4802$ and $Re_{\max} = 3790$. In the study of Peacock et al. [224], the authors mention an RMS error of 15.2% between equation 4.7 and experimental data giving a threshold between 4072 and 5523 for Re_{critical}. Therefore, since $Re_{\max} < Re_{\text{critical}}$, the flow in the aorta can be classified as **subcritical (laminar pulsatile flow)**.

Supplementary S4: Additional figures

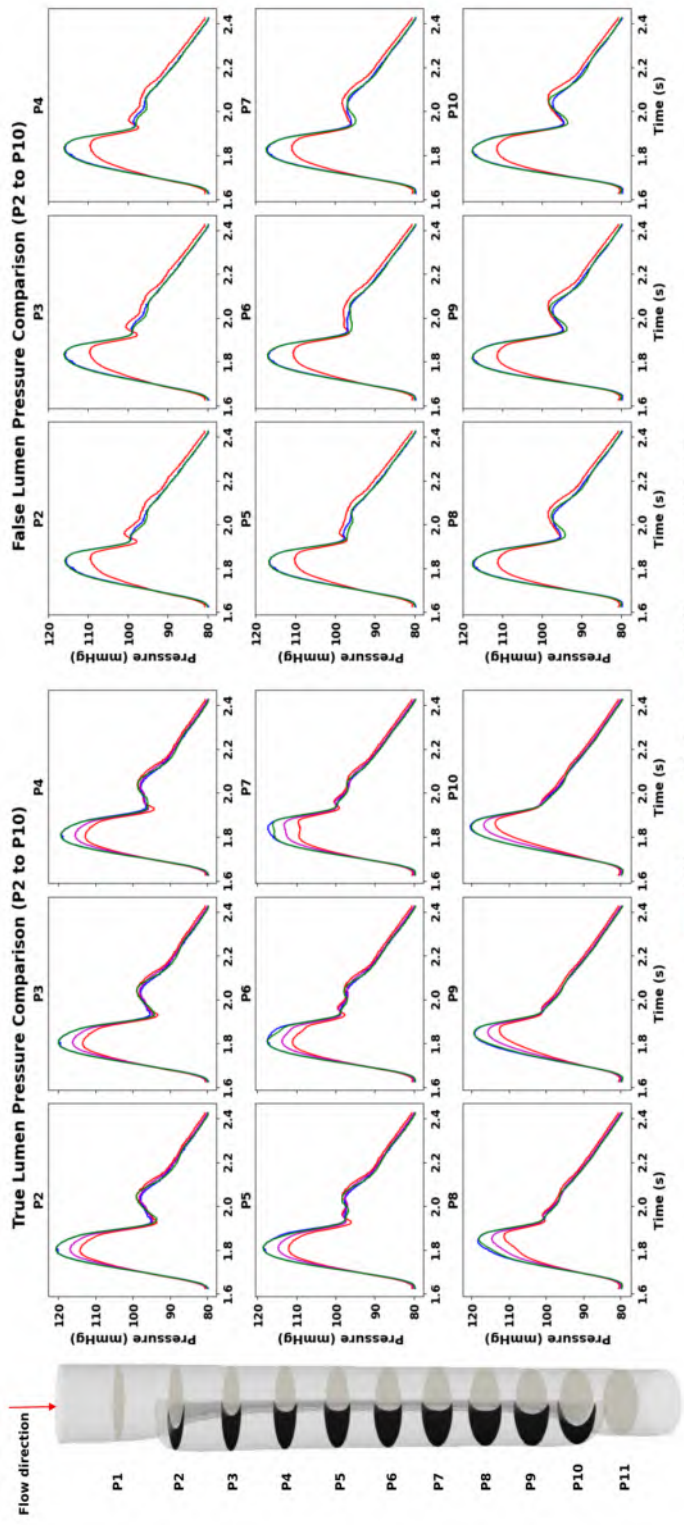

Figure S2: Temporal TL and FL pressure calculated at all planes in the dissection.

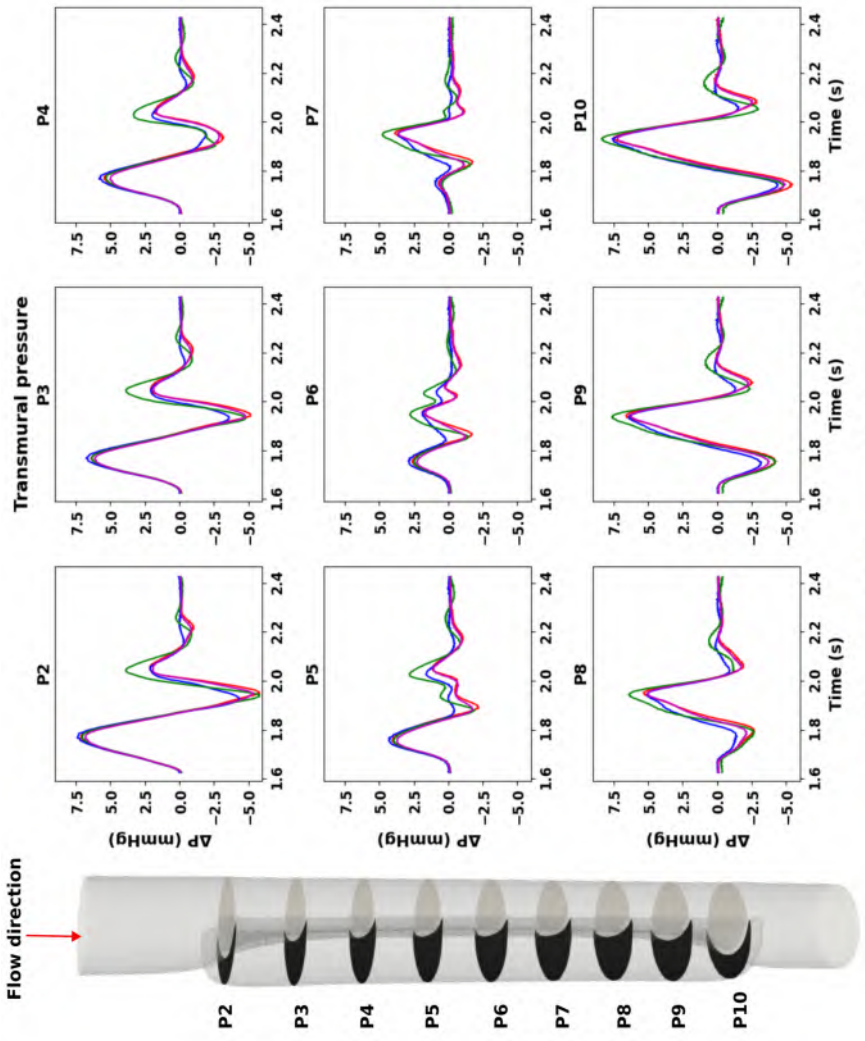

Figure S3: TMP for all planes of interest for our cases.

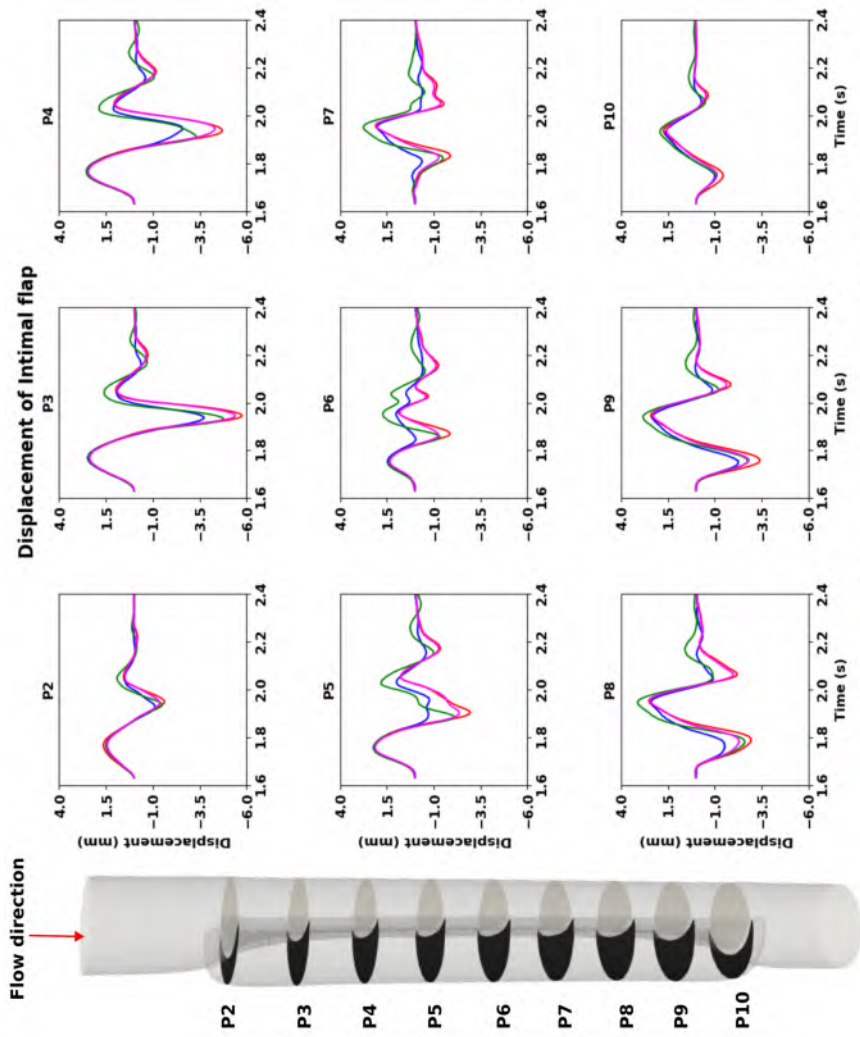

Figure S4: Nodal displacement for all cases at all planes

CHAPTER 4A

Wave Propagation in the Aortic Dissection Model

4A.1 Background and methodology

The rationale for this (sub)study stems from the results obtained in Chapter 4 while comparing FSI results with and without the presence of a side branch (SB) emanating from the false lumen(FL). While intuitively we speculated that the presence of a SB would alleviate pressure in the FL, results however indicate an increased FL (and true lumen) pressure in presence of a SB, with maintained total vascular resistance in the model.

Since the inlet flow into the model was kept constant, increased pressure in the presence of a SB should be due to an increase in input impedance (Z_{in}). From a lumped model perspective, the increase in impedance may result from altered compliance and inertial forces, possibly due to TL-FL interactions. From a wave dynamics perspective, changes in pressure should be explicable from altered wave reflection and dynamics. To better understand pressure dynamics in the dissection, a wave separation analysis is performed to observe how the pressure and flow waves behave with and without the presence of a dissection, applying wave separation analysis in the time domain.

Variations in pressure (dP) and flow rate (dQ) propagate along compliant vessels as waves with propagation in the distal direction (away from the heart) referred to as a forward wave [227]. Due to

age and continuous change in the structure of the arteries, the characteristic impedance along the travel path from the aorta towards the periphery changes continuously, leading to these forward waves being completely or partially reflected back (backward wave) [227]. A pressure and flow waveform at any location is a combination of these forward and backward waves. Hence, decomposing these waveforms helps to understand how the dynamics downstream determine the pressure and flow at a location. If a wave produces an increase in pressure (i.e., $dP > 0$), it is referred to as a compression wave; conversely, a decrease in pressure ($dP < 0$) corresponds to a expansion wave [227]. These waves propagate at a velocity known locally as the wave speed (c) and link pressure and flow through the characteristic impedance (Z_c), which depends on both the local area (A) and the wave speed (c) and is defined as:

$$Z_c = \frac{\rho c}{A} \tag{4A.1}$$

where ρ is the blood density. The incremental relationships for forward and backward waves are:

$$dP_+ = Z_c\, dQ_+, \tag{4A.2}$$
$$dP_- = -Z_c\, dQ_-. \tag{4A.3}$$

where $+$ refers to the forward and $-$ refers to the backward components of pressure and flow.
Decomposing these measured or simulated pressure and flow waveforms into their forward- and backward-traveling components is called Wave separation analysis (WSA). In computational modeling, WSA is often implemented one-dimensional (1D) hemodynamic frameworks [228, 229], however some studies exist where WSA for pressure and flow waves from 3D-FSI data have been investigated [158, 230]. Regarding aortic dissections, while all studies detailed in Table 4.1 calculate pressure or flow waves at different locations in the dissected geometry, only Chen et al.[231] studied wave separation, specifically in Type-B aortic dissections. The authors use a hybrid 0D1D model where they study how tear size and location modulate forward and backward wave components in the true and false lumina. The authors posit that smaller re-entry tears damp the retrograde flow and calculated wave intensity can be used as a marker for degree of dissection.

4A.2 Geometry, material properties and boundary conditions

In total, four geometries are analyzed in this study. The first two correspond to geometries with a dissection previously simulated in [214], and the procedure being illustrated in Figure 4.2. These include Case NSB (representing a dissection without a side branch), and Case SB_FL, (representing a dissection with a side branch in the false lumen). The remaining two geometries represent non-dissected, straight-tube models that mimic the healthy descending thoracic aorta. These geometries are generated following the same procedure shown in Figure 4.2, as detailed in Chapter 4 with the primary difference being, that the tears and dissected membrane are not explicitly modeled as shown in Figure 4A.1. Similar to the first two cases, one of the geometries does not contain a side-branch (Case ST), while the other does (ST_SB).

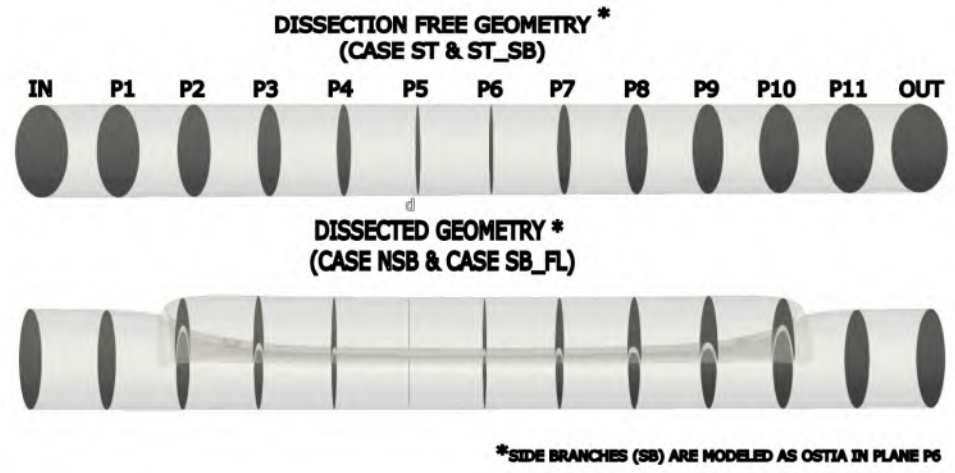

Figure 4A.1: Geometries of interest with the upper figure representing the two dissection free geometries modeled as a straight tube with side branch modeled as an ostia in P6 and lower figure represents the geometries used in Chapter 4 with side branch modeled as an ostia at P6.

For even comparison, dimensions of the non-dissected geometries are consistent with those used in [214] and summarized in Table 4.3 which results in a total length of $L_{tot} = 240\,\text{mm}$ and a wall thickness of $h = 1.85\,\text{mm}$. A structured hybrid hexahedral mesh with 72000 elements are generated using the in-house meshing tool pyFormex [103].

The initial tube geometry at diastolic pressure, accounting for residual stresses, was generated using the deposition stretch algorithm

proposed by Famaey et al. [99], following a similar approach previously adopted in [92, 214], and as detailed in 4. Characteristic material response of the tissue was described using the GOH (Gasser-Ogden-Holzapfel) model [88], employing the same parameters as in [214] and outlined in 4. Once the resulting stressed geometries are obtained at diastolic pressure, the surrounding lumen was filled with 890,955 and 818,710 tetrahedral cells for cases ST and ST_SB respectively. The cell sizes were matched to those used in the dissected geometry described in 4.

A flat Dirichlet type inflow profile given by a piecewise sinusoidal function was prescribed at the inlet and a 3-element windkesel model was used to describe downstream vasculature similar to [214] and detailed in Chapter 4. The governing fluid dynamics equations were solved using the finite volume solver Ansys Fluent (Ansys Inc., USA), with an absolute convergence criterion of 10^{-5}. To account for mesh deformation due to fluid motion, the Arbitrary Lagrangian-Eulerian (ALE) method was employed [111], using the Laplace equation for mesh smoothing. The governing equations for tissue mechanics were solved in a finite element framework in Abaqus (Dassault Systemes, France) with a cyclindrical co-ordinate system defined and movement confined to only the radial direction. The fluid and structural solver were strongly coupled using the in-house coupling tool CoCoNuT similar to [164, 214] with L_2 norm of displacement being used to determine convergence.

Wave speed and decomposition

Decomposing the waves at the location of interest requires the calculation of local wave speed. Multiple methods exist to obtain the wave speed as detailed in a review by Segers et al.[232]. Among these, the Bramwell-Hill equation is used given mathematically by:

$$c = \sqrt{\frac{A}{\rho} \cdot \frac{\Delta P}{\Delta A}}$$

Where change in pressure ΔP is calculated for 10 time steps during the systolic phase and the resultant change in area is given by ΔA. ρ is the density of blood which is 1060 kgm^{-3}.
The pressure and flow signals were decomposed into forward (+) and backward (−) components using the local characteristic impedance

(Z_c):

$$P_{\pm} = \frac{1}{2}\left[P \pm Z_c Q\right], \tag{4A.4}$$

$$Q_{\pm} = \frac{1}{2}\left[Q \pm \frac{P}{Z_c}\right], \tag{4A.5}$$

From these decomposed quantities, the incremental forward and backward wave powers are given by:

$$d\pi_{\pm} = \pm\frac{(dP \pm Z_c\, dQ)^2}{4Z_c}, \tag{4A.6}$$

such that $d\pi_+$ corresponds to the energy flux associated with the forward wave and $d\pi_-$ with the backward (reflected) wave. The cumulative or integrated wave power, $\Pi_{\pm}$, over a cardiac cycle provides a measure of the total energy transmitted or reflected at the location of interest. Compared to traditional wave intensity analysis, which expresses wave strength in $\mathrm{W\,m^{-2}}$, wave power has the advantage of being expressed directly in units of *Watts*, thereby offering a more intuitive representation without being sensitive to cross-sectional area [227].

4A.3 Results

Results after the 3^{rd} cardiac cycle are used for post-processing. Following the methodology applied in Case NSB and SB_FL [214] and as detailed in Chapter 4, Case ST and ST_FL are divided into 12 equidistant planes 20 mm apart as shown in Figure 4A.1. Pressure (mmHg) and flow-rate Q ($m^3 s^-1$) at Plane P1 are extracted for wave decomposition. P1 is chosen as it is the closest plane proximal to dissection initiation. Wave speed calculated using the Bramwell-Hill equation and used to decompose the waves are presented in Table 4A.1 below:

Table 4A.1: Wave speed in m/s calculated using the Bramwell-Hill equation for all cases

No Dissection		Dissection	
Wave speed (ST)	**Wave speed (ST_{SB})**	**Wave speed (NSB)**	**Wave speed (SB_{FL})**
7.39	7.64	6.90	6.96

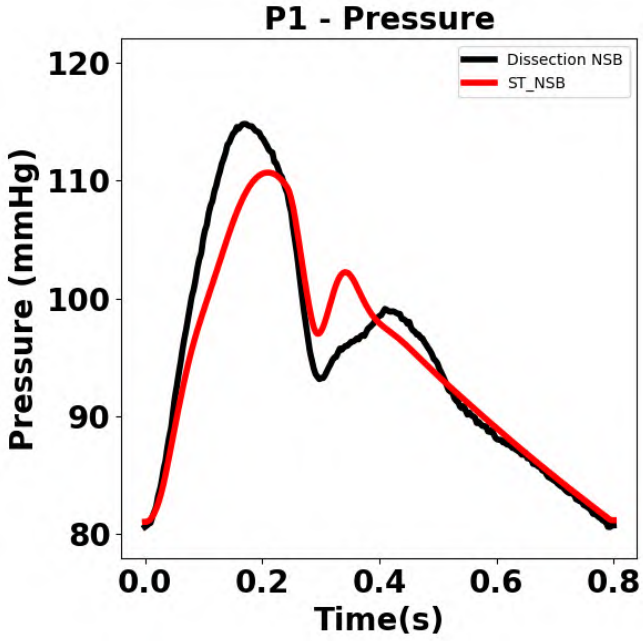

Figure 4A.2: Figure comparing pressure at Plane P1 for Case NSB and Case ST

Cases with dissections present an elevated systolic pressure compared to those without, as shown in Figure 4A.2. The dissection, which located immediately distal to plane P1 (see Figure 4A.1), introduces a distinct impedance mismatch that reflects part of the forward-traveling pressure wave back toward the inlet. The resulting backward pressure wave increases the total pressure measured at P1. This effect is amplified by the "see-saw"-like motion of the flap described in Chapter 4. During systole, the flap deflects toward the true lumen, reducing the TL cross-sectional area distally. This strengthens the reflected component, as illustrated in Figure 4A.3 where Case NSB and SB_FL present increased backward pressure, leading to a pronounced rise in proximal systolic pressure.

In contrast, the straight-tube geometries lack such a proximal reflection site. In Case ST, the main reflection occurs only at the distal outlet, while in Case ST_SB, minor reflections originate from the side-branch ostia. Therefore, the combination of an immediate impedance mismatch just distal to P1 and the dynamic flap motion of dissected models produces stronger backward pressure waves and a greater systolic pressure relative to the dissection-free geometries.

As the flow decelerates, a distinct backward compression wave (BCW) is observed across all cases (Figure 4A.4, 4A.3). The BCW manifests as a negative pulse in wave power and a rise in backward pressure (P_-) at P1. This response is most pronounced in the straight-tube geometries, consistent with their larger P_- compared to the dissected cases. A more dampened backward wave pulse can be seen in dissected cases because during flow deceleration, the "see-saw" like motion leads to the intimal flap deflecting towards the true lumen proximally (see Figure 4.7 in Chapter 4) which may dampen/absorb the reflected wave downstream.

Following the backward compression wave, a distinct forward expansion wave (FEW) is observed for all cases as the inflow approaches zero (Figure 4A.4). This FEW is characterized by a positive pulse in forward wave power and a rapid pressure decrease at P1, marking the transition from the decelerating phase of the cycle to near-stagnant flow. It arises from the steep negative gradient of the prescribed inlet waveform, which generates a strong expansion effect as the driving flow ceases. Consequently, the expansion wave is markedly stronger than the initial forward compression wave (FCW) for all cases, reflecting the greater deceleration imposed at the end of the inflow pulse.

During diastole, the forward and backward pressure components in the straight-tube geometries become nearly identical at P1, indicating that the system reaches a quasi-steady state as the inflow approaches zero. The absence of geometric complexity allows wave reflections to settle rapidly, leading to minimal ongoing wave activity. This is reflected in the wave-power profiles, where both $d\Pi_+$ and $d\Pi_-$ tends to be constant. In contrast, the dissected models retain small but persistent differences between P_+ and P_- due to residual flap motion and TL–FL coupling. These subtle motions give rise to weak backward expansion waves, visible as small negative fluctuations in the backward wave-power signal (see Figure 4A.3).

A comparison of the backward wave power ($d\Pi_-$) between the straight-tube geometries reveals the effect of the side branch on wave

reflections (Figure 4A.4). In the ST case (no side branch), two distinct sharp negative peaks are observed around $t \approx 1.9$ s, corresponding to coherent backward compression waves generated by strong reflections at the distal outlet. When a side branch is introduced ST_-SB, the magnitude of the backward wave power decreases and the distinctive peak seen in ST becomes less evident. This likely reflects attenuation of the returning wave as some energy is diverted into the side branch and partially lost at the junction, reducing the amplitude of the backward compression response at P1.

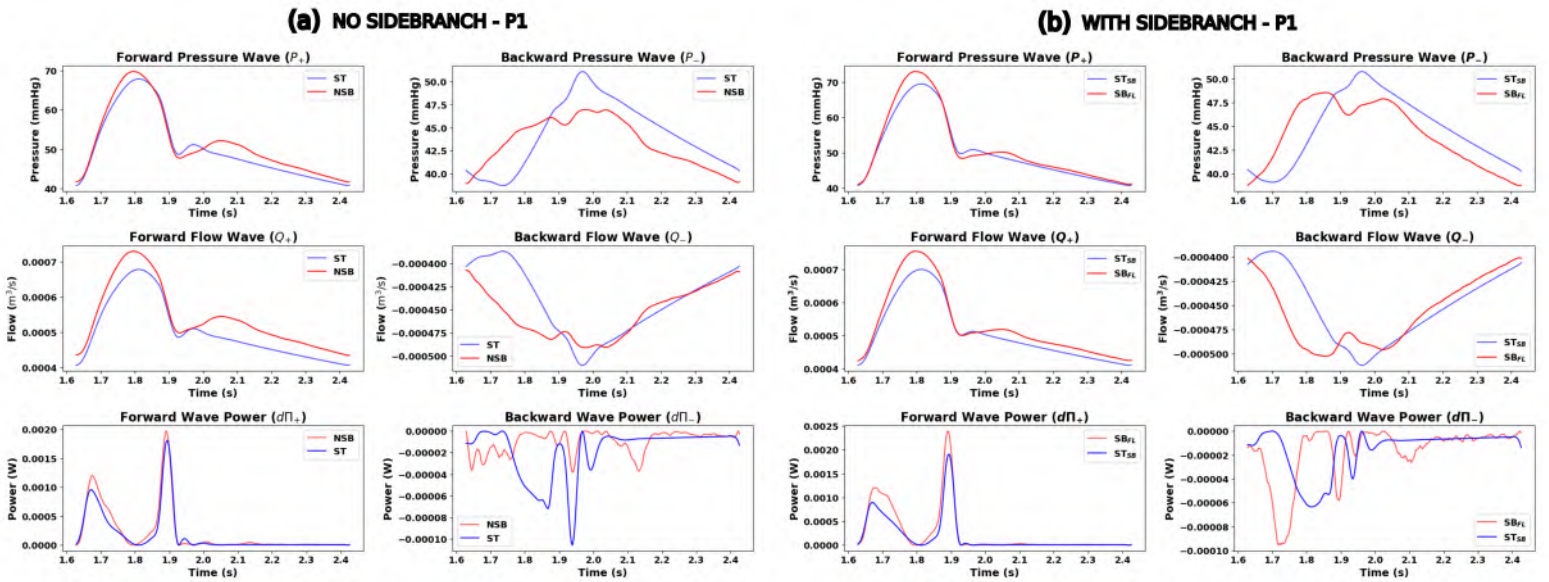

Figure 4A.3: The four vertical panels (a-d) represent the simulated cases with the horizontal panels representing forward (blue), backward (red) and total(black) pressure, flow-rate and wave power respectively

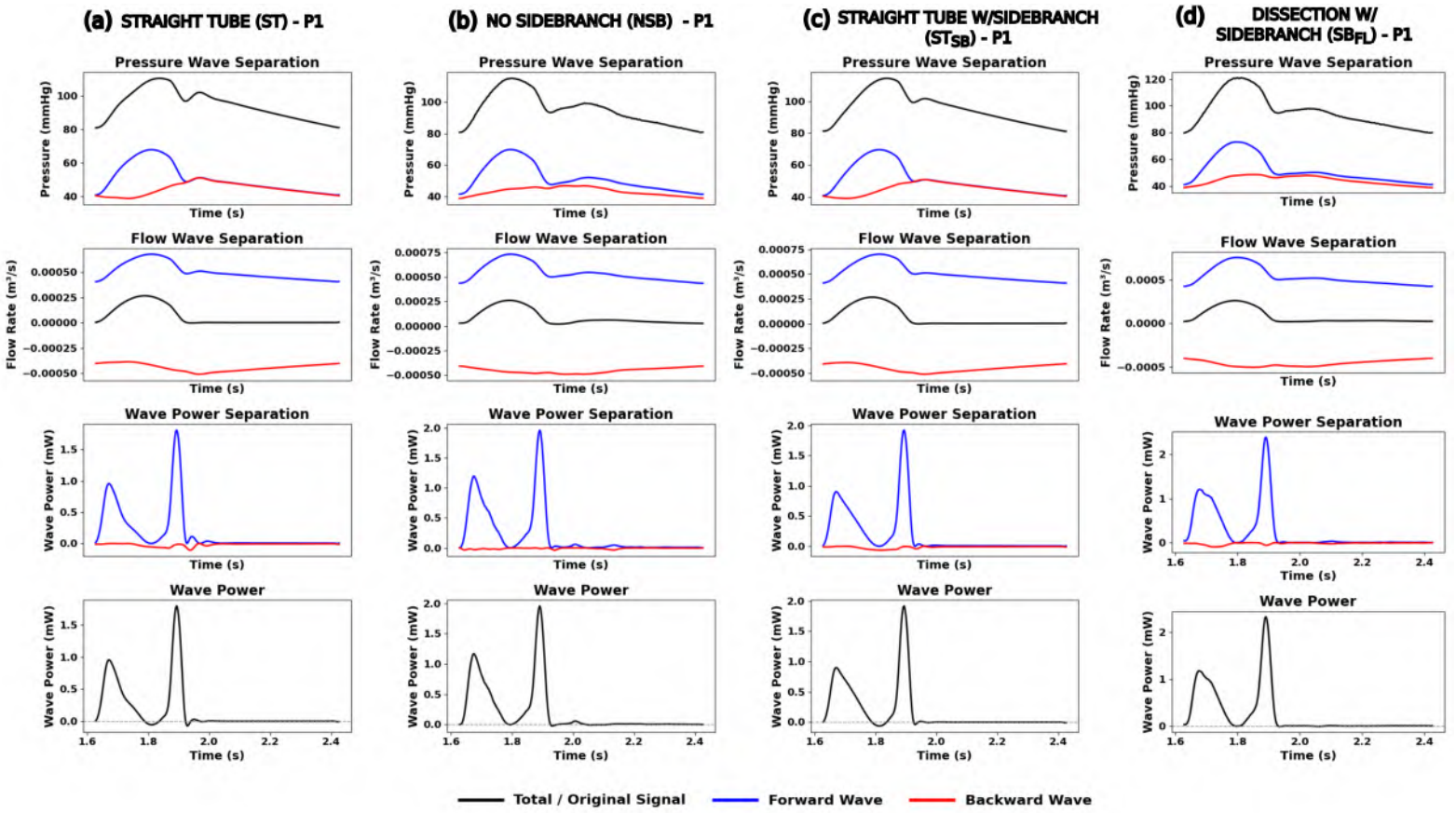

Figure 4A.4: The four vertical panels (a-d) represent the simulated cases with the horizontal panels representing forward (blue), backward (red) and total(black) pressure, flow-rate and wave power respectively

III

Discussion

Chapters

5 Conclusions and outlook **149**

Chapter 5

Conclusion and Outlook

'All models are wrong, but some are useful' was a famous phrase coined by British statistician George Box [233]. While suggesting that the models are wrong/lack value literally, Box emphasized that computer models are often simplifications of reality and are built upon assumptions. This is also directly relevant to the computational models developed during the course of this dissertation, which despite incorporating state-of-the-art material models and boundary conditions, have various assumptions and simplifications. In this chapter, we evaluate the 'usefulness' of these models by summarizing the key findings and assessing how effectively they address the research questions posed in the introductory chapter. We try to take a bird's eye view and reflect on the broader limitations and underlying assumptions in the models. This reflection provides the foundation for discussing the potential translation of these models from their current computational form into clinical applications, as well as the challenges that such translation may present.

5.1 Key results - Did we achieve our objective?

This thesis aimed to investigate how fluid-solid interaction (FSI) modeling can offer critical insights into bio(fluid)mechanical parameters, valuable by themselves but also key to future models incorporating long-term growth and remodeling (G&R), especially models

aiming to provide understanding of and clinical decision support in aortic pathologies characterized by large displacements. The primary goal presented in the introductory chapter was developing a strongly coupled FSI framework for gaining insight into specific pathologies of interest, which was achieved. Despite a few assumptions, the importance of FSI was highlighted in capturing hemodynamic parameters that also drive vascular growth and remodeling.

5.1.1 Pulmonary autograft

In addressing the first primary objective regarding pulmonary autografts, a robust, strongly coupled FSI model was successfully developed for three distinct ovine geometries, representing yet to remodel pulmonary autografts. A qualitative and quantitative comparison between a distensible model (using FSI) and a rigid-wall model (using CFD) models were conducted. CFD models were shown to adequately predict bulk flow patterns and traditional wall shear stress (WSS) metrics such as time-averaged wall shear stress (TAWSS) and oscillatory shear index (OSI) magnitudes similar to the FSI model. However, non-traditional metrics based on WSS skeletons such as topological shear variation index (TSVI), showed a moderate relationship with FSI. We hypothesize that wall displacements alter the near wall hemodynamical structures leading to a moderate correlation between the distensible and rigid wall approach while computing TSVI.

Importance of FSI- High values of TSVI have a strong colocation with regions of increased wall thickness in coronary arteries of porcine models [139], suggesting a potential link with vascular growth. In our study, we observed poor spatial collocation at high TSVI thresholds between FSI and CFD (Figure 3.9). Hence, if TSVI were to be evaluated as a potential driver for G&R, an FSI approach would be suggested. If canonical metrics are to be used as a driver for G&R, the computational expense of FSI is not warranted as evidenced by a successful CFD based G&R approach adopted by Mousavi et al.[137] in healthy and aneurysmal (ascending thoracic) subjects using relative residence time (RRT), which is a function of TAWSS and OSI.

Contribution to literature- A significant contribution of this study to literature was the generation of an original dataset that directly compares multiple WSS metrics known to influence vascular G&R. While this comparison had been performed in coronary arteries [127, 173], this was the first of its kind in pulmonary autografts. Further, TSVI has been assessed for distensible walls for a

healthy human ascending aorta [174] using the prescribed moving boundary method and in coronary arteries using FSI [127]. Here, we extend the WSS skeleton analysis for large displacements in pulmonary autografts using strongly coupled FSI simulations. We hope to provide the community with data to choose the right modeling approach depending on the WSS metrics used for long term G&R, thus extending the state-of-the-art.

5.1.2 Aortic dissection

The second primary objective involved developing a strongly-coupled FSI model designed to explore pressure and other related hemodynamic metrics within the false lumen of an idealized dissected aorta, with specific emphasis on the impact of side branches that emanate from true and false lumen. The investigation revealed that the presence of side branches consistently resulted in elevated luminal pressures especially at systole, reduced false lumen ejection fraction and mobility of the dissected flap, both critical indicators influencing dissection progression and potential long-term growth [5, 6].

Importance of FSI- Any flap motion regardless of magnitude affects false lumen pressure and hemodynamics [194, 197]. This statement in itself should explain the importance of FSI while modeling aortic dissections. While comparable values with FSI can be obtained with a distensible flap through the computationally efficient prescribed moving boundary method [234], the displacements were small. Further, the novel approach used in this thesis to initialize a dissection from a healthy geometry (see Figure 4.2 and Movie M1 in [214]) requires a structural model. Further, Baumler et al.[93] demonstrated that neglecting pre-stress and external tissue support leads to unphysiological wall motion and pressure deviation, with radial displacement of the outer wall deviating from the segmentation by ≈6mm when pre-stress was disregarded compared to sub 1mm when pre-stress was included. This underscores the importance of incorporating physiologically realistic initial stresses and mechanical support in computational models. All these salient points from literature along with our approach of initiating the dissection, incorporating state-of-the-art boundary conditions showcases the importance of utilizing FSI in modeling aortic dissections. Finally, the complex disturbed flow features observed due to large displacements in the acute phase cannot be captured effectively using a rigid-wall approach [194].

Contribution to literature- This quantitative analysis represents a novel contribution to the field, especially illustrating how anatomical features such as side branches or the number of tears can

significantly modify local hemodynamic environments. Despite the idealized nature, this insight emphasizes the importance of incorporating detailed anatomical features into computational models, which are often neglected. Aside from being the first FSI study to quantitatively compare pressure build-up in such a case, this approach of actually initiating a dissection alluded to in the last paragraph is close to pathophysiological reality despite the idealized nature. If imaging quality permits, this study thus urges the community to incorporate side-branches that emanate from true and false lumen in their computational studies.

Collectively, though these pathologies are not linked to one another, we can appreciate the importance of FSI in delivering insights into parameters that are key by themselves, but are also essential components needed for long-term vascular G&R models. The advanced FSI modeling approach developed in this thesis represents a small step forward in potentially predictive vascular biomechanics. We can say that the objectives outlined i.e. developing strongly coupled FSI for pathologies of interest were successfully achieved. However, we need to take an honest look at the assumptions and limitations that made these results possible before delving into clinical translation.

5.2 Assumptions and limitations

Famous Princeton physicist Freeman Dyson once stated 'the computer models are very good at solving equations of fluid dynamics but very bad at describing the real world'. Although Dyson's comment specifically addressed climate modeling, this observation extends broadly, including the complex dynamics of cardiovascular systems. Fundamentally, any model is a representation of reality, limited by availability of data and assumptions required to simplify said reality.
In previous chapters (Chapters 3, 4, and 4A), we have explored specific limitations and assumptions in individual studies. Now, let us step back and consider more broadly the overarching constraints and limitations that affect FSI modeling. Understanding these limitations is essential for contextualizing results and improving future methodologies.

Geometrical - Idealized geometries are often used in parametric studies to study how anatomical variations affect flow, structure and vice-versa, as these models often simplify the anatomy. For

instance, in this thesis, while modeling aortic dissections, the descending aortic section is modeled as a straight tube. Among elderly patients where dissections predominantly occur, the aorta becomes increasingly tortuous, thereby altering flow patterns and wall stress distributions [235]. Also, our simulations omit the ascending aorta and the arch, which do have considerable effect downstream, particularly with helical flow patterns that have been shown to influence aortic expansion in patients with dissections [236].

Fluid modeling - Blood was modeled as an incompressible Newtonian fluid, using a laminar flow assumption which is supported by the peak Reynolds number being less than the critical Reynolds numbers (see Chapters 4). However, Saqr et al. [237] have challenged this view, proposing that Reynolds number may not be sufficient to determine turbulence transition and arterial blood flow is inherently turbulent [237]. As bold as the claim may be, it may be worth exploring the validity of our laminar assumption through comparison with a turbulence model. While the SST transitional model is often used to model turbulence in aortic flows [11, 238], the most ideal comparison would be with a high-fidelity Direct Numerical Simulation (DNS) simulation, albeit at the risk of very high computational cost [239].
It has already been discussed in Chapter 1 that blood is a complex suspension with non-Newtonian shear-thinning viscosity and a particulate nature due to its red blood cell (RBC) content. This particulate nature has not been modeled in all studies as blood is modeled as a single phase fluid. While this Newtonian assumption is a very standard assumption in large arteries [25, 240], a non-Newtonian assumption can play a role in local blood velocity and relevant metrics [240] in regions characterized by low shear or recirculating flow, for instance in false lumen or possible blood recirculation zones in bulged pulmonary autografts. However, Arzani [178] proposed that non-Newtonian effects become relevant only when red blood cells remain in low-shear regions long enough to form rouleaux aggregates.
Additionally, our simulations were run under one cardiac cycle repeated periodically. This means, beat-to-beat variations or longer-term hemodynamic changes (e.g., heart rate variation, blood pressure trends) were not included. While this is standard modeling practice in the community, it might certainly have an impact on the results.

Solid modeling - While state-of-the-art boundary conditions are utilized to model the tissue, external tissue support was disregarded

for the pulmonary autograft study [164]. It is possible that the large displacements could be reduced if a viscoelastic boundary condition similar to the one introduced in Chapter 4 were applied. While material parameters are obtained from stress–stretch curves for the pulmonary autograft [47], no such data is available for the idealized dissection case. The dissected wall is different microstructurally and mechanically than the rest of the aorta [55, 241]. However, the dissected wall parameters chosen in our case are reliant on parameters obtained for a healthy thoracic aorta [92, 214]. Furthermore some material tests indicate that the intimal flap in the dissection is linear but anisotropic [241]. Therefore, relevant data from material testing should be incorporated similar to the autograft study described in Chapter 3.

Boundary Conditions- While we do prescribe boundary conditions based on ovine echography data and pressure measurements during surgery for the pulmonary autograft (see Chapter 3), these conditions assumed a resting state i.e the sheep were anesthetized. Therefore, larger displacements might be prevalent for awake and active conditions. We prescribed idealized boundary conditions based on literature for the study regarding aortic dissections in Chapters 4 and 4A, which while evident in literature [192], might differ from patient-specific conditions.

Inflow profiles, specifically the type of profile used, play an important role in determining downstream hemodynamics [77, 78, 183, 242, 243]. Madhavan et al. [77] suggested that different inflow profiles only affect the flow region close to the inlet of the aorta, and beyond two diameters distal to the inlet, differences in flow solution are small [77].

Similarly Armour et al. [78] studied the impact of inflow velocity profiles and their consequences in Type-B Aortic dissections. The results of this study suggest that irrespective of the type of inflow profile used, all yield reasonably similar velocity and time-averaged wall shear stress results qualitatively if sufficiently far from the inlet. Low TAWSS thresholds are predicted better using 3D profiles [78]. The authors suggest that if data is available, a 3D, through plane inflow profile must be used for a better prediction of pressure [78]. While a subject specific flow was prescribed for the pulmonary autograft study, a flat inflow profile was prescribed for both studies. Larger inflow length needs to be chosen for the pulmonary autograft study based on these observations, or coupling should be performed with a model incorporating upstream structures, ideally including the heart and aortic valve.

While the general consensus agrees that a 3-element WK model predicts the closest to physiological flows [217], Madhavan et al. [77] suggested that solutions vary up to 5 times the diameter proximally. Hence, larger downstream lengths have to be chosen for all studies based on these observations.

5.3 Future work and translation to clinic

We have so far discussed the assumptions and some limitations, both geometrically and numerically. A natural future work is to ensure that these points are addressed. However, addressing just these will not be sufficient to translate the current work to the clinic. Factors needed to be considered in order to translate this work to the clinic are discussed below.

Growth and Remodeling: It is a long term objective of the research groups to build digital twins for clinical decision support in aortic pathology. These models should be able to predict the longer term evolution of the tissues involved. We have stated explicitly during the thesis, especially in the introductory chapter that we do not simulate long-term vascular growth and remodeling (G&R), rather we focus our investigation on hemodynamic parameters that influence long term G&R. Naturally, the next step would be incorporate these hemodynamic parameters into a fluid driven G&R framework.

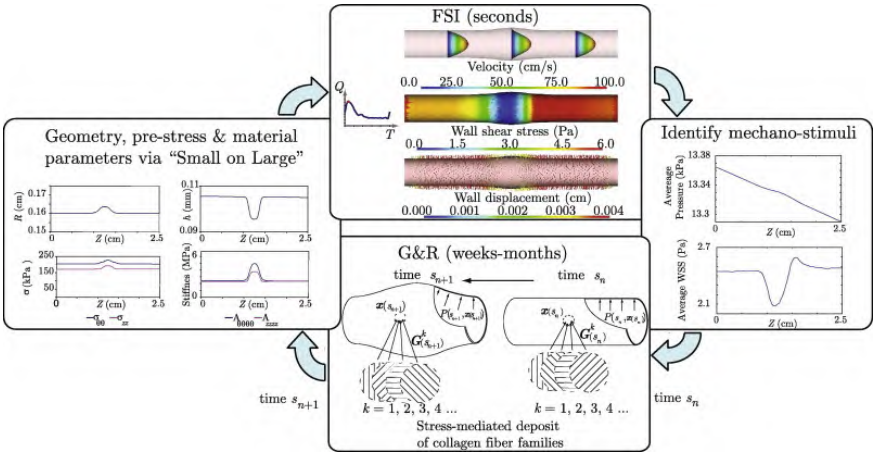

Figure 5.1: Iterative loop showcasing a FSG framework proposed by Figueroa et al. [8].

As shown in Figure 5.1, a small-on-large formulation enables pulsatile FSI simulations to be performed on a physiologically

prestressed vessel, after which the resulting wall shear stress and constituent-level stresses can be used to drive biologically motivated G&R laws. Iterating between FSI and G&R allows the model to predict long-term changes in geometry and microstructure, forming the basis of a prospective digital-twin framework for aortic disease. The conceptual FSG workflow proposed at the end of Chapters 3 and 4 represents an initial step in this direction, although substantial work remains to validate such models and to obtain reliable patient-specific G&R parameters.

Uncertainty Quantification and Risk Analysis: Three important factors to be considered for a model to be credible are: verification, validation and uncertainty quantification (UQ) [244]. The simulations run during the course of this thesis are deterministic and numerically robust and the solvers used are verified or benchmarked. Validation involves comparing our simulations to experimental data (if it exists) like flow validation in the pulmonary autograft case. However, despite being numerically robust, computational simulations are subject to uncertainty. UQ involves identifying how variations in input parameters (geometric details, boundary conditions, constitutive models in our case) result in variations in outputs (e.g., wall shear stress metrics in pulmonary autografts or pressure build-up in aortic dissections) [244]. In this thesis we did not explicitly perform uncertainty quantification (UQ), but it should be considered as a definite next step.

A first step could be extending the work of Gheysen et al. [245], who used a physiologically inspired finite element model with 300 latin hypercube samples to quantify how uncertainties in thickness and stiffness predict deformation and stress in Type-B aortic dissections. However, the strongly coupled nature of FSI in our work means it isn't just deformation and stress, but impact of stiffness affects flow as well [246]. Further, uncertainty in inflow waveforms [247] and outlet WK parameters [248] affect crucial hemodynamic parameters.

Even though latin hypercube sampling is more computationally efficient than brute forcing like Monte Carlo [245], each FE simulation takes minutes compared to the hours that a partitioned FSI simulation takes. Multiplying each simulation time by 300 gives a perspective on the computational time necessary. An interesting alternative that has been proposed is a complex FSI model might be complemented by many cheaper simulations (1D surrogates or coarser meshes) to estimate variability, with selective

high fidelity FSI runs. Fleeter et al. [249] showed that such a strategy can reduce the computational costs by 10 to 100 times while still accurately capturing hemodynamic variability. More recently, Schäfer et al. [250] applied a hybrid of multi-fidelity Monte Carlo Sobol' sensitivity analysis and polynomial chaos expansion to an idealized carotid FSI model and showed that combining multi-fidelity runs yields consistent sensitivity rankings and superior variance reduction compared to traditional brute forcing like Monte Carlo. Additionally, when the model response is smooth, polynomial chaos expansion alone can offer even lower computational cost, serving as an efficient surrogate for global sensitivity analysis. These works suggest a multi-fidelity approach or polynomial chaos expansion is the route to go to run UQ's for FSI models.

Digital twins: The phrase *digital twin* is being increasingly used in biomedical literature, often being broadly applied to any patient-specific simulation. In its actuality, a digital twin (in cardiovascular perspective), refers to a virtual counterpart that is updated with clinical and physiological data continuously [251]. Ideally, digital twins would be used in forecasting diseases and their evolution [252] and importantly, personalized planning [253]. Ideally, building a digital twin and translating it to the clinic would be our end goal.

Although this thesis focuses on short-term hemodynamic analysis (a snapshot in time), incorporating a fluid-solid growth (FSG) frameworks as previously alluded to would mean bridging temporal scales as G&R frameworks take weeks/months to simulate [254]. However, for a state-of-the-art digital twin, it isn't just temporal scales, but also spatial ones which have to be bridged. Maes et al. [255] proposed a multi-scale model in pulmonary autografts at the cellular and tissue level where change in cellular activity led to changes in mechanical properties of tissue. Though non-trivial, extending this to an FSI framework would be a natural next step.

Apart from continuum mechanics based methods for biological growth, another exciting alternative are agent based models (ABM) where spatial (organs to cells) and temporal (seconds to years) scales can be bridged successfully. ABM's have been used in conjunction with hemodynamic descriptors like WSS as a driver to predict vascular growth and remodeling [144, 256–259] from cellular to organ level. Because diseases progress over months if not years, FSG and ABM being continuously updated with real-time data could lead to a

state-of-the-art digital twin capable of studying evolution of disease from cellular to organ scale.

So, how important is FSI while setting up a long–term digital twin? While this work has emphasized the importance of FSI for scenarios with large displacements and recommended the community to use FSI if certain WSS metrics are used as drivers for growth, most FSG and ABM frameworks utilize FSI/CFD snapshot to initialize the model, after which the growth model takes over [179, 256]. This limits the ability to accurately track the evolving biomechanical environment. We do not possess the technology for continuous, high-fidelity implementation of FSI or real-time FSI for the clinical use, but emerging surrogates (see PINN later) and reduced order models can offer a promising path. Factors that aid and hamper translation to the clinic are discussed below.

5.3.1 Translation to the clinic - What is in our favor and what isn't

From a broader perspective, our work contributes to the long-term goal of incorporating high-fidelity fluid-solid interaction modeling for long–term growth predictors in aortic pathologies and eventually translate this into clinical decision-making and working towards a digital twin. Achieving this will require overcoming current computational and workflow barriers. Discussed below are the upcoming strategies:

Why Mo(o)re is good - One challenge of FSI models highlighted in chapters 3, 4 are their significant computational cost. This is far from ideal in a clinical setting if insights are needed real-time. Fortunately, the continual progress in computing power which is governed by **Moore's law** which states that the computer power roughly doubles every two years [260], is steadily addressing this issue. Additionally, modern hardware such as GPUs and parallel processors have accelerated solver performance dramatically [261]. Therefore, if we continue to double computational speed every few years, the gap between a research-grade FSI simulation and a clinically useful turnaround time will narrow. This is evident in the number of studies related to cardiovascular FSI, which has increased two folds in the last 10 years [262].

However, it is worth noting that while raw speed helps, there is also a tendency for models to grow more detailed (and thus computationally hungry) as our ambitions expand. In summary, computational cost, while a limiting factor today, is likely to become less of a bottleneck in the near future, keeping the vision of expanding this work

to a digital twin and eventually simulations performed within clinical time frames alive. How far in the future? We cannot be sure of that.

Human Error and How to overcome it? A big barrier to clinical translation is the potential for human error in the modeling workflow. Building a patient-specific model involves multiple steps (image acquisition, segmentation, mesh generation, assigning boundary conditions, etc.) as highlighted in Chapter 2, each of which can introduce inconsistencies and uncertainities. For instance, in the 2013 CFD Challenge on cerebral aneurysms [263], multiple research groups were given the same geometry to simulate. The boundary conditions were standardized, whereas the users were free to choose their workflows like choice of solver etc. Around 80% of the groups produced quantitatively similar flow fields and pressures [263]. This suggests that if the geometry and boundary conditions are similar, result reproducibility is easier.
However, a follow-up 2015 CFD Challenge [264] allowed participants to use their own complete workflows (including imaging and segmentation choices) for a given set of aneurysm cases. The outcome was less favorable with WSS predictions varying widely between teams, with interquartile ranges of sac-averaged WSS differing by up to 56% from one group to another [264]. Notably, the ranking of "high-risk" areas in the aneurysm showed only modest agreement among participants. These two challenges demonstrated that user-dependent decisions such as geometry reconstrucion, boundary condition choices lead to inconsistent outcomes. Naturally, in a clinical context, such variability is unacceptable.

What is the way forward? While human error cannot be completely eliminated, the way forward lies in automating the modeling pipeline. Machine learning and convolutional neural network based algorithms are being incorporated to ensure automatic segmentation of vascular geometries from clinical imaging. These techniques not only reduce time but also minimize observer variability, with uncertainties on par with manual segmentation [254]. These techniques reduce a bottleneck by drastically reducing segmentation time, hence accelerating transition to a digital twin and eventually the clinic.

While automatic segmentation streamlines the pre-processing, another computational bottleneck is the solution or physics based modeling stage. An exciting technique gaining traction is physics-informed neural networks (PINN), where instead of writing a traditional solver, a neural network is trained to satisfy the governing equations (eg: Navier-Stokes) as part of its loss

function [265]. While the initial computational expense is high while training, the simulations in itself don't take too long [266]. One major advantage of PINNs, which might be relevant in clinical settings with sparse and uncertain patient data, are their ability to assimilate limited measurements (e.g., a few velocity points away from the vessel wall) and infer near-wall hemodynamics and predict WSS without the knowledge of boundary conditions [267]. Recent work has extended PINNs to fluid–solid interaction (FSI) problems where hybrid CFD–PINN frameworks have been applied to coronary artery trees [268] and aneurysmal flows [269], while Zhang et al. [270] demonstrated that fully PINN-based formulations can predict coupled FSI responses in good agreement with results from conventional numerical solvers. These approaches mark important steps toward physiologically realistic vascular Digital Twins, though challenges remain in training stability, working with complex domains [271].

In summary, while this thesis lays only the groundwork, the integration of fluid–solid growth models, uncertainty quantification, and data-driven approaches such as PINNs into the existing workflow will be essential for building a true vascular digital twin. Such a framework will evolve with real-time data, paving the way for more personalized and informed clinical decision-making. The time-frame for achieving this however will require sustained efforts in automation, computational acceleration. How far in the future is difficult to tell. Companies such as HeartFlow (CA,USA) provide virtual prediction of fractional flow reserve using CFD and deep-learning techniques, yet extending these methods to incorporate more complex features will present significant challenges.

Appendices

APPENDIX A

An Overset Meshing Approach for Aortic Dissection

The following work proposes an alternative strategy for grid deformation in an idealized dissection using the Chimera (overset) technique, for which a brief description was provided in Section 2.4.2.2. This work was presented as a talk at the 19th National Day on Biomedical Engineering. *

Rationale and Background

It has been alluded to in the state-of-the-art that the flap motion in acute dissections can reach up to 10 mm [185]. Given the fact that excessive distortion can sometimes lead to poor mesh quality while using Arbitrary Lagrangian-Eulerian (ALE) approach, an alternative methodology for grid motion is accounted. Movement of the intimal flap over the cardiac cycle and resultant pressure differences between the TL and FL have been well studied in an Arbitrary Lagrangian-Eulerian (ALE) framework [111], and more so in great detail for our study in Chapter 4. In this proof-of-concept study, we utilize an overset technique (Chimera) to move the intimal flap where the fluid mesh is embedded over a uniform cartesian grid. This method combines

*Balasubramanya, A. et al. (2020). CFD study of type-B aortic dissections with flap motion: proof of concept of overset meshing. Presented at the 19th National Day on Biomedical Engineering, Brussels.

the body conforming advantages of ALE and the large displacement of the Immersed Boundary Method to ensure the fluid grid can move to a large extent with minimal loss in grid quality. Some initial results and lessons learnt as to why this approach was not extended to an FSI framework are provided.

Methodology

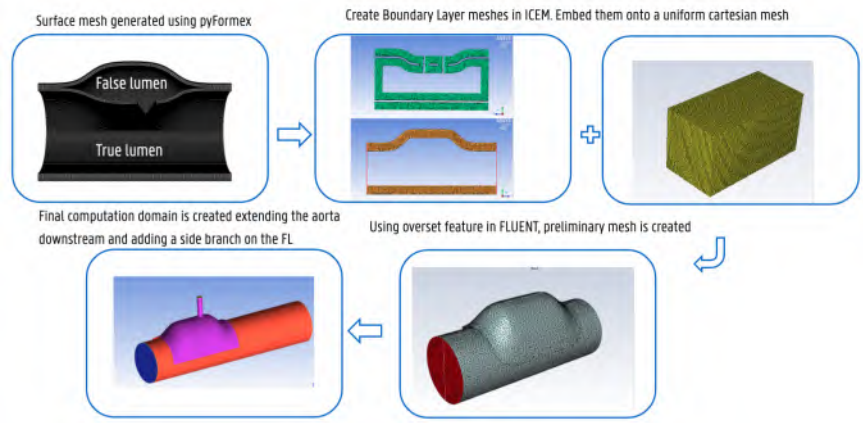

Figure A1: Methodology to create the final computational domain using overset meshes.

The methodology to generate the final computational domain is shown in Figure A1. Initially, a patient-inspired model was generated using the in-house open source tool pyFormex [103]. The surface mesh is extracted and two component grids shown in the second panel (one representing the regions around the intimal flap and the other representing the outer layer of the false lumen) are created as boundary layer meshes in the meshing tool ICEM(Ansys Inc, USA). These component meshes are embedded in a uniform cartesian grid shown in the third panel. A side branch was added towards the distal exit of the false lumen as shown in the last panel of Figure A1 and the overset feature in FLUENT 2019R3 (Ansys Inc, PA, USA) was used to generate the final geometry and solve the governing flow equations. A net displacement of 4 mm was prescribed on the flap throughout the cardiac cycle with a 2 mm amplitude during peak systole and early diastole respectively using a user-defined function in Ansys Fluent (Ansys Inc, USA) as shown in Figure A2.

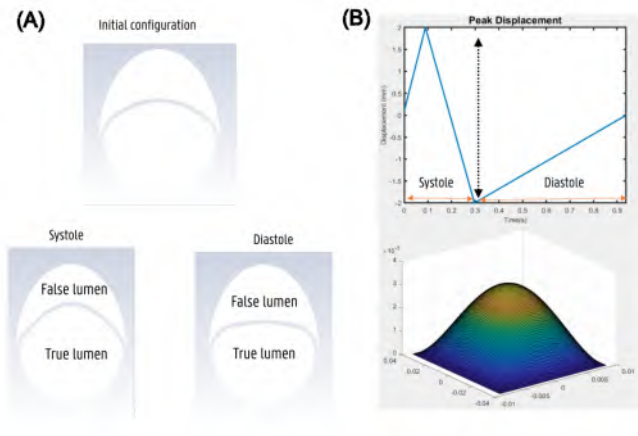

Figure A2: Panel (A) shows the initial configuration along with the final configurations at systole and diastole. Panel (B) shows the imposed profile at the intimal flap resulting in a net displacement of 4 mm.

The outlet pressure waveform was calculated using a 3- element windkessel model similar to the methodology in Chapter 4. The windkessel parameters were manually tuned to ensure 5%, 2.5% or 0% of total flow through the side branches for a systolic to diastolic pressure range of 120/80 mm Hg throughout the domain using a user defined function in Ansys Fluent (Ansys Inc, USA). An inlet velocity profile was prescribed such that the flow is laminar for a constant dynamic viscosity of 0.0035 Pa · s with blood assumed to be a Newtonian fluid.

Results, Issues and Lessons Learnt

The side branch flow minimally affects true-to-false lumen pressure difference, which increases marginally with increase in side branch flow rate in systole as observed in Figure A3. This proof of concept approach is a precursor to a fully coupled FSI simulation which would give a more accurate representation of flap motion, hemodynamics and true-to-false lumen pressure variation.

A net displacement of 8 mm

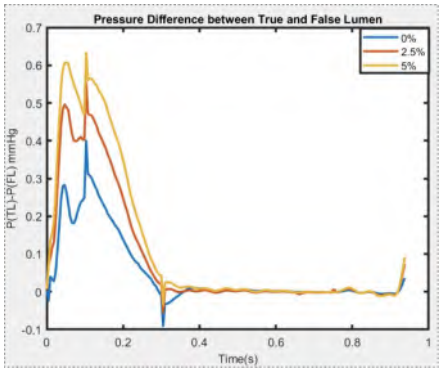

Figure A3: Pressure difference between true and false lumen for different flow rates through the side branch.

was also successfully tested. Although the overset approach was able to capture such large displacements, the robustness decreased when more than two component grids were used, as illustrated in Figure A4. During some time steps, the entire primary tear component temporarily disappeared, only to reappear in subsequent step. In other instances, only a single mesh component remained active. These instabilities highlight the challenges of maintaining consistent grid connectivity for multi-component overset simulations. Moreover, achieving a stable and reliable setup was not only computationally expensive, but time-consuming particularly during the grid generation and overset connectivity stages.

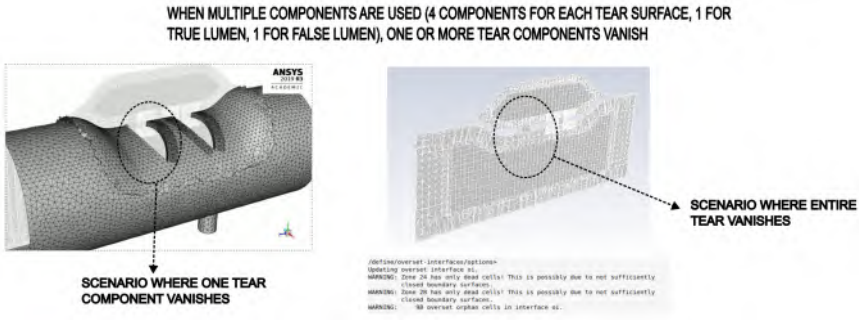

Figure A4: Issues highlighted when multiple component meshes are used.

APPENDIX B

Linear Elastic Constitutive Model for Type-B Aortic Dissection

Introduction

This study is an extension of Appendix A and a pre-cursor to the method finalized in Chapter 4. As highlighted in Appendix A, a multi-component overset approach was computationally very expensive along with issues with robustness. Therefore, a translation to FSI for overset meshes was not done. Keeping these issues in mind, the traditional arbitrary Lagrangian-Eulerian [111] method, for which a brief theoretical overview was discussed in Section 2.4.2.1 is used. The focus here is to perform a strongly coupled FSI simulation using a linear elastic model for aorta and the intimal flap. This can be considered as Step 2 towards achieving the desired result in Chapter 4. This work was presented as a poster at an international conference *

*Balasubramanya, A. et al. (2023). Fluid-structure interaction simulations in an idealized model of the dissected aorta: relation between false lumen pressure and outflow via side branches. Presented at the 2023 Summer Biomechanics, Bioengineering and Biotransport Conference (SB3C 2023), Vail, CO, USA.

Methods

An idealized dissection model with an axial length of 60 mm, a dissection length 40 mm and two tears were generated similar to [92] using the in house geometry and mesh generation tool PyFormex [103].Two new parameters were defined called extent of dissection (s/S= 0.66 and s/S=0.5) where 's' is the circumference of the FL and 'S' is the total aortic circumference and flap thickness ratio (t/T= 0.4454) where 't' is the thickness of the dissected membrane and 'T' is the overall aortic thickness. To the resulting configuration, a side branch with a diameter (d) of 3 mm ($\approx$ 0.1 time the diameter of the aorta) and a length of 15mm was added in the FL resulting in a geometries as seen in Figure B1.

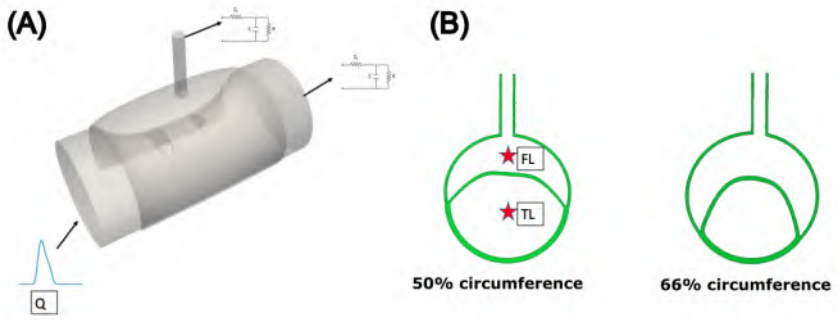

Figure B1: Panel (A) shows the boundary conditions applied in the fluid model; Panel (B) shows the two geometries of interest with figure showing a cross sectional view of the geometry with 50% circumference and 66% circumference of the false lumen respectively.

The resultant structural models were meshed using 151128 linear tetrahedral (C3D4H) elements in Abaqus (Dassault Systems, USA) and the surrounding lumen was filled with 374592 tetrahedral elements using ICEMCFD (Ansys Inc, PA, USA). A flat velocity profile was prescribed at the inlet based on literature [77] and scaled to match a mean flow of 3.87 l/min [194] in the descending aorta. Downstream, 3-element windkessel models (WK) were imposed and the WK parameters were tuned to achieve diastolic/systolic pressure of 80/120 mmHg. Two cases were considered: one with 5% and the other with 0.5% of the total flow through the side branch. For the soft tissue, a linear elastic model was considered to model the material properties chosen from Delpano [203]. Stiffness of the aortic tissue was 5.39MPa and that of the intimal flap was 0.51MPa with a Poisson's ratio of 0.45. Nodes at the inlet and outlets were constrained except for movement along the radial direction. Initial stresses in the

structural model without a side branch were determined using the pre-stretch algorithm previously implemented by Famaey [99]. The resulting stresses were mapped to the configuration with side branch using nearest neighbor interpolation using an in-house implemented python script. The governing fluid equations were solved using the finite volume solver Fluent (Ansys Inc, PA, USA) and structural equations were solved using the finite element solver Abaqus (Dassault Systems, USA). Coupling between the flow and structural solver was performed using the in-house coupling code CoCoNuT [106]. A partitioned FSI simulation where 72 cores were used for the fluid solver and 48 for the structural solver took 27 hours for four cardiac cycles where a time period of 0.6 seconds for each cardiac cycle was chosen for a time step size of 3.2 ms.

Results and lessons learnt

Since the intention of this study is to assess the impact of outflow via side branches, pressure variation across the TL and FL are studied. As observed from Figure B2, an increased side branch outflow resulted in an increased pressure in the TL at systole, leading to an increased transmembrane pressure difference (TMP) for both configurations as seen in Figure B2. This is consistent with the obtained results in Chapters 4 and 4A.

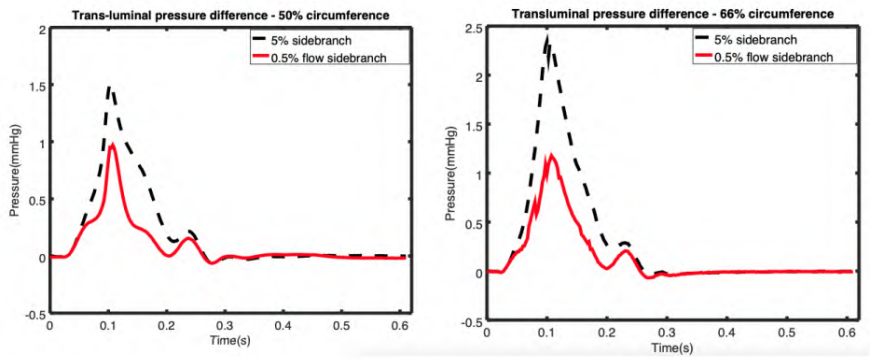

Figure B2: Pressure comparison between true and false lumen for different flow rates for 50% and 66% circumference of the false lumen respectively.

Flap motion was limited (0.9 mm displacement in the intimal flap at peak systole) and FL volume changes were mainly due to outer wall expansion rather than flap displacements. This can be attributed to increased s/S, high membrane thickness and material stiffness in the configuration. While a partitioned FSI study that includes variable

flow through the side branch in the FL has never before been studied, there are some limitations which need to be addressed. Even though realistic initial stresses are used, rather simplistic material properties are considered for the flap and the aortic tissue.

Lessons learnt to achieve results from Chapter 4

- Sub 1 mm flap displacement can be attributed to increased flap stiffness as discussed previously. Attempts were made to reduce the flap stiffness to 20 kPa similar to Baumler et al. [93]. However, any reduction of flap stiffness below 0.5 MPa led to convergence issues. Resorting to structured meshes and accounting for more realistic material properties might be a good start.

- Though pre-stress was not directly incorporated, a stress free configuration is obtained by applying the deposition stretch algorithm for the geometry from Gheysen et al. [92] which has the same dimensions and utilizes a GOH model to characterize tissue behavior. Then a nearest neighbor interpolation was performed from Gheysen et al's configuration to the current geometry. Utilizing Gheysen et al.'s geometry as a starting point can be a good approach.

- Finally, the chosen dissected length of 40 mm might be too small. While Gheysen et al.'s geometry was patient inspired, longer dissection geometries in line with measurements from literature can be the final step 1

Bibliography

[1] J. D. Humphrey and M. A. Schwartz, 'Vascular Mechanobiology: Homeostasis, Adaptation, and Disease', *Annual Review of Biomedical Engineering*, vol. 23, no. 1, pp. 1–27, 2021 (cit. on pp. 1, 55).

[2] D. Ambrosi et al., *Growth and remodelling of living tissues: Perspectives, challenges and opportunities*, 2019 (cit. on pp. 1, 3).

[3] D. N. Ross, 'Replacement of aortic and mitral valves with a pulmonary autograft.' *Lancet*, vol. 2, no. 7523, pp. 956–958, 1967 (cit. on pp. 1, 17).

[4] L. Van Hoof et al., 'Understanding Pulmonary Autograft Remodeling After the Ross Procedure: Stick to the Facts', *Frontiers in Cardiovascular Medicine*, vol. 9, p. 141, 2022 (cit. on pp. 2, 18–20).

[5] N. S. Burris et al., 'False lumen ejection fraction predicts growth in type B aortic dissection: preliminary results.' *European journal of cardio-thoracic surgery : official journal of the European Association for Cardio-thoracic Surgery*, vol. 57, no. 5, pp. 896–903, 2020 (cit. on pp. 2, 24, 111, 112, 123, 151).

[6] D. Marlevi et al., 'False lumen pressure estimation in type B aortic dissection using 4D flow cardiovascular magnetic resonance: comparisons with aortic growth.' *Journal of cardiovascular magnetic resonance : official journal of the Society for Cardiovascular Magnetic Resonance*, vol. 23, no. 1, p. 51, 2021 (cit. on pp. 2, 4, 24, 100, 102, 120, 123, 151).

[7] L. Gheysen, L. Maes, N. Famaey and P. Segers, 'Growth and remodeling of the dissected membrane in an idealized dissected aorta model', *Biomechanics and Modeling in Mechanobiology*, no. 0123456789, 2023 (cit. on pp. 2, 24, 51, 126).

[8] C. Alberto Figueroa, S. Baek, C. A. Taylor and J. D. Humphrey, 'A computational framework for fluid–solid-growth modeling in cardiovascular simulations', *Computer Methods in Applied Mechanics and Engineering*, vol. 198, no. 45-46, pp. 3583–3602, 2009 (cit. on pp. 2, 93, 155).

[9] I. E. Hoefer, B. den Adel and M. J. A. P. Daemen, 'Biomechanical factors as triggers of vascular growth', *Cardiovascular Research*, vol. 99, no. 2, pp. 276–283, 2013 (cit. on p. 2).

[10] M. J. Ramaekers et al., 'A clinician's guide to understanding aortic 4D flow MRI', *Insights into Imaging*, vol. 14, no. 1, pp. 1–14, 2023 (cit. on p. 2).

[11] C Stokes et al., 'The Influence of Minor Aortic Branches in Patient-Specific Flow Simulations of Type-B Aortic Dissection.' *Annals of biomedical engineering*, vol. 51, no. 7, pp. 1627–1644, 2023 (cit. on pp. 4, 100, 101, 122, 125, 132, 153).

[12] G. J. Tortora and B. H. Derrickson, 'Principles of anatomy and physiology'. John Wiley & Sons, 2018 (cit. on pp. 11, 12, 14).

[13] G. G. Belz, 'Elastic properties and Windkessel function of the human aorta', *Cardiovascular Drugs and Therapy*, vol. 9, no. 1, pp. 73–83, 1995 (cit. on p. 11).

[14] M. Rolf-Pissarczyk et al., 'Mechanisms of aortic dissection: From pathological changes to experimental and in silico models', *Progress in Materials Science*, vol. 150, p. 101 363, 2025 (cit. on pp. 12, 14, 21, 24, 25).

[15] G. Georges, T. Couture and P. Voisine, 'Assessment of large animal vascular dimensions for intra-aortic device research and development: A systematic review', *Innovations: Technology and Techniques in Cardiothoracic and Vascular Surgery*, vol. 18, pp. 144–151, 2 2023 (cit. on p. 13).

[16] A. M. Malek, S. L. Alper and S. Izumo, 'Hemodynamic shear stress and its role in atherosclerosis', *JAMA*, vol. 282, pp. 2035–2042, 21 1999 (cit. on pp. 14, 46).

[17] J. G. Augoustides and A. T. Cheung, 'Aneurysms and dissections', *Perioperative Transesophageal Echocardiography: A companion to Kaplan's Cardiac Anesthesia*, pp. 191–217, 2014 (cit. on p. 14).

[18] P. Lacolley, V. Regnault, P. Segers and S. Laurent, 'Vascular smooth muscle cells and arterial stiffening: Relevance in development, aging, and disease', *Physiological Reviews*, vol. 97, pp. 1555–1617, 4 2017 (cit. on p. 14).

[19] A. Bulut et al., 'Aortic intima-media thickness can be used to determine target organ damage in adult patients with coronary artery disease risk factors', *Archives of Medical Science – Atherosclerotic Diseases*, vol. 4, pp. 183–190, 1 2019 (cit. on p. 14).

[20] G. A. Holzapfel, T. C. Gasser and R. W. Ogden, 'A New Constitutive Framework for Arterial Wall Mechanics and a Comparative Study of Material Models', *Journal of Elasticity*, vol. 61, pp. 1–48, 2000 (cit. on pp. 14, 34).

[21] P. R. Hoskins, P. V. Lawford and B. J. Doyle, 'Cardiovascular Biomechanics'. Springer International Publishing, 2017, pp. 1–462 (cit. on pp. 14–16).

[22] E. W. Errill, 'Rheology of blood', *Physiological Reviews*, vol. 49, no. 4, pp. 863–888, 1969 (cit. on p. 15).

[23] F. Yilmaz, M. Y. Gundogdu et al., 'A critical review on blood flow in large arteries; relevance to blood rheology, viscosity models, and physiologic conditions', *Korea-Australia Rheology Journal*, vol. 20, no. 4, pp. 197–211, 2008 (cit. on p. 15).

[24] R. Fåhræus and T. Lindqvist, 'The viscosity of the blood in narrow capillary tubes', *https://doi.org/10.1152/ajplegacy.1931.96.3.562*, vol. 96, pp. 562–568, 3 1931 (cit. on p. 15).

[25] D. N. Ku, 'Blood flow in arteries', *Annual Review of Fluid Mechanics*, vol. 29, no. 1, pp. 399–434, 1997 (cit. on pp. 15, 153).

[26] K. G. Lyras and J. Lee, 'Haemodynamic analysis using multiphase flow dynamics in tubular lesions', *Computer Methods and Programs in Biomedicine*, vol. 220, p. 106 780, 2022 (cit. on p. 16).

[27] J. Jung and A. Hassanein, 'Three-phase CFD analytical modeling of blood flow', *Medical Engineering & Physics*, vol. 30, no. 1, pp. 91–103, 2008 (cit. on p. 16).

[28] M. O. Bernabeu et al., 'Impact of blood rheology on wall shear stress in a model of the middle cerebral artery', *Interface Focus*, vol. 3, no. 2, p. 20 120 094, 2013 (cit. on p. 16).

[29] C. F. Barker and J. F. Markmann, 'Historical Overview of Transplantation', *Cold Spring Harbor Perspectives in Medicine*, vol. 3, no. 4, a014977–a014977, 2013 (cit. on p. 16).

[30] A. N. Oli et al., 'Classic and current opinions in human organ and tissue transplantation', *Cureus*, vol. 14, 11 2022 (cit. on pp. 16, 17).

[31] C. A. Janeway, P. Travers, M. Walport, M. J. Shlomchik et al., 'Immunobiology: the immune system in health and disease'. Garland Pub. New York, NY, USA, 2001, vol. 2 (cit. on pp. 16, 17).

[32] Y. Ando et al., 'Size and stiffness of the pulmonary autograft after the ross procedure in children', *Pediatric Cardiology*, vol. 40, pp. 776–783, 4 2019 (cit. on pp. 16, 17).

[33] W. Flameng, R. Jashari, G. D. Visscher, L. Mesure and B. Meuris, 'Calcification of allograft and stentless xenograft valves for right ventricular outflow tract reconstruction: An experimental study in adolescent sheep', *The Journal of Thoracic and Cardiovascular Surgery*, vol. 141, pp. 1513–1521, 6 2011 (cit. on p. 17).

[34] A. H. Chester, I. El-Hamamsy, J. T. Butcher, N. Latif, S. Bertazzo and M. H. Yacoub, 'The living aortic valve: From molecules to function', *Global Cardiology Science and Practice*, vol. 2014, p. 11, 1 2014 (cit. on p. 17).

[35] K. Pohle et al., 'Progression of aortic valve calcification', *Circulation*, vol. 104, pp. 1927–1932, 16 2001 (cit. on p. 17).

[36] A. Vahanian et al., '2021 esc/eacts guidelines for the management of valvular heart disease: Developed by the task force for the management of valvular heart disease of the european society of cardiology (esc) and the european association for cardiothoracic surgery (eacts)', *European Heart Journal*, vol. 43, pp. 561–632, 7 2022 (cit. on p. 17).

[37] T. E. David, 'Surgical treatment of aortic valve disease', *Nature Reviews Cardiology*, vol. 10, pp. 375–386, 7 2013 (cit. on p. 17).

[38] A. Mazine et al., 'Ross Procedure in Adults for Cardiologists and Cardiac Surgeons', *Journal of the American College of Cardiology*, vol. 72, no. 22, pp. 2761–2777, 2018 (cit. on p. 17).

[39] E. Rabkin-Aikawa et al., 'Clinical pulmonary autograft valves: Pathologic evidence of adaptive remodeling in the aortic site', *The Journal of Thoracic and Cardiovascular Surgery*, vol. 128, pp. 552–561, 4 2004 (cit. on p. 18).

[40] P. H. Schoof et al., 'Degeneration of the pulmonary autograft: An explant study', *The Journal of Thoracic and Cardiovascular Surgery*, vol. 132, no. 6, pp. 1426–1432, 2006 (cit. on pp. 18, 19).

[41] M. H. Yacoub, V. Tsang, P. Sarathchandra, H. Jensen, S. Hughes and N. Latif, 'Long-term adaptive versus maladaptive remodelling of the pulmonary autograft after the ross operation', *European Journal of Cardio-Thoracic Surgery*, vol. 57, pp. 977–985, 5 2020 (cit. on p. 18).

[42] A. Mookhoek et al., 'Biomechanics of Failed Pulmonary Autografts Compared With Normal Pulmonary Roots', in *Annals of Thoracic Surgery*, vol. 102, Elsevier, 2016, pp. 1996–2002 (cit. on p. 18).

[43] P. H. Schoof et al., 'Disproportionate enlargement of the pulmonary autograft in the aortic position in the growing pig', *Journal of Thoracic and Cardiovascular Surgery*, vol. 115, no. 6, pp. 1264–1272, 1998 (cit. on p. 19).

[44] P. H. Schoof, A. C. Gittenberger-de Groot, E. De Heer, J. A. Bruijn, M. G. Hazekamp and H. A. Huysmans, 'Remodeling of the porcine pulmonary autograft wall in the aortic position', *Journal of Thoracic and Cardiovascular Surgery*, vol. 120, no. 1, pp. 55–64, 2000 (cit. on p. 19).

[45] E. Vanderveken et al., 'Reinforcing the pulmonary artery autograft in the aortic position with a textile mesh: a histological evaluation', *Interactive CardioVascular and Thoracic Surgery*, vol. 27, no. 4, pp. 566–573, 2018 (cit. on pp. 19, 20).

[46] J. Vastmans et al., 'Biomechanical evaluation of a personalized external aortic root support applied in the Ross procedure', *Journal of the Mechanical Behavior of Biomedical Materials*, vol. 78, pp. 164–174, 2018 (cit. on pp. 19, 20).

[47] E. Vanderveken et al., 'Mechano-biological adaptation of the pulmonary artery exposed to systemic conditions.' *Scientific reports*, vol. 10, no. 1, p. 2724, 2020 (cit. on pp. 19, 59, 61, 154).

[48] P. Panpho et al., 'Macro- and micro-mechanical properties of the ovine aorta: Correlation with regional variations in collagen, elastin and glycosaminoglycan levels', *Artery Research*, vol. 25, pp. 27–36, 1-2 2019 (cit. on p. 20).

[49] S. M. Wells, B. L. Langille, J. M. Lee and S. L. Adamson, 'Determinants of mechanical properties in the developing ovine thoracic aorta', *https://doi.org/10.1152/ajpheart.1999.277.4.H1385*, vol. 277, 4 46-4 1999 (cit. on p. 20).

[50] E. Rivera et al., 'Biomechanical characterization of the passive response of the thoracic aorta in chronic hypoxic newborn lambs using an evolutionary strategy', *Scientific Reports 2021 11:1*, vol. 11, pp. 13 875–, 1 2021 (cit. on p. 20).

[51] B. Fata et al., 'Regional structural and biomechanical alterations of the ovine main pulmonary artery during postnatal growth', *Journal of Biomechanical Engineering*, vol. 135, 2 2013 (cit. on p. 20).

[52] M. S. Cabrera, C. W. Oomens, C. V. Bouten, A. J. Bogers, S. P. Hoerstrup and F. P. Baaijens, 'Mechanical analysis of ovine and pediatric pulmonary artery for heart valve stent design', *Journal of Biomechanics*, vol. 46, pp. 2075–2081, 12 2013 (cit. on p. 20).

[53] V. Kapur and W. A. Gray, 'Management of aneurysmal disease of the aorta', *Interventional Cardiology Clinics*, vol. 3, pp. 545–555, 4 2014 (cit. on p. 20).

[54] A. Pepe et al., 'Detection, segmentation, simulation and visualization of aortic dissections: A review', *Medical Image Analysis*, vol. 65, p. 101 773, 2020 (cit. on pp. 21, 22).

[55] L. Gheysen, 'On the uncertainty of biomechanical modeling of the aortic wall in type b dissections', eng, Ph.D. dissertation, Ghent University, 2024, XXVI, 173 (cit. on pp. 21, 37, 38, 154).

[56] M. E. DEBAKEY, W. S. HENLY, D. A. COOLEY, G. C. MORRIS, E. S. CRAWFORD and A. C. BEALL, 'Surgical management of dissecting aneurysms of the aorta', *The Journal of Thoracic and Cardiovascular Surgery*, vol. 49, pp. 130–149, 1 1965 (cit. on p. 21).

[57] P. O. Daily, H. W. Trueblood, E. B. Stinson, R. D. Wuerflein and N. E. Shumway, 'Management of acute aortic dissections', *The Annals of Thoracic Surgery*, vol. 10, pp. 237–247, 3 1970 (cit. on p. 21).

[58] S. Peterss et al., 'Changing Pathology of the Thoracic Aorta From Acute to Chronic Dissection: Literature Review and Insights', *Journal of the American College of Cardiology*, vol. 68, no. 10, pp. 1054–1065, 2016 (cit. on pp. 21, 23, 24, 99, 124).

[59] R. O. Tadros et al., 'Optimal treatment of uncomplicated type b aortic dissection: Jacc review topic of the week', *Journal of the American College of Cardiology*, vol. 74, pp. 1494–1504, 11 2019 (cit. on p. 22).

[60] T. T. Tsai et al., 'Partial thrombosis of the false lumen in patients with acute type B aortic dissection.' *The New England journal of medicine*, vol. 357, no. 4, pp. 349–59, 2007 (cit. on pp. 22, 100, 124).

[61] M. Strehlow and J. Tabas, 'Chest pain', *Emergency Medicine: Clinical Essentials, SECOND EDITION*, 445–451.e1, 2013 (cit. on p. 22).

[62] K. Rajagopal, C. Bridges and K. R. Rajagopal, 'Towards an understanding of the mechanics underlying aortic dissection', *Biomechanics and Modeling in Mechanobiology*, vol. 6, pp. 345–359, 5 2007 (cit. on p. 23).

[63] N. F. MacLean, N. L. Dudek and M. R. Roach, 'The role of radial elastic properties in the development of aortic dissections', *Journal of Vascular Surgery*, vol. 29, pp. 703–710, 4 1999 (cit. on p. 23).

[64] B. Trachet et al., 'Angiotensin II infusion into ApoE-/- mice: a model for aortic dissection rather than abdominal aortic aneurysm?', *Cardiovascular Research*, vol. 113, no. 10, pp. 1230–1242, 2017 (cit. on p. 23).

[65] E. Sueyoshi, I. Sakamoto, K. Hayashi, T. Yamaguchi and T. Imada, 'Growth rate of aortic diameter in patients with type b aortic dissection during the chronic phase', *Circulation*, vol. 110, 11 SUPPL. 2004 (cit. on p. 23).

[66] D. Spinelli et al., 'Current evidence in predictors of aortic growth and events in acute type b aortic dissection', *Journal of Vascular Surgery*, vol. 68, 1925–1935.e8, 6 2018 (cit. on p. 24).

[67] M. K. Ganten et al., 'Motion characterization of aortic wall and intimal flap by ecg-gated ct in patients with chronic b-dissection', *European Journal of Radiology*, vol. 72, pp. 146–153, 1 2009 (cit. on p. 24).

[68] H. Dong et al., ‘Protective biomechanical and histological changes in the false lumen wall in chronic type b aortic dissection’, *JTCVS Open*, vol. 23, pp. 60–68, 2025 (cit. on p. 24).

[69] D. Thakkar and M. D. Dake, ‘Management of type b aortic dissections: Treatment of acute dissections and acute complications from chronic dissections’, *Techniques in Vascular and Interventional Radiology*, vol. 21, pp. 124–130, 3 2018 (cit. on p. 24).

[70] E. M. Isselbacher et al., ‘2022 acc/aha guideline for the diagnosis and management of aortic disease: A report of the american heart association/american college of cardiology joint committee on clinical practice guidelines’, *Circulation*, vol. 146, E334–E482, 24 2022 (cit. on p. 25).

[71] H. Versteeg and W. Malalasekera, ‘An Introduction to Computational Fluid Dynamics: The Finite Volume Method’. Pearson Education Limited, 2007 (cit. on pp. 27, 30, 38, 39).

[72] L. Reid, ‘An introduction to biomedical computational fluid dynamics’, *Advances in Experimental Medicine and Biology*, vol. 1334, pp. 205–222, 2021 (cit. on p. 27).

[73] J. H. Ferziger and M. Perić, ‘Computational Methods for Fluid Dynamics’, J. F. Wendt, Ed. Berlin, Heidelberg: Springer Berlin Heidelberg, 2002 (cit. on pp. 28, 30, 38, 39).

[74] A. Updegrove, N. M. Wilson, J. Merkow, H. Lan, A. L. Marsden and S. C. Shadden, ‘SimVascular: An Open Source Pipeline for Cardiovascular Simulation’, *Annals of Biomedical Engineering*, vol. 45, no. 3, pp. 525–541, 2017 (cit. on pp. 28, 38).

[75] C. J. Arthurs et al., ‘CRIMSON: An open-source software framework for cardiovascular integrated modelling and simulation’, *PLOS Computational Biology*, vol. 17, no. 5, D. Schneidman-Duhovny, Ed., e1008881, 2021 (cit. on pp. 28, 38).

[76] F. M. White, ‘Fluid Mechanics’, 8th. New York: McGraw–Hill Education, 2016 (cit. on p. 28).

[77] S. Madhavan and E. M. Kemmerling, ‘The effect of inlet and outlet boundary conditions in image-based CFD modeling of aortic flow’, *BioMedical Engineering Online*, vol. 17, no. 1, pp. 1–20, 2018 (cit. on pp. 30, 154, 155, 168).

[78] C. H. Armour et al., 'The influence of inlet velocity profile on predicted flow in type B aortic dissection.' *Biomechanics and modeling in mechanobiology*, vol. 20, no. 2, pp. 481–490, 2021 (cit. on pp. 30, 95, 124, 154).

[79] B. Ramazanli, O. Yagmur, E. C. Sarioglu and H. E. Salman, 'Modeling Techniques and Boundary Conditions in Abdominal Aortic Aneurysm Analysis: Latest Developments in Simulation and Integration of Machine Learning and Data-Driven Approaches', *Bioengineering*, vol. 12, no. 5, p. 437, 2025 (cit. on p. 30).

[80] N. Westerhof, J. W. Lankhaar and B. E. Westerhof, 'The arterial windkessel', *Medical and Biological Engineering and Computing*, vol. 47, no. 2, pp. 131–141, 2009 (cit. on pp. 31, 32, 97, 125, 131).

[81] I. E. Vignon-Clementel, C. A. Figueroa, K. E. Jansen and C. A. Taylor, 'Outflow boundary conditions for three-dimensional finite element modeling of blood flow and pressure in arteries', *Computer Methods in Applied Mechanics and Engineering*, vol. 195, pp. 3776–3796, 29-32 2006 (cit. on p. 31).

[82] J. Degroote, 'Partitioned Simulation of Fluid-Structure Interaction', *Archives of Computational Methods in Engineering 2013 20:3*, vol. 20, no. 3, pp. 185–238, 2013 (cit. on pp. 31, 36, 40, 41, 43–45).

[83] M. R. Pfaller, J. Pham, N. M. Wilson, D. W. Parker and A. L. Marsden, 'On the Periodicity of Cardiovascular Fluid Dynamics Simulations', *Annals of Biomedical Engineering*, vol. 49, no. 12, pp. 3574–3592, 2021 (cit. on p. 31).

[84] P. Segers and J. A. Chirinos, 'Arterial wall stiffness: basic principles and methods of measurement in vivo', *Textbook of Arterial Stiffness and Pulsatile Hemodynamics in Health and Disease*, pp. 111–124, 2022 (cit. on p. 32).

[85] P. Cardiff, I. Batistić and Ž. Tuković, 'solids4foam: A toolbox for performing solid mechanics and fluid-solid interaction simulations in OpenFOAM', *Journal of Open Source Software*, vol. 10, no. 108, p. 7407, 2025 (cit. on p. 33).

[86] I. Bijelonja, I. Demirdžić and S. Muzaferija, 'A finite volume method for large strain analysis of incompressible hyperelastic materials', *International Journal for Numerical Methods in Engineering*, vol. 64, no. 12, pp. 1594–1609, 2005 (cit. on p. 33).

[87] G. A. Holzapfel, 'Nonlinear Solid Mechanics: A Continuum Approach for Engineering'. Chichester: John Wiley & Sons, 2000 (cit. on pp. 33–36, 39).

[88] T. C. Gasser, R. W. Ogden and G. A. Holzapfel, *Hyperelastic modelling of arterial layers with distributed collagen fibre orientations*, 2006 (cit. on pp. 34, 35, 61, 105, 140).

[89] J. D. Humphrey and K. R. Rajagopal, 'A constrained mixture model for growth and remodeling of soft tissues', *Mathematical Models and Methods in Applied Sciences*, vol. 12, no. 3, pp. 407–430, 2002 (cit. on pp. 34, 50, 56).

[90] G. A. Holzapfel and R. W. Ogden, 'Constitutive modelling of arteries', *Proceedings of the Royal Society A: Mathematical, Physical and Engineering Sciences*, vol. 466, pp. 1551–1597, 2118 2010 (cit. on p. 34).

[91] H. Fehervary, M. Smoljkić, J. V. Sloten and N. Famaey, 'Planar biaxial testing of soft biological tissue using rakes: A critical analysis of protocol and fitting process', *Journal of the Mechanical Behavior of Biomedical Materials*, vol. 61, pp. 135–151, 2016 (cit. on p. 36).

[92] L. Gheysen, L. Maes, N. Famaey and P. Segers, 'Pulse wave velocity: A clinical measure to aid material parameter estimation in computational arterial biomechanics', *Journal of Biomechanics*, vol. 149, p. 111 482, 2023 (cit. on pp. 36, 105, 107, 140, 154, 168, 170).

[93] K. Bäumler et al., 'Fluid-structure interaction simulations of patient-specific aortic dissection.' *Biomechanics and modeling in mechanobiology*, vol. 19, no. 5, pp. 1607–1628, 2020 (cit. on pp. 36, 100, 101, 104, 108, 122, 123, 125, 151, 170).

[94] P. Moireau et al., 'External tissue support and fluid-structure simulation in blood flows', *Biomechanics and modeling in mechanobiology*, vol. 11, no. 1-2, pp. 1–18, 2012 (cit. on pp. 36, 108).

[95] L. Cardamone, A. Valentín, J. F. Eberth and J. D. Humphrey, 'Origin of axial prestretch and residual stress in arteries', *Biomechanics and Modeling in Mechanobiology*, vol. 8, pp. 431–446, 6 2009 (cit. on p. 36).

[96] J. Bols, J. Degroote, B. Trachet, B. Verhegghe, P. Segers and J. Vierendeels, 'A computational method to assess the in vivo stresses and unloaded configuration of patient-specific blood vessels', *Journal of Computational and Applied Mathematics*, vol. 246, pp. 10–17, 2013 (cit. on p. 37).

[97] S. de Putter, B. J. Wolters, M. C. Rutten, M. Breeuwer, F. A. Gerritsen and F. N. van de Vosse, 'Patient-specific initial wall stress in abdominal aortic aneurysms with a backward incremental method', *Journal of Biomechanics*, vol. 40, pp. 1081–1090, 5 2007 (cit. on p. 37).

[98] M. L. Raghavan, B. Ma and M. F. Fillinger, 'Non-invasive determination of zero-pressure geometry of arterial aneurysms', *Annals of Biomedical Engineering*, vol. 34, pp. 1414–1419, 9 2006 (cit. on p. 37).

[99] N. Famaey et al., 'Numerical simulation of arterial remodeling in pulmonary autografts', *ZAMM - Journal of Applied Mathematics and Mechanics / Zeitschrift für Angewandte Mathematik und Mechanik*, vol. 98, no. 12, pp. 2239–2257, 2018 (cit. on pp. 37, 55, 56, 59, 60, 140, 169).

[100] C. Bellini, J. Ferruzzi, S. Roccabianca, E. S. D. Martino and J. D. Humphrey, 'A microstructurally motivated model of arterial wall mechanics with mechanobiological implications', *Annals of Biomedical Engineering*, vol. 42, pp. 488–502, 3 2014 (cit. on p. 37).

[101] L. Maes, N. Famaey and J. Vander Sloten, 'Predicting the long-term effects of mechanical overload to arterial tissue: A chemo-mechano-biological computational framework', eng, Ph.D. dissertation, 2022-09-27 (cit. on p. 38).

[102] J. Vastmans et al., 'Growth and remodeling in the pulmonary autograft: Computational evaluation using kinematic growth models and constrained mixture theory', *International Journal for Numerical Methods in Biomedical Engineering*, vol. 38, no. 1, 2022 (cit. on pp. 38, 56, 59, 61, 62, 93–95).

[103] G. De Santis, P. Mortier, M. De Beule, P. Segers, P. Verdonck and B. Verhegghe, 'Patient-specific computational fluid dynamics: structured mesh generation from coronary angiography', *Medical & Biological Engineering & Computing*, vol. 48, no. 4, pp. 371–380, 2010 (cit. on pp. 38, 59, 139, 164, 168).

[104] O. C. Zienkiewicz and R. L. Taylor, 'The Finite Element Method: Volume 1, The Basis', 5th. Oxford: Butterworth-Heinemann, 2005 (cit. on pp. 38, 39).

[105] W. K. Liu, S. Li and H. S. Park, 'Eighty years of the finite element method: Birth, evolution, and future', *Archives of Computational Methods in Engineering*, vol. 29, pp. 4431–4453, 6 2021 (cit. on p. 39).

[106] N. Delaissé, T. Demeester, R. Haelterman and J. Degroote, 'Quasi-Newton Methods for Partitioned Simulation of Fluid–Structure Interaction Reviewed in the Generalized Broyden Framework', *Archives of Computational Methods in Engineering*, vol. 30, no. 5, pp. 3271–3300, 2023 (cit. on pp. 40, 43, 63, 94, 110, 169).

[107] F. Syed, S. Khan and M. Toma, 'Modeling dynamics of the cardiovascular system using fluid-structure interaction methods', *Biology 2023, Vol. 12, Page 1026*, vol. 12, p. 1026, 7 2023 (cit. on p. 41).

[108] N. Delaissé, T. Demeester, D. Fauconnier and J. Degroote, 'Surrogate-based acceleration of quasi-Newton techniques for fluid-structure interaction simulations', *Computers and Structures*, vol. 260, p. 106 720, 2022 (cit. on pp. 41, 63, 93).

[109] Dolfen, Henri, 'Deterministic and stochastic simulation of flow-induced vibrations in tube bundles', eng, Ph.D. dissertation, Ghent University, 2023, XXVI, 255 (cit. on p. 42).

[110] Delaissé, Nicolas, 'Development of fluid-structure interaction algorithms and application to elastohydrodynamic lubrication', eng, Ph.D. dissertation, Ghent University, 2023, XXXVIII, 248 (cit. on pp. 42, 43).

[111] J. Donea, A. Huerta, J. Ponthot and A. Rodríguez-Ferran, 'Arbitrary L agrangian– E ulerian Methods', in *Encyclopedia of Computational Mechanics*, Wiley, 2004 (cit. on pp. 43, 140, 163, 167).

[112] P. D. Thomas and C. K. Lombard, 'Geometric conservation law and its application to flow computations on moving grids', *AIAA Journal*, vol. 17, pp. 1030–1037, 10 1979 (cit. on p. 43).

[113] I. ANSYS, *Ansys fluent theory guide, release 2023*, Chapter on Mesh Motion / Dynamic Mesh Methods, 2023 (cit. on p. 45).

[114] Canè, Federico and Selmi, Matteo and De Santis, Gianluca and Redaelli, Alberto and Segers, Patrick and Degroote, Joris, 'Mixed impact of torsion on LV hemodynamics : a CFD study based on the Chimera technique', eng, *COMPUTERS IN BIOLOGY AND MEDICINE*, vol. 112, 12, 2019 (cit. on p. 45).

[115] Canè, Federico and Delcour, Lucas and Luigi Redaelli, Alberto Cesare and Segers, Patrick and Degroote, Joris, 'A CFD study on the interplay of torsion and vortex guidance by the mitral valve on the left ventricular washout making use of overset meshes (Chimera technique)', eng, *FRONTIERS IN MEDICAL TECHNOLOGY*, vol. 4, 17, 2022 (cit. on p. 45).

[116] M. G. Al-Azawy, A. Turan and A. Revell, 'An overset mesh approach for valve closure: An lvad application', in *Proceedings of the 9th International Joint Conference on Biomedical Engineering Systems and Technologies*, SCITEPRESS - Science, and Technology Publications, 2016, pp. 145–151 (cit. on p. 45).

[117] L. Wang et al., 'Role of biomechanical factors in plaque rupture and erosion: Insight from intravascular imaging based computational modeling', *npj Cardiovascular Health 2025 2:1*, vol. 2, pp. 1–11, 1 2025 (cit. on p. 46).

[118] J. J. Chiu and S. Chien, 'Effects of disturbed flow on vascular endothelium: Pathophysiological basis and clinical perspectives', *https://doi.org/10.1152/physrev.00047.2009*, vol. 91, pp. 327–387, 1 2011 (cit. on p. 46).

[119] J. Biasetti, F. Hussain and T. Christian Gasser, 'Blood flow and coherent vortices in the normal and aneurysmatic aortas: A fluid dynamical approach to intraluminal thrombus formation', *Journal of the Royal Society Interface*, vol. 8, no. 63, pp. 1449–1461, 2011 (cit. on pp. 46, 90).

[120] F. Gijsen et al., 'Expert recommendations on the assessment of wall shear stress in human coronary arteries: Existing methodologies, technical considerations, and clinical applications', *European Heart Journal*, vol. 40, pp. 3421–3433, 41 2019 (cit. on p. 46).

[121] H. Meng, V. M. Tutino, J. Xiang and A. Siddiqui, 'High WSS or Low WSS? Complex Interactions of Hemodynamics with Intracranial Aneurysm Initiation, Growth, and Rupture: Toward a Unifying Hypothesis', *American Journal of Neuroradiology*, vol. 35, no. 7, pp. 1254–1262, 2014 (cit. on p. 46).

[122] J. R. Cebral, F. Mut, J. Weir and C. M. Putman, 'Association of hemodynamic characteristics and cerebral aneurysm rupture', *American Journal of Neuroradiology*, vol. 32, pp. 264–270, 2 2011 (cit. on p. 46).

[123] P. D. Achille, G. Tellides, C. A. Figueroa and J. D. Humphrey, 'A haemodynamic predictor of intraluminal thrombus formation in abdominal aortic aneurysms', *Proceedings of the Royal Society A: Mathematical, Physical and Engineering Sciences*, vol. 470, 2172 2014 (cit. on p. 46).

[124] H. A. Himburg, D. M. Grzybowski, A. L. Hazel, J. A. LaMack, X.-M. Li and M. H. Friedman, 'Spatial comparison between wall shear stress measures and porcine arterial endothelial permeability', *American Journal of Physiology-Heart and Circulatory Physiology*, vol. 286, H1916–H1922, 5 2004 (cit. on p. 46).

[125] Y. Mohamied, S. J. Sherwin and P. D. Weinberg, 'Understanding the fluid mechanics behind transverse wall shear stress', *Journal of Biomechanics*, vol. 50, pp. 102–109, 2017 (cit. on p. 46).

[126] M. A. Abazari, D. Rafieianzab, M. Soltani and M. Alimohammadi, 'The effect of beta-blockers on hemodynamic parameters in patient-specific blood flow simulations of type-B aortic dissection: a virtual study', *Scientific Reports 2021 11:1*, vol. 11, no. 1, pp. 1–14, 2021 (cit. on pp. 46, 133).

[127] H. J. Carpenter, M. H. Ghayesh, A. C. Zander and P. J. Psaltis, 'On the nonlinear relationship between wall shear stress topology and multi-directionality in coronary atherosclerosis', *Computer Methods and Programs in Biomedicine*, vol. 231, 2023 (cit. on pp. 46, 67, 89, 150, 151).

[128] O. Mutlu, H. E. Salman, H. Al-Thani, A. El-Menyar, U. A. Qidwai and H. C. Yalcin, 'How does hemodynamics affect rupture tissue mechanics in abdominal aortic aneurysm: Focus on wall shear stress derived parameters, time-averaged wall shear stress, oscillatory shear index, endothelial cell activation potential, and relative residence time', *Computers in Biology and Medicine*, vol. 154, p. 106 609, 2023 (cit. on pp. 46, 47, 75).

[129] D. N. Ku, D. P. Giddens, C. K. Zarins and S. Glagov, 'Pulsatile flow and atherosclerosis in the human carotid bifurcation. Positive correlation between plaque location and low and oscillating shear stress', *Arteriosclerosis*, vol. 5, no. 3, pp. 293–302, 1985 (cit. on pp. 46, 49, 63).

[130] V. Mazzi et al., 'A Eulerian method to analyze wall shear stress fixed points and manifolds in cardiovascular flows', *Biomechanics and modeling in mechanobiology*, vol. 19, no. 5, pp. 1403–1423, 2020 (cit. on pp. 46–48, 57, 63–65, 67, 86, 89–91).

[131] V. Mazzi et al., 'Wall shear stress topological skeleton analysis in cardiovascular flows: Methods and applications', *Mathematics*, vol. 9, no. 7, 2021 (cit. on pp. 46, 48, 49, 63, 91).

[132] M Tobak and D. J. Peake, 'Topology of three-dimensional separated flows', *Annual Review of Fluid Mechanics*, vol. 14, pp. 61–85, 1 1982 (cit. on p. 46).

[133] S. Bailoor, J. H. Seo, S. Schena and R. Mittal, 'Changes in aorta hemodynamics in left-right type 1 bicuspid aortic valve patients after replacement with bioprosthetic valves: An in-silico study', *PLOS ONE*, vol. 19, e0301350, 4 2024 (cit. on p. 47).

[134] A. Gnasso et al., 'Association between intima-media thickness and wall shear stress in common carotid arteries in healthy male subjects', *Circulation*, vol. 94, no. 12, pp. 3257–3262, 1996 (cit. on pp. 47, 49, 75).

[135] Y. Yu et al., 'The orphan nuclear receptor Nur77 inhibits low shear stress-induced carotid artery remodeling in mice', *International Journal of Molecular Medicine*, vol. 36, no. 6, pp. 1547–1555, 2015 (cit. on p. 47).

[136] M. Rezaeitaleshmahalleh et al., 'Characterization of small abdominal aortic aneurysms' growth status using spatial pattern analysis of aneurismal hemodynamics', *Scientific Reports*, vol. 13, no. 1, p. 13 832, 2023 (cit. on pp. 47, 92).

[137] S. Jamaleddin Mousavi et al., 'Coupling hemodynamics with mechanobiology in patient-specific computational models of ascending thoracic aortic aneurysms', *Computer Methods and Programs in Biomedicine*, vol. 205, p. 106 107, 2021 (cit. on pp. 47, 92, 150).

[138] A. Arzani, A. M. Gambaruto, G. Chen and S. C. Shadden, 'Lagrangian wall shear stress structures and near-wall transport in high-Schmidt-number aneurysmal flows', *J. Fluid Mech*, vol. 790, pp. 158–172, 2016 (cit. on pp. 47, 64, 91).

[139] V. Mazzi et al., 'Early Atherosclerotic Changes in Coronary Arteries are Associated with Endothelium Shear Stress Contraction/Expansion Variability', *Annals of Biomedical Engineering*, vol. 49, no. 9, pp. 2606–2621, 2021 (cit. on pp. 48, 63, 68, 69, 91, 94, 150).

[140] G. De Nisco et al., 'Predicting Lipid-Rich Plaque Progression in Coronary Arteries Using Multimodal Imaging and Wall Shear Stress Signatures', *Arteriosclerosis, Thrombosis, and Vascular Biology*, vol. 44, pp. 976–986, 2024 (cit. on p. 48).

[141] U. Morbiducci et al., 'Wall Shear Stress Topological Skeleton Independently Predicts Long-Term Restenosis After Carotid Bifurcation Endarterectomy', *Annals of Biomedical Engineering*, vol. 48, no. 12, p. 2936, 2020 (cit. on pp. 48, 89, 91).

[142] G. De Nisco et al., 'Deciphering ascending thoracic aortic aneurysm hemodynamics in relation to biomechanical properties', *Medical Engineering & Physics*, vol. 82, pp. 119–129, 2020 (cit. on pp. 48, 67).

[143] N. Bappoo et al., 'Low shear stress at baseline predicts expansion and aneurysm-related events in patients with abdominal aortic aneurysm', *Circulation: Cardiovascular Imaging*, vol. 14, pp. 1112–1121, 12 2021 (cit. on p. 49).

[144] S. Chen, H. Zhang, Q. Hou, Y. Zhang and A. Qiao, 'Multiscale Modeling of Vascular Remodeling Induced by Wall Shear Stress', *Frontiers in Physiology*, vol. 12, p. 2543, 2022 (cit. on pp. 49, 157).

[145] J. D. Humphrey, J. F. Eberth, W. W. Dye and R. L. Gleason, 'Fundamental role of axial stress in compensatory adaptations by arteries', *Journal of Biomechanics*, vol. 42, pp. 1–8, 1 2009 (cit. on p. 50).

[146] A Valentín, J. D. Humphrey and G. A. Holzapfel, 'A Finite Element Based Constrained Mixture Implementation for Arterial Growth, Remodeling, and Adaptation: Theory and Numerical Verification', (cit. on p. 50).

[147] L. Maes, T. Vervenne, L. Van Hoof, E. A. Jones, F. Rega and N. Famaey, 'Computational modeling reveals inflammation-driven dilatation of the pulmonary autograft in aortic position', *Biomechanics and Modeling in Mechanobiology*, pp. 1–14, 2023 (cit. on pp. 50, 55, 56).

[148] K. V. Linden, M. Ghasemi, L. Maes, J. Vastmans and N. Famaey, 'Layer-specific fiber distribution in arterial tissue modeled as a constrained mixture', *International Journal for Numerical Methods in Biomedical Engineering*, vol. 39, e3608, 4 2023 (cit. on p. 51).

[149] T. Vervenne, L. Maes, L. V. Hoof, F. Rega and N. Famaey, 'Drivers of vascular growth and remodeling: A computational framework to promote benign adaptation in the ross procedure', *Journal of the Mechanical Behavior of Biomedical Materials*, vol. 148, p. 106 170, 2023 (cit. on p. 51).

[150] D Ambrosi et al., 'Perspectives on biological growth and remodeling', *Journal of the Mechanics and Physics of Solids*, vol. 59, no. 4, pp. 863–883, 2011 (cit. on p. 56).

[151] E. K. Rodriguez, A. Hoger and A. D. McCulloch, 'Stress-dependent finite growth in soft elastic tissues', *Journal of Biomechanics*, vol. 27, no. 4, pp. 455–467, 1994 (cit. on p. 56).

[152] C. J. Cyron, R. C. Aydin and J. D. Humphrey, 'A homogenized constrained mixture (and mechanical analog) model for growth and remodeling of soft tissue', *Biomechanics and Modeling in Mechanobiology*, vol. 15, no. 6, pp. 1389–1403, 2016 (cit. on p. 56).

[153] J. D. Humphrey, 'Constrained Mixture Models of Soft Tissue Growth and Remodeling – Twenty Years After', *Journal of Elasticity 2021 145:1*, vol. 145, no. 1, pp. 49–75, 2021 (cit. on p. 56).

[154] L. Maes and N. Famaey, 'How to implement constrained mixture growth and remodeling algorithms for soft biological tissues', *Journal of the Mechanical Behavior of Biomedical Materials*, vol. 140, p. 105 733, 2023 (cit. on p. 56).

[155] A. D. Wisneski, Z. Wang, Y. Xuan, J. M. Guccione, L. Ge and E. E. Tseng, 'Range of Pulmonary Autograft Responses to Systemic Pressure Immediately After Ross Procedure', *The Journal of heart valve disease*, vol. 28, no. 1, pp. 22–31, 2019 (cit. on p. 56).

[156] Y. Xuan et al., 'Wall stresses of early remodeled pulmonary autografts', *Journal of Thoracic and Cardiovascular Surgery*, vol. 164, no. 6, 1728–1738.e2, 2022 (cit. on p. 56).

[157] D. A. Shcherbakova et al., 'A finite element model to study the effect of tissue anisotropy on ex vivo arterial shear wave elastography measurements', *Physics in Medicine & Biology Phys. Med. Biol*, vol. 62, pp. 5245–5275, 2017 (cit. on p. 61).

[158] L. Taelman, J. Degroote, A. Swillens, J. Vierendeels and P. Segers, 'Fluid–structure interaction simulation of pulse propagation in arteries: Numerical pitfalls and hemodynamic impact of a local stiffening', *International Journal of Engineering Science*, vol. 77, pp. 1–13, 2014 (cit. on pp. 61, 138).

[159] S. Usami, S. Chien and M. I. Gregersen, 'Viscometric characteristics of blood of the elephant, man, dog, sheep, and goat.' *The American journal of physiology*, vol. 217, no. 3, pp. 884–890, 1969 (cit. on p. 61).

[160] R. I. Issa, 'Solution of the implicitly discretised fluid flow equations by operator-splitting', *Journal of Computational Physics*, vol. 62, no. 1, pp. 40–65, 1986 (cit. on pp. 62, 109).

[161] J. Donea, A. Huerta, J. Ponthot and A. Rodríguez-Ferran, 'Arbitrary Lagrangian–Eulerian Methods', in *Encyclopedia of Computational Mechanics Second Edition*, Wiley, 2017, pp. 1–23 (cit. on p. 63).

[162] D. Gallo, D. A. Steinman and U. Morbiducci, 'Insights into the co-localization of magnitude-based versus direction-based indicators of disturbed shear at the carotid bifurcation', *Journal of Biomechanics*, vol. 49, no. 12, pp. 2413–2419, 2016 (cit. on p. 68).

[163] J. Jeong and F. Hussain, 'On the identification of a vortex', *Journal of Fluid Mechanics*, vol. 285, pp. 69–94, 1995 (cit. on p. 69).

[164] A. Balasubramanya et al., 'Hemodynamics and wall shear metrics in a pulmonary autograft: Comparing a fluid-structure interaction and computational fluid dynamics approach', *Computers in Biology and Medicine*, vol. 176, p. 108 604, 2024 (cit. on pp. 86, 110, 111, 131, 140, 154).

[165] Z. Li and C. Kleinstreuer, 'A comparison between different asymmetric abdominal aortic aneurysm morphologies employing computational fluid-structure interaction analysis', *European Journal of Mechanics, B/Fluids*, vol. 26, no. 5, pp. 615–631, 2007 (cit. on p. 88).

[166] V. Mendez, M. Di Giuseppe and S. Pasta, 'Comparison of hemodynamic and structural indices of ascending thoracic aortic aneurysm as predicted by 2-way FSI, CFD rigid wall simulation and patient-specific displacement-based FEA', *Computers in Biology and Medicine*, vol. 100, pp. 221–229, 2018 (cit. on p. 88).

[167] S. Lin, X. Han, Y. Bi, S. Ju and L. Gu, 'Fluid-structure interaction in abdominal aortic aneurysm: Effect of modeling techniques', *BioMed Research International*, vol. 2017, pp. 1–10, 2017 (cit. on p. 88).

[168] N. T. Philip, B. S. Patnaik and B. J. Sudhir, 'Hemodynamic simulation of abdominal aortic aneurysm on idealised models: Investigation of stress parameters during disease progression', *Computer Methods and Programs in Biomedicine*, vol. 213, p. 106 508, 2022 (cit. on p. 88).

[169] J. H. Fonken, E. J. Maas, A. H. Nievergeld, M. R. van Sambeek, F. N. van de Vosse and R. G. Lopata, 'Ultrasound-Based Fluid-Structure Interaction Modeling of Abdominal Aortic Aneurysms Incorporating Pre-stress', *Frontiers in Physiology*, vol. 12, p. 717 593, 2021 (cit. on p. 88).

[170] D. De Wilde et al., 'Assessment of shear stress related parameters in the carotid bifurcation using mouse-specific FSI simulations', *Journal of Biomechanics*, pp. 1–8, 2015 (cit. on pp. 88, 89).

[171] S. Kumar, B. V. Kumar and S. K. Rai, 'Influence of abdominal aortic aneurysm shape on hemodynamics in human aortofemoral arteries: A transient open-loop study', *Physics of Fluids*, vol. 35, no. 4, 2023 (cit. on p. 88).

[172] M. Y. Salmasi et al., 'Geometry and flow in ascending aortic aneurysms are influenced by left ventricular outflow tract orientation: Detecting increased wall shear stress on the outer curve of proximal aortic aneurysms', *Journal of Thoracic and Cardiovascular Surgery*, vol. 166, no. 1, 11–21.e1, 2023 (cit. on pp. 88, 100).

[173] P. Eslami et al., 'Effect of Wall Elasticity on Hemodynamics and Wall Shear Stress in Patient-Specific Simulations in the Coronary Arteries', *Journal of Biomechanical Engineering*, vol. 142, no. 2, 2020 (cit. on pp. 89, 150).

[174] K. Caì et al., 'Impact of wall displacements on the large-scale flow coherence in ascending aorta', *Journal of Biomechanics*, vol. 154, p. 111 620, 2023 (cit. on pp. 89–91, 151).

[175] K. Natsume et al., 'Characterizing saccular aortic arch aneurysms from the geometry-flow dynamics relationship', *Journal of Thoracic and Cardiovascular Surgery*, vol. 153, no. 6, 1413–1420.e1, 2017 (cit. on p. 89).

[176] C. Stokes et al., 'A novel MRI-based data fusion methodology for efficient, personalised, compliant simulations of aortic haemodynamics', *Journal of Biomechanics*, vol. 129, no. September, p. 110 793, 2021 (cit. on p. 89).

[177] A. Arzani and S. C. Shadden, 'Characterizations and Correlations of Wall Shear Stress in Aneurysmal Flow', *Journal of Biomechanical Engineering*, vol. 138, no. 1, 2016 (cit. on pp. 89, 91).

[178] A. Arzani and S. C. Shadden, 'Wall shear stress fixed points in cardiovascular fluid mechanics', *Journal of Biomechanics*, vol. 73, pp. 145–152, 2018 (cit. on pp. 89, 153).

[179] S. J. Mousavi, S. Farzaneh and S. Avril, 'Patient-specific predictions of aneurysm growth and remodeling in the ascending thoracic aorta using the homogenized constrained mixture model', *Biomechanics and Modeling in Mechanobiology*, vol. 18, no. 6, pp. 1895–1913, 2019 (cit. on pp. 92, 158).

[180] R. Rotsaert, 'Development of a fluid-structure-growth framework for aortic adaptation in healthy aging', M.S. thesis, Ghent University, 2025, pp. 1–121 (cit. on p. 93).

[181] M. Latorre and J. D. Humphrey, 'A mechanobiologically equilibrated constrained mixture model for growth and remodeling of soft tissues', *ZAMM Zeitschrift fur Angewandte Mathematik und Mechanik*, vol. 98, pp. 2048–2071, 12 2018 (cit. on p. 93).

[182] A. Petuchova and A. Maknickas, 'Comparison of Newtonian and Non-Newtonian Blood Flow in an Ascending Aortic Aneurysm', *Computing in Cardiology*, no. Figure 1, pp. 1–4, 2022 (cit. on p. 94).

[183] S. Pirola et al., 'Computational study of aortic hemodynamics for patients with an abnormal aortic valve: The importance of secondary flow at the ascending aorta inlet', *APL Bioengineering*, vol. 2, 2 2018 (cit. on pp. 95, 154).

[184] M. Alimohammadi, O. Agu, S. Balabani and V. Díaz-Zuccarini, 'Development of a patient-specific simulation tool to analyse aortic dissections: Assessment of mixed patient-specific flow and pressure boundary conditions', *Medical Engineering & Physics*, vol. 36, pp. 275–284, 2014 (cit. on p. 97).

[185] S. Yang et al., 'Abdominal aortic intimal flap motion characterization in acute aortic dissection: assessed with retrospective ECG-gated thoracoabdominal aorta dual-source CT angiography.' *PloS one*, vol. 9, no. 2, e87664, 2014 (cit. on pp. 99–101, 122, 123, 163).

[186] Y. Y. Ge et al., 'Preoperative thoracic false lumen branches relate to aortic remodeling after thoracic endovascular aortic repair for DeBakey IIIb aortic dissection', *Journal of Vascular Surgery*, vol. 65, no. 3, 659–668.e2, 2017 (cit. on pp. 100, 101).

[187] G. Logghe et al., 'Outflow Through Aortic Side Branches Drives False Lumen Patency in Type B Aortic Dissection.' *Frontiers in cardiovascular medicine*, vol. 8, p. 710 603, 2021 (cit. on pp. 100, 101, 120).

[188] D. J. Martin, T. D. Martin, P. J. Hess, M. J. Daniels, R. J. Feezor and W. A. Lee, 'Spinal cord ischemia after TEVAR in patients with abdominal aortic aneurysms', *Journal of Vascular Surgery*, vol. 49, no. 2, pp. 302–306, 2009 (cit. on p. 100).

[189] A. M. Sailer et al., 'Computed Tomography Imaging Features in Acute Uncomplicated Stanford Type-B Aortic Dissection Predict Late Adverse Events.' *Circulation. Cardiovascular imaging*, vol. 10, no. 4, 2017 (cit. on pp. 100, 120).

[190] A. V. Kamman et al., 'Predictors of aortic growth in uncomplicated type B aortic dissection from the Acute Dissection Stent Grafting or Best Medical Treatment (ADSORB) database', *Journal of Vascular Surgery*, vol. 65, no. 4, 964–971.e3, 2017 (cit. on pp. 100, 120).

[191] P. Ryzhakov, E. Soudah and N. Dialami, 'Computational modeling of the fluid flow and the flexible intimal flap in type B aortic dissection via a monolithic arbitrary Lagrangian/Eulerian fluid-structure interaction model', *International Journal for Numerical Methods in Biomedical Engineering*, vol. 35, no. 11, e3239, 2019 (cit. on pp. 100, 103).

[192] H. Keramati, E. Birgersson, J. P. Ho, S. Kim, K. J. Chua and H. L. Leo, 'The effect of the entry and re-entry size in the aortic dissection: a two-way fluid-structure interaction simulation.' *Biomechanics and modeling in mechanobiology*, vol. 19, no. 6, pp. 2643–2656, 2020 (cit. on pp. 100, 103, 109, 154).

[193] T. Kim et al., 'A computational study of dynamic obstruction in type b aortic dissection', *Journal of biomechanical engineering*, vol. 145, 3 2023 (cit. on pp. 100, 103).

[194] M. Y. Chong, B. Gu, B. T. Chan, Z. C. Ong, X. Y. Xu and E. Lim, 'Effect of intimal flap motion on flow in acute type B aortic dissection by using fluid-structure interaction', *International Journal for Numerical Methods in Biomedical Engineering*, vol. 36, no. 12, 2020 (cit. on pp. 100, 101, 103, 122, 123, 151, 168).

[195] M. Y. Chong et al., 'An integrated fluid-structure interaction and thrombosis model for type B aortic dissection', vol. 21, pp. 261–275, 2022 (cit. on pp. 100, 103, 127).

[196] M. Alimohammadi, J. M. Sherwood, M. Karimpour, O. Agu, S. Balabani and V. Díaz-Zuccarini, 'Aortic dissection simulation models for clinical support: fluid-structure interaction vs. rigid wall models.' *Biomedical engineering online*, vol. 14, no. 1, p. 34, 2015 (cit. on pp. 100, 104).

[197] R. Schussnig, M. Rolf-Pissarczyk, K. Bäumler, T. P. Fries, G. A. Holzapfel and M. Kronbichler, 'On the role of tissue mechanics in fluid–structure interaction simulations of patient-specific aortic dissection', *International Journal for Numerical Methods in Engineering*, vol. 125, no. 14, e7478, 2024 (cit. on pp. 101, 104, 122, 123, 151).

[198] K. Bäumler et al., 'Assessment of aortic dissection remodeling with patient-specific fluid-structure interaction models', *IEEE Transactions on Biomedical Engineering*, pp. 1–17, 2024 (cit. on pp. 101, 123).

[199] C. H. Armour, C. Menichini, L. Hanna, R. G. J. Gibbs and X. Y. Xu, 'Computational Modeling of Flow and Thrombus Formation in Type B Aortic Dissection: The Influence of False Lumen Perfused Side Branches', in *Studies in Mechanobiology, Tissue Engineering and Biomaterials*, vol. 24, Springer Science and Business Media Deutschland GmbH, 2022, pp. 53–72 (cit. on p. 101).

[200] H. Chen et al., 'Editor's Choice – Fluid–Structure Interaction Simulations of Aortic Dissection with Bench Validation', *European Journal of Vascular and Endovascular Surgery*, vol. 52, no. 5, pp. 589–595, 2016 (cit. on p. 103).

[201] H. Keramati, E. Birgersson, S. Kim, J. P. Ho and H. L. Leo, 'Using a reduced-order model to investigate the effect of the heart rate on the aortic dissection', *International Journal for Numerical Methods in Biomedical Engineering*, vol. 38, no. 6, e3596, 2022 (cit. on p. 103).

[202] G. H. Lee et al., 'Fluid–structure interaction simulation of visceral perfusion and impact of different cannulation methods on aortic dissection', *Scientific Reports 2023 13:1*, vol. 13, no. 1, pp. 1–15, 2023 (cit. on p. 103).

[203] V. Deplano and C. Guivier-Curien, 'Fluid-structure interaction in aortic dissections', *Biomechanics of the Aorta*, pp. 547–568, 2024 (cit. on pp. 104, 168).

[204] F. Khannous, C. Guivier-Curien, M. Gaudry, P. Piquet and V. Deplano, 'Residual type B aortic dissection FSI modeling', *Computer Methods in Biomechanics and Biomedical Engineering*, vol. 23, no. sup1, S153–S155, 2020 (cit. on p. 104).

[205] Y. Qiao, Y. Zeng, Y. Ding, J. Fan, K. Luo and T. Zhu, 'Numerical simulation of two-phase non-Newtonian blood flow with fluid-structure interaction in aortic dissection', *Computer Methods in Biomechanics and Biomedical Engineering*, vol. 22, no. 6, pp. 620–630, 2019 (cit. on p. 104).

[206] J. Zimmermann et al., 'Hemodynamic effects of entry and exit tear size in aortic dissection evaluated with in vitro magnetic resonance imaging and fluid–structure interaction simulation', *Scientific Reports 2023 13:1*, vol. 13, no. 1, pp. 1–15, 2023 (cit. on pp. 104, 122).

[207] F. U. Mattace-Raso et al., 'Determinants of pulse wave velocity in healthy people and in the presence of cardiovascular risk factors: 'establishing normal and reference values'', *European Heart Journal*, vol. 31, no. 19, pp. 2338–2350, 2010 (cit. on p. 105).

[208] S. Wu et al., 'Age-related differences in acute aortic dissection', *Journal of vascular surgery*, vol. 75, no. 2, 473–483.e4, 2022 (cit. on p. 105).

[209] M. Amabili, P. Balasubramanian, I. Bozzo, I. D. Breslavsky and G. Ferrari, 'Layer-specific hyperelastic and viscoelastic characterization of human descending thoracic aortas.' *Journal of the mechanical behavior of biomedical materials*, vol. 99, pp. 27–46, 2019 (cit. on p. 107).

[210] B. L. McComb, R. F. Munden, F. Duan, A. A. Jain, C. Tuite and C. Chiles, 'Normative reference values of thoracic aortic diameter in American College of Radiology Imaging Network (ACRIN 6654) arm of National Lung Screening Trial', *Clinical Imaging*, vol. 40, no. 5, pp. 936–943, 2016 (cit. on p. 107).

[211] A. Khoynezhad, I. Walot, M. J. Kruse, T. Rapae, C. E. Donayre and R. A. White, 'Distribution of intimomedial tears in patients with type B aortic dissection', *Journal of Vascular Surgery*, vol. 52, no. 3, pp. 562–568, 2010 (cit. on pp. 107, 124).

[212] Z. Cheng, C. Juli, N. B. Wood, R. G. Gibbs and X. Y. Xu, 'Predicting flow in aortic dissection: Comparison of computational model with PC-MRI velocity measurements', *Medical Engineering & Physics*, vol. 36, no. 9, pp. 1176–1184, 2014 (cit. on p. 109).

[213] H. Xu et al., 'Computed tomography-based hemodynamic index for aortic dissection', *The Journal of Thoracic and Cardiovascular Surgery*, vol. 162, no. 2, e165–e176, 2021 (cit. on pp. 112, 122).

[214] A. Balasubramanya, L. Gheysen, M. U. Wagenhäuser, N. Famaey, J. Degroote and P. Segers, 'Hemodynamics in aortic dissections: A fluid-solid interaction study in an idealized dissection model with a false lumen side branch', *Journal of Biomechanics*, p. 112 771, 2025 (cit. on pp. 115, 118, 125, 139–141, 151, 154).

[215] J. Birjiniuk et al., 'Pulsatile Flow Leads to Intimal Flap Motion and Flow Reversal in an In Vitro Model of Type B Aortic Dissection', *Cardiovascular Engineering and Technology*, vol. 8, no. 3, pp. 378–389, 2017 (cit. on p. 122).

[216] T. T. Tsai et al., 'Tear size and location impacts false lumen pressure in an ex vivo model of chronic type B aortic dissection.' *Journal of vascular surgery*, vol. 47, no. 4, pp. 844–51, 2008 (cit. on p. 124).

[217] S. Pirola et al., 'On the choice of outlet boundary conditions for patient-specific analysis of aortic flow using computational fluid dynamics', *Journal of Biomechanics*, vol. 60, pp. 15–21, 2017 (cit. on pp. 124, 155).

[218] P Segers et al., 'Pulmonary arterial compliance in dogs and pigs: the three-element windkessel model revisited.' *The American journal of physiology*, vol. 277, no. 2, H725–31, 1999 (cit. on p. 125).

[219] B. Mees, D. Robinson, H. Verhagen and J. Chuen, 'Non-aortic aneurysms - natural history and recommendations for referral and treatment.' *Australian family physician*, vol. 42, no. 6, pp. 370–4, 2013 (cit. on p. 125).

[220] A. Aghilinejad, H. Wei, G. A. Magee and N. M. Pahlevan, 'Model-Based Fluid-Structure Interaction Approach for Evaluation of Thoracic Endovascular Aortic Repair Endograft Length in Type B Aortic Dissection', *Frontiers in Bioengineering and Biotechnology*, vol. 10, p. 825 015, 2022 (cit. on p. 125).

[221] C. Menichini and X. Y. Xu, 'Mathematical modeling of thrombus formation in idealized models of aortic dissection: initial findings and potential applications', *Journal of Mathematical Biology*, vol. 73, no. 5, pp. 1205–1226, 2016 (cit. on p. 127).

[222] A. Jafarinia, C. H. Armour, R. G. J. Gibbs, X. Y. Xu and T. Hochrainer, 'Shear-driven modelling of thrombus formation in type B aortic dissection', *Frontiers in Bioengineering and Biotechnology*, vol. 10, 2022 (cit. on p. 127).

[223] P. J. Roache, 'Quantification of uncertainity in computational fluid dynamics', *Annual Review of Fluid Mechanics*, vol. 29, no. 1, pp. 123–160, 1997 (cit. on pp. 127, 128).

[224] J. Peacock, T. Jones, C. Tock and R. Lutz, 'The onset of turbulence in physiological pulsatile flow in a straight tube', *Experiments in Fluids*, vol. 24, no. 1, pp. 1–9, 1998 (cit. on p. 133).

[225] J. R. Womersley, 'Method for the calculation of velocity, rate of flow and viscous drag in arteries when the pressure gradient is known', *The Journal of Physiology*, vol. 127, no. 3, pp. 553–563, 1955 (cit. on p. 133).

[226] A. F. Stalder et al., 'Assessment of flow instabilities in the healthy aorta using flow-sensitive MRI', *Journal of Magnetic Resonance Imaging*, vol. 33, no. 4, pp. 839–846, 2011 (cit. on p. 133).

[227] J. P. Mynard, A. Kondiboyina, R. Kowalski, M. M. H. Cheung and J. J. Smolich, 'Measurement, Analysis and Interpretation of Pressure/Flow Waves in Blood Vessels', *Frontiers in Physiology*, vol. 11, pp. 1–26, 2020 (cit. on pp. 137, 138, 141).

[228] J. Alastruey et al., 'Pulse wave propagation in a model human arterial network: Assessment of 1-d visco-elastic simulations against in vitro measurements', *Journal of Biomechanics*, vol. 44, pp. 2250–2258, 12 2011 (cit. on p. 138).

[229] J. P. Mynard and J. J. Smolich, 'One-dimensional haemodynamic modeling and wave dynamics in the entire adult circulation', *Annals of Biomedical Engineering*, vol. 43, pp. 1443–1460, 6 2015 (cit. on p. 138).

[230] A. Swillens, L. Taelman, J. Degroote, J. Vierendeels and P. Segers, 'Comparison of non-invasive methods for measurement of local pulse wave velocity using fsi-simulations and in vivo data', *Annals of Biomedical Engineering*, vol. 41, pp. 1567–1578, 7 2013 (cit. on p. 138).

[231] H. Chen, Q. Chi, Y. He, L. Mu and Y. Luan, 'Effects of size and location of distal tear on hemodynamics and wave propagation in type B aortic dissection', *Applied Mathematics and Mechanics*, vol. 43, no. 9, pp. 1449–1468, 2022 (cit. on p. 138).

[232] P. Segers, A. Swillens, L. Taelman and J. Vierendeels, 'Wave reflection leads to over- and underestimation of local wave speed by the PU- and QA-loop methods: theoretical basis and solution to the problem', *Physiological Measurement*, vol. 35, no. 5, pp. 847–861, 2014 (cit. on p. 140).

[233] G. E. P. Box, 'Science and statistics', *Journal of the American Statistical Association*, vol. 71, no. 356, pp. 791–799, 1976 (cit. on p. 149).

[234] M. Bonfanti, S. Balabani, M. Alimohammadi, O. Agu, S. Homer-Vanniasinkam and V. Diaz-Zuccarini, 'A simplified method to account for wall motion in patient-specific blood flow simulations of aortic dissection: Comparison with fluid-structure interaction', *Medical Engineering & Physics*, vol. 58, pp. 72–79, 2018 (cit. on p. 151).

[235] V. M. Belvroy et al., 'Tortuosity of the Descending Thoracic Aorta in Patients with Aneurysm and Type B Dissection', *World Journal of Surgery*, vol. 44, no. 4, pp. 1323–1330, 2020 (cit. on p. 153).

[236] R. E. Clough, M. Waltham, D. Giese, P. R. Taylor and T. Schaeffter, 'A new imaging method for assessment of aortic dissection using four-dimensional phase contrast magnetic resonance imaging', *Journal of Vascular Surgery*, vol. 55, no. 4, pp. 914–923, 2012 (cit. on p. 153).

[237] K. M. Saqr et al., 'Physiologic blood flow is turbulent', *Scientific Reports*, vol. 10, no. 1, p. 15 492, 2020 (cit. on p. 153).

[238] A. Benim, A. Nahavandi, A. Assmann, D. Schubert, P. Feindt and S. Suh, 'Simulation of blood flow in human aorta with emphasis on outlet boundary conditions', *Applied Mathematical Modelling*, vol. 35, no. 7, pp. 3175–3188, 2011 (cit. on p. 153).

[239] Mancini, Viviana and Bergersen, Aslak W. and Vierendeels, Jan and Segers, Patrick and Valen-Sendstad, Kristian, 'High-frequency fluctuations in post-stenotic patient specific carotid stenosis fluid dynamics : a computational fluid dynamics strategy study', eng, *CARDIOVASCULAR ENGINEERING AND TECHNOLOGY*, vol. 10, no. 2, 277–298, 2019 (cit. on p. 153).

[240] V. Thondapu et al., 'Non-Newtonian Endothelial Shear Stress Simulation: Does It Matter?', *Frontiers in Cardiovascular Medicine*, vol. 9, 2022 (cit. on p. 153).

[241] V. Deplano et al., 'Mechanical characterisation of human ascending aorta dissection', *Journal of Biomechanics*, vol. 94, pp. 138–146, 2019 (cit. on p. 154).

[242] U. Morbiducci, R. Ponzini, D. Gallo, C. Bignardi and G. Rizzo, 'Inflow boundary conditions for image-based computational hemodynamics: Impact of idealized versus measured velocity profiles in the human aorta', *Journal of Biomechanics*, vol. 46, no. 1, pp. 102–109, 2013 (cit. on p. 154).

[243] P. Youssefi, A. Gomez, C. Arthurs, R. Sharma, M. Jahangiri and C. Alberto Figueroa, 'Impact of Patient-Specific Inflow Velocity Profile on Hemodynamics of the Thoracic Aorta', *Journal of Biomechanical Engineering*, vol. 140, no. 1, 2018 (cit. on p. 154).

[244] K. Tsaneva-Atanasova, G. Pederzanil and M. Laviola, 'Decoding uncertainty for clinical decision-making', *Philosophical Transactions of the Royal Society A: Mathematical, Physical and Engineering Sciences*, vol. 383, no. 2292, 2025 (cit. on p. 156).

[245] L. Gheysen, L. Maes, A. Caenen, P. Segers, M. Peirlinck and N. Famaey, 'Uncertainty quantification of the wall thickness and stiffness in an idealized dissected aorta', *Journal of the Mechanical Behavior of Biomedical Materials*, vol. 151, p. 106 370, 2024 (cit. on p. 156).

[246] B. M. Fanni, M. N. Antonuccio, A. Pizzuto, S. Berti, G. Santoro and S. Celi, 'Uncertainty Quantification in the In Vivo Image-Based Estimation of Local Elastic Properties of Vascular Walls', *Journal of Cardiovascular Development and Disease*, vol. 10, no. 3, p. 109, 2023 (cit. on p. 156).

[247] S. C. Y. Lo, J. W. S. McCullough, X. Xue and P. V. Coveney, 'Uncertainty quantification of the impact of peripheral arterial disease on abdominal aortic aneurysms in blood flow simulations', *Journal of The Royal Society Interface*, vol. 21, no. 213, 2024 (cit. on p. 156).

[248] M. N. Antonuccio et al., 'Effects of Uncertainty of Outlet Boundary Conditions in a Patient-Specific Case of Aortic Coarctation', *Annals of Biomedical Engineering*, vol. 49, no. 12, pp. 3494–3507, 2021 (cit. on p. 156).

[249] C. M. Fleeter, G. Geraci, D. E. Schiavazzi, A. M. Kahn and A. L. Marsden, 'Multilevel and multifidelity uncertainty quantification for cardiovascular hemodynamics', *Computer Methods in Applied Mechanics and Engineering*, vol. 365, p. 113 030, 2020 (cit. on p. 157).

[250] F. Schäfer, D. E. Schiavazzi, L. R. Hellevik and J. Sturdy, 'Global sensitivity analysis with multifidelity Monte Carlo and polynomial chaos expansion for vascular haemodynamics', *International Journal for Numerical Methods in Biomedical Engineering*, vol. 40, no. 8, 2024 (cit. on p. 157).

[251] K. Sel et al., 'Building Digital Twins for Cardiovascular Health: From Principles to Clinical Impact', *Journal of the American Heart Association*, vol. 13, no. 19, 2024 (cit. on p. 157).

[252] G. Coorey et al., 'The health digital twin to tackle cardiovascular disease—a review of an emerging interdisciplinary field', *npj Digital Medicine*, vol. 5, no. 1, p. 126, 2022 (cit. on p. 157).

[253] P. M. Thangaraj, S. H. Benson, E. K. Oikonomou, F. W. Asselbergs and R. Khera, 'Cardiovascular care with digital twin technology in the era of generative artificial intelligence', *European Heart Journal*, vol. 45, no. 45, pp. 4808–4821, 2024 (cit. on p. 157).

[254] E. L. Schwarz, L. Pegolotti, M. R. Pfaller and A. L. Marsden, 'Beyond cfd: Emerging methodologies for predictive simulation in cardiovascular health and disease', *Biophysics Reviews*, vol. 4, no. 1, 2023 (cit. on pp. 157, 159).

[255] L. Maes et al., 'Cell signaling and tissue remodeling in the pulmonary autograft after the Ross procedure: A computational study', *Journal of Biomechanics*, vol. 171, p. 112 180, 2024 (cit. on p. 157).

[256] A. Corti, C. Chiastra, M. Colombo, M. Garbey, F. Migliavacca and S. Casarin, 'A fully coupled computational fluid dynamics – agent-based model of atherosclerotic plaque development: Multiscale modeling framework and parameter sensitivity analysis', *Computers in Biology and Medicine*, vol. 118, p. 103 623, 2020 (cit. on pp. 157, 158).

[257] A. Corti, M. Colombo, F. Migliavacca, J. F. Rodriguez Matas, S. Casarin and C. Chiastra, 'Multiscale Computational Modeling of Vascular Adaptation: A Systems Biology Approach Using Agent-Based Models', *Frontiers in Bioengineering and Biotechnology*, vol. 9, 2021 (cit. on p. 157).

[258] N. Hampwaye et al., 'Growth in a two-dimensional model of coarctation of the aorta: A CFD-informed agent based model', *Journal of Biomechanics*, vol. 182, p. 112 514, 2025 (cit. on p. 157).

[259] J. Warren, A. Corti, C. A. Meyer and H. N. Hayenga, 'Bridging hemodynamics, tissue mechanics, and pathophysiology in coronary artery disease: A new agent-based model with tetrahedral mesh integration', *Journal of Biomechanics*, vol. 183, p. 112 631, 2025 (cit. on p. 157).

[260] G. E. Moore, 'Cramming more components onto integrated circuits, reprinted from electronics, volume 38, number 8, april 19, 1965, pp.114 ff.' *IEEE Solid-State Circuits Society Newsletter*, vol. 11, no. 3, pp. 33–35, 2006 (cit. on p. 158).

[261] P. Ma, L. Cai, X. Wang and H. Gao, *Fully gpu-accelerated, matrix-free immersed boundary method for complex fiber-reinforced hyperelastic cardiac models*, 2025 (cit. on p. 158).

[262] Z. A. Saib, F. Abed, M. H. Ghayesh and M. Amabili, 'A review of fluid-structure interaction: Blood flow in arteries', *Biomedical Engineering Advances*, vol. 9, p. 100 171, 2025 (cit. on p. 158).

[263] P. Berg et al., 'The Computational Fluid Dynamics Rupture Challenge 2013—Phase II: Variability of Hemodynamic Simulations in Two Intracranial Aneurysms', *Journal of Biomechanical Engineering*, vol. 137, no. 12, 2015 (cit. on p. 159).

[264] K. Valen-Sendstad et al., 'Real-World Variability in the Prediction of Intracranial Aneurysm Wall Shear Stress: The 2015 International Aneurysm CFD Challenge', *Cardiovascular Engineering and Technology*, vol. 9, no. 4, pp. 544–564, 2018 (cit. on p. 159).

[265] M. Raissi, P. Perdikaris and G. Karniadakis, 'Physics-informed neural networks: A deep learning framework for solving forward and inverse problems involving nonlinear partial differential equations', *Journal of Computational Physics*, vol. 378, pp. 686–707, 2019 (cit. on p. 160).

[266] S. Markidis, 'The Old and the New: Can Physics-Informed Deep-Learning Replace Traditional Linear Solvers?', *Frontiers in Big Data*, vol. 4, 2021 (cit. on p. 160).

[267] A. Arzani, J.-X. Wang and R. M. D'Souza, 'Uncovering near-wall blood flow from sparse data with physics-informed neural networks', *Physics of Fluids*, vol. 33, no. 7, 2021 (cit. on p. 160).

[268] N. Alzhanov, E. Y. K. Ng and Y. Zhao, 'Hybrid CFD PINN FSI Simulation in Coronary Artery Trees', *Fluids*, vol. 9, no. 12, p. 280, 2024 (cit. on p. 160).

[269] M. A. Ur Rehman et al., 'Fluid–structure interaction analysis of pulsatile flow in arterial aneurysms with physics-informed neural networks and computational fluid dynamics', *Physics of Fluids*, vol. 37, no. 3, 2025 (cit. on p. 160).

[270] H. Zhang, R. H. Chan and X.-C. Tai, 'A Meshless Solver for Blood Flow Simulations in Elastic Vessels Using a Physics-Informed Neural Network', *SIAM Journal on Scientific Computing*, vol. 46, no. 4, pp. C479–C507, 2024 (cit. on p. 160).

[271] X. Chen et al., ‘Hemodynamics modeling with physics-informed neural networks: A progressive boundary complexity approach’, *Computer Methods in Applied Mechanics and Engineering*, vol. 438, p. 117 851, 2025 (cit. on p. 160).